DISSERTATION

zur
Erlangung der Doktorwürde (Dr. rer. nat.)
der
Naturwissenschaftlich-Mathematischen Gesamtfakultät
der
Ruprecht-Karls-Universität Heidelberg

vorgelegt von

Maximilian Brohmann

aus Pinneberg

Tag der mündlichen Prüfung
18. Dezember 2020

Investigation and Modification of Charge Transport in Semiconducting Carbon Nanotube Networks

Gutachter

Prof. Dr. Jana Zaumseil

Prof. Dr. Martijn Kemerink

DANKSAGUNG

Diese Dissertation und die vergangenen Jahre wissenschaftlicher Arbeit wären ohne die großartige Hilfe, Anleitung, Zusammenarbeit und Unterstützung vieler Personen nicht möglich gewesen, denen ich an dieser Stelle danken möchte.

Zuerst möchte ich mich bei *Prof. Jana Zaumseil* für die Möglichkeit bedanken, meine Arbeit zu einem spannenden, interdisziplinären Forschungsthema in ihrer Arbeitsgruppe anfertigen zu können. Danke, *Jana*, für die damalige Einladung nach Heidelberg und das mir vorab entgegengebrachte Vertrauen. Danke für Deinen fachlichen Rat, Dein fortwährendes Interesse an meiner Arbeit, das Vorleben hoher wissenschaftlicher Standards, die Gelegenheiten, früh Verantwortung zu übernehmen, die Möglichkeit, meine Forschungsergebnisse auf etlichen internationalen Konferenzen vorzustellen sowie Deine stets offene Tür.

Vielen Dank auch an *Prof. Martijn Kemerink* für die bereitwillige Übernahme des Zweitgutachtens.

Ein großer Dank gilt meinen ehemaligen Kollegen der *Nanomaterials for Optoelectronics* (NMOE)-Gruppe für die großartige Zusammenarbeit sowie die vielen tollen Erlebnisse während und nach der Arbeit, aus denen sich zudem einige gute Freundschaften entwickelt haben. In diesem Zusammenhang möchte ich die folgenden Personen besonders hervorheben: danke, *Marcel Rother*, für die herzliche Aufnahme in Heidelberg, die vielen Unterweisungen, u.a. in das Aerosol-Jet-Drucken und die Lithographie, sowie unsere (Dienst-)Reise nach Brasilien. Danke an *Stefan Schießl* für die umfassende Einarbeitung in die Welt der SWNT-Netzwerktransistoren, die Erstellung des Simulationsprogramms und weitere bedeutende Vorarbeiten zum Thema Ladungstransport. Danke, *Severin Schneider*, für die stetige Steigerung unseres mehr oder weniger nützlichen Allgemeinwissens, Nachhilfe in Kulinarik und das sehr hilfreiche gegenseitige Sparring. Danke an *Martin Held* für die Einarbeitung in die nicht unaufwendige Pflege der ALD, spätere Ferndiagnosen hierzu sowie die unverhoffte Nachtwanderung durch Schnee auf der Zugspitze. Danke, *Maik Matthiesen*, für die jahrelange Kameradschaft seit Beginn unseres Studiums und die Einführung in die Sternenkunde. Danke an *Kevin Synnatschke* für das Beispiel, dass wenig Schlaf und ein hohes Arbeitspensum nicht als Ausreden zählen. Danke, *Arko Graf*, für das Aufbauen der (6,5) SWNT-Produktion und die sportliche Herausforderung beim Bouldern und Laufen. Den anderen Mitgliedern und Alumni der NMOE-Gruppe: *Stefan Grimm*, *Yuriy Zakharko*, *Andreas Malhofer*, *Thomas Higgins*, *Fabian Paulus*, *Katelyn Goetz*, *Felix Berger*, *Jan Lüttgens*, *Vaishnavi Rao*, *Merve Balcı*, *Daniel Heimfarth*, *Jan Gotthardt* und *Nicolas Zorn* danke ich für die schöne Zeit, die große Hilfsbereitschaft sowie viele nette Mittags- und Kaffeepausen und Feierabendaktivitäten.

Gleiches gilt für die weiteren Mitglieder der *Physchem2D*-Gruppe: *Claudia Backes*, *Farnia Rashvand*, *Beata Szydłowska*, *Maximilian Krings*, *Sebastian Grieger* und *Steffen Ott*.

Als nächstes möchte ich meinen Studenten danken, deren Abschlussarbeiten oder Praktika ich betreuen durfte: danke, *Thines Kanagasundaram*, *Eric Winter*, *Erik Filbeck*, *Niklas Hermann*, *Simon Angstenberger* und *Sonja Wieland* für die wissenschaftlichen Ergebnisse sowie die Möglichkeit, während dieser Zeit selbst viel dazuzulernen.

Ein spezieller Dank geht an meine Korrekturleser *Severin*, *Martin* und *Sonja*, die sich die Zeit genommen haben, diese Arbeit von vielen mehr oder weniger kleinen Fehlern zu befreien.

Des Weiteren danke ich den Mitarbeitern des Lehrstuhls für Angewandte Physikalische Chemie für die angenehme und unkomplizierte Zusammenarbeit. Danke an *Karin Jordan*, *Swetlana Duchnay* und *Benjamin Scherke* für die Hilfe bei allerlei Verwaltungsthemen und an *Günter Meinusch*, *Peter Jeschka* und *Reinhold Jehle* für die enorme Unterstützung bei technischen Problemen und die oftmals sehr schnelle Lösungsfindung. In diesem Zusammenhang möchte ich außerdem *Klaus Schmitt* und den weiteren Kollegen der Feinmechanikwerkstatt danken.

Zudem danke ich *Stefan Kauschke* sowie *Olaf Skibbe* für die Zusammenarbeit und die Organisation des Reinraum-Betriebs am Center for Advanced Materials.

Ein weiteres Dankeschön geht an meine Familie, insbesondere meine Eltern *Sabine* und *Jörg* sowie meine Oma *Dorothea*, für die kontinuierliche Unterstützung und die Ermöglichung meines bisherigen Werdegangs. Des Weiteren danke ich meinen Freunden aus der Heimat für die schöne gemeinsame Zeit sowie die Ablenkung und dafür, dass wir uns in all den Jahren nicht aus den Augen verloren haben.

Mein besonderer Dank gilt meiner Freundin *Constanze* für ihre unermüdliche Unterstützung, Geduld und den Rückhalt während meiner aktiven Promotionszeit und insbesondere in den letzten Monaten vor der Fertigstellung dieser Arbeit. Danke für alles.

ABSTRACT

The extraordinary mechanical and charge transport properties of semiconducting single-walled carbon nanotubes (SWNTs) make them a promising material for solution-processable, flexible and stretchable electronics. Many of these remarkable features are even obtained in randomly-oriented SWNT networks that are compatible with established large-scale thin-film processes based on printing techniques or optical lithography. Given the enormous progress in the purification of solely semiconducting nanotubes as well as in the preparation of SWNT networks with a uniform and defined morphology in recent years, their widespread application as active layers in field-effect transistors (FETs) has become feasible. Likewise, this progress raised subsequent questions of what key parameters determine the charge transport processes across these networks and how they can further be optimized.

This thesis investigates charge transport and its limitations in polymer-sorted semiconducting SWNT networks with a focus on the precise nanotube network composition. The employed FET geometry enabled a reproducible and undistorted analysis of composition- and temperature-dependent transport parameters such as the charge carrier mobility. A comparison between nanotube networks with various selected or even precisely defined SWNT species distributions and average tube diameters reveals that additional energy barriers created at the junctions of adjacent nanotubes with different diameters result in inferior transport properties. While the network charge transport was formerly considered to be solely limited by the charge transfer across these inter-nanotube junctions, the results of this work imply that also the transport within each individual SWNT is important. The specific diameter dependence of this intra-nanotube transport can rationalize the substantially higher carrier mobilities observed for large-diameter networks with a certain SWNT bandgap distribution compared to monochiral networks that contain only a single small-diameter nanotube species. These findings suggest that composition optimizations for SWNT network FETs with maximum carrier mobilities should aim at monochiral large-diameter nanotubes.

Aside from insights into the underlying transport mechanisms, this work demonstrates a novel approach to intentionally modify charge transport in semiconducting SWNT network FETs by adding photochromic spiropyran compounds to the dielectric layer. The strong impact of the spiropyran and its photoinduced isomerization to merocyanine on the charge carrier mobilities give these transistors the properties of basic optical memory devices. Upon UV illumination the carrier mobilities are severely reduced until their recovery is induced by annealing or illumination with visible light. This implemented light responsiveness illustrates the fundamental suitability of SWNT network FETs for multifunctional applications beyond integrated circuits.

KURZFASSUNG

Die außergewöhnlichen mechanischen und Ladungstransporteigenschaften von halbleitenden einwandigen Kohlenstoffnanoröhren (engl. *Single-Walled Carbon Nanotubes*, SWNTs) machen diese zu einem vielversprechenden Material für lösungsprozessierbare, flexible und dehnbare elektronischer Bauteile. Viele dieser bemerkenswerten Eigenschaften bleiben selbst in zufällig ausgerichteten, halbleitenden Kohlenstoffnanoröhrennetzwerken erhalten, welche zudem eine hohe Kompatibilität mit gängigen Dünnschichtprozessen, wie beispielsweise Druckprozessen oder der optischen Lithographie, aufweisen. Der enorme Fortschritt sowohl bei der Aufreinigung von halbleitenden Nanoröhren als auch bei der Herstellung von Nanoröhrennetzwerken mit einer homogenen und definierten Morphologie führte in den vergangenen Jahren zu der weitverbreiteten Anwendung dieses Materials in der aktiven Schicht von Feldeffekttransistoren. Gleichzeitig wirft dieser Fortschritt weiterführende Fragen bezüglich der Schlüsselparameter für den Ladungstransport in diesen Netzwerken sowie deren Optimierung auf.

Diese Dissertation behandelt den Ladungstransport und seine Limitierungen in polymerselektierten, halbleitenden SWNT-Netzwerken mit einem Hauptaugenmerk auf der jeweiligen Nanoröhrennetzwerkzusammensetzung. Die hierfür verwendete Transistorstruktur ermöglichte die reproduzierbare und unverfälschte Analyse von Ladungstransportparametern, wie der Ladungsträgermobilität, sowie deren Abhängigkeiten von der SWNT-Netzwerkzusammensetzung und der Temperatur. Der Vergleich verschiedener Nanoröhrennetzwerke mit unterschiedlichen Verteilungen an SWNT-Spezies hebt hierbei den negativen Einfluss von zusätzlichen Energiebarrieren an den Schnittstellen zwischen SWNTs unterschiedlichen Durchmessers auf die Transporteigenschaften hervor. Entgegen der bisherigen Annahme, dass der Gesamtladungstransport einzig durch die Beschaffenheit dieser Schnittstellen bestimmt wird, deuten die Ergebnisse in dieser Arbeit einen zusätzlichen, signifikanten Einfluss des Transports innerhalb der Nanoröhren an. Die charakteristische Abhängigkeit dieses Transports entlang der Nanoröhren von deren Durchmesser liefert in diesem Zusammenhang eine mögliche Erklärung für die deutlich höheren Ladungsträgermobilitäten in SWNT-Netzwerken mit größeren Nanoröhrendurchmessern und einer gewissen Speziesverteilung im Vergleich zu Netzwerken, die nur eine einzige SWNT-Spezies mit geringem Durchmesser enthalten. Für die Realisierung von SWNT-Netzwerktransistoren mit maximalen Ladungsträgermobilitäten sollten zukünftige Optimierungen der Netzwerkzusammensetzung somit auf einzelne Nanoröhrenspezies mit großen Durchmessern abzielen.

Neben diesen Einblicken in die zugrundeliegenden Transportmechanismen umfasst diese Arbeit einen neuartigen Ansatz für die gezielte Modifikation des Ladungstransports in halbleitenden Nanoröhrennetzwerktransistoren mithilfe photochromer Spiropyran-Verbindungen, die dem Dielektrikum beigemischt wurden. Das Spiropyran und insbesondere seine photoinduzierte

Isomerisierung zu Merocyanin üben einen starken Einfluss auf die Ladungsträgermobilitäten aus, was diesen Transistoren die grundlegenden Eigenschaften optisch schaltbarer Bauteile verleiht. Die Bestrahlung mit UV-Licht führt zu einer erheblichen Reduktion der Ladungsträgermobilität, die durch Erhitzen oder Bestrahlung mit sichtbaren Licht wiederhergestellt werden kann. Das auf diese Weise umgesetzte optische Schaltverhalten veranschaulicht die grundsätzliche Eignung von SWNT-Netzwerktransistoren für multifuntionale Anwendungen, die über integrierte Schaltkreise hinausgehen.

LIST OF ABBREVIATIONS

AC	Alternating Current
AFM	Atomic Force Microscopy
ALD	Atomic Layer Deposition
CoMoCAT	Cobalt Molybdenum Catalyst
CVD	Chemical Vapor Deposition
DC	Direct Current
DNA	Deoxyribonucleic Acid
DOS	Density of States
EL	Electroluminescence
FET	Field-effect Transistor
FIT	Fluctuation-induced Tunneling
gFPP	Gated Four-point Probe
HiPco	High-pressure Carbon Monoxide
HOMO	Highest Occupied Molecular Orbital
IPA	Isopropanol
LUMO	Lowest Unoccupied Molecular Orbital
MC	Merocyanine
nIR	Near Infrared
P3DDT	Poly(3-dodecylthiophene-2,5-diyl)
PFO-BPy	Poly[(9,9-di-*n*-octylfluorene- 2,7-diyl)-*alt*-(2,2’-bipyridine-6,6’-diyl)]
PMMA	Poly(methyl methacrylate)
RBM	Radial Breathing Mode
SP	Spiropyran
SWNT	Single-Walled Carbon Nanotube
THF	Tetrahydrofuran
UV	Ultraviolet
vis	Visible
VRH	Variable Range Hopping

Contents

CHAPTER 1

INTRODUCTION

Technological progress has led to new applications of optoelectronic devices beyond conventional integrated circuits, e.g., in thin and flexible displays, wearable health-monitoring sensors or Internet of Things technology. Consequently, these applications have resulted in additional requirements for the active layer materials and components.[1] These include not only the continuous miniaturization but also unprecedented specifications with regard to mechanical flexibility and stretchability or optical transparency in the visible range. While silicon is still the dominant material for field-effect transistors (FETs) to date and will most likely remain at the heart of semiconductor technology for quite some time to come, it has already reached its limitations for certain applications.[2–4] Hence, there has been a high demand for new semiconducting materials that could complement silicon especially for large-area and low-cost applications. Solution-processable metal oxide and organic semiconductors have emerged in this context and have already found application in commercially relevant products.[5,6]

Another promising candidate for future electronic devices are semiconducting single-walled carbon nanotubes (SWNTs), that is, hollow carbon cylinders with diameters in the range of one nanometer and typical lengths of a few micrometers. These nanoscale tubes feature outstanding electrical properties that enable ballistic charge transport and carrier mobilities exceeding those of single-crystal silicon by more than an order of magnitude, combined with excellent mechanical properties, such as a high tensile strength. However, as-produced carbon nanotube raw materials typically suffer from very heterogeneous properties, as they contain a broad mixture of various SWNT species with different molecular structures and diameters in a statistical distribution of 33 % metallic and 67 % semiconducting nanotubes. Over the past few years, substantial progress in post-synthesis nanotube sorting has been made. Especially, the polymer-wrapping technique has enabled the large-scale, selective dispersion of only semiconducting SWNTs in organic solvents and promoted the application of these purified tubes in FETs.[7,8] Despite the remarkable transport properties of semiconducting SWNTs their integration into single nanotube or SWNT array FETs, whose channel is bridged directly by individual tubes, in a scalable and reproducible way still remains a challenge. On the other hand, random networks of semiconducting SWNTs are compatible with established thin-film processes and can be readily deposited from purified dispersions employing conventional printing techniques. Although the achievable charge carrier mobilities in these networks are substantially lower than those within single nanotubes due to SWNT-SWNT junctions, values of up to $100\,\mathrm{cm^2\,V^{-1}\,s^{-1}}$ have been reported that are already comparable to polycrystalline silicon.[9,10] In addition, the network structure of such SWNT thin-films makes them highly bendable and stretchable and thus compatible with flexible substrates.[11,12]

Yet, the selective dispersion of semiconducting SWNTs and their deposition into networks does not necessarily lead to defined material properties. Depending on the utilized nanotube raw material as well as the sorting and dispersion protocols, a large variety of different semiconducting nanotube mixtures with different mean tube lengths and diameters can be obtained ranging from broad diameter distributions to even monochiral dispersions, containing only a single SWNT species. Together with the deposition process and the respective processing conditions the resulting network composition and morphology, i.e., network density, degree of alignment or the presence of bundles, can vary considerably. In addition, FET configurations with various dielectric and contact materials produce substantially different device characteristics, often affected by extrinsic effects, such as contact resistance or the presence of charge traps or dopants. The multitude of parameters makes reproducible and comparable device performances but also the extraction of intrinsic charge transport properties rather difficult.

For actual application in commercial products further optimizations with regard to the nanotube networks are desired based on rational design guidelines. However, current guidelines are restricted to obvious geometrical parameters. The impact of the network composition, that is, the distribution of SWNT species on charge transport, still remains unclear. While transport in individual semiconducting SWNTs is well understood, many open questions remain to be answered with regard to the fundamental transport processes in nanotube networks. The theoretical description of charge transport in these networks relies on models for conventional disordered semiconductors that lack a direct relation to the specific properties of semiconducting SWNTs and a comprehensive overall picture is still missing.

Nevertheless, the recent progress in the preparation of semiconducting nanotube networks enables subsequent studies on how charge transport could be modified in a useful manner in order to integrate responsiveness to external stimuli, e.g., light, and thus additional functionalities into SWNT network transistors. This way future multifunctional optoelectronic devices for applications beyond electrical circuits could be realized, e.g., for optical memory or sensing applications.

This thesis addresses the question of what key parameters determine charge transport in randomly-oriented, polymer-sorted semiconducting SWNT networks and how their transport properties can be evaluated reliably. In particular, the influence of nanotube-nanotube junctions, energetic disorder, charge traps and the intrinsic charge carrier mobilities on the overall network transport and their dependence on the SWNT network composition are examined. In addition, the purposeful modification of these parameters is achieved by a number of experimental measures such as mixing of nanotube ensembles with different diameter distributions or the addition of a photochromic compound to the SWNT networks.

This work is organized as follows. Chapter 2 provides the theoretical background and introduces the current state of research that is relevant for interpreting the results of the experiments. It gives an overview of the optoelectronic properties as well as common synthesis and sorting routes of SWNTs. Furthermore, it includes important charge transport models for disordered semiconductors that still represent the basis for the description of transport in SWNT networks. Then the device class of field-effect transistors is introduced both in general and with particular reference to SWNTs. Finally, the origin of contact resistance, its impact on the device characteristics and experimental approaches for its extraction are outlined.

Chapter 3 details the materials and experimental procedures for device fabrication and characterization that were developed and employed throughout this thesis.

The first part of the experimental work is presented in Chapter 4. It contains a comparative charge transport study of SWNT network FETs with three different nanotube species distributions, employing a transistor structure that enables the reproducible observation of intrinsic properties and the correction for contact resistance. The impact of the network composition on charge transport is investigated based on temperature-dependent current-voltage measurements and the role of residual wrapping polymer in these networks is examined. The experimental results are compared to those of a previously established random resistor model in order to learn more about the transport mechanisms in semiconducting SWNT networks.

These insights are expanded in Chapter 5 that includes a subsequent transport analysis of mixed SWNT network FETs with tailored compositions created by mixing of large- and small-diameter nanotubes in various ratios. With this more controlled experimental setup the effects of a gradually changing network composition on the network charge transport are revealed. Especially the interplay between inter-nanotube hopping and transport along the individual SWNTs depending on the present nanotube species is discussed.

Chapter 6 examines the deliberate modification of charge transport in SWNT network FETs by the addition of a photochromic spiropyran compound to the dielectric layer in order to implement light-responsiveness. The impact of the photoswitchable molecules and their photoinduced isomerization on the device characteristics is investigated and the underlying mechanism is discussed based on a temperature-dependent charge transport analysis. Finally, the ability to reversibly direct current pathways in such nanotube network FETs by selective photopatterning of only certain areas of the transistor channel as visualized by electroluminescence imaging is demonstrated.

The thesis concludes with a summary of the gained insights and perspectives on future research and novel optoelectronic devices based on semiconducting SWNT networks in Chapter 7.

CHAPTER 2

BACKGROUND

This chapter covers the optoelectronic properties of semiconducting single-walled carbon nanotubes and charge transport models for the description of disordered semiconductors. It further gives an overview of field-effect transistors and the effects of contact resistance.

2.1 Single-Walled Carbon Nanotubes

Over the past few decades, low-dimensional nanomaterials have attracted increasing attention not only with respect to fundamental research but also with regard to commercial applications. Associated with the reduced dimensionality in these systems, quantum confinement effects start to play a role that can affect the material properties in a beneficial way and enable superior performances in various applications, such as displays, sensing or electronic circuitry.

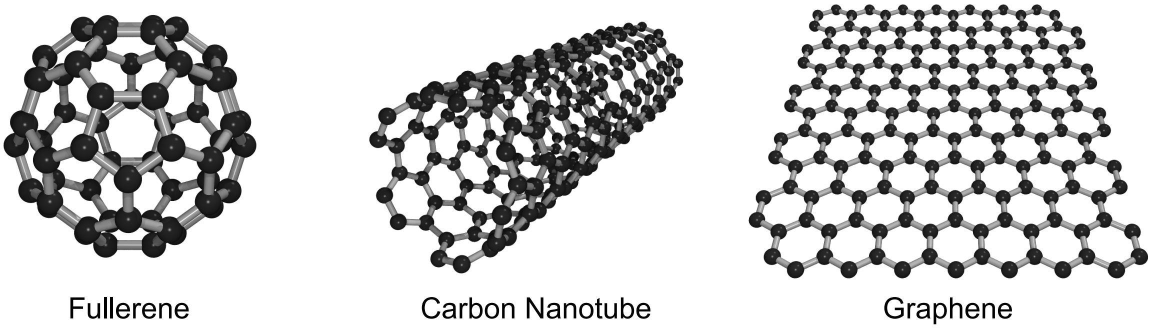

Figure 2.1: Molecular structures of low-dimensional sp^2-hybridized carbon allotropes: zero-dimensional fullerene, one-dimensional single-walled carbon nanotube and two-dimensional graphene sheet.

Aside from inorganic semiconducting nanoparticles and nanowires, the low dimensional synthetic carbon allotropes, i.e., fullerenes, graphene and carbon nanotubes, are particularly versatile and promising classes of nanomaterials.[13] All of these allotropes consist of networks of covalently bound sp^2-hybridized carbon atoms, although in different spatial arrangements (see Figure 2.1). First discovered in 1985, the zero-dimensional fullerenes, which are composed of carbon atoms arranged in hexagons and pentagons resembling the shape of a soccer ball, have become an established acceptor material in organic solar cells and were applied as molecular vessels for drug delivery.[14–16] In graphene, that is, one monolayer of the layered and very common bulk carbon allotrope graphite, which was first isolated in 2004, all carbon atoms are arranged in planar hexagons that form a two-dimensional honeycomb lattice leading to intriguing electronic, optical, thermal and mechanical properties.[17–22] The one-dimensional carbon nanotubes can conceptually be seen as rolled-up graphene sheets forming hollow, seamless cylinders and were first observed in 1991.[23] Depending on the number of involved graphene layers/walls, carbon nanotubes can be categorized into single-walled carbon nanotubes (SWNTs) and multi-walled carbon nanotubes, with the latter consisting of concentrically nested SWNTs similar to Russian Matryoshka dolls.[24] The one-dimensionality of carbon nanotubes is based on their high aspect ratios, i.e., typical diameters on the order of 1 nm compared to tube lengths from several hundreds of nanometers to few centimeters.[25] Along with their structure based on the hexagonal carbon lattice, SWNTs share several properties with graphene, such as an exceptional mechanical strength and extraordinarily high charge carrier mobilities along the tube axis.[26] On the other hand, graphene has no bandgap whereas SWNTs are either metallic or semiconducting depending in their precise structure.

2.1.1 Structural Properties

The electronic and optical properties of a SWNT with a certain tube length are determined by the roll-up direction of the virtual graphene sheet with respect to the hexagonal carbon lattice and the resulting nanotube diameter. The roll-up scheme in Figure 2.2a illustrates the large variety of ways to roll a graphene sheet to obtain a SWNT. The chiral vector $\vec{C}_\mathrm{h}$ indicates the direction and length along which the nanotube is rolled up and defines the tube circumference:

$$\vec{C}_\mathrm{h} = n \cdot \vec{a}_1 + m \cdot \vec{a}_2 \tag{2.1}$$

with the two unit vectors $\vec{a}_1 = \frac{a}{2} \cdot (\sqrt{3}, 1)$ and $\vec{a}_2 = \frac{a}{2} \cdot (\sqrt{3}, -1)$ and the hexagonal lattice constant $a = 0.246\,\mathrm{nm}$ of the graphene unit cell.[27] The chiral indices (n,m) with $0 \leq m \leq n$ are integers, that are used to unambiguously identify all different SWNT species, which are also often referred to as 'chiralities'. Based on this pair of indices, both the SWNT diameter d_t

$$d_\mathrm{t} = \frac{|\vec{C}_\mathrm{h}|}{\pi} = \frac{a}{\pi}\sqrt{n^2 + nm + m^2} \tag{2.2}$$

and the chiral angle θ which defines the rolling direction with respect to $\vec{a}_1$

$$\cos(\theta) = \frac{2n + m}{2\sqrt{n^2 + nm + m^2}} \tag{2.3}$$

can be derived.[28–30] Due to the sixfold symmetry of the hexagonal graphene lattice only chiral angles between 0° and 30° result in nonequivalent SWNT species, while larger θ values lead to enantiomeric duplicates. With reference to the carbon bond structure along their circumference species with chiral indices of $(n,0)$ and (n,n) are called 'zigzag' and 'armchair' SWNTs. Based on their symmetry both of these SWNT types are achiral, whereas all other (n,m) species are chiral.

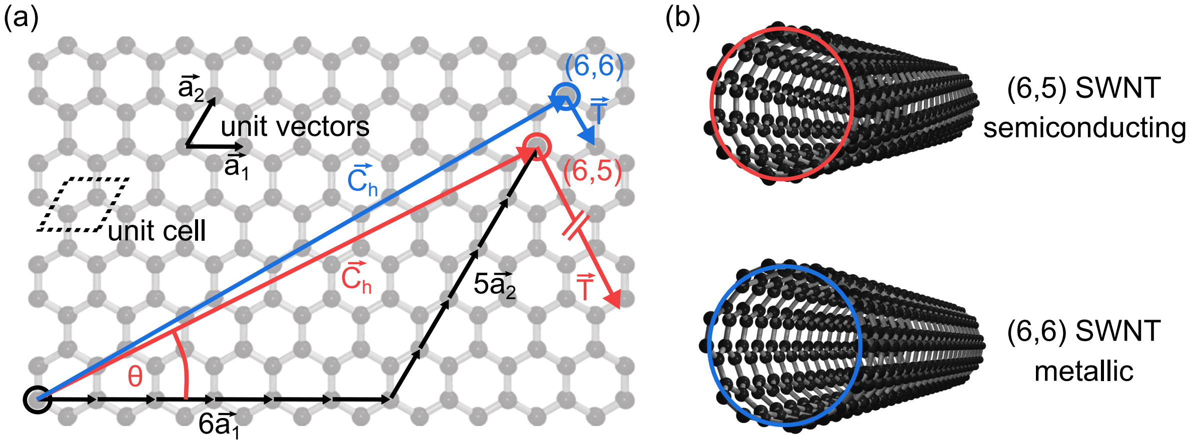

Figure 2.2: Rolling scheme for the creation of (n, m) SWNTs: (a) graphene lattice with chiral vectors of (6,5) SWNTs (red) and (6,6) SWNTs (blue) and (b) resulting molecular structures of both SWNT species with a tube length of 5 nm.

Aside from $\vec{C}_\mathrm{h}$ and θ, SWNTs are characterized by the translational vector $\vec{T}$, which is orthogonal to the chiral vector and denotes the direction of the tube axis. Its length defines the periodicity of the carbon lattice along this axis and determines together with $\vec{C}_\mathrm{h}$ the size of the SWNT unit cell. Figure 2.2b shows the molecular structures of two exemplary SWNT species, namely (6,5) and (6,6) nanotubes. Although both possess similar diameters of 0.75 nm and 0.82 nm and chiral angles of 27° and 30°, their unit cells differ significantly in size and contain 364 carbon atoms for the (6,5) SWNT and 24 for the (6,6) SWNT. Furthermore, their electronic properties are quite different: (6,5) nanotubes exhibit semiconducting behavior, while (6,6) SWNTs are metallic.

2.1.2 Electronic Structure

Along with the geometric structure, the electronic properties of SWNTs can be derived from graphene and its band structure. Owing to their energetic proximity to the Fermi level, the bonding and antibonding π-bands of graphene stemming from the delocalized p_z-orbitals of the sp^2 carbon atoms dominate their optical and charge transport properties.[31] Thus, the bonding π-band is often referred to as the valence band and the antibonding π^*-band as conduction band. Both bands and their position in the reciprocal space are commonly calculated by a tight-binding approach using the expression:[27,31–33]

$$E^{\pm}_{\mathrm{g2D}}(\vec{k}) = \frac{\epsilon_{2\mathrm{p}} \pm \gamma_0 \cdot w(\vec{k})}{1 \mp s \cdot w(\vec{k})} \tag{2.4}$$

with

$$w(\vec{k}) = \sqrt{1 + 4\cos\left(\frac{\sqrt{3}k_\mathrm{x}a}{2}\right)\cos\left(\frac{k_\mathrm{y}a}{2}\right) + 4\cos^2\left(\frac{k_\mathrm{y}a}{2}\right)} \tag{2.5}$$

and $\vec{k}$ being the wave vector. Typically, the energy of the $2p$ atomic orbital $\epsilon_{2\mathrm{p}}$ is set to zero, the nearest neighbor interaction energy between two adjacent carbon atoms γ_0 to values around 3 eV and the tight-binding overlap integral s to 0.129.[29,33,34] The corresponding calculated valence band in the range of the first Brillouin zone of the likewise hexagonal reciprocal graphene lattice is shown in Figure 2.3a. It contains the high symmetry points Γ (located in the center of the Brillouin zone), K and K' (alternatingly located at the vertices of the Brillouin zone) and M (located directly between K and K'). As illustrated in Figure 2.3b both the π-band and the π^*-band touch at the K and K' points only, which are often referred to as 'Dirac cones' due to the linear dispersion relation in the vicinity of these points, while a bandgap is present for all other wave vectors. As the Fermi surface consists only of these individual points with a vanishing density of states (DOS) at the Fermi level, graphene is considered as zero-gap semiconductor or semimetal.

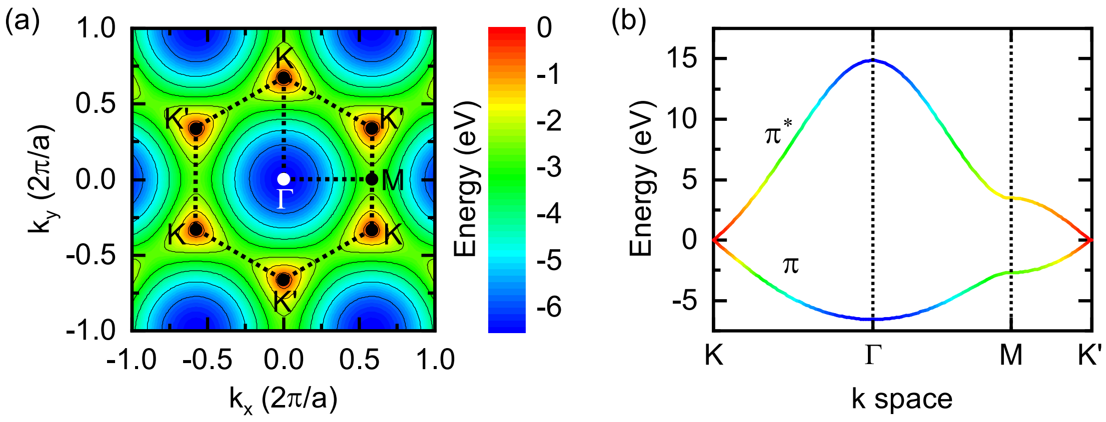

Figure 2.3: Band structure of graphene in the reciprocal space based on the tight-binding model: (a) two-dimensional contour plot of the valence band (π-band) revealing the hexagonal first Brillouin zone with the high symmetry points K, Γ, K' and M and (b) one-dimensional energy dispersion of the valence and conduction band (π^*-band) between these points.

When the graphene sheet is conceptually rolled into a SWNT, its wave function is confined in another dimension resulting in additional boundary conditions in direction of the tube circumference. Consequently, the wave vector along the circumferential direction becomes quantized, whereas it remains quasi-continuous along the nanotube axis. Based on these boundary conditions only wave vectors are allowed, that fulfill the following equation:[29,30,34,35]

$$\exp\left[i(\vec{K}_\mathrm{a} + \vec{K}_\mathrm{c}) \cdot (\vec{C}_\mathrm{h} + \vec{T})\right] = 1 \tag{2.6}$$

with the reciprocal lattice vectors along the nanotube circumference $\vec{K}_\mathrm{c}$ and along the tube axis $\vec{K}_\mathrm{a}$. This reduces the former two-dimensional Brillouin zone of graphene to a series of N parallel lines with $N = \frac{2(n^2+nm+m^2)}{d_\mathrm{R}}$ being the number of carbon hexagons per SWNT unit cell and d_R the greatest common divisor of $(2n + m)$ and $(2m + n)$. The length and orientation of these cutting lines is determined by $\vec{K}_\mathrm{a}$ and its length:

$$\vec{K}_\mathrm{a} = \frac{1}{N}(m \cdot \vec{b}_1 - n \cdot \vec{b}_1) \tag{2.7}$$

$$|\vec{K}_\mathrm{a}| = \frac{2\pi}{|\vec{T}|} = \frac{2\pi d_\mathrm{R}}{\sqrt{3} \cdot |\vec{C}_\mathrm{h}|} \tag{2.8}$$

with $\vec{b}_1 = \frac{2\pi}{a} \cdot \left(\frac{1}{\sqrt{3}}, 1\right)$ and $\vec{b}_2 = \frac{2\pi}{a} \cdot \left(\frac{1}{\sqrt{3}}, -1\right)$ being the unit vectors of the reciprocal graphene lattice. In the circumferential direction the set of allowed discrete wave vectors is given by:

$$|\vec{K}_\mathrm{c}| j = \frac{2\pi}{|\vec{C}_\mathrm{h}|} j, \quad j = 0, 1, \ldots, N - 1 \tag{2.9}$$

with $|\vec{K}_\mathrm{c}|$ defining the spacing of the cutting lines. Based on this 'zone-folding' scheme, the band structure of a given SWNT can be constructed by the superposition of all corresponding line cuts in the band structure of graphene.[29,34,35] Depending on their spacing and direction, one of these lines will cross the reciprocal graphene lattice at a K-point or not. The SWNT will exhibit metallic properties if any of its cutting lines crosses a K- or K'-point, while it will be semiconducting if these points are not part of its band structure. This is illustrated in Figure 2.4a showing the cutting lines of a (6,5) SWNT (top) and a (6,6) nanotube (bottom) in the first Brillouin zone of the graphene lattice. Analogous to the band structure of graphene the resulting SWNT band structures can be calculated by using Equation 2.4 and inserting the allowed wave vectors only as shown in Figure 2.4b. Consequently, the band structure of the (6,5) SWNT exhibits a gap, while the valence and conduction band touch each other for the (6,6) SWNT, resulting in its metallic properties. As the chiral vector directly determines the direction and spacing of the line cuts, the electronic properties of a given SWNT are determined by its (n,m) values. For $(n-m)\,\mathrm{mod}\,(3)=0$ the SWNT is metallic, whereas it possesses semiconducting properties if $(n-m)\,\mathrm{mod}\,(3)=1$ or 2. Hence, one third of all (n,m) SWNT species is metallic and two thirds are semiconducting.[29,36]

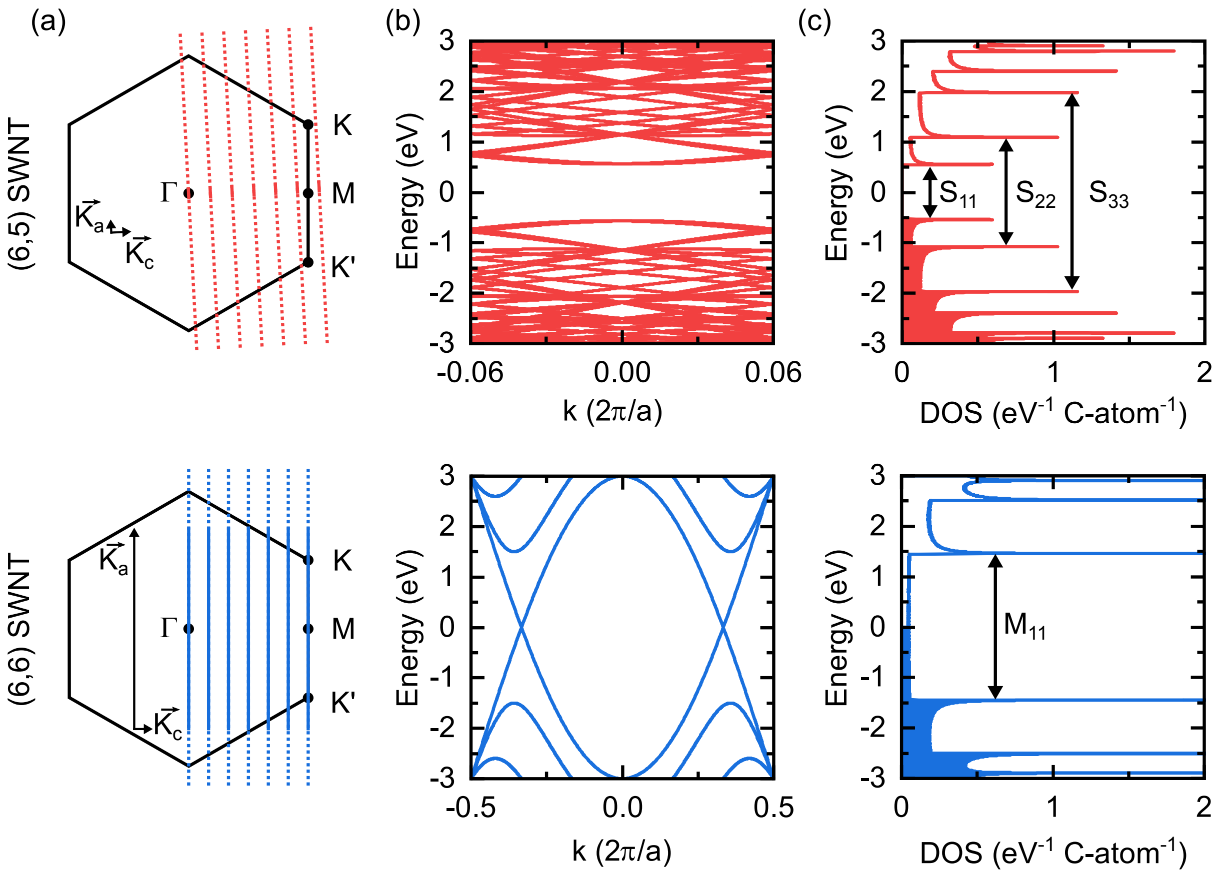

Figure 2.4: Energy band and DOS calculations of (6,5) SWNTs (top) and (6,6) SWNTs (bottom) based on the zone-folding approach: (a) first Brillouin zone of graphene with high symmetry points and parts of the cutting lines (solid lines represent the actual length of $\vec{K}_\mathrm{a}$ and are elongated with dashed lines for better visibility) of the corresponding SWNT species, (b) resulting two-dimensional band structure and (c) derived DOS with characteristic energetic transitions (S_ii and M_{11}) between the subbands (van Hove singularities) of these nanotubes.

From the SWNT band structure the respective DOS can be calculated:[34]

$$D(E) = \frac{2}{N}\sum_{d=1}^{N}\int \frac{1}{\left|\frac{dE_{\mathrm{d}(k)}}{dk}\right|}\delta(E_{\mathrm{d}}(k) - E)dE \tag{2.10}$$

as shown in Figure 2.4c. The DOS of both SWNTs exhibits sharp peaks at the edges of the subbands, so-called van Hove singularities, which are a specific feature of SWNTs and other one-dimensional (semi-)conductors. In agreement with the obtained band structure, the DOS for the (6,6) SWNT is small but continuous around the Fermi level, further confirming its metallic character, while a band gap is present between the first van Hove singularities of the valence and conduction band of the (6,5) SWNT. The energetic difference between the first van Hove singularities of the valence and conduction band for semiconducting (S_{11}) and metallic (M_{11}) SWNTs scales inversely with the nanotube diameter and can be estimated based on the following expressions:

$$S_{11}(d_{\mathrm{t}}) = \frac{2a\gamma_0}{\sqrt{3}d_{\mathrm{t}}} \qquad \text{and} \qquad M_{11}(d_{\mathrm{t}}) = \frac{6a\gamma_0}{\sqrt{3}d_{\mathrm{t}}}. \tag{2.11}$$

The underlying zone-folding model relies on several simplifications, e.g., it disregards the curvature of the graphene sheet which leads to deviations especially for small diameter SWNTs. Furthermore, it assumes a linear, rotational symmetric energy dispersion around the K-points which is not the case for small tube diameters due to the trigonal warping effect.[34] Nevertheless, the presented model is in good agreement with experimental data, e.g., from scanning probe, optical absorption and photoluminescence measurements and gives thus a good estimation for the SWNT bandgap and its diameter dependence.[37–39]

While these values are good approximations for individual, freestanding nanotubes, their immediate environment impacts their electronic properties. Bundles of several nanotubes formed due to strong van der Waals forces between their carbon atom shells might result in the formation of a small bandgap for metallic armchair (*n*,*n*) SWNTs or in a bandgap reduction and broadening of the absorption band by up to 20 % for semiconducting nanotubes.[40,41]

2.1.3 Optical Properties

As shown in Figure 2.4 semiconducting carbon nanotubes have a direct bandgap which should enable direct excitation by optical absorption as well as photoluminescence. Due to their reduced dimensionality, the optical properties of SWNTs are dominated by many-body effects and upon optical excitation electron-hole pairs bound by attractive Coulomb interaction, so-called excitons, are formed instead of free electrons and holes.[42,43] In contrast to inorganic semiconductors, in which these quasiparticles are weakly bound and only observable at low temperatures, excitons in nanotubes exhibit large binding energies of several hundred meV due to their one-dimensional character and reduced electrostatic screening.[43,44] Hence, in SWNTs excitons are stable at room temperature and have to be considered for optical analysis.

Furthermore, the one-dimensional nanotube structure results in a pronounced polarization anisotropy, namely considerably higher polarizabilities in parallel to the tube axis than in perpendicular direction, especially for small SWNT diameters.[45,46] Consequently, optical absorption and emission of SWNTs are highly polarized along this axis, while transitions in perpendicular direction are barely detectable. Based on quantum mechanical selection rules only those transitions between the respective i-th subbands of the valence and the conduction band, i.e., S_{ii} and M_{ii}, are allowed for incident light polarized in parallel to the tube axis, while asymmetric subband combinations are forbidden.[47] Some of the allowed transitions for (6,5) and (6,6) SWNTs are highlighted in Figure 2.4c. The respective transition energies can be predicted for all SWNT species with different diameters based on tight-binding calculations as described above, leading to the well-known Kataura plot as shown in Figure 2.5a.[48] These calculated energies (open circles) show a significant deviation from experimentally determined values (solid circles) by up to 20 % for the S_{11} transitions probably due to the simplifications of the tight-binding model (e.g., neglected electron-electron interaction).[49–52] Nevertheless, this plot enables the assignment of experimentally determined transition energies to single SWNT species as demonstrated with the purple circles, that indicate the S_{11} and S_{22} transitions of (6,5) SWNTs. The plot further illustrates, that basically all lower subband transitions up to S_{44} of SWNTs with diameters of ≤2 nm can be probed optically with excitation energies from the ultraviolet (UV) over the visible (vis) up to the near infrared (nIR) range which corresponds to wavelengths of 300–3000 nm.

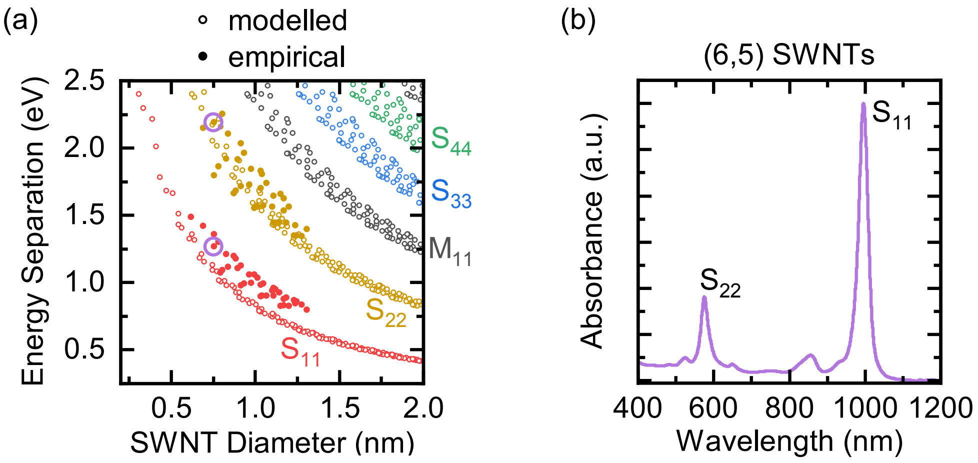

Figure 2.5: (a) Kataura plot illustrating the different transition energies between the corresponding van Hove singularities for metallic (M_{11}) and semiconducting (S_{11}, S_{22}, S_{33} and S_{44}) SWNT species depending on their tube diameter based on tight-binding calculations[48] (open circles) and empirical data[49] (solid circles). (b) Representative UV-vis-nIR absorption spectrum of a dispersion of polymer-wrapped (6,5) nanotubes in toluene showing the characteristic narrow S_{11} and S_{22} transitions.

Consequently, UV-vis-nIR absorption spectroscopy represents an effective technique to analyze SWNT samples, that commonly contain mixtures of metallic and semiconducting SWNT species, with respect to their composition and diameter distribution. Thus, it enables a first discrimination between semiconducting and metallic nanotubes to be made, although this method lacks sensitivity for minor amounts of certain SWNTs species. The sharp peak shape of the van Hove singularities results in well-defined and narrow optical absorption and emission bands with half-widths at half-maximum of less than 25 meV, as shown in the representative absorption spectrum of a polymer-sorted (6,5) SWNT dispersion in toluene in Figure 2.5b.[39,53] The precise peak positions are affected by the environment of the nanotubes, i.e., by dispersing agents and the solvent, or by the presence of SWNT bundles which typically result in a substantial broadening of the peak linewidths.[41] In addition, UV-vis-nIR absorption measurements can be utilized to estimate the concentration of a given SWNT species in a mixed nanotube dispersion based on the Beer-Lambert law using experimentally determined absorption cross sections.[54–57]

While higher subband transitions and metallic SWNT species can be detected by absorption spectroscopy, luminescence from sufficiently debundled semiconducting nanotubes is observed only for the S_{11} transition due to non-radiative relaxation of the electron-hole pairs to the lowest excited state. A combination of both techniques in the form of so-called photoluminescence excitation emission maps enables a more unambiguous species assignment of semiconducting SWNTs compared to absorption spectroscopy alone, as each nanotube chirality possesses a unique pair of S_{11} and S_{22} energies, while the absorption peaks of some species overlap.[39]

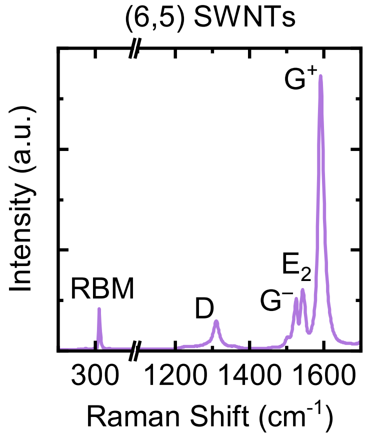

Figure 2.6: (a) Representative Raman spectrum (excited at 532 nm) of dropcast polymer-sorted (6,5) nanotubes on aluminum illustrating the characteristic Raman features of SWNTs.

Another well-established experimental technique to analyze the electronic properties of SWNTs is resonant Raman spectroscopy. It enables investigations of their vibrational modes by inelastic light scattering and was one of the first methods for nanotube characterization due to its non-invasiveness, ease of implementation and remarkable sensitivity.[58–60] This high sensitivity is based on the fact that the intensity of the Raman-active SWNT modes can be resonantly enhanced if the excitation wavelength matches one of the S_{ii} or M_{ii} transition energies of the corresponding nanotube species. This resonant Raman scattering is several orders of magnitude stronger compared to non-resonant Raman processes and even enables the detection of single SWNTs.[61–63] As shown in the Kataura plot (see Figure 2.5a) the necessary excitation energies for SWNTs with diameters ≤2 nm lie within the vis-nIR range and conveniently coincide with commonly available laser wavelengths.

The characteristic SWNT modes are shown in the Raman spectrum of (6,5) nanotubes (see Figure 2.6). These are the so-called radial breathing mode (RBM, 100–350 cm^{-1}), the D-mode (1300–1350 cm^{-1}), and the G-modes G^{+}, G^{-} and E_2 (1500–1600 cm^{-1}).[64,65] While the D-mode and the G-modes are also found for graphene, RBMs are solely observed for SWNTs and correspond to an in-phase expansion and compression of the nanotube in radial direction. The RBM wavenumber ω_{RBM} inversely depends on the SWNT diameter, i.e., smaller Raman shifts for larger tube diameters:

$$\omega_{\mathrm{RBM}} = \frac{C_1}{d_{\mathrm{t}}} + C_2 \tag{2.12}$$

with C_1 (220–260 cm^{-1} nm) and C_2 (0–20 cm^{-1}) being empirical fit parameters associated with the sample substrate, the degree of nanotube bundling and other environmental effects.[59,65] Hence, based on this relation the tube diameter range of a SWNT sample can be estimated. In addition, the thus calculated SWNT diameters in combination with the given excitation wavelength can be utilized to discriminate between semiconducting and metallic nanotube species using the Kataura plot.

The D-mode is commonly regarded as measure for disorder and defects, such as vacancies, heteroatoms or amorphous carbon in the hexagonal sp^2 carbon lattice not only in nanotubes but also other graphitic materials.[66,67] Typically, the defect density is quantified by comparing its intensity with the intensity of the most prominent band of the G-modes, i.e., the G^{+}-mode in case of nanotubes.[60] As the G-modes originate from in-plane vibrations of the carbon honeycomb lattice, the modes are degenerate for graphene, whereas they split into the G^{+}- and the G^{-}-modes (transverse and longitudinal) for SWNTs due to the loss of the hexagonal symmetry as a result of the tube curvature. The G^{+}-band corresponds to a vibrational C–C bond stretching in direction of the tube axis, while the G^{-}-band originates from displacements in circumferential direction.[65] The E_2-band is associated with an intermediate mode, whose vibration contains contributions of both aforementioned directions; it highly depends on the chiral angle of the respective SWNT species.[68,69] All of these SWNT Raman modes have in common that their intensities and frequencies are strongly affected by electrostatic or (electro-)chemical doping.[70–73]

2.1.4 Synthesis and Separation

In the past few decades, several synthesis routes have been established that produce SWNT raw materials of different purity and quality, in different quantities and with different nanotube diameter distributions.[29,74] The most important class of these techniques is chemical vapor deposition (CVD) . The CVD procceses involve the decomposition of gaseous carbon precursor molecules, such as methane, ethane or CO, at transition metal catalyst nanoparticles, e.g., Fe, Ni or Co at temperatures ≤1200 °C.[75] After decomposition of the precursor molecules the carbon atoms are considered to diffuse on the surface and/or into the bulk of metal nanoparticles, from which the nucleation and growth of a SWNT is initiated.[76] The metal particles, whose size and crystallographic symmetry directly affects the diameter and species of the growing nanotubes, are either added to the gas phase or deposited on a substrate.[75]

Two commercially relevant examples of these CVD methods are the so-called HiPco process and the CoMoCAT process. The HiPco (high-pressure carbon monoxide) process is based on the disproportionation reaction of CO on the surface of iron catalyst clusters that are formed in situ by the decomposition of iron pentacarbonyl at high pressures of up to 10 bar and temperatures in the range of 800–1200 °C.[77,78] This continuous-flow synthesis enables the production of SWNTs with diameters in the range of 0.8–1.3 nm in large quantities with yields of up to 97 %. The CoMoCAT (cobalt molybdenum catalyst) process also utilizes CO as carbon source but instead of iron it employs a bimetallic CoMo catalyst on a SiO_2 support substrate inside a fluidized bed reactor.[79,80] Reaction conditions at lower pressures (~5 bar) and temperatures (700–850 °C) enabled the preparation of SWNTs with much more defined diameter distributions of 0.7–1.0 nm and an enrichment of certain nanotube species, e.g., (6,5) and (7,5) SWNTs.

Other SWNT synthesis methods are based on the vaporization of graphite composites filled with metal catalyst particles in an inert atmosphere either by laser ablation or arc-discharge.[81–83] These techniques produce a broad range of large-diameter nanotubes (1–2 nm) with comparatively low defect densities, but have the disadvantage to they yield SWNTs only batchwise, thereby limiting the material throughput. A related but continuous and highly economical method is the so-called plasma torch process which allows for the production of several kilograms of SWNT raw material per day.[84–88] It is based on the decomposition of carbon precursors (carbon black, ethylene or toluene) and catalyst particles (ferrocene or NiCo alloys) that are continuously fed into a plasma torch. The argon plasma, which is either radio frequency-induced or driven by a direct current, results in very high reaction temperatures of 5000–15 000 K, enabling the synthesis of high quality SWNTs with diameters between 0.9 and 1.5 nm.

For the application of SWNTs in the active layer of optoelectronic devices a defined and preferably narrow distribution of exclusively semiconducting nanotubes species is required. However, the SWNT raw materials produced by all of the aforementioned techniques contain statistical mixtures of mostly 67 % semiconducting and 33 % metallic nanotubes with more or less broad diameter distributions as well as impurities, such as residual catalyst particles and amorphous carbon. Furthermore, the as-synthesized SWNTs are typically aggregated into tight bundles due to strong van der Waals interactions between the individual tubes and they are insoluble in essentially all solvents.[89,90] Hence, several post-synthesis processing steps are necessary to disperse individualized, purely semiconducting nanotubes in solution and separate those from metallic SWNT species and other byproducts.

The first step includes the de-bundling and dispersion of nanotubes in a suitable solvent by liquid exfoliation processes based on sonication induced cavitation (e.g., bath sonication) or based on the application of somewhat milder shear forces (e.g., shear-force mixing).[8,91,92] To prevent immediate re-aggregation conventional surfactants, such as sodium dodecyl sulfate or sodium cholate are commonly employed to create stable SWNT dispersions in water.[93–95] A stable aqueous nanotube dispersion can also be obtained by using deoxyribonucleic acid (DNA) as dispersing agent with the additional advantage that it even allows for the separation of different SWNT species when combined with ion exchange chromatography.[96–98] However, this is only the case for tailored sequences of synthetic DNA and the achieved nanotube yields in the nanogram range are still quite low.[99] Other DNA as well as all common surfactants non-selectively disperse all kinds of semiconducting and metallic SWNT species. Hence, these dispersion methods usually require a subsequent processing step for the separation of SWNTs species. One possible method is density gradient ultracentrifugation. It is based on the different buoyant densities of SWNTs with their surfactant shell depending on their tube diameter and electronic properties enabling the separation of individual nanotube species from one another.[100,101] Other more scalable separation techniques are the gel chromatography which relies on the different binding affinities of the different SWNT species to polysaccharide-based gel columns[102–105] and aqueous two-phase extraction that exploits slight differences in the chemical potential of nanotubes with different (n,m) in aqueous phases of polyethylene glycol and dextran for partitioning.[106,107]

A completely different approach for SWNT dispersion and separation is the single-step selective dispersion of only certain semiconducting nanotube species in organic solvents with the help of π-conjugated polymers as first reported by Nish *et al.*[7] It involves the dispersion of a given nanotube raw material in a toluene (or other organic solvent) solution of a corresponding polymer through the application of strong shear forces analogous to dispersion in aqueous media. So far, a large variety of conjugated polymers have been utilized for this purpose.[108] The most common classes are polyfluorenes,[109–112] polycarbazoles,[113,114] polythiophenes,[115,116] donor-acceptor polymers[117,118] and copolymers thereof.[119–121] Depending on the structure of the polymer, its molecular chains wrap around certain semiconducting SWNT species only, most likely due to π-π-stacking of the polymer backbone with the nanotube surface.[122] The alkyl side chains of most polymers ensure their good solubility in organic solvents and likewise a colloidal stabilization (probably steric and electrostatic) of the wrapped SWNTs. In contrast, the unwrapped SWNT species as well as impurities can be removed from the dispersion by subsequent centrifugation as they sediment quickly after the liquid exfoliation step. However, this is only the ideal case and both the wrapping selectivity and the selection yield might vary substantially depending on the employed materials and processing conditions, such as the length of the polymer alkyl side chains,[110,115] the molecular weight of the polymer,[123,124] the solvent,[125–127] the dispersion temperature[128] and the composition of the SWNT raw material.[129] So far, only empirical guidelines for an effective SWNT selection exist, while a complete understanding of the exact wrapping mechanism is still missing. Based on the chosen nanotube raw material and polymer vastly different ensembles of semiconducting SWNTs can be selected ranging from broad ranges of SWNT chiralities with different diameters up to nearly monochiral dispersions that contain only a single SWNT species.[130]

After successful SWNT sorting the obtained mixture usually contains large amounts of wrapping polymer which stabilizes the dispersion and inhibits fast re-aggregation and bundling of the nanotubes. On the other hand, the high polymer concentration might be problematic for subsequent solution-processing and application of the dispersion in electronic devices due to the orders of magnitude lower charge carrier mobilities of the conjugated polymers compared to semiconducting SWNTs. Hence, a removal of the unwrapped excess polymer is highly desired which can be achieved by simple vacuum filtration of the dispersion or by sedimentation of the SWNTs from their dispersion into a pellet via ultracentrifugation at high accelerations ($\geq$200 000 g). After subsequent washing steps, the obtained SWNT filter cake or pellet can be redispersed in pure solvent providing a purified SWNT dispersion for further spectroscopic analyses or solution processing.

2.1.5 Charge Transport Properties

Individual SWNTs exhibit extraordinary charge transport properties. While metallic nanotubes are capable of withstanding very high current densities $\geq 10^9$ A cm^{-2} surpassing even copper as an interconnect material, field-effect transistors (FETs) based on single semiconducting SWNTs reach remarkable charge carrier mobilities of the order of 10^4 cm^2 V^{-1} s^{-1} at room temperature.[131–135] These observations rely on the ability of SWNTs to transport charge carriers under more or less ideal conditions, i.e., without significant hindrance by charge carrier scattering. In the ideal case, the so-called ballistic transport regime, the mean free path l_{mfp} of the charge carriers, which denotes the average length between two scattering events, is significantly larger than the SWNT length. This mean free path consists of scattering contributions and corresponding mean free paths due to defects (l_{d}), acoustic phonons (l_{ac}) as well as the emission and/or absorption of optical phonons (l_{op}) according to Matthiessen's rule:[29]

$$l_{\mathrm{mfp}} = \left(\frac{1}{l_{\mathrm{d}}} + \frac{1}{l_{\mathrm{ac}}} + \frac{1}{l_{\mathrm{op}}}\right)^{-1} . \tag{2.13}$$

As l_d is essentially independent of temperature and the applied electric field, reaching values of several micrometers for CVD-grown SWNTs,[136] it only becomes relevant at very low temperatures, as phonons typically dominate scattering processes at ambient conditions. At low bias and room temperature l_mfp is mainly determined by acoustic phonon scattering with $l_\mathrm{ac} \propto \frac{d_\mathrm{t}}{T}$ and mean free paths in the range of 1 µm for both metallic and semiconducting SWNTs were experimentally reported.[137–140] Under high-field conditions, i.e., for lateral electric fields exceeding a few volts per micrometer, the emission of optical phonons starts to significantly hinder charge transport. The overall mean free path in this case is dominated by l_op, that is considerably shorter, namely about 10 nm for semiconducting SWNTs and 100 nm for metallic nanotube species, resulting in current saturation at ~25 µA for longer tube lengths than that.[141–145] Similar to l_ac the optical phonon scattering mean free path scales linearly with d_t, but on the other hand l_op decreases strongly with the electric field and is rather temperature-independent at high biases.[146]

Yet, even in the ballistic transport regime for a given interconnect with ideal ohmic contacts between the SWNT and its metal electrodes a minimum intrinsic resistance R_i of 6.45 kΩ or $\frac{h}{4e^2}$ will be found with h being Planck's constant and e the elementary charge.[147] This finite value is the result of the different dimensionality of a one-dimensional ballistic conductor and its higher dimensional metal contacts that leads to a fundamental contact resistance at the interfaces and gives rise to a quantized conductance in units of $G_0 = \frac{2e^2}{h}$ depending on the number of available conducting channels.[148] Based on their twofold subband degeneracy a quantum conductance limit of $2G_0$ and thus a corresponding minimum resistance was proposed and confirmed experimentally for metallic SWNTs at equilibrium and semiconducting nanotubes that are excited to their first conduction subband.[147,149,150]

If the SWNT length L_t exceeds the l_mfp, which is the more common case in real devices, repeated charge carrier scattering will lead to an additional ohmic resistance R_ohm, increasing the overall nanotube resistance. Even in this so called diffusive transport regime SWNTs exhibit outstanding transport properties and resistances per unit length of down to 7 kΩ µm^{-1} were measured for up to centimeter long nanotubes (both metallic and semiconducting) at room temperature.[151,152] The total minimum resistance R_t of a given SWNT with arbitrary tube length can thus be expressed as:

$$R_\mathrm{t} = R_\mathrm{i} + R_\mathrm{ohm} = \frac{h}{4e^2}\left(1 + \frac{L_\mathrm{t}}{l_\mathrm{mfp}}\right). \tag{2.14}$$

Still, Equation 2.14 does not take into account injection barriers at the nanotube contacts. In most single nanotube devices an additional contact resistance contribution due to an energetic mismatch between the nanotube and the electrodes (see section 2.4 for details) results in substantially larger device resistances especially for short SWNTs. This energy level mismatch does not only play a role at the interface between a SWNT and its metal contacts, but also leads to an additional resistance at the intersection between two different nanotubes.

It has to be noted that metallic SWNTs exhibit the above mentioned low resistance values already at equilibrium, whereas the conductivity in semiconducting nanotubes is several orders of magnitude lower unless a high charge carrier density is accumulated, e.g., by an applied gate voltage inside a FET, similar to conventional semiconductors. Yet, when the SWNT FET is switched to its on-state, resistance values comparable to those of metallic nanotubes can be reached.

Furthermore, the charge carrier mobility in semiconducting SWNTs shows a strong charge carrier density dependence that arises from the characteristic shape of their van Hove singularities.[134,153] As long as the Fermi level does not approach the upper edge of the first nanotube subband, the mobility rises monotonously with the carrier concentration. Once the Fermi level reaches the second SWNT subband, the mobility decreases due to the abruptly increased DOS and thus higher phonon scattering rates, before it slowly rises again while the second subband is filled.[28,153] Hence, the charge carrier density-dependent mobility of semiconducting SWNTs typically exhibits a pronounced peak. In addition to that, the coupling of the gate bias to the carrier density in real SWNT FETs is strongly influenced by the quantum capacitance arising from the one-dimensional nanotube structure in relation to the geometric gate capacitance.[154–156] This SWNT quantum capacitance is proportional to the DOS at the Fermi level and commonly smaller (on the order of $4 \times 10^{-10}\,\mathrm{F\,m^{-1}}$) than the geometric capacitance.[157] Thus, it has to be taken into account to obtain a reliable charge carrier concentration for a given gate bias.

Given the aforementioned dependencies of l_{ac} and l_{op} on the nanotube diameter and temperature it follows that the resistance of semiconducting SWNTs is likewise influenced by both. According to theoretical and experimental reports the maximum conductance and the peak mobility in single SWNT FETs scale inversely with temperature due to a lower phonon scattering rate at lower temperatures indicating that individual semiconducting SWNTs exhibit band transport.[158,159] Additionally, the phonon scattering rate and the effective mass decrease linearly with increasing nanotube diameter resulting in a quadratic dependence of the SWNT peak mobility on d_{t}. Both dependencies of the peak mobility are reflected in the empirical relation:

$$\mu_{\mathrm{peak}} = 0.48 \frac{e v_0}{\hbar \alpha} \frac{d_{\mathrm{t}}^2}{T} \tag{2.15}$$

with v_0 being the Fermi velocity of graphene, $\hbar = \frac{h}{2\pi}$ the reduced Planck constant, $\alpha = 12\,\mathrm{m\,K^{-1}\,s^{-1}}$ an empirical coefficient and T the temperature.[158]

Due to the almost perfect mirror symmetry of the lower van Hove singularities in the valence and conduction band and the equal effective masses for both carrier types semiconducting SWNTs are intrinsically ambipolar, i.e., they show electron and hole transport.[140,154,160–162] The comparatively narrow nanotube bandgaps ($<1.5\,\mathrm{eV}$) and the rather small injection barriers at the interface with common electrode metals such as gold or palladium further promote this ambipolarity which is typically observed for SWNTs when they are not doped extrinsically.[163,164]

So far, this section only covered charge transport in individual nanotubes. However, due to processing reasons the active layer of most SWNT-based optoelectronic devices, such as transistors or light-emitting diodes, consists of randomly-oriented nanotube networks containing thousands of SWNT intersections which the charge carriers have to cross on their way through the device channel with lengths of the order of several tens of micrometers. These nanotube-nanotube junctions in SWNT networks are commonly regarded to limit the overall charge transport, as they typically possess substantially higher resistances in the range of 10^2–10^5 kΩ compared to the resistance within each nanotube.[152,165–168] While the junction resistances were reported to depend on the presence and diameter of SWNT bundles, their magnitude is mainly influenced by the different electronic properties of the intersecting SWNT species. Especially the junctions between metallic and semiconducting nanotubes substantially hinder charge transport due to the formation of additional Schottky-barriers which the charge carriers have to overcome.[169]

In the early days of research on nanotube network FETs, when effective SWNT sorting techniques had not yet been established, experiments were restricted to mixtures of more or less enriched metallic and semiconducting SWNTs.[170] These networks were described as two-dimensional percolating systems and their conductance was commonly characterized with respect to basic geometric parameters, e.g., channel length, SWNT density, nanotube length or degree of alignment, determining the number of available percolating paths and the minimum number of junctions necessary to bridge the distance between the electrodes.[171–174] Depending on the accumulated charge carrier density the conductance of semiconducting nanotubes can be tuned over at least six orders of magnitude, while metallic SWNTs barely exhibit any current modulation. Hence, optimizations of the network properties aimed for an ideal trade-off between maximum on-currents/carrier mobilities realized by shorter channels and higher nanotube densities and the achievable on/off current ratio limited by percolating paths of metallic SWNTs.[175,176]

2.2 Charge Transport Models for SWNT Networks

In contrast to individual nanotubes the charge transport and its temperature dependence of purely semiconducting SWNT networks are not fully understood. With the aim to elucidate the underlying mechanisms in more detail, the charge transport processes in such nanotube networks are commonly modeled using conventional approaches for disordered systems inspired by the extensive knowledge on organic semiconductors.[177–179] This section presents the most relevant models for the description of disordered semiconductors in general and with particular reference to semiconducting nanotube networks. Furthermore, it introduces computational methods for the simulation of charge transport properties in these systems with a focus on a recently developed random resistor network model.

2.2.1 Models for Disordered Semiconductors

Depending on their degree of crystallinity inorganic and organic semiconductors exhibit charge transport properties that can deviate entirely from the ideal band transport behavior observed for highly ordered single-crystals and also for individual semiconducting SWNTs.[180,181] The presence of grain boundaries, impurities and other kinds of structural defects in, e.g., polycrystalline or even amorphous materials, leads to localized trap states within the gap between the delocalized energy bands of the ordered crystal lattice. If the degree of structural disorder is low, which is the case for many (poly-)crystalline materials, charge transport is often explained by the so-called multiple trapping and release model, assuming the existence of a narrow but extended transport band and of such localized energy levels within the bandgap.[182,183] The overall charge transport process is described as superposition of band-like transport of charge carriers within the bands and trapping at the statistically distributed, localized states until the carriers are thermally excited above the transport band edge again. Consequently, the carrier mobility increases non-linearly with increasing temperature in contrast to pure band transport for which the mobility exhibits an opposing temperature dependence.[184]

In amorphous or polymer semiconductors the degree of disorder is even higher, thereby hindering or completely preventing the formation of delocalized energy bands. Instead, charge transport occurs predominantly by thermally activated hopping between localized states with a certain variation of site energies (see Figure 2.7) whose distribution is commonly described by a gaussian DOS.[185]

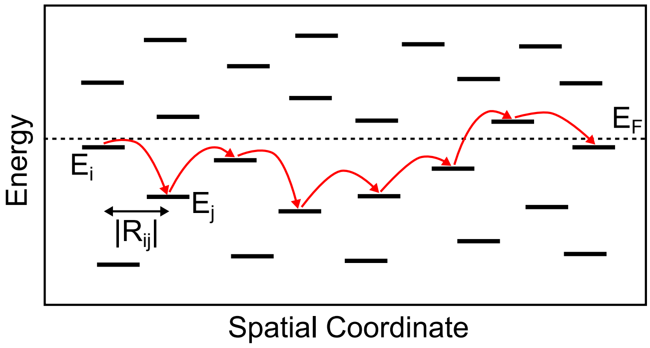

Figure 2.7: Schematic representation of the energy landscape in a disordered semiconductor in which charge carriers are transported by hopping between localized states that are separated in space and energy.

Based on the model of Miller and Abrahams the hopping mechanism is interpreted as phonon-assisted tunneling process resulting in the expression for the hopping rate w_{ij} between the two sites i and j:[186,187]

$$w_{\mathrm{ij}} = w_0 \exp\left(-2\alpha|R_{\mathrm{ij}}|\right) \begin{cases} \exp\left(-\frac{E_{\mathrm{j}}-E_{\mathrm{i}}}{kT}\right) & \forall E_{\mathrm{j}} > E_{\mathrm{i}} \\ 1 & \text{else} \end{cases} \tag{2.16}$$

with w_0 being the hopping prefactor that is related to the phonon vibration frequency, α being the inverse wavefunction decay length, $|R_{\mathrm{ij}}|$ the spatial distance between the two sites, E_{i} and E_{j} their energies, k the Boltzmann constant and T the temperature. While for jumps downward in energy the hopping rate only depends on the tunneling probability determined by the wavefunction overlap, upward hops additionally require thermal activation represented by the Boltzmann term. Due to the exponential dependence of the tunneling probability on the intersite distance the Miller-Abrahams model only allows for jumps between nearest neighbor sites.

This approach was later extended to the so-called variable range hopping model (VRH) which also includes hops over distances beyond nearest neighbors to sites of more similar or even lower energy.[181,188,189] The maximum transition rate in this case is obtained by a convolution of the tunneling probability and the thermal activation. The corresponding charge carrier mobility of the disordered semiconductor is directly proportional to this hopping rate and exhibits likewise a thermally activated temperature dependence:

$$\mu_{\mathrm{VRH}} \propto \exp\left[-\left(\frac{T_0}{T}\right)^{1/(n+1)}\right] \tag{2.17}$$

with T_0 being a characteristic temperature determined by α and the inverse DOS in the vicinity of the Fermi level and n the dimensionality of the hopping space.[189] This temperature dependence of the carrier mobility shows good agreement with experimental results for various disordered systems including amorphous inorganic and polymer semiconductors.[190–192]

Similar to grain boundaries or other defects in polycrystalline or amorphous semiconductors, the nanotube-nanotube junctions in semiconducting SWNT networks are conventionally interpreted as energy barriers giving rise to disorder and charge localization. Consequently, VRH models have also been utilized to describe charge transport in SWNT networks by respective fitting of the temperature-dependent conductance or carrier mobility values.[177,193] Yet, especially for cryogenic temperatures below 100 K these models fail to reproduce the experimental data recorded for purely semiconducting nanotube networks.[178,179,194]

A better fit over a broad temperature range could be obtained using the so-called fluctuation-induced tunneling (FIT) model which was originally proposed by Sheng for the description of disordered systems such as carbon-polyvinyl chloride composites, doped GaAs or polyacethylene.[195,196] According to this model, which was later applied to other (semi-)conducting polymers,[197] the charge carriers are transported across tunneling barriers between extended conducting segments. While for low temperatures the tunneling process is considered to be temperature-independent, at higher temperatures thermally activated voltage fluctuations across the insulating barrier reduce the barrier height and enhance the tunneling probability. The corresponding temperature dependence of the charge carrier mobility can be expressed as:

$$\mu_{\mathrm{FIT}} = A \exp\left(-\frac{T_{\mathrm{B}}}{T_{\mathrm{S}} + T}\right) \tag{2.18}$$

with A being a temperature-independent prefactor, T_{B} a characteristic temperature representing the height and shape of the insulating barrier and T_{S} being a critical temperature above which the thermally activated potential fluctations affect the tunneling process thus indicating the transition between temperature-dependent and -independent charge transport.

2.2.2 Computational Approaches

In order to better understand the obtained experimental data for disordered semiconductors several computational methods have been utilized to simulate and evaluate their charge transport properties based on the above mentioned hopping transport models. A large variety of algorithms for disordered systems is based on the Monte Carlo technique[185,198] or on the Master equation approach.[199–201] Although Monte Carlo methods enable a time-dependent description of the hopping motion of a certain number of charge carriers (electrons and holes) across a created grid of localized sites including the Coulomb interactions between all charges, they have the disadvantage of comparatively high computational cost. The Master equation approach on the other hand allows for a more computationally efficient modeling of hopping transport by monitoring the occupation probability for only one charge carrier type at all sites of the grid, instead of keeping track of every charge. Commonly, the Master equation is solved in the steady-state regime resulting in the following expression:

$$\frac{\partial p_{\mathrm{i}}}{\partial t} = \sum_{i \neq j} \left[w_{\mathrm{ji}}\, p_{\mathrm{j}}(1 - p_{\mathrm{i}}) - w_{\mathrm{ij}}\, p_{\mathrm{i}}(1 - p_{\mathrm{j}}) \right] = 0 \tag{2.19}$$

with w_{ij} being the Miller-Abrahams hopping rate (see Equation 2.16) from site i to site j and p_{i}, p_{j} being the occupation probabilities for both sites. Starting with initial values for p_{i} and p_{j}, e.g., using the Fermi-Dirac distribution, the Master equation is solved numerically in order to obtain the bond currents for each pair of sites and finally the overall current through the grid as well as the charge carrier mobility of the system at a given Fermi level.

A recent example for a Master equation-based computational model was introduced by Schießl *et al.* for the simulation of the charge carrier density-dependent charge transport properties of semiconducting SWNT networks.[202] Within this model, a nanotube network is created by randomly distributing one-dimensional sticks with a certain length and an assigned nanotube chirality inside a two-dimensional simulation box with a predefined size until a preset network density is reached (see Figure 2.8), using the Monte Carlo method. At the points where two sticks i and j intersect with each other, a nanotube-nanotube junction resistor is created, while each SWNT segment is treated as node with zero resistance in accordance with the experimentally observed orders of magnitude lower intra-nanotube resistances. Consequently, the simulated nanotube network is converted into a random resistor network consisting of SWNT-SWNT junctions only.

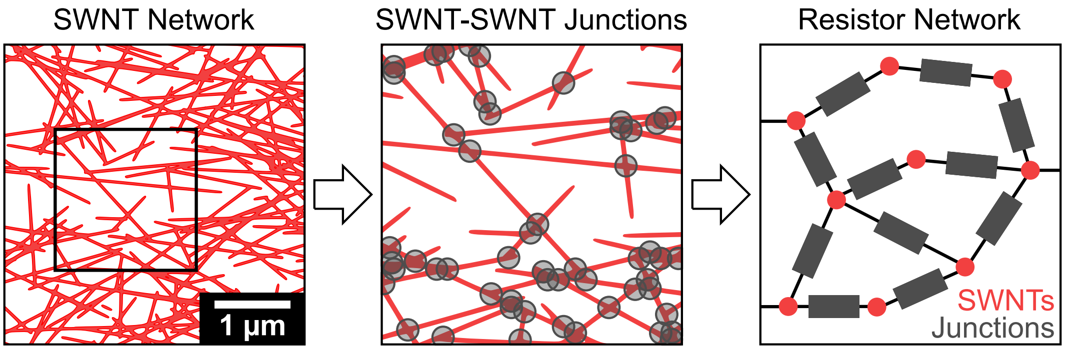

Figure 2.8: Schematic illustration of a simulated two-dimensional network of one-dimensional sticks representing a SWNT network (left), magnified view (middle) with highlighted nanotube-nanotube junctions (grey) between individual SWNTs (red) and deduced resistor network with nodes and resistors representing nanotubes and junctions respectively (right).

The charge transfer between two intersecting nanotubes is described as Miller-Abrahams hopping process and a bond conductance is obtained for each junction resistor in a mean field approximation and assuming small lateral electric fields:

$$G_{\mathrm{ij}} = \frac{e^2\, w_{\mathrm{ij}}^{\mathrm{symm}}}{4kT \cosh\left(\frac{E_{\mathrm{i}}-E_{\mathrm{F}}}{2kT}\right) \cosh\left(\frac{E_{\mathrm{j}}-E_{\mathrm{F}}}{2kT}\right)} = \frac{e^2\, w_0 \exp\left(-\frac{|\Delta E_{\mathrm{ij}}|}{2kT}\right)}{4kT \cosh\left(\frac{E_{\mathrm{i}}-E_{\mathrm{F}}}{2kT}\right) \cosh\left(\frac{E_{\mathrm{j}}-E_{\mathrm{F}}}{2kT}\right)} \tag{2.20}$$

with $w_{\mathrm{ij}}^{\mathrm{symm}}$ being the symmetrized Miller-Abrahams hopping rate between the sites i and j,[201] ΔE_{ij} the energy difference between both and E_{F} being the Fermi energy. However, so far this model is only suitable for conventional disordered systems and does not take into account specific SWNT properties, such as a negligibly small Coulomb charging energy[203] and a continuous DOS with van Hove singularities instead of single energy levels. In order to implement these properties the equation for the bond conductance at each SWNT-SWNT junction is adapted:

$$G_{\mathrm{ij}}^{\mathrm{jun}} = \iint G_{\mathrm{ij}}(E_{\mathrm{F}}, E_{\mathrm{i}}, E_{\mathrm{j}})\, D_{\mathrm{i}}(E_{\mathrm{i}})\, D_{\mathrm{j}}(E_{\mathrm{j}})\, \mathrm{d}E_{\mathrm{i}} \mathrm{d}E_{\mathrm{j}} \tag{2.21}$$

with D_{i} and D_{j} being the absolute DOS of the intersecting SWNTs i and j including their first conduction subband only. Depending on the respective nanotube length and chirality the DOS is calculated and the resulting energetic position of the band edge is superimposed with a Gaussian distribution whose width is representing additional energetic disorder of the system.

Next, the local potential at each SWNT can be computed by solving Kirchhoff's current law in a node using a numerical solver:

$$\sum_{i\neq j} I_{\mathrm{ij}} = \sum_{i\neq j} G_{\mathrm{ij}}^{\mathrm{jun}} \cdot V_{\mathrm{ij}} = 0 \tag{2.22}$$

with I_{ij} being the bond current and $V_{\mathrm{ij}} = V_{\mathrm{i}} - V_{\mathrm{j}}$ the difference in the local electrostatic potential between the nanotubes i and j. As soon as all V_{i} are obtained, the current passing through a vertical slice (in the y-direction) of the simulation box I_0 can be derived and with that the overall conductance of the resistor network G_0 by using Ohm's law:

$$G_0(E_{\mathrm{F}}) = \frac{I_0(E_{\mathrm{F}})}{L_{\mathrm{y}}\, F_{\mathrm{x}}} \tag{2.23}$$

with L_{y} being the length of the simulation box in the y-direction and F_{x} the external electric field in the x-direction. The whole simulation is performed for various Fermi energies and thus charge carrier densities which are obtained by:

$$n(E_{\mathrm{F}}) = \frac{1}{L_{\mathrm{x}}\, L_{\mathrm{y}}} \sum_{i=1}^{N} \int_{-\infty}^{\infty} D_{\mathrm{i}}(E_{\mathrm{i}}) \cdot f(E_{\mathrm{i}}, E_{\mathrm{F}})\, \mathrm{d}E_{\mathrm{i}} \tag{2.24}$$

with the length of the simulation box in the x-direction L_{x}, the total number of SWNTs in the box N and the Fermi-Dirac distribution $f(E_{\mathrm{i}}, E_{\mathrm{F}})$. Finally, the charge carrier density-dependent carrier mobility of the network is given by:

$$\mu_0 = \frac{G_0}{en}. \tag{2.25}$$

Aside from the network mobility the model enables the calculation of the local power dissipation at each junction as well as of the current distribution among the individual nanotubes of the network at different charge carrier densities.

Yet, this random resistor model is based on several simplifications and assumptions leading to limitations in its ability to describe charge transport in semiconducting SWNT networks.[202] As the model completely neglects the Coulomb charging energy of the SWNTs, it is only valid for temperatures >100 K to ensure that the thermal energy is substantially larger than the charging energy. Furthermore, the two-dimensional network structure is no longer valid for very dense nanotube films whose thickness is larger than a few nanometers. In addition, the hopping prefactor w_0 is kept constant at an arbitrary value for all SWNT species which is why only normalized network mobilities and their relative changes can be obtained. Lastly, the model neglects the intra-nanotube resistance and its temperature and diameter dependence entirely which could lead to deviations from the experiment for sparse networks with long tube lengths and at high charge carrier densities. Still, this model was able to consistently describe the carrier density-dependent transport properties of SWNT networks depending on input network parameters such as the length and species distribution of the SWNTs, the network density, energetic disorder, temperature or the simulation box size. In addition, it could reproduce experimental results obtained for both monochiral and mixed semiconducting SWNT networks.[202]

2.3 Field-effect Transistors

Experimentally, charge transport in semiconducting SWNT networks and other (disordered) semiconductors depending on charge carrier density and temperature is commonly investigated in FETs. These electronic devices with three terminals enable the modulation of the current flow between two electrodes, that are connected by a semiconducting layer, by means of an external electric field in transversal direction.[204,205] In common thin-film FETs this field is created across an insulated gate, i.e., a biased third electrode separated by a dielectric layer from the semiconductor.

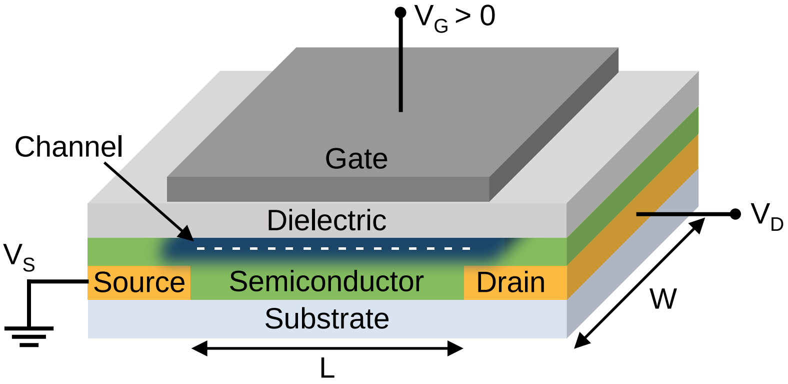

Figure 2.9: Schematic illustration of an n-type FET in accumulation mode with source, drain and gate electrode, dielectric and semiconducting layer in a bottom-contact/top-gate geometry.

A schematic representation of an FET in a staggered bottom-contact/top-gate configuration, as used throughout this thesis, is shown in Figure 2.9. In this layout, the contacts at which charge carriers are injected (source electrode) and extracted (drain electrode) are located below the semiconductor, while the insulating dielectric and the gate electrode are placed on top of it. Depending on the desired application FETs are fabricated also in other architectures, such as bottom-contact/bottom-gate, top-contact/top-gate and top-contact/bottom-gate, based on a trade-off between ease of processing and improved device properties, e.g., by enhanced charge injection.[206] In all cases, a conductive channel is induced and mobile charge carriers are accumulated at the interface of dielectric and semiconductor when a sufficiently high voltage is applied to the gate electrode (gate voltage V_G) in relation to the potential at the source electrode which is typically grounded ($V_\mathrm{S} = 0$). When a lateral field is created between source and drain by applying a voltage to the drain electrode ($|V_\mathrm{D}| > 0$), the accumulated charges move across the active channel from source to drain (i.e., current flow I_D), while the dielectric typically limits leakage currents between source and gate (gate current I_G) to the picoampere range. The distance between source and drain (channel length L) and the width of both contacts (channel width W)

geometrically determine the channel area and thus the number of charge carriers that can be transported. Aside from their application as an electronic switch, FETs enable charge carrier density-dependent transport investigations of semiconducting materials at considerably higher carrier densities compared to other device classes such as diodes.

Conventional FETs based on inorganic semiconductors typically exhibit unipolar conduction of either electrons or holes due to doping. While so-called n-type FETs transport electrons at positive gate bias ($V_G > 0$), p-type devices exhibit hole transport for negative gate voltages. However, various (in-)organic semiconducting materials, including SWNTs, intrinsically are capable of accumulating both carrier types at the same time which is referred to as ambipolar transport. The following section introduces the basic operating principle of unipolar FETs, the special class of ambipolar and light-emitting transistors as well as state-of-the-art SWNT FETs.

2.3.1 Basic Principle

The FET operation relies on a Fermi level shift in the semiconductor next to the semiconductor/dielectric interface depending on the gate voltage. When a sufficiently high gate bias is applied, the Fermi level of the semiconductor approaches the conduction band (for positive V_G), resulting in the accumulation of electrons at the semiconductor/dielectric interface as illustrated in Figure 2.9 with the blue-shaded area representing accumulated electrons in an n-type FET. For negative gate voltages holes can be accumulated in the channel instead. The required gate voltage for accumulation of mobile charge carriers, the so-called threshold voltage V_{th}, depends on the energetic position of the semiconductor band edges and the presence of additional energy levels within its bandgap due to dopants, impurities or defects either within the semiconductor itself or at its interface with the dielectric. Once these trap states are filled, mobile carriers are available for charge transport through the transistor channel. A metal-insulator-semiconductor capacitor between the gate electrode and the accumulation layer is formed with a capacitance per unit area C_i given by:

$$C_i = \frac{\epsilon_r \, \epsilon_0}{d_i} \tag{2.26}$$

with ϵ_0 and ϵ_r being the permittivities of free space and of the insulating material and d_i the layer thickness of the dielectric. Consequently, the number of induced charge carriers per unit area in the accumulation layer Q_{mob} is proportional to the effective gate voltage $V_G - V_{th}$ and the gate capacitance:

$$Q_{mob} = C_i \, (V_G - V_{th}) \, . \tag{2.27}$$

Yet, the accumulation layer only exhibits a uniform carrier density as implied in Figure 2.9 with typical thicknesses reaching a few nanometers if both V_S and V_D are grounded.[207] When a bias between source and drain is applied, the change of the channel potential $V(x)$ depending on the lateral position in the channel x (from $V(0) = 0$ at the source electrode to $V(L) = V_{\mathrm{DS}}$ at the drain electrode) has to be considered.[208,209] This channel potential directly affects the local charge carrier density and results, e.g., in a decreasing electron density from source to drain for $V_{\mathrm{DS}} > 0$ and $V_{\mathrm{G}} - V_{\mathrm{th}} > 0$:

$$Q_{\mathrm{mob}}(x) = C_{\mathrm{i}} \left(V_{\mathrm{G}} - V_{\mathrm{th}} - V(x) \right). \tag{2.28}$$

As long as the channel length is significantly larger than the thickness of the dielectric, i.e., $L > 10d_{\mathrm{i}}$, the gate field is likewise larger than the lateral electric field between source and drain. In this case the gradual channel approximation adequately describes the position-dependent increase of the channel potential from the source to the drain electrode.[210,211] Based on this model and considering drift transport only, i.e., diffusion currents are neglected, the current flow through the transistor channel I_{D} can be derived from Ohm's law:

$$I_{\mathrm{D}} = W \, \mu \, Q_{\mathrm{mob}}(x) \, \frac{dV}{dx}, \tag{2.29}$$

resulting in:

$$I_{\mathrm{D}} = \frac{W}{L} C_{\mathrm{i}} \, \mu \left[\left(V_{\mathrm{G}} - V_{\mathrm{th}} \right) V_{\mathrm{DS}} - \frac{1}{2} V_{\mathrm{DS}}^2 \right], \tag{2.30}$$

assuming that the charge carrier mobility μ is independent of the charge carrier density. For small drain voltages compared to $V_{\mathrm{G}} - V_{\mathrm{th}}$ a linear increase of the channel potential $V(x)$ results in a linear gradient of the accumulated carrier density from source to drain as shown in Figure 2.10a. In this so-called linear regime the current scales linearly with V_{DS} as the V_{DS}^2 term in Equation 2.30 can be neglected:

$$I_{\mathrm{D}}^{\mathrm{lin}} = \frac{W}{L} C_{\mathrm{i}} \, \mu_{\mathrm{lin}} \left(V_{\mathrm{G}} - V_{\mathrm{th}} \right) V_{\mathrm{DS}}. \tag{2.31}$$

For larger V_{DS} the accumulated charge carrier density next to the drain electrode is further decreased up to the point, at which $V_{\mathrm{DS}} = V_{\mathrm{G}} - V_{\mathrm{th}}$ leading to a pinch-off of the channel, i.e., a local depletion region is formed as $V_{\mathrm{G}} - V(x) < V_{\mathrm{th}}$ (see Figure 2.10b). In this case the current still flows through the space-charge zone although it can no longer increase with increasing V_{DS}. Instead, for larger drain voltages the pinch-off point moves towards the source electrode and the current saturates. The drain current in this so-called saturation regime can be expressed as follows by substituting V_{DS} with $V_{\mathrm{G}} - V_{\mathrm{th}}$ in Equation 2.30:

$$I_{\mathrm{D}}^{\mathrm{sat}} = \frac{W}{2L} C_{\mathrm{i}} \, \mu_{\mathrm{sat}} \left(V_{\mathrm{G}} - V_{\mathrm{th}} \right)^2. \tag{2.32}$$

Both operating regimes are reflected in the output characteristics, i.e., drain voltage sweeps for different constant V_G, of a unipolar n-type transistor as shown in Figure 2.10c. The other typical kind of current-voltage characteristics of FETs are the transfer characteristics (see Figure 2.10d) that show the logarithmic increase of the drain current depending on the gate voltage at one or more constant V_D.

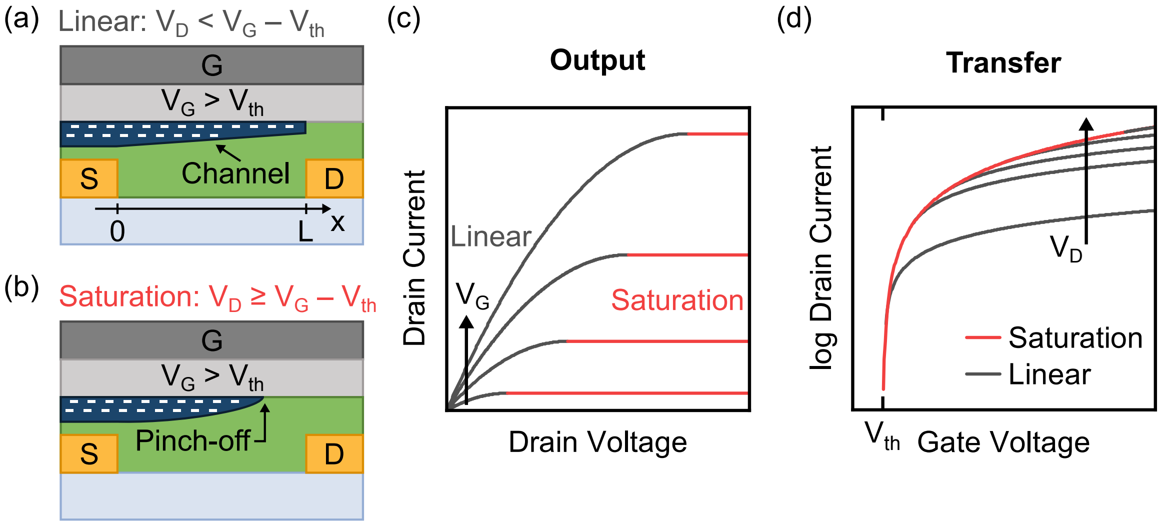

Figure 2.10: (a) Schematic illustration of the charge carrier distribution in a unipolar n-type FET operating in the linear regime and (b) in the saturation regime. (c) Corresponding ideal current-voltage characteristics at constant V_G (output characteristics) and (d) at constant V_D (transfer characteristics) showing the voltage dependencies of the drain current in both regimes. Note, only for $V_D << V_G - V_{th}$ the voltage dependence of I_D is truly linear.

While the output curves allow for the discrimination between the linear and saturation regime of a FET at a given gate voltage range, the transfer characteristics can be utilized for the evaluation of the device performance based on figures of merit such as the charge carrier mobility, the on/off current ratio or the threshold voltage. The charge carrier mobility is commonly considered to be one of the most important device parameters for FETs. It is the proportionality constant between the drift velocity of the charge carriers and the applied electric field and thus determines the device current per voltage as well as the maximum switching frequency. Depending on the chosen gate and drain voltage ranges μ can either be extracted by Equation 2.33 when the transistor is operated in the linear regime:

$$\mu_{\mathrm{lin}} = \frac{\partial I_D}{\partial V_G} \frac{L}{W C_i V_{DS}} \tag{2.33}$$

or by Equation 2.34 in the saturation mode:

$$\mu_{\mathrm{sat}} = \frac{\partial^2 I_D}{\partial V_G^2} \frac{L}{W C_i}. \tag{2.34}$$

However, both expressions rely on the gradual channel approximation that only applies to ideal devices in which, e.g., the gate voltage dependence of the mobility, contact resistance or other extrinsic effects are neglected. Especially contact resistance is expected to play a role in real thin-film FETs requiring a correction of the apparent mobilities as extracted with the two aforementioned equations (see Chapter 2.4 for details).[212–214]

Another important device parameter is the on-current I_{ON} and more so its comparison with the off-current I_{OFF}, the on/off current ratio. To keep the overall power consumption low and to enable, e.g., a good brightness contrast when applying the FET in active matrix displays, a high on/off ratio of at least 10^6 is desired.[215] This ratio can be easily determined by extracting I_{ON} and I_{OFF} from the transfer characteristics when plotted in the semilog scale as illustrated in Figure 2.11 showing the transfer curve of a plasma torch SWNT network FET. The off-current is ideally limited by the gate leakage current I_{G} as shown by the dashed red line in Figure 2.11 that should be minimized by a proper choice of dielectric materials and processing conditions. In the case of SWNT networks I_{OFF} might be higher than I_{G} due to percolating paths of metallic nanotube species or by the small bandgap of large-diameter tubes.[216]

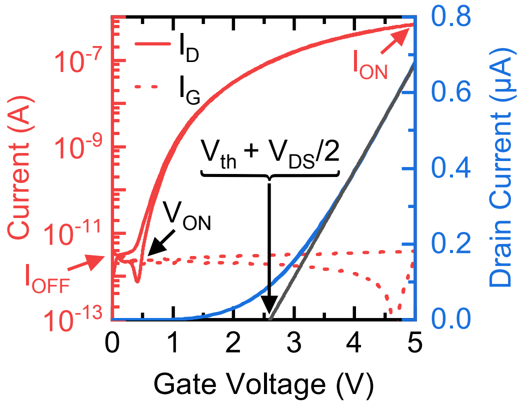

Figure 2.11: Transfer characteristics (forward and reverse gate voltage sweep) of a plasma torch SWNT network FET in the linear regime ($V_{\mathrm{DS}} = -10\,\mathrm{mV}$) in semilog scale (red) and in linear scale (blue). Both the drain current (solid line) and the gate current (dashed line) can be compared in the semilogarithmic plot enabling the extraction of the on- and off-current and of the onset voltage. The position of V_{th} can be determined from the x-intercept of the linear fit (grey line) to the drain current in the linear plot.

Furthermore, depending on the operating regime the threshold voltage can be obtained from the transfer characteristics. When the transistor is operated in the linear regime, V_{th} can be extracted from the x-intercept of the linear fit based on Equation 2.30 (solid grey line) to I_{D} (solid blue line) as shown in Figure 2.11. Similarly, the intercept of a linear fit to $\sqrt{I_{\mathrm{D}}}$ gives V_{th} in the saturation regime. For ideal FETs V_{th} indicates the gate voltage, at which the current increases abruptly (see Figure 2.10d). However, for real devices the position of the onset voltage V_{ON}, commonly defined as the point at which I_{D} exceeds the gate leakage and/or the noise level, differs substantially from V_{th} as shown in Figure 2.11. Between V_{ON} and V_{th}, the so-called subthreshold region, already a non-negligible current is flowing through the device but the induced charge carriers are still affected by traps resulting in a more or less steep current increase with V_G depending on the trap density.[207,217] For real FETs an often observed non-linear current increase can make the precise extraction of V_{th} by linear fitting difficult. Hence, the use of V_{ON} as a metric to characterize the FET onset instead of V_{th} has been suggested due its less ambiguous definition and ease of determination especially for non-ideal thin-film transistors based on, e.g., organic semiconductors or metal oxides.[218–220]

2.3.2 Ambipolar and Light-Emitting Transistors

So far, unipolar FETs were introduced in this section via the example of n-type transistors. However, not only semiconducting SWNTs but a variety of other semiconductors exhibit both hole and electron transport when being integrated into FETs.[160,221–224] The simultaneous accumulation of both charge carriers, i.e., ambipolar operation, is considered as superposition of a unipolar p-type and a unipolar n-type FET and can be observed if the transistor is suitably biased (see Figure 2.12a). Depending on the applied gate and drain voltage in relation to the threshold voltages for holes $V_{th,h}$ and electrons $V_{th,e}$ both charge carriers are injected and induced either separately or at once. In the latter case their respective accumulation layers coexist in series within the channel. The transfer characteristics of an ambipolar FET can be likewise regarded as sum of the two overlapping curves for electrons (I_D increases with increasing V_G) and holes (I_D increases with decreasing V_G) resulting in the typical V-shape as shown in Figure 2.12b for various positive V_D. As indicated by the different line colors, the operating regimes change during each gate voltage sweep.

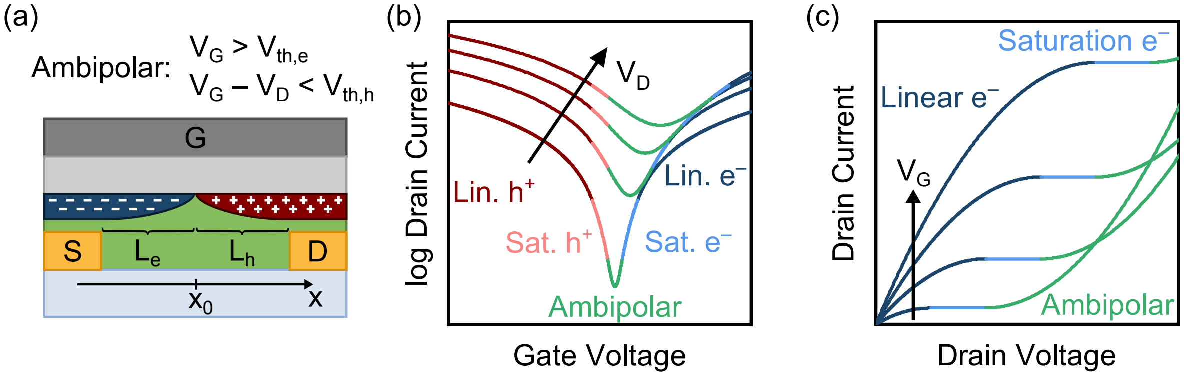

Figure 2.12: (a) Schematic representation of the charge carrier distribution in an ambipolar FET when operated in the ambipolar regime: electrons (blue) and holes (red) are simultaneously accumulated. (b) Transfer characteristics of an ideal ambipolar transistor with equal carrier mobilities for holes and electrons for various positive V_D and (c) corresponding output characteristics for positive V_G and V_D. Line colors indicate the different operating regimes.

Assuming that $V_S = 0\,V$ and $V_D > 0\,V$ only holes are accumulated in the channel and injected from the drain electrode that serves as hole source under these conditions when $V_G - V_D < V_{th,h}$

and $V_G < V_{th,e}$.[208,209,225] Analogous to the above mentioned electron accumulation mode, this unipolar hole transport regime (red) splits into a linear (for $V_G < V_{th,h}$) and a saturation regime (for $V_{th,h} < V_G < V_{th,e}$).

As soon as V_G is increased such that $V_G > V_{th,e}$ while $V_G - V_D < V_{th,h}$ the FET enters the true ambipolar regime (green), in which electrons are injected from the source and holes from the drain forming two separate, pinched-off accumulation layers whose lengths L_e and L_h add up to the full length of the channel L. The point at which both accumulation zones meet x_0 can be described as an induced pn-junction where the charge carrier density approaches zero and all electrons and holes have to recombine. Its position highly depends on the applied voltages compared to the respective threshold voltage for electrons and holes as well as on their charge mobilities μ_e and μ_h and can be estimated for an ideal device using the following expression:[208,226]

$$x_0 = \frac{L \cdot (V_G - V_{th,e})^2}{(V_G - V_{th,e})^2 + \frac{\mu_e}{\mu_h}(V_D - (V_G - V_{th,h}))^2}. \tag{2.35}$$

The overall source-drain current in this case equals the current in each of the two accumulation layers ($I_D = I_e = I_h$) and is given by:[208,227]

$$I_D = \frac{W}{2L} C_i \left(\mu_e \left(V_G - V_{th,e} \right)^2 + \mu_h \left(V_G - V_{DS} - V_{th,h} \right)^2 \right). \tag{2.36}$$

When the gate voltage is further increased up to the point at which $V_G > V_{th,e}$ while $V_G - V_D > V_{th,h}$ the FET reaches the aforementioned unipolar electron transport regime (blue).

As shown in Figure 2.12b both the magnitude of ambipolar current and the gate voltage range, in which ambipolar conduction occurs, are strongly influenced by V_D leading to higher currents and a shift of the ambipolar regime to higher positive gate biases when V_D is increased. Consequently, the output characteristics of an ambipolar FET (see Figure 2.12c) exhibit a superlinear current increase beyond the saturation level for large drain voltages due to the additional injection of opposite charge carriers.

As a result of the recombination of electrons and holes excitons are formed in the channel of ambipolar FETs that can relax radiatively. Analogous to optically excited photoluminescence, this electrically induced emission, the so-called electroluminescence (EL), has been observed from FETs based on various organic semiconductors including polymers[227–229] as well as single-crystals[230,231] and on SWNTs (both individual and networks).[232–234] Depending on the applied gate and drain voltages such FETs emit light from a defined position in their channel, i.e., the recombination zone x_0. Assuming a homogeneous semiconducting layer the recombination and thus emission zone has the shape of a narrow line parallel to the source and drain electrodes as it represents an equipotential line in the transistor channel with typical widths of up to one micrometer.[235–237] Yet, in real devices the emission zone is strongly affected by any voltage

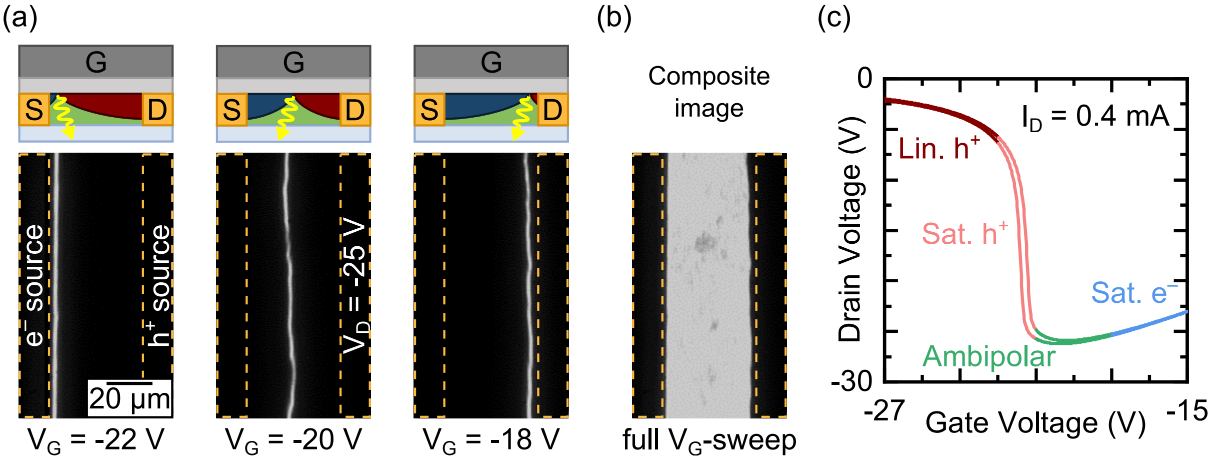

Figure 2.13: (a) Optical micrographs showing the motion of the line-shaped electroluminescence emission zone in the channel of a (6,5) SWNT network transistor during a V_G-sweep at constant $V_D = -25$ V for three different gate voltages (bottom) and schematic illustration of the corresponding electron and hole accumulation layers in the ambipolar FET (top), orange dashed lines indicate electrode positions. (b) Composite image based on a series of EL images collected during a full V_G-sweep showing the maximum intensity of each pixel and (c) constant current characteristics ($I_D = 0.4$ mA) of a (6,5) SWNT network FET, line colors indicate the different operating regimes.

drops, e.g., due to injection barriers, defects or grain boundaries and is rather wavy than perfectly straight.[238,239]

Based on Equation 2.35 the emission zone can be spatially controlled and moved, e.g., from source to drain and vice versa through the channel, by adjusting the gate and drain voltages. This is illustrated in Figure 2.13a with the example of a (6,5) SWNT network FET whose EL emission was recorded during a transfer sweep at constant V_D using a nIR InGaAs camera (see schematic illustration of the respective hole and electron accumulation layers in the FET channel at the top). Note that the drain electrode serves as the hole source under these conditions.

The EL intensity and thus the brightness at each pixel of the micrographs is determined by the local current density and the photoluminescence quantum yield of the semiconductor. Hence, EL imaging represents a powerful technique to directly visualize the charge transport pathways in the semiconducting layer, assuming a homogeneous quantum yield throughout the channel. Such EL images can either be evaluated individually or in the form of composite images that are obtained by the superposition of a large number of images recorded during a full voltage sweep showing the EL emission from the whole channel (see Figure 2.13b).[240,241] Yet, even at large V_D the drain current in the ambipolar regime can vary substantially during transfer sweeps (see Figure 2.12b), often affecting the brightness of the EL emission zone depending on its position in the channel. Fortunately, the fact that ambipolar FETs do not turn off when the drain voltage is sufficiently high allows for the application of a so-called constant current sweep.[227] In this mode, a constant drain current is maintained during a gate voltage sweep by adjusting V_D accordingly resulting in hook shaped current-voltage characteristics (see Figure 2.13c) that pass through the same operation regimes as during a transfer sweep . This measurement mode thus enables EL imaging with an ideally homogeneous brightness contrast for all positions of the recombination zone.

2.3.3 Single-Walled Carbon Nanotube Transistors

As described above semiconducting SWNTs are regarded as promising candidate for the development of post-silicon electronic devices and circuits. Over the past two decades a vast number of examples of FETs using semiconducting SWNTs as active material has been demonstrated. Apart from the species of SWNTs or mix thereof, the FET geometry as well as injection barriers, the respective device performance is mainly determined by the morphology of the SWNT transistor channel, especially by the number of SWNT-SWNT junctions between source and drain that the charge carriers have to overcome. Consequently, the overall carrier mobilities and on/off current ratios of SWNT FETs can vary by several orders of magnitude ranging from outstanding to mediocre values with latter being comparable to those of established organic semiconductors.[4,242–250] As described in section 2.1.5 exceptionally high carrier mobilities are achieved in devices whose channel is bridged by individual nanotubes, i.e., for single SWNT transistors and SWNT array FETs with the latter containing an array of parallel aligned SWNTs, directly connecting the source and drain electrode. Single nanotube FETs with channel lengths of less than 10 nm have been realized that outperformed silicon FinFETs with respect to current density and energy consumption while exhibiting on/off current ratios of up to 10^7.[251,252] However, aside from a poor device-to-device reproducibility, time-consuming processing steps, involving the separate localization of each individual SWNT and contacting by electron beam lithography, make a large-scale device fabrication difficult.

Aligned nanotube arrays with a high density have the advantage that they can be grown directly on a substrate,[253–256] enabling a less costly preparation of SWNT FETs based on photo- or electron beam lithography and subsequent deposition of the remaining device layers. However, due to the lack of suitable monochiral nanotube growth protocols this approach requires further postgrowth treatments to remove the formed metallic SWNTs that limit the current modulation when spanning the transistor channel.[257,258] Nevertheless, high carrier mobilities on the order of $10^3\,\mathrm{cm^2\,V^{-1}\,s^{-1}}$, on/off current ratios of 10^5 and significantly higher on-currents compared to single SWNT devices were achieved with this concept. Other routes for the fabrication of aligned SWNT array FETs are based on the deposition of semiconducting SWNTs from a purified dispersion, e.g., using Langmuir-Schaefer or evaporation-driven self-assembly techniques[234,259–262] followed by electrode patterning. Another alternative is the aligned nanotube deposition by dielectrophoresis, i.e., the application of an electric field between predefined bottom electrodes during solution-based SWNT deposition.[263] Given the short channel lengths, all of these methods necessitate nanotube dispersions with very high semiconducting purity (>99.8 %) because even one single metallic nanotube could short-circuit the device. Although carrier mobilities of several hundred $\mathrm{cm^2\,V^{-1}\,s^{-1}}$ and on/off ratios of 10^8 could be reached for FETs fabricated based on these techniques, they are quite elaborate or lack further scalability.

Provided that lower carrier mobilities comparable to those of polycrystalline or amorphous silicon (1–$100\,\mathrm{cm^2\,V^{-1}\,s^{-1}}$) are sufficient, the use of semiconducting SWNT networks as active layer substantially reduces the complexity of the necessary processing steps. Such randomly oriented or semi-aligned networks can be deposited as macroscopic thin-films from dispersion by a broad range of techniques. These methods include immersion of the substrate,[115,176,264–266] simple dropcasting[9,267,268] or combined with dielectrophoresis,[73,269–273] blade- or dip-coating,[274,275] spin-coating[124,276–278] as well as printing processes (e.g., inkjet printing,[121,279–282] aerosol-jet printing[283–288] or gravure printing[289,290]) with the latter enabling a patterned nanotube deposition and being best suited for mass production. As the charge transport in these networks is percolation limited, higher contents of residual metallic nanotubes can be tolerated for longer channel lengths. Besides the semiconducting purity various parameters, such as the FET channel geometry, nanotube length, etc. (see Chapter 2.1.5 for details), considerably affect the device performance. At best, SWNT network FETs with charge carrier mobilities exceeding $100\,\mathrm{cm^2\,V^{-1}\,s^{-1}}$ together with on/off current ratios larger than 10^6 have been reported.

For application in actual circuitry the intrinsic ambipolarity of semiconducting SWNTs with balanced electron and hole transport is an issue as it results in an incomplete turn-off and thus a larger power dissipation[124,291] compared to complementary circuits consisting of truly unipolar p- and n-type FETs.[292–294] While p-doping of SWNTs can be easily achieved by device processing in air due to the adsorption of oxygen and water molecules,[164,295] stable and reproducible n-doping remains a challenge. This is mainly because the commonly utilized molecular n-dopants, such as metallocenes,[296,297] viologen,[298] polyethylene imine[299] or guanidino-functionalized aromatic compounds,[294] are rather difficult to handle and lack stability in air which is why they require subsequent encapsulation. Other n-doping strategies are based on the deposition of silicon nitride[300] or metal oxides[293] but result in undesired onset voltage shifts.

2.4 Charge Carrier Injection

Aside from doping and the morphology of the active layer, the performance of nanotube FETs can be strongly affected by contact barriers. Especially for high-frequency applications and the necessary realization of FETs with short channel lengths ($<1\,\mu\mathrm{m}$) and correspondingly low channel resistances, efficient charge injection from the contacting electrodes into the semiconductor is an important requirement.[301] Recently, complementary ring oscillators based on SWNT array FETs reaching switching frequencies of up to the GHz range were demonstrated by tailoring the work function of the injecting electrodes separately for p- and n-type transistors.[302]

Apart from that, a meaningful characterization of the charge transport properties in real FETs requires a profound analysis of the charge injection process as it affects the extracted device parameters. For example, the common evaluation of FETs based on the idealized gradual channel approximation (see Chapter 2.3.1) inevitably leads to distorted charge carrier mobilities if considerable contact barriers are present. The following section introduces the material properties of metal semiconductor interfaces, leading to injection barriers that result in contact resistance. It further presents gated four-point probe measurements as reliable experimental approach for the extraction of contact resistance and undistorted charge carrier mobilities.

2.4.1 Metal Semiconductor Interfaces

When a semiconductor and a metal electrode are brought into contact, the Fermi levels E_F of both equilibrate, i.e., electrons move from the material with higher E_F (e.g., the semiconductor) into the material with lower E_F (in this case the metal electrode) until they are aligned (see Figure 2.14a). This charge flow results in an energy level bending for the semiconductor and the formation of a space-charge zone of a certain width W_{SC}. In general, the energetic mismatch between the two band edges of the semiconductor and the Fermi level of the metal represented by its work function Φ_M with reference to the vacuum level E_{vac} leads to the formation of a contact barrier. For ideal interfaces the height of the contact barrier Φ_{SB} for electrons (holes) is simply determined by the difference between Φ_M and the edge of the conduction band E_C (valence band E_V) represented by the electron affinity χ (ionization potential I_P) of the semiconductor, according to the Schottky-Mott model:[204,303]

$$\Phi_{SB,e} = \Phi_M - \chi \qquad \text{and} \qquad \Phi_{SB,h} = I_P - \Phi_M. \tag{2.37}$$

Especially for organic semiconductors and several inorganic systems this idealized model delivers only one part of the overall picture and the height of these so-called Schottky barriers is strongly affected by interfacial dipoles and the Fermi level pinning effect, leading to large deviations from the predicted values based on Equation 2.37.[204,304–306] However, these effects play a secondary role for SWNTs due to their one-dimensional structure and their high charge carrier density at the van Hove singularities as illustrated by previous theoretical and experimental studies.[160,307–309] Hence, the Schottky-Mott model delivers a good estimation for the Schottky barrier heights in metal-SWNT contacts simply based on Φ_M and the band edges of the SWNT.[309,310] Choosing a suitable electrode material whose work function coincides with the respective band edge is thus a widespread strategy to establish so-called ohmic contacts with negligible injection barriers. The rather narrow bandgaps of semiconducting SWNTs typically result in comparatively small injection barriers for both electrons and holes, enabling the common observation of ambipolar transport. Yet, in this case a smaller energy barrier for one carrier type results in a somewhat larger barrier for the opposite carrier which is why often either an energetically centered electrode material (e.g., gold) is used or two different materials for the source and the drain contact, respectively.

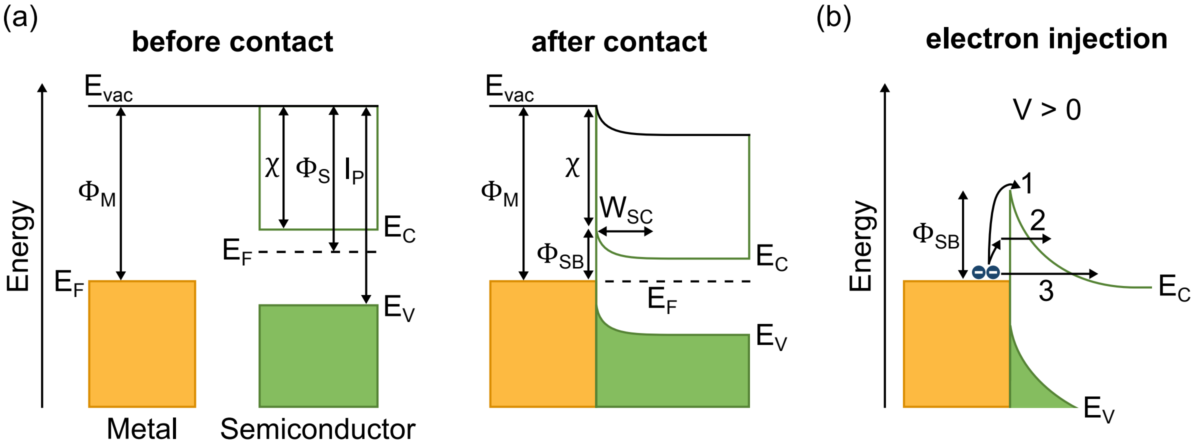

Figure 2.14: (a) Energy level diagrams of the interface between a metal electrode and a semiconductor before and after contact resulting in the formation of an injection barrier for electrons and (b) schematic illustration of the charge transport mechanisms thermionic emission (1), thermionic field emission (2) and tunneling (3) for electron injection across the Schottky barrier.

For the description of charge carrier injection from the metal into the semiconductor or vice versa two main approaches are commonly discussed. The charge carriers are considered to overcome the Schottky barrier by thermionic emission or pass through it by tunneling as shown in Figure 2.14b.[204,303,306] Thermionic emission in its pure form is a thermally activated process with an Arrhenius-type temperature dependence:

$$I_{TE} \propto T^2 \exp\left(-\frac{e\,\Phi_{SB}}{kT}\right) \tag{2.38}$$

with I_{TE} being the thermionic emission current across the interface. Pure charge carrier tunneling on the other hand is temperature-independent and increases with the applied electric field while scaling inversely with the barrier width W_{sc}. Depending on the operating conditions (e.g., temperature or charge carrier density in the semiconductor) the overall charge injection mechanism is often described as a superposition of both extremes, namely transport by thermally assisted tunneling or thermionic field emission.[204,311,312] In particular, this applies to SWNT-metal contacts as demonstrated by temperature-dependent transport measurements on single nanotube FETs, revealing varying contributions of pure tunneling transport and thermionic field emission depending on the temperature and the applied voltages.[160,313] Due to a substantial contribution of charge carrier tunneling in these devices, the experimentally determined energy barrier heights are typically significantly lower than the predicted values based on the electrode work function.[305]

2.4.2 Contact Resistance

The injection barriers at the contacts of a FET manifest themselves in additional resistances that add up with those stemming from the semiconducting layer. Hence, the total device resistance can be expressed as sum of the channel resistance R_{ch} and the contact resistance R_{C}:

$$R_{\text{tot}} = R_{\text{ch}} + R_{\text{C}} = R_{\text{ch}} + R_{\text{S}} + R_{\text{D}} \tag{2.39}$$

with R_{S} and R_{D} being the contact resistance of the source and drain electrodes. According to Equation 2.32 the current in a FET and thus R_{ch} scales directly with the channel dimensions (defined by L and W), whereas R_{C} is channel length-independent and scales inversely with W.[303] A larger impact of the contact resistance on R_{tot} is thus expected for transistors with short channel lengths and narrow widths. In addition to that, several aspects, such as the charge carrier mobility of the semiconductor, the height of the injection barriers or the applied gate-voltage, determine whether the charge transport is injection limited or whether the conductance of the semiconducting channel is the bottleneck. In the latter case, i.e., for $R_{\text{C}} << R_{\text{ch}}$ a minor impact of the contact resistance on the current-voltage characteristics is expected and the charge injection is described as 'ohmic' referring to a contact resistance that is not depending on the applied drain voltage. On the other hand, 'non-ohmic' contacts manifest themselves in the output characteristics of a FET as a non-linear current increase (first suppressed and then superlinear) and in a significantly limited on-current of the device.

However, the simple picture in which R_{C} originates from the injection barrier between semiconductor and metal only, applies primarily to coplanar FETs (bottom-contact/bottom-gate or top-contact/top-gate geometry) in which the charge carrier can be injected/extracted directly into/from the accumulated channel. In contrast to that, in FETs with staggered architectures (bottom-contact/top-gate or top-contact/bottom-gate) the injected charge carriers need to travel through the bulk semiconductor on their way to the accumulation layer (see Figure 2.10a). Consequently, an additional, vertical component of the contact resistance arises especially for thick semiconducting layers with low charge carrier mobilities.[303,304,314] On the other hand, the electrode area that is used for charge injection is significantly larger for staggered FETs in which the whole contact area can be utilized for injection, whereas for coplanar transistors charges are injected only from one edge of the contacts. In most cases, lower contact resistances are obtained for staggered FETs than for those with coplanar configuration.[315,316]

2.4.3 Methods for Contact Resistance Extraction

So far, several techniques for contact resistance extraction have been developed, each of them with certain advantages and drawbacks. The most important ones can be classified into the following categories: Kelvin probe force microscopy,[317] modeling of current-voltage characteristics (Y-function method),[318] transmission line methods[315,319] and gated four-point probe measurements[320–322] with the latter being utilized throughout this study.

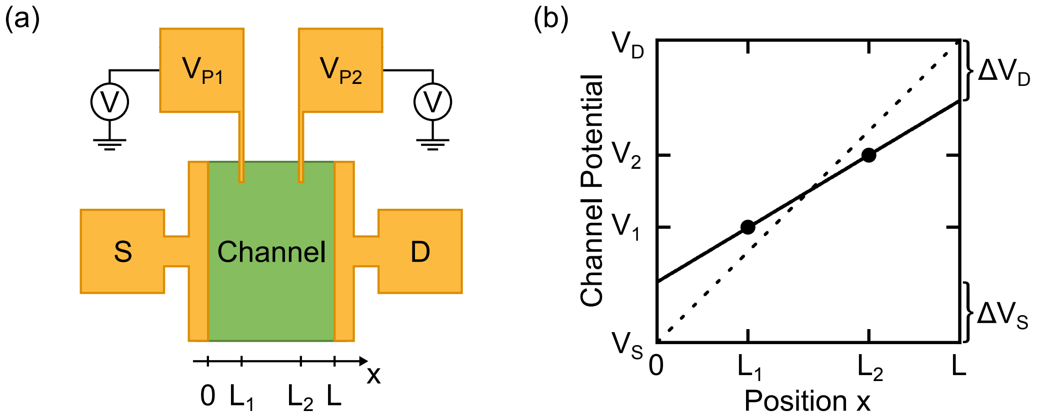

Figure 2.15: (a) Schematic illustration of a FET in a gated four-point probe layout with two probes (V_{P1}, V_{P2}) for voltage sensing between the source and drain electrode. (b) Exemplary channel potential profile (solid line) determined by linear extrapolation of the two measured voltage values revealing the voltage drops at the source and drain electrodes and hypothetical potential profile for the same transistor without contact resistances (dashed line).

Gated four-point probe measurements (gFPP) have the advantage that they enable direct determination of the contact resistance and its gate voltage dependence in single FETs for the source and drain electrode separately. The method involves a specific transistor electrode layout including two voltage sensing probes ($\mathrm{V_{P1}}$, $\mathrm{V_{P2}}$) between source and drain protruding at a defined position (L_1, L_2) into the FET channel as shown in Figure 2.15a. When connected to a high-resistance voltmeter these probes allow for the measurement of the local channel potential during standard FET operation. Assuming a linear potential gradient over the channel the voltage drops due to injection barriers at the source ΔV_{S} and drain ΔV_{D} contacts can be determined by linear extrapolation of the two values obtained with the voltage probes (see Figure 2.15b):

$$\Delta V_{\mathrm{S}} = \left[V_1 - \frac{V_2 - V_1}{L_2 - L_1} L_1\right] - V_{\mathrm{S}} \qquad \text{and} \qquad \Delta V_{\mathrm{D}} = V_{\mathrm{D}} - \left[V_2 + \frac{V_2 - V_1}{L_2 - L_1}(L - L_2)\right]. \tag{2.40}$$

Based on Ohm's current law the respective contact resistances at the source and drain electrode can be calculated using the recorded drain current:

$$R_{\mathrm{S}} = \frac{\Delta V_{\mathrm{S}}}{I_{\mathrm{D}}} \qquad \text{and} \qquad R_{\mathrm{D}} = \frac{\Delta V_{\mathrm{D}}}{I_{\mathrm{D}}}. \tag{2.41}$$

The total contact resistance for the device is then obtained by the sum of R_{S} and R_{D}. Likewise the contact resistance-corrected linear charge carrier mobility can be determined:[320,323]

$$\mu_{\mathrm{RC}} = \frac{D}{W\,C_{\mathrm{i}}} \frac{\partial(I_{\mathrm{D}}/V_{\mathrm{4P}})}{\partial V_{\mathrm{G}}} \tag{2.42}$$

with D and $V_{4\mathrm{P}}$ being the distance and the voltage difference between the voltage probes V_{P1} and V_{P2}, respectively. This carrier mobility correction is essential for an undistorted transport analysis of devices with non-negligible contact resistances for which a standard mobility extraction based on Equations 2.33 and 2.34 will be inaccurate. Given the temperature dependence of contact resistance, this is particularly true for temperature-dependent charge transport studies.

It is important to note that gFPP measurements provide only meaningful contact resistance and carrier mobility values when the FET is operated in the linear regime as it relies on a linear gradient of the channel potential. For the same reason, it requires a uniform semiconducting layer which might be an issue for SWNT network transistors with a low nanotube network density. Furthermore, the semiconducting layer needs to be patterned so that it is confined to the gated channel area to avoid any distortions by partially probing ungated areas outside the channel.[316] Still, despite the necessary, complex device fabrication the gFPP technique remains a powerful tool for direct contact resistance evaluation in an individual device, being merely based on one assumption, namely a linear channel potential gradient.

CHAPTER 3

EXPERIMENTAL METHODS

This chapter presents the materials, the fabrication procedures and the analytical methods that were utilized throughout this study.

3.1 Device Fabrication

3.1.1 Preparation of Semiconducting SWNT Dispersions

Purely semiconducting SWNT dispersions were prepared by using the polymer-wrapping method and combining different conjugated polymers with SWNT raw materials from various sources as stated in the lists below.

Wrapping Polymers

- Poly[(9,9-di-*n*-octylfluorene- 2,7-diyl)-*alt*-(2,2'-bipyridine-6,6'-diyl)] (PFO-BPy), supplier: American Dye Source Inc.
- Poly(3-dodecylthiophene-2,5-diyl) (P3DDT), supplier: E. Preis and U. Scherf, Bergische Universität Wuppertal, synthesized via Grignard metathesis reaction

Single-walled Carbon Nanotube Raw Materials

- CoMoCAT SWNTs, 0.7–1.0 nm diameter, SG65i-L58, supplier: CHASM Advanced Materials Inc.
- HiPco SWNTs, 0.8–1.3 nm diameter, supplier: Unidym Inc., batch: P-2172
- Plasma torch SWNTs, 0.9–1.5 nm diameter, RN-220, supplier: Raymor Industries Inc., batches: RN23-118 (Chapter 4.2) and RNB739-220-A329 (Chapter 5.2)

First, the respective wrapping polymer (see Figure 3.1 for molecular structures) was dissolved in toluene (analytic grade, VWR International LLC) while stirring at 80 °C. Before adding the corresponding SWNT raw material, the polymer solutions were cooled down to room temperature. Dispersion of the mixtures by liquid exfoliation at ~20 °C was realized either by bath sonication (2510, Branson Ultrasonics Corp.) for 50 min or by shear-force mixing (L2/Air, Silverson Machines Ltd.) at 10 230 rpm for 72 h.

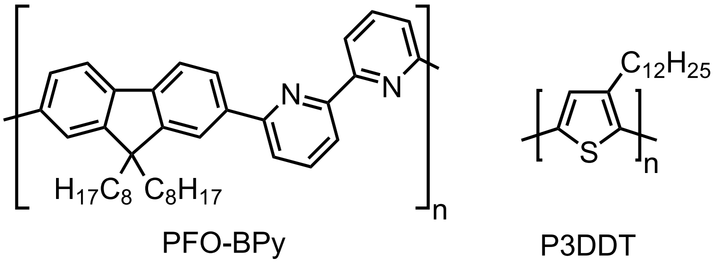

Figure 3.1: Molecular structures of the wrapping polymers PFO-BPy and P3DDT.

Table 3.1 shows the employed SWNT/polymer combinations as well as the molecular weights (M_w) of the polymer, the respective SWNT and polymer concentrations and the utilized liquid exfoliation method. The exfoliation process was followed by centrifugation (Avanti J-26XP, Beckmann Coulter GmbH) at 60 000 g for 45 min. The supernatant containing the wrapped semiconducting SWNTs was collected and the centrifugation process was repeated once. The excess polymer was removed from the remaining supernatant by sedimentation of the wrapped SWNTs based on two different methods. In Chapter 4.2 ultracentrifugation (Optima XP, Beckman Coulter GmbH) at 284 600 g for 13 h and repeated washing of the obtained pellets with tetrahydrofuran (THF, analytic grade, VWR International LLC) was used to separate the SWNTs from the unwrapped excess polymer. In Chapter 5.2 and Chapter 6.2 the separation was achieved by vacuum filtration of the supernatant through poly(tetrafluoroethylene) membrane filters (JVWP, 0.1 µm pore size, Merck KGaA) and repeated washing of the received SWNT filter cake in hot toluene (80 °C). Finally, the SWNT pellets or filter cakes were redispersed in fresh toluene by bath sonication for 30 min at 20 °C immediately before further usage.

Table 3.1: Combinations of SWNT raw materials and wrapping polymers for the preparation of semiconducting SWNT dispersions by liquid exfoliation in the respective chapters of this thesis.

SWNT Raw Material	Polymer	M_w (kg mol^{-1})	Concentration (g L^{-1}) SWNTs	Polymer	Exfoliation Method	Chapter
CoMoCAT	PFO-BPy	34 40	0.38	0.5	shear-force mixing	4.2 5.2, 6.2
HiPco	P3DDT	9.7	1.5	2	bath sonication	4.2
Plasma torch	PFO-BPy	34 40	1.5 1.5	2 0.5	bath sonication	4.2 5.2

3.1.2 Bottom Electrode Patterning

For the fabrication of bottom-contact/top-gate field-effect transistors, bottom electrodes were structured by photolithography on 25 × 20 × 0.3 mm^3 glass substrates (AF 32 eco, Schott AG). Prior to the lithography process the glass slides were cleaned by subsequent bath sonication for 10 min in acetone (>99.5 %, Sigma Aldrich GmbH) and isopropanol (IPA, >99.7 %, Sigma Aldrich GmbH) followed by blow-drying with nitrogen (99.999 %, Air Liquide GmbH).

The cleaned substrates were coated with a double-layer resist that consisted of the positive photoresist MICROPOSIT S1813 (Dow Chemical Co.) on top of a non-photosensitive layer LOR5B (MicroChem Corp.) to achieve an undercut structure for the subsequent lift-off process. The LOR5B resist was spin-coated onto the glass substrates for 30 s at 4000 rpm followed by softbaking at 185 °C for 4 min. After cooling the substrates down to room temperature the S1813 resist was spin-coated at 4000 rpm for 30 s and softbaked at 115 °C for 1 min.

The coated substrates were exposed to UV light (i-line, λ = 365 nm, 182 mJ cm^{-2} dose) through chrome-on-glass photomasks (Soda Lime, Compugraphics Jena GmbH) using a mask aligner (MA6 Gen4, SÜSS MicroTec SE) in hard contact mode. After exposure, the photoresist was

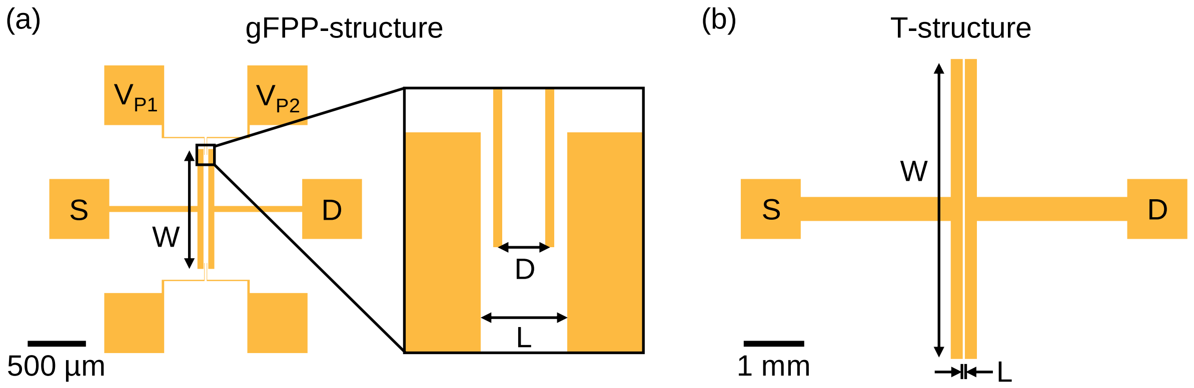

Figure 3.2: Photomask structures for bottom electrode patterning: (a) Gated four-point probe (gFPP)-structure containing two pairs of voltage probes in the channel (L = 40 µm, W = 1000 µm) separated by D = 24 µm from each other and by 6 µm from the respective source/drain electrode and (b) T-structure with wide channels (L = 40 µm, W = 5000 µm).

developed by immersion in the alkaline MICROPOSIT MF-319 developer (Dow Chemical Co.) for 20–25 s with constant agitation. Depending on the selected photomask structure two different electrode patterns were produced (see Figure 3.2) to define the dimensions of the bottom electrodes. These electrodes were deposited by electron beam evaporation (HVB-130, Winter Vakuumtechnik GbR) of 2 nm chromium (rate: 0.2 Å s^{-1}) and 30 nm gold (rate: 0.5 Å s^{-1}). Lift-off by immersion in N-methyl-2-pyrrolidone (anhydrous, Sigma Aldrich GmbH) for several hours followed by rinsing with ultrapure water and blow-drying with nitrogen completed the electrode patterning process.

3.1.3 SWNT Network Deposition

For the preparation of semiconducting nanotube networks on the electrode substrates, SWNTs were deposited from their purified dispersions in toluene either by aerosol-jet printing (Chapter 4.3) or by spin-coating (Chapter 5.3 and Chapter 6.2). Prior to SWNT deposition the glass slides with the electrodes were cleaned by bath sonication in acetone and IPA for 10 min each and blow-dried with nitrogen. In Chapter 5.3 and Chapter 6.2 the electrode substrates were additionally UV/ozone-treated (UV Ozone Cleaner E511, Ossila Ltd.) for 10 min.

The whole aerosol-jet printing process was established by Marcel Rother who also modified the commercially available printing system (Aerosol Jet 200, Optomec Inc.) for more convenient use when printing from different SWNT inks. These SWNT inks were finalized by dilution of the respective SWNT dispersion (see Chapter 4.2) with toluene to achieve the desired nanotube concentration followed by the addition of 5 vol‰ terpineol (anhydrous, Sigma Aldrich GmbH) to promote the formation of a stable and dense aerosol. The respective SWNT concentration was adjusted to a corresponding S_{11} peak absorbance of 1.0 cm^{-1} (at 996 nm for CoMoCAT SWNTs and at 1637 nm for plasma torch SWNTs) or to 0.5 cm^{-1} (at 1141 nm for HiPco SWNTs). The nanotube inks were aerosolized by sonicating the respective ink vial at 20 °C. The resulting aerosol was jet-printed using a nitrogen carrier and sheath gas flow of about 15 sccm and 30 sccm through a 200 µm ceramic nozzle in vertical and horizontal lines with a 25 µm pitch over the channel areas of the electrode substrates while heating the sample stage to 100 °C. After printing, the deposited SWNT networks were rinsed with THF and IPA to remove excess polymer and terpineol and blow-dried with nitrogen.

To deposit SWNT networks via spin-coating as stated in Chapter 5.3, the nanotube concentrations in the SWNT stock dispersions were adjusted to a corresponding absorbance of $11.0\,\mathrm{cm}^{-1}$ at the S_{11} transition at 996 nm for the CoMoCAT SWNTs and to $1.1\,\mathrm{cm}^{-1}$ at the strongest S_{22} transition at 936 nm for the plasma torch SWNTs. For the deposition of sparse, non-percolating SWNT networks on silicon substrates (single-side polished Si(100), Siegert Wafer GmbH) shown in Figure 5.1, the two stock dispersions were used in a 20-fold dilution. Mixed dispersions with tailored mixing ratios were obtained by volumetric mixing of the PFO-BPy-wrapped CoMoCAT and plasma torch SWNT stock dispersions (see Chapter 5.2). In Chapter 6.2, (6,5) SWNTs with a similar concentration represented by a S_{11} peak absorbance of $10.3\,\mathrm{cm}^{-1}$ at 996 nm were utilized for spin-coating. The standard procedure consisted of three consecutive spin-coating steps in air (WS-400BZ-6NPP-LITE, Laurell Technologies Corp.) using the desired SWNT dispersion at 2000 rpm for 30 s per substrate. After each spin-coating step the substrate was annealed at 90 °C for 2 min. Afterwards, the substrates were rinsed with THF and IPA to remove excess wrapping polymer followed by another annealing step at 90 °C for 2 min.

3.1.4 Removal of the Wrapping Polymer

The polymer-stripping experiments in Chapter 4.5 were realized by annealing as-printed PFO-BPy-wrapped CoMoCAT SWNT networks for 60 min at 400 °C under vacuum (5×10^{-3} mbar). Next, these SWNT films were immersed in a toluene solution of $70\,\mathrm{mg\,L}^{-1}$ rhenium(I) pentacarbonyl chloride ($\mathrm{Re(CO)_5Cl}$, 98 %, Sigma Aldrich GmbH) while stirring it at 110 °C for 2.5 h. Subsequently, the treated SWNT network samples were washed twice with toluene at 110 °C and twice with THF 60 °C for 60 min respectively followed by blow-drying with nitrogen to remove precipitated polymer and rhenium salt. For the evaluation of the polymer-stripping process by UV-vis-nIR absorption measurements (see Figure 4.15) reference CoMoCAT/PFO-BPy SWNT networks with higher optical density were printed from a dispersion with higher SWNT concentration (S_{11} peak absorbance of $1.8\,\mathrm{cm}^{-1}$) onto blank glass substrates and treated with $\mathrm{Re(CO)_5Cl}$ analogous to the device samples.

3.1.5 SWNT Film Patterning

For the integration into SWNT network FETs the nanotube films were patterned by photolithography and consecutive oxygen plasma etching. The patterning was achieved by another double-layer resist (LOR5B/S1813) lithography step (see Chapter 3.1.2) using a photomask that covered only the channel regions as well as parts of the source and drain bottom electrodes. After UV exposure and resist development, the partially resist-covered SWNT network samples were etched by an oxygen plasma (100 W power, AP-600/300, Nordson Corp.) at 0.3 mbar for 2 min resulting in the complete decomposition of SWNTs outside the covered areas. The resist was subsequently removed by lift-off in *N*-methyl-2-pyrrolidone for 30 min followed by rinsing with ultrapure water and blow-drying with nitrogen.

3.1.6 Dielectric Deposition

The utilized hybrid dielectrics for the fabrication of top-gated field-effect transistors in Chapters 4.3, 5.4 and 6.2 consisted of a metal oxide layer on top of a poly(methyl methacrylate) (PMMA, see Figure 3.3 for molecular structure) layer that were deposited on the SWNT networks after the nanotube film patterning. Before applying the PMMA layer, the SWNT network samples were annealed at 300 °C for 60 min inside a dry nitrogen glovebox (MB200-G, M. Braun Inertgas-Systeme GmbH) to remove any remaining solvents or moisture. The PMMA (syndiotactic, $M_\mathrm{w} = 315\,\mathrm{kg\,mol^{-1}}$, Polymer Source Inc.) was dissolved in *n*-butyl acetate (analytic grade, Sigma Aldrich GmbH) for 60 min at 80 °C before depositing the solution onto the SWNT networks via spin-coating at 4000 rpm for 60 s (MB-SC-210, M. Braun Inertgas-Systeme GmbH) in the same glovebox.

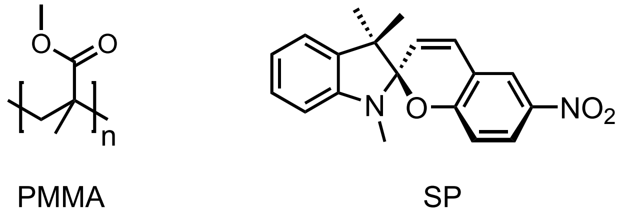

Figure 3.3: Molecular structures of the dielectric polymer PMMA and of the utilized spiropyran compound (SP).

In Chapter 6.2 the PMMA was used and dissolved not only purely, but also together with the spiropyran compound 1,3,3-trimethylindolino-6'-nitrobenzopyrylospiran (>98 %, Tokyo Chemical Industry UK Ltd., see Figure 3.3 for molecular structure), resulting in spiropyran-filled PMMA layers. The employed PMMA and spiropyran (SP) concentrations, as well as the resulting dielectric film thicknesses on the different SWNT network samples presented in the following chapters are shown in Table 3.2. After spin-coating the respective nanotube network samples were annealed at 80 °C for about 15 min to remove remaining solvent from the deposited PMMA films.

Table 3.2: PMMA and SP concentrations in the *n*-butyl acetate solutions utilized for spin-coating and resulting dielectric layer thicknesses in the respective chapters of this thesis.

Concentration ($g\,L^{-1}$)		SP:PMMA mass ratio	Layer thickness (nm)	Dielectric labeled as	Chapter
PMMA	SP				
6	0	0	11	PMMA	4.3, 5.4
12	0	0	20	reference	6.2
11	2	0.19	20	low SP	6.2
10	3.8	0.38	20	high SP	6.2

Subsequently, the upper layer of the hybrid dielectric, namely 61 nm of HfO_x (Chapters 4.3 and 5.4) or 100 nm of AlO_x (Chapter 6.2) were deposited on top of the PMMA layer by atomic layer deposition (ALD). To minimize the impact of moisture from the ambient air on the PMMA-covered samples, they were immediately transferred to the reaction chamber of the ALD system (Savannah S100, Ultratech Inc.) and annealed for 30 min under vacuum (<1.3 mbar). Depending on the chosen metal oxide, the annealing temperature was set to 100 °C (HfO_x) or to 80 °C (AlO_x). For the deposition of HfO_x, ultrapure water and tetrakis(dimethylamino)hafnium (>98 %, Strem Chemicals Inc.) were used as precursors which were pulsed alternatingly in 500 cycles into the reaction chamber at a nitrogen gas flow of 20 sccm and a reaction temperature of 100 °C. Analogously, AlO_x was deposited using trimethylaluminum (>98 %, Strem Chemicals Inc.) and ultrapure water as aluminum and oxygen sources in 1270 reaction cycles at 80 °C.

3.1.7 Top-Gate Electrode Deposition

This process represented the final step for the fabrication of SWNT network field-effect transistors. Silver top-gate electrodes were patterned on top of the samples covered with hybrid dielectric by evaporation of 30 nm Ag through stainless steel shadow masks (thickness: 0.2 mm, CADiLAC Laser GmbH or Becktronic GmbH) inside a thermal evaporator (MB-ProVap-3, M. Braun Inertgas-Systeme GmbH). The initial evaporation rate of $0.1\,Å\,s^{-1}$ was increased to $0.5\,Å\,s^{-1}$ after reaching a film thickness of 5 nm to ensure a uniform coverage of the dielectric.

3.2 Characterization Techniques

3.2.1 Absorption Spectroscopy

Absorption spectra of SWNT dispersions, SWNT networks or SP-filled PMMA films in the UV-vis-nIR spectral range (300–1650 nm) were acquired using a dual-beam absorption spectrometer (Cary 6000i, Varian Inc.) equipped with a silicon (175–800 nm) and an InGaAs (800–1800 nm) detector. SWNT dispersions were measured using cuvettes with 1 cm path length. All spectra were background-corrected by baseline measurements using the respective pure solvent in the same cuvette prior to the sample measurement. Thin films (SWNT networks or PMMA/SP films) were measured using a substrate sample holder. In this case, the background correction was performed using analogous blank glass substrates.

3.2.2 Raman Spectrocscopy

Raman spectra and maps of SWNT networks were recorded using a confocal Raman microscope (inVia Reflex, Renishaw plc.) with a 50x objective (numerical aperture 0.75, Leica Microsystems GmbH). The system was equipped with three different lasers with excitation wavelengths of 532 nm, 633 nm and 785 nm. Prior to all measurements the spectrometer was calibrated to a silicon standard sample ($520.6\,\mathrm{cm}^{-1}$). Single spectra of SWNT films dropcast from dispersion on aluminum foil were recorded for 3–5 measuring spots with all three lasers in Streamline mode (see Chapter 4.2). Deposited SWNT networks on electrode substrates were characterized using Raman maps, that consisted of about 1600 spectra over an $100 \times 100\,\mu\mathrm{m}^2$ area (see Chapter 5.3) and were recorded for excitation with the 532 nm and the 785 nm laser in StreamLine mode. For each SWNT network, the obtained spectra were averaged and baseline corrected.

3.2.3 Profilometry

The layer thicknesses of polymer and metal oxide films were determined by surface profilometry (DektakXT Stylus Profiler, Bruker Corp.). Spin-coated reference films on glass substrates equal to the polymer layers of the hybrid dielectric utilized for device fabrication were measured by scanning across grooves that were created beforehand by scratching with a razor blade. Metal oxide film thicknesses were determined by using lithographically pre-structured and thus partially photoresist-covered reference substrates that were placed and coated in the ALD reaction chamber together with the SWNT network transistor substrates. After lift-off in *N*-methyl-2-pyrrolidone overnight, rinsing with ultrapure water followed by blow-drying with nitrogen, defined metal oxide film edges were obtained. The respective layer thickness was measured by scanning across the film edge.

3.2.4 Atomic Force Microscopy

The surface topography of SWNT networks was characterized by atomic force microscopy (AFM), using an atomic force microscope (Dimension Icon, Bruker Corp.) in ScanAsyst mode. The microscope was equipped with ScanAsyst tips (SCANASYST-AIR, Bruker Corp.) held by a cantilever holder (DAFMCH, Bruker Corp.). The recorded AFM images were processed (background and z-range leveling, line error correction) using the open-source Gwyddion 2.45 software.

3.2.5 Electrical Characterization

The current-voltage measurements (transfer and output characteristics) of SWNT network transistors were recorded in a dry nitrogen glovebox (I-Lab 3GB, Inert Corp.) using a semiconductor parameter analyzer (4155C, Agilent Technologies Inc.).

Temperature-dependent current-voltage characteristics (continuous scan mode) were measured under vacuum ($\leq 10^{-6}$ mbar) inside a cryogenic probe station (CRX-6.5K, Lake Shore Cryotronics Inc.) with a closed helium cooling cycle, starting from the base temperature of the system (10 K). After each temperature step (20 K) a hold time of 20 min ensured the thermal equilibration of the sample before the corresponding transport measurement.

Capacitance-voltage measurements were performed using an impedance spectrometer (Modulab XM MTS, Ametek Inc., see Chapter 4) or a LCR meter (E4980A, Agilent Technologies Inc., see Chapters 5 and 6) in dry nitrogen atmosphere. The effective areal gate capacitance (C_i) of each SWNT network transistor was determined while the respective FET was in the on-state, i.e., at DC gate biases of ±5 V (Chapter 4) or ±10 V (Chapters 5 and 6) with an AC modulation signal of 0.5 V amplitude at a frequency of 1 kHz. Figure 3.4 shows an example of capacitance-voltage characteristics of a plasma torch SWNT network transistor with a PMMA/HfO$_\mathrm{x}$ hybrid dielectric. Depending on the thickness and the composition of the hybrid dielectric and the nanotube network density, typically obtained capacitance values for SWNT network FETs were in the range of 103–127 nF cm^{-2} for PMMA/HfO$_\mathrm{x}$ (see Chapters 4 and 5) or around 40 nF cm^{-2} for PMMA:SP/AlO$_\mathrm{x}$ (see Chapter 6).

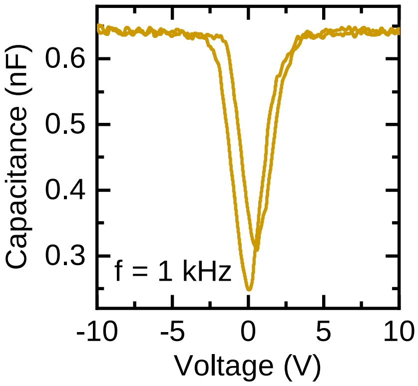

Figure 3.4: Representative capacitance-voltage characteristics (forward and reverse sweep) of a dense plasma torch SWNT network FET with a PMMA/HfO$_\mathrm{x}$ hybrid dielectric and a gFPP electrode layout with a total capacitor area of 6×10^{-3} cm^2. The extracted capacitance per unit area is 106 nF cm^{-2}.

3.2.6 Electroluminescence Imaging

Electroluminescence (EL) imaging of the SWNT network transistor channels was performed using a home-built optical setup. The SWNT network FETs were contacted on a XYZ substrate stage and driven in constant current mode, i.e., with a V_D *vs* V_G sweep to maintain a constant transistor current, using a semiconductor parameter analyzer (B1500A, Keysight Technologies Inc.). The EL emission was collected through the glass substrate of the respective device by a 50x nIR objective (numerical aperture 0.65, LCPLN50XIR, Olympus Corp.) and projected onto a two-dimensional thermoelectrically-cooled nIR InGaAs camera (resolution 320 × 256 pixels, XEVA-CL-TE3, Xenics nv). This way movies or single images of the EL emission zone in the SWNT network transistor channel were recorded. EL composite images were obtained by combining a series of frames (maximum intensity for each pixel) into a single image followed by background correction and contrast enhancement using the open-source software ImageJ.

3.2.7 Photoswitching of SWNT Network Field-Effect Transistors

The SP-loaded SWNT network samples were illuminated with UV light (i-line, $\lambda = 365\,\text{nm}$, dose $1000\,\text{mJ}\,\text{cm}^{-2}$) inside a mask aligner (MA6 Gen4, SÜSS MicroTec SE) either via mask-free flood exposure (see Chapters 6.3 and 6.4) or through a chrome-on-glass photomask (Soda Lime, Compugraphics Jena GmbH, see Chapter 6.5) in soft contact mode. The reverse reaction of the SP molecules in the PMMA/SP layer of an entire SWNT network sample that was previously exposed with UV light was induced by heating of the respective substrate at 90 °C for 60 min in a dry nitrogen atmosphere. An optically induced reverse isomerization in only selected channel areas of a SP-loaded SWNT network FET (see Chapter 6.5) was achieved by local laser exposure using a confocal Raman microscope (inVia Reflex, Renishaw plc.) with a 532 nm laser and a 50x objective (numerical aperture 0.75, Leica Microsystems GmbH). The laser spot (37.2 µW continuous wave power, 0.5 s integration time) was scanned across a $50 \times 20\,\mu\text{m}^2$ grid inside the channel area of a SP-loaded SWNT network transistor with a step width of 0.5 µm for a total period of ~30 min.

3.3 Network Simulations

The SWNT network simulations presented in Chapters 4.6 and 5.5 were performed using a MATLAB program developed by Stefan Schießl that ran on a workstation (CELSIUS M740, Fujitsu Technology Solutions GmbH) equipped with a multicore processor (14 cores, 28 threads, 2.6 GHz, Xeon E5-2697v3, Intel Corp.) and 128 GB RAM. The program code is based on a random resistor network model (see Chapter 2.2.2 for details) and is capable of utilizing the MATLAB parallel computing toolbox, resulting in a reduced computation time.

CHAPTER 4

CHARGE TRANSPORT IN SWNT NETWORKS WITH DIFFERENT DIAMETER DISTRIBUTIONS

This chapter investigates the impact of the carbon nanotube diameter distribution on the overall charge transport properties in aerosol-jet-printed networks of semiconducting nanotubes sorted from different SWNT raw materials and wrapping polymers.

The results presented in this chapter were partially published in the article Brohmann *et al.* *Journal of Physical Chemistry C* **2018**, 122, *34*, 19886-19896.[324] Adapted figures and tables are presented with permission from the American Chemical Society. The carbon nanotube network simulations were performed based on a MATLAB code developed by Stefan Schießl.[202]

4.1 Introduction

During the last decade, random networks of semiconducting SWNTs have emerged as promising active material for large-scale applications in solution-processable thin-film electronics.[248,325–328] So far, several bulk nanotube growth methods have been developed, but they all have in common that they always yield mixtures of semiconducting and metallic SWNTs in different diameter distributions. Thus, a highly efficient and selective separation method is essential for the required high semiconducting purity to ensure high device performance and reproducibility. One of the most established techniques for selective dispersion of semiconducting SWNTs in organic solvents is based on wrapping with conjugated polymers and enables both high yield and selectivity (>99.8 %).[7,8,108,124] In this process, the chosen conjugated wrapping polymer and the nanotube raw material determine the mixture of dispersed semiconducting SWNT species of certain diameter and thus bandgap. Because the exact selection mechanism of this method still is unclear, many different combinations of wrapping polymers and SWNT raw materials have been tested and used for SWNT sorting and with a wide range of applications in optoelectronics.[215,286,289,329–332] In order to optimize these SWNT networks for use in FETs with large on/off current ratios and high charge carrier mobilities, a deeper understanding of all relevant nanotube network parameters is necessary.

Besides the network density and the nanotube length, especially the nanotube network composition, i.e., the distribution of present nanotube species of different diameters and thus bandgaps, is expected to affect the overall charge transport in a network. Individual semiconducting SWNTs exhibit high charge carrier mobilities of up to 10^4 $\mathrm{cm^2\,V^{-1}\,s^{-1}}$ and even reach the ballistic transport regime if the scattering mean free path exceeds the nanotube length.[158,159] In random nanotube network transistors the charge carriers (electrons or holes) have to hop across junctions between adjacent nanotubes on their way through the transistor channel which is considered to be the transport bottleneck and limits typical network mobilities to values below 100 $\mathrm{cm^2\,V^{-1}\,s^{-1}}$.[10] This notion is corroborated by conductive atomic force microscopy experiments which show orders of magnitude higher junction resistances than the resistance values within each nanotube.[152,167,169] However, the critical factors dominating the hopping process (e.g., residual wrapping polymer, contact angle, energetic landscape of the nanotube network, etc.) still remain unclear.

A well-established method for charge transport investigations on all kinds of semiconductors are temperature-dependent current-voltage measurements in order to determine the change in conductivity or charge carrier mobility with temperature. While the carrier mobility in individual semiconducting SWNTs scales inversely with temperature,[158,159] the behavior of nanotube networks was found to be different. All previous temperature-dependent transport studies on semiconducting SWNT networks indicated thermally activated transport which is in good agreement with the suggested hopping of charge carriers across the inter-nanotube junctions.[177–179,194,333] In order to reveal the exact transport mechanism many different classical transport models were utilized to describe the temperature-dependent mobility data. So far, the fluctuation-induced tunneling (FIT) model[195,196] gave the best qualitative fit to the experimental carrier mobilities, although it does not include specific and diameter-dependent SWNT properties such as the density of states (DOS) or the intra-nanotube mobility. The variable range hopping (VRH) model,[189] which is the standard concept for the description of charge transport in classical disordered materials, could not describe the data properly especially in the low temperature regime. Although an impact of the SWNT diameter distribution on charge transport in nanotube network FETs has been observed recently,[273] all previous transport studies included just one network composition each. A comprehensive overall picture of charge transport in random SWNT networks with all its different contributions, including the influence of residual wrapping polymer is still lacking.

In the following chapter, the specific impact of the SWNT network composition on charge transport and its temperature dependence in SWNT network FETs is investigated.[324] For this purpose, three different aerosol-jet-printed semiconducting nanotube networks with different diameter distributions are compared. They are obtained by polymer-sorting of commercially available SWNT raw materials with two different conjugated polymers. The often controversially discussed role of residual wrapping polymer on the overall network charge transport is analyzed by polymer removal experiments based on a rhenium salt treatment of the prepared SWNT networks.[334] A gated four-point probe (gFPP) transistor geometry is used as it permits direct measurement of the contact resistance and the extraction of undistorted network field-effect mobilities over the whole temperature range from 300 to 100 K. The significant impact of the nanotube diameter distribution and the mean diameter in a given SWNT network on charge injection and transport is shown based on the temperature dependence of the experimental carrier mobilities and compared to a theoretical random resistor network model.[202]

4.2 Dispersion of Semiconducting SWNTs by Polymer Wrapping

To obtain purely semiconducting SWNT networks with very different compositions, i.e., nanotube diameter distributions, stable and purely semiconducting SWNT dispersions of analogous composition had to be prepared in toluene. For this purpose, three commercially available SWNT raw materials produced by the CoMoCAT, the HiPco and the plasma torch process were utilized. These materials contain already pre-defined ensembles of SWNT species with more or less broad diameter ranges. The CoMoCAT raw material consists of a mixture of small-diameter SWNTs with a rather narrow diameter spread from 0.7 to 1.0 nm while the HiPco process yields a broader range of medium diameters from 0.8 to 1.3 nm. The plasma torch material contains large-diameter SWNTs between 0.9 nm and 1.5 nm. All three raw materials have to be polymer-sorted in order to extract their semiconducting SWNTs only. This separation was performed by using two different conjugated wrapping polymers dissolved in toluene. The commercially available polyfluorene derivative poly[(9,9-di-*n*-octylfluorene- 2,7-diyl)-*alt*-(2,2'-bipyridine-6,6'-diyl)] (PFO-BPy, see Figure 4.1a for molecular structure) was found to succesfully disperse semiconducting nanotubes with both large and small diameters[111,130] and could even enrich almost monochiral (6,5) SWNTs when combined with CoMoCAT raw material.[8] The polythiophene derivative poly(3-dodecylthiophene-2,5-diyl) (P3DDT, see Figure 4.1a) was synthesized by Eduard Preis (see Chapter 3.1.1) and disperses a broad range of SWNT diameters with excellent semiconducting selectivity and relatively high yield.[115,127] Both polymers absorb in the UV-vis region with maxima at 362 nm (PFO-BPy) and 445 nm (P3DDT) as shown in Figure 4.2b. Their peak extinction coefficients were determined to be 95 mL mg^{-1} cm^{-1} for PFO-BPy and 27 mL mg^{-1} cm^{-1} for P3DDT.

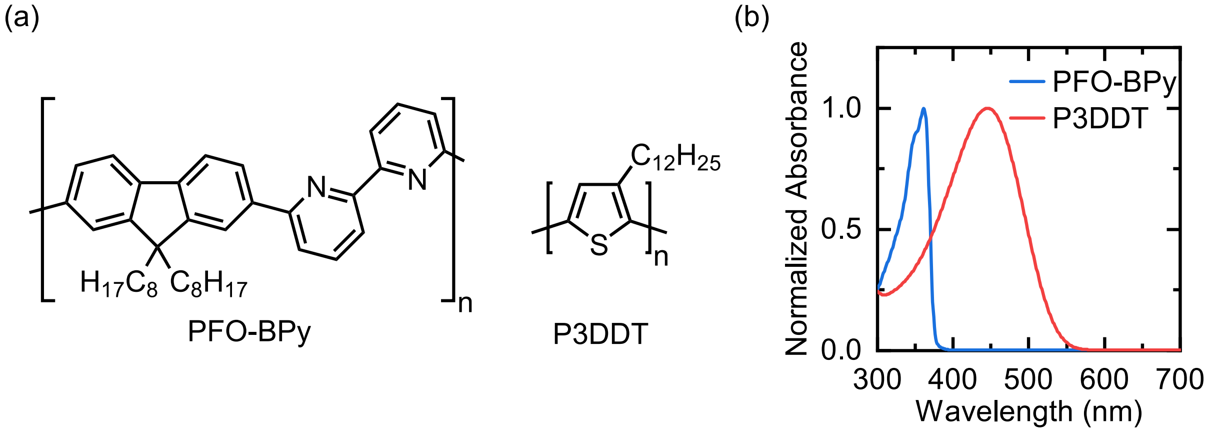

Figure 4.1: Molecular structures of the wrapping polymers PFO-BPy and P3DDT (a) and normalized UV-vis absorption spectra of both dissolved in toluene (b).

The PFO-BPy was utilized to disperse CoMoCAT and plasma torch SWNTs in toluene, whereas the P3DDT was combined with the HiPco raw material. For both polymers, batches with low molecular weight (M_w) below <40 kg mol^{-1} were chosen due to the strong impact of the polymer molecular weight on the dispersion selectivity, i.e., higher selectivity for polymers with lower M_w.[123,124] The dispersion process for all SWNT dispersions consisted of a liquid exfoliation and a centrifugation step (see Chapter 3.1.1 for details). The unwrapped excess wrapping polymer was then removed by pelletizing the purified semiconducting SWNT dispersions followed by repeated washing of the resulting nanotube pellets with THF and redispersion in toluene. All three redispersed SWNT mixtures were analyzed by UV-vis-nIR absorption spectrocopy as depicted in Figure 4.2. The UV-vis-nIR spectra of the three dispersions show the typical sharp excitonic transitions of semiconducting SWNTs between their first (S_{11}), second (S_{22}) and third

(S_{33}) van Hove singularities. However, the latter cannot be assigned unambigously in the spectra of the CoMoCAT and the HiPco SWNTs due to spectral overlap with the absorption bands of the wrapping polymer. The present nanotube bandgaps and diameters can be estimated by the spectral positions of the different SWNT absorption peaks using the Kataura plot.[48,49,335] Based on this, the quite different diameter distributions of the three SWNT dispersions are evident. The quasi-monochiral CoMoCAT/PFO-BPy dispersion contains almost exclusively (6,5) SWNTs with a corresponding large bandgap of 1.27 eV and small diameter of 0.76 nm without any detectable amounts of other nanotube species as shown before.[8] The HiPco dispersion includes a very broad distribution of nanotubes with diameters between 0.76 and 1.27 nm and corresponding bandgaps from 0.80 to 1.31 eV. In the plasma torch dispersion an ensemble of large diameter SWNTs (1.17–1.55 nm) is present with small bandgaps (0.70 and 0.88 eV) and a narrower energetic spread compared to the HiPco nanotubes.

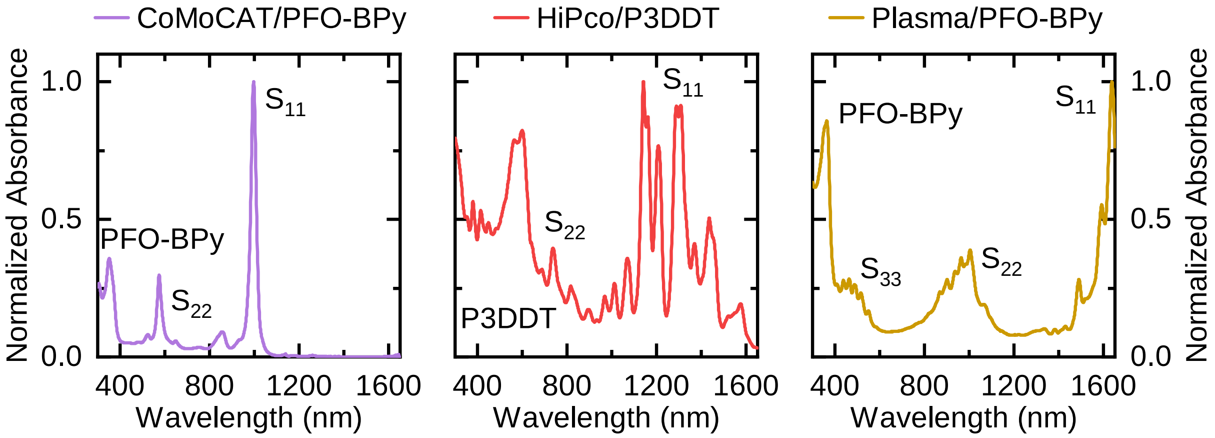

Figure 4.2: UV-vis-nIR absorption spectra of the SWNT dispersions in toluene (normalized to the strongest SWNT S_{11} absorption peak).

The UV-vis-nIR absorption spectra of all three dispersions show only weakly pronounced absorption bands of the two sorting polymers. To further assess the polymer content, the polymer:SWNT mass ratio was estimated to be $\leq$1:1 for all dispersions based on the extinction coefficients of several SWNT species determined by Streit *et al.*[55] A more precise estimation is difficult due to the above mentioned overlap of the polymer absorption bands and the higher subband transitions of the SWNTs. According to studies of Shea *et al.* a polymer:SWNT mass ratio of 3.6:1 corresponds to a 100 % saturation coverage of another polyfluorene sorting polymer bound to (7,5) SWNTs, suggesting no excess, unwrapped polymer below this value. Assuming a similar behavior for the prepared SWNT mixtures, this indicates a negligible amount of residual unwrapped PFO-BPy or P3DDT in the nanotube dispersions. Furthermore, the lack of significant amounts of metallic SWNT species is implied by their absence in the absorption spectra of all dispersions.

Although UV-vis-nIR absorption spectrocopy is a reliable method to quantitatively assess the SWNT species distribution in a given nanotube dispersion, it lacks sensitivity for the detection of both semiconducting and metallic minority SWNT species with low contents $\ll$1 %. However, in SWNT network FETs already a single path of metallic nanotubes percolating across the transistor channel can lead to significantly increased off-currents. Resonant Raman spectroscopy represents a much more sensitive method that enables the detection of minimal amounts of SWNTs and was utilized to analyze dropcast samples of all three dispersions with respect to their SWNT content. The respective Raman spectra of the SWNT mixtures in the radial breathing mode (RBM) region excited with three different lasers are shown in Figure 4.3.

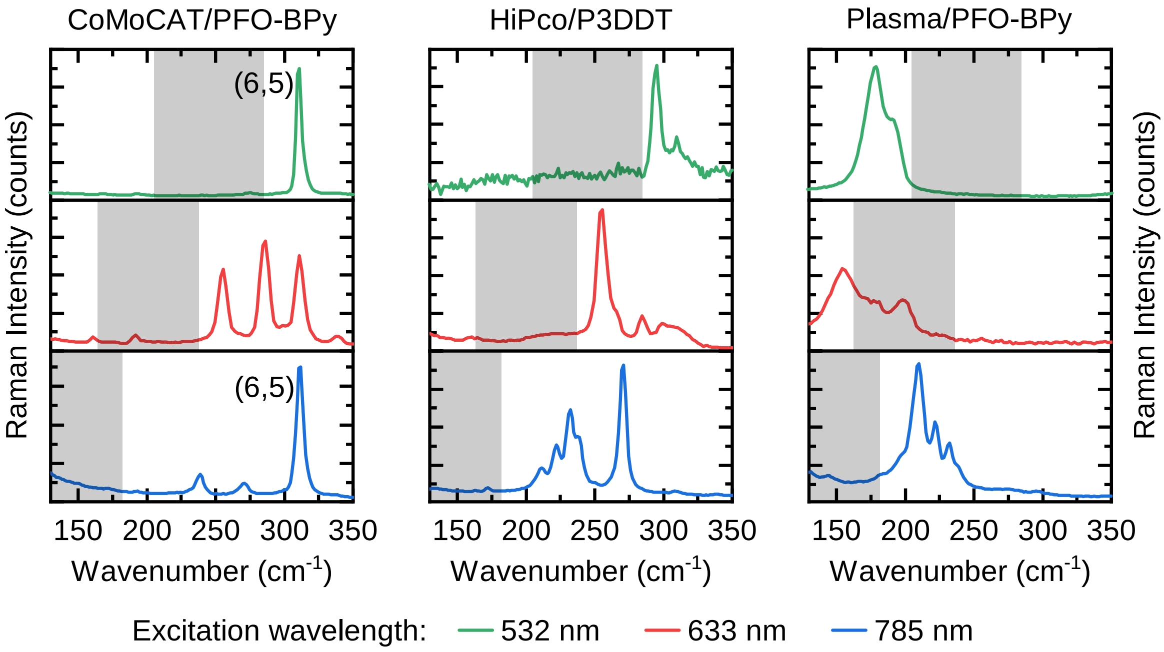

Figure 4.3: Raman RBM spectra of dropcast samples of all SWNT dispersions excited at 532 nm, 633 nm and 785 nm. Shaded areas indicate RBM range of metallic SWNT species.

As mentioned in Chapter 2.1.3, the spectral position of the RBMs for a given excitation energy can be utilized to discriminate between semiconducting and metallic SWNTs and is directly related to the tube diameter, i.e., higher wavenumbers for smaller tube diameters.[59,336] Interestingly, the CoMoCAT sample shows several RBM peaks aside from the (6,5) SWNT signal located at 311 cm^{-1} when excited with the 633 nm or the 785 nm laser. This suggests the presence of a few minority SWNT species with small and medium diameters in this mixture despite their absence in the UV-vis-nIR absorption spectrum. Except for the excitation with the 633 nm laser, all RBM peaks can directly be assigned to semiconducting SWNT species only. The weak RBM signals in the metallic region when excited at 633 nm (with more than an order of magnitude lower signal strength) may arise from very small amounts of metallic nanotubes with high scattering efficiency. In general, resonant Raman spectroscopy is not considered as a valid method to quantitatively determine the nanotube specie distribution, as the resonance of the excitation energy with the respective SWNT transition highly affects the scattering intensity. Still, the overall scattering intensity could serve as rough measure for the abundance of nanotube species. Given the almost two orders of magnitude lower intensity values for the plasma torch RBMs excited at 633 nm compared to the other excitation wavelengths, the content of metallic nanotube species should be negligible. The absence of metallic SWNT bands (between 600 and 750 nm) in the UV-vis-nIR absorption spectrum corroborates this notion.

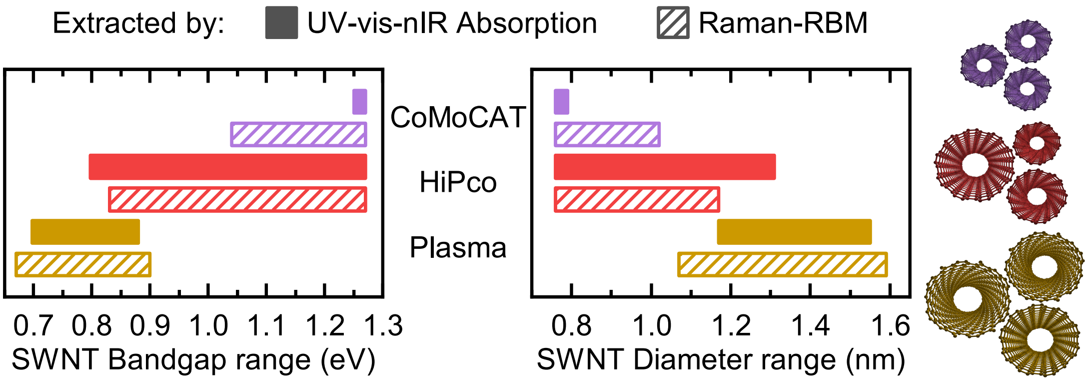

Figure 4.4: Extracted nanotube bandgap and diameter ranges of all three SWNT dispersion based on UV-vis-nIR absorption and Raman RBM measurements. Correspondingly colored nanotube illustrations (right) display the respective differences in SWNT diameter.

Overall, the SWNT diameters and bandgaps in the dispersions determined by the RBM positions are in agreement with the values extracted from the absorption spectra as shown in Figure 4.4. The main difference arises from the presence of minority SWNT species in the CoMoCAT sample. For the other two dispersions the diameter/bandgap distributions extracted from both methods differ also slightly from each other. An exact SWNT species assignment by UV-vis-nIR spectra alone is not always possible due to peak overlap of different chiralities as well as spectral shifts caused by the solvent, the wrapping polymer or bundled nanotubes. A combination with excitation-emission spectroscopy or electron diffraction would be required to be unambiguous.[39] Nevertheless, absorption spectroscopy allows for the quantitative estimation of nanotube bandgap and diameter ranges and should deliver a more representative image of the present SWNT species compared to the Raman analysis.

In summary, the CoMoCAT dispersion contains by far the narrowest, quasi monochiral distribution of small-diameter (6,5) SWNTs, whereas the plasma torch and especially the HiPco dispersions consist of a broader range of tube diameters. Although the difference between HiPco and plasma torch SWNTs with respect to their diameter spread is not substantial, the energetic bandgap distribution is much larger for the HiPco mixture compared to the small-bandgap plasma torch nanotubes.

4.3 Carbon Nanotube Network Field-Effect Transistors

As a next step, the three nanotube dispersions were deposited on substrates to form randomly oriented SWNT networks. Here, aerosol-jet printing was used as the deposition technique because it enables the reproducible preparation of dense nanotube networks while keeping the material consumption low (see Chapter 3.1.3).[286] For all three nanotube mixtures a comparable and high SWNT network density ($\geq 40\,\mu\mathrm{m}^{-1}$) was adjusted during the printing process as shown in Figure 4.5a. Since the charge carrier mobility in SWNT network FETs typically saturates for linear network densities higher than $\sim 15\,\mu\mathrm{m}^{-1}$,[278] this density ensures a robust comparison of the three nanotube networks with respect to some variations in SWNT length (~1 µm). The high nanotube network density also minimizes current hysteresis in bottom-contact/top-gate network FETs on glass substrates as utilized in this work, as the active transistor channel is spatially separated from the polar substrate surface.[278,286]

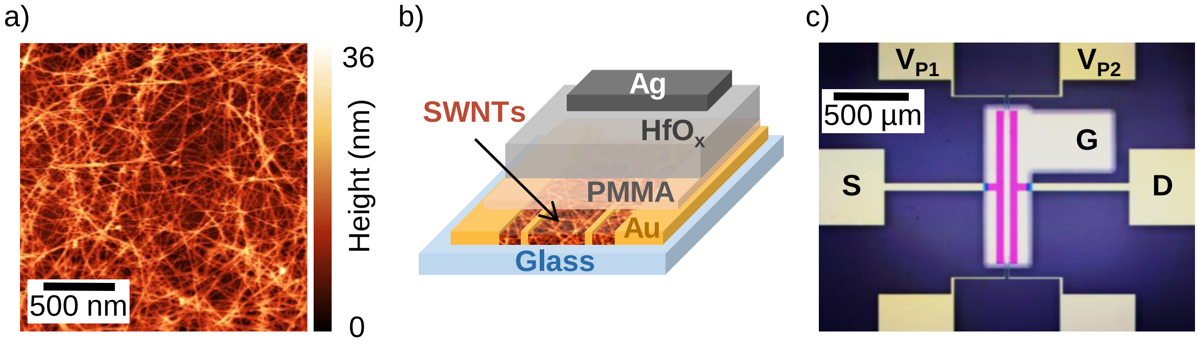

Figure 4.5: (a) Atomic force microscopy image showing the high network density of a representative printed SWNT film, (b) schematic representation of a SWNT network FET with gFPP electrode layout (layers are shifted for better visibility) and (c) optical micrograph of a typical network FET containing two voltage probe pairs (V_{P1}, V_{P2}) within the transistor channel.

All printed nanotube networks were integrated into FETs with a staggered device architecture as shown in Figure 4.5b. The transistors were fabricated by photolithographic patterning and evaporation of 2 nm chromium and 30 nm gold bottom-contacts which defined the source (S) and drain (D) electrodes as well as two voltage probe pairs (V_{P1}, V_{P2}) on glass substrates (see Chapter 3.1.2 and Figure 3.2a). The three SWNT dispersions were printed directly onto the contacts followed by another photolithographic patterning and oxygen plasma etching step in order to confine the resulting nanotube networks to the FET channel area. A bilayer dielectric consisting of 11 nm PMMA and 61 nm hafnium oxide combines several advantages of both materials. That is, a smooth interface of the PMMA with the SWNTs with a low dipolar disorder and trap density and on the other hand encapsulation, bias stress stability and low-voltage operation due to the $\mathrm{HfO_x}$ and its high dielectric constant as shown previously.[337] The devices were completed by evaporation of 30 nm silver top-gate electrodes. As shown in Chapter 2.4.3 the voltage-probes (see Figure 4.5c) enable the direct measurement of the contact resistance (R_{C}) and its gate voltage dependence. This measurement allows the extraction of the intrinsic charge carrier mobility and its temperature dependence within the nanotube networks free of any contact resistance effects.

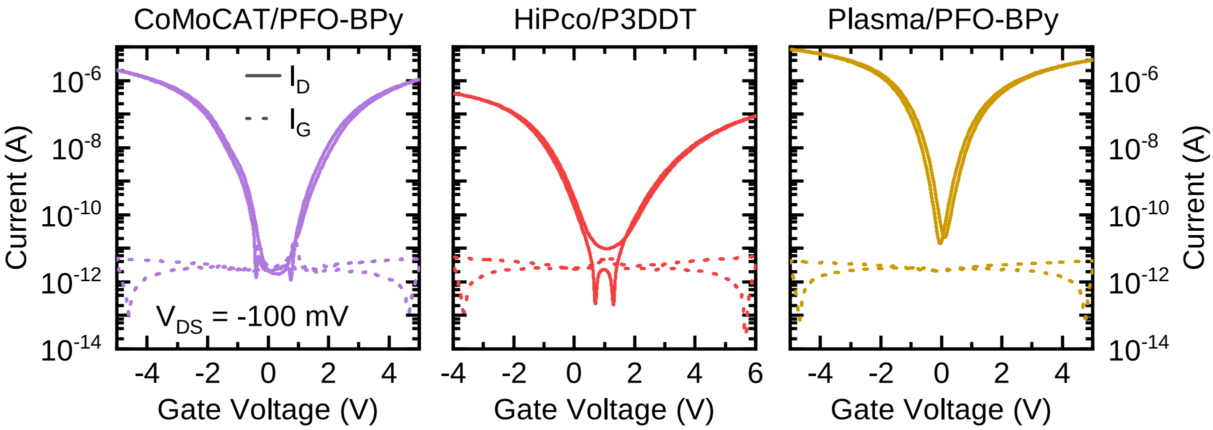

Figure 4.6: Transfer characteristics (forward and reverse gate voltage sweeps at $V_{\mathrm{DS}} = -0.1\,\mathrm{V}$) of FETs with all three network compositions measured at room temperature.

The transfer characteristics of SWNT network FETs measured at small source-drain voltages ($V_{\mathrm{DS}} = -0.1\,\mathrm{V}$) reveal almost ideal transistor behavior for all three network compositions measured within a small gate voltage range at room temperature as shown in Figure 4.6. That is, ambipolar and balanced electron and hole transport represented by the drain current (I_{D}), negligible hysteresis, low onset voltages and high on/off current ratios of about 10^6. These transport properties imply that unintended effects originating from the dielectric (dipolar disorder), the contacts (injection barriers), the polar substrate (e.g., electron traps), or impurities do not play a major role here which is essential for a meaningful transport study. Given the high network densities, the on/off current ratios further confirm the high semiconducting purity of all three nanotube network without any detectable amounts of metallic SWNT species, as already suggested by the UV-vis-nIR absorption and Raman spectroscopy. The gate leakage current (I_{G}) in the order of a few pA limited the transistor off-currents except for the plasma torch network. Here, the incomplete turn-off of the transistor can be explained by the overlap of the electron and hole current branches being typical for SWNT networks consisting of narrow bandgap nanotubes.[124,278] At lower source-drain bias and at lower temperatures the off-state current of the plasma torch network drops below the gate current as shown in Chapter 4.4. Aside from the off-currents a few more differences are directly apparent when comparing the three SWNT networks. First, the on-currents are highest for the plasma torch SWNT network (4.1–8.5 µA) and lowest for the HiPco nanotubes (0.1–0.4 µA) with the (6,5) SWNTs between both (1.1–2.0 µA). Second, the onset voltages (defined as the lowest gate voltage at which I_{D} exceeds I_{G} significantly) are largest for the small diameter (6,5) nanotubes, lower for the HiPco network and lowest for the plasma torch SWNTs for both electron and hole transport. Considering the different diameter distributions of the three SWNT networks, the mean nanotube diameter appears to correlate with the onset voltages and the gap between the hole and electron transport onsets, i.e., higher onset voltages for tubes with smaller diameter and thus larger bandgap. Overall, the transfer curve of the HiPco network FET is shifted by about 1 V to positive gate voltages, suggesting slight p-doping of this device, although the exact reason for this behavior is not clear. The gate voltage range for this transistor was adjusted accordingly.

Moreover, the output characteristics in Figure 4.7 further corroborate the differences in the transfer characteristics of the three SWNT network devices (see Figure 4.6), as the maximum on-currents follow the same trend. The perfectly linear current increase for small source-drain voltages indicates ohmic charge injection of holes and electrons for all network transistors and further confirm the high quality of the devices. However, this observation might also be ascribed to the rather long device channel lengths (L = 40 µm) resulting in relatively low R_C values compared to the resistance of the FET channels. Recently, the distorting impact of the contact resistance and its gate voltage dependence on the charge carrier mobility extraction of high-mobility organic semiconductors was pointed out.[323,338–340] This poses a problem especially for temperature-dependent mobility studies where already small variations might lead to wrong conclusions. Thus, a thorough and quantitative analysis of the contact resistance is still necessary.

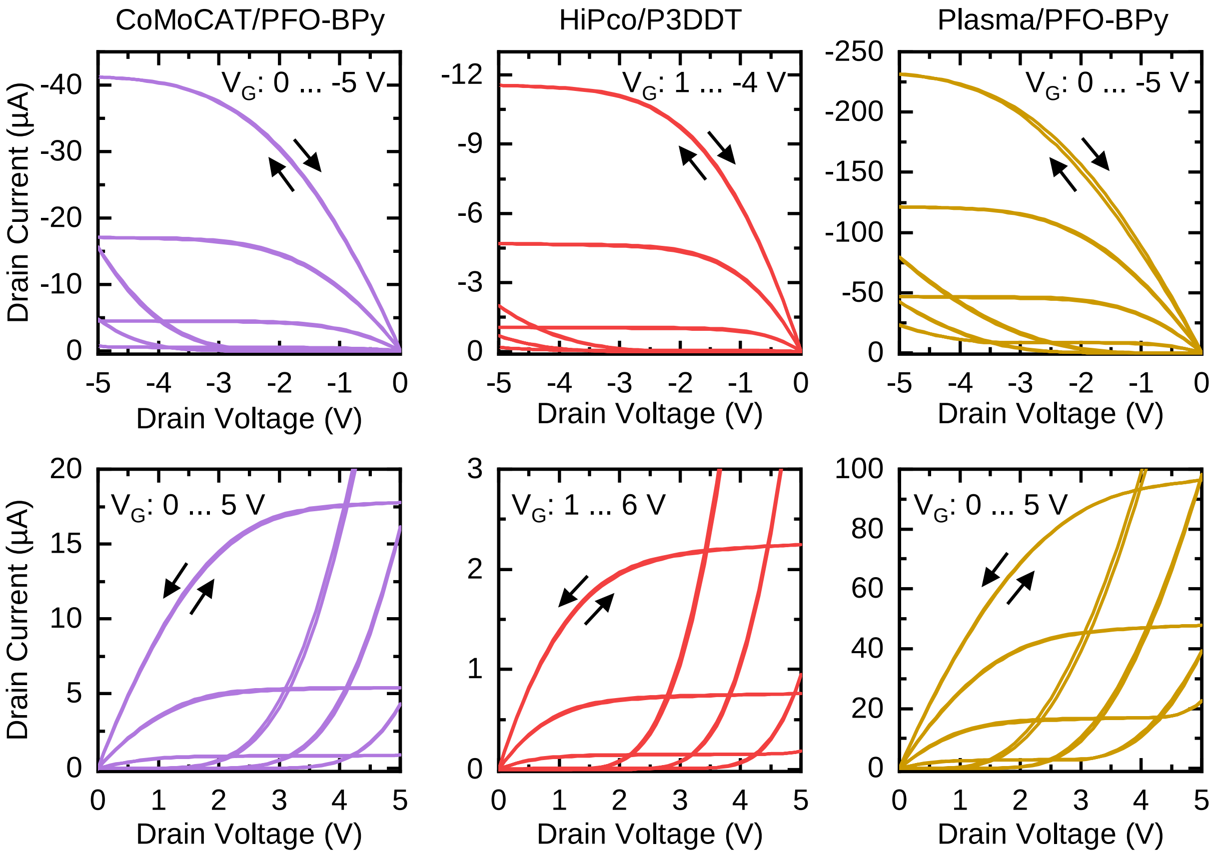

Figure 4.7: Output characteristics (forward and reverse V_{DS}-sweeps at constant V_G, 1 V steps) of FETs with all three network types for negative (top row) and positive (bottom row) applied voltages measured at room temperature.

The SWNT network patterning and thus the complete removal of nanotubes outside the channel area (as described in Chapter 3.1.5) was required for accurate gate capacitance and contact resistance measurements. Both are essential for a reliable charge carrier mobility extraction. For the capacitance measurement, the semiconducting SWNT network cannot be treated as homogeneous thin film and the metal-insulator-semiconductor capacitor inside the FET not as parallel-plate capacitor. Instead, other methods have been proposed to determine more precise capacitance and mobility values.[341,342] The capacitance extraction by capacitance-voltage measurements directly on structured SWNT network FETs, while the transistors were in the on-state, turned out to be the most feasible way and is thus used in this study.[278]

To completely remove any contact resistance contributions to the charge carrier mobilities, the gFPP transistor layout is used in this work. It enables the direct measurement of the local potential at two precise points inside the transistor channel using the two voltage probes. Assuming a linear potential gradient in the channel, which should be the case in the linear regime, i.e., at low V_{DS} and high V_{G}, the voltage drops at the contacts due to injection barriers can be estimated via extrapolation of the known channel potentials (see Chapter 2.4.3 for details).[322,343] For an undistorted voltage measurement without the influence of stray fields, it is crucial that the SWNT network is confined to the gated channel area and that the voltage probes protrude only slightly into the transistor channel.[316,344] The contact resistances of the source and drain electrode can be calculated for a given drain current based on Ohm's law depending on the respective voltage loss at the contacts. The total contact resistance is then obtained from the sum of the source and the drain resistance.

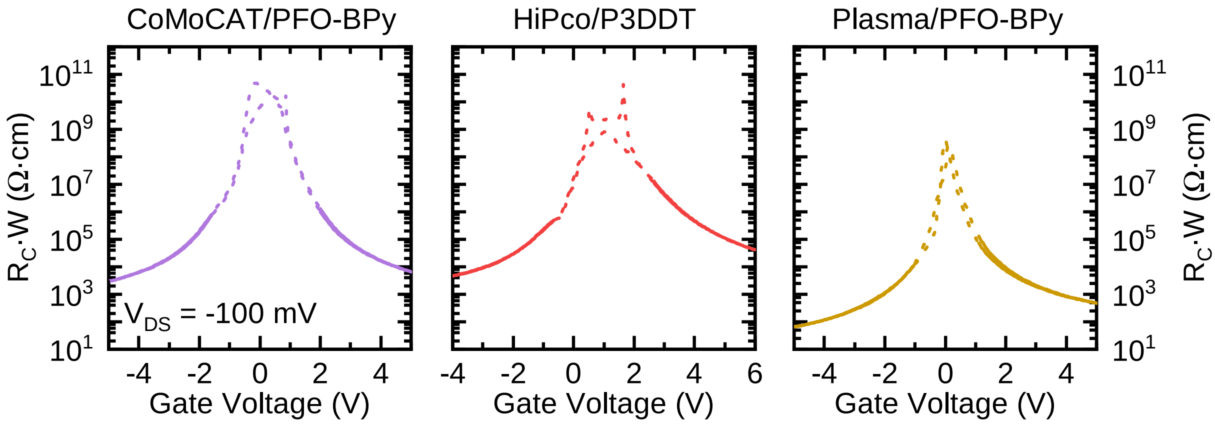

Figure 4.8: Gate voltage-dependent (forward and reverse V_{G}-sweeps at $V_{\mathrm{DS}} = -0.1$ V) and width-normalized contact resistances of FETs with all three network compositions measured at room temperature. The dashed lines indicate voltage rages for which the contact resistance values are unreliable.

A comparison of the channel width-normalized and gate voltage-dependent contact resistances for the three SWNT network FETs is displayed in Figure 4.8. Note, that the extracted contact resistance values are only reliable in the linear regime and thus for gate voltages of at least ±1 V above the respective onset voltage. For all network compositions, the R_C values for electron and hole injection show a distinct gate voltage dependence over several orders of magnitude, i.e., lower contact resistances for higher V_G. The small-diameter (6,5) SWNTs gave fairly balanced minimum contact resistances, namely 6.6 kΩ cm for electrons and 2.9 kΩ cm for holes. These values suggest an electrode work function that is energetically centered in the middle of the nanotube bandgap. The HiPco nanotubes showed the largest contact resistances for electron injection (41 kΩ cm) and lower values for hole injection (4.7 kΩ cm). This imbalance in contact resistance was reported previously for an analogous SWNT network composition.[194] The overall lowest R_C values of 0.07 kΩ cm for holes and 0.47 kΩ cm for electrons were obtained for the large-diameter plasma torch network, which is in agreement with reported literature values and a direct result of their small bandgap.[124,277]

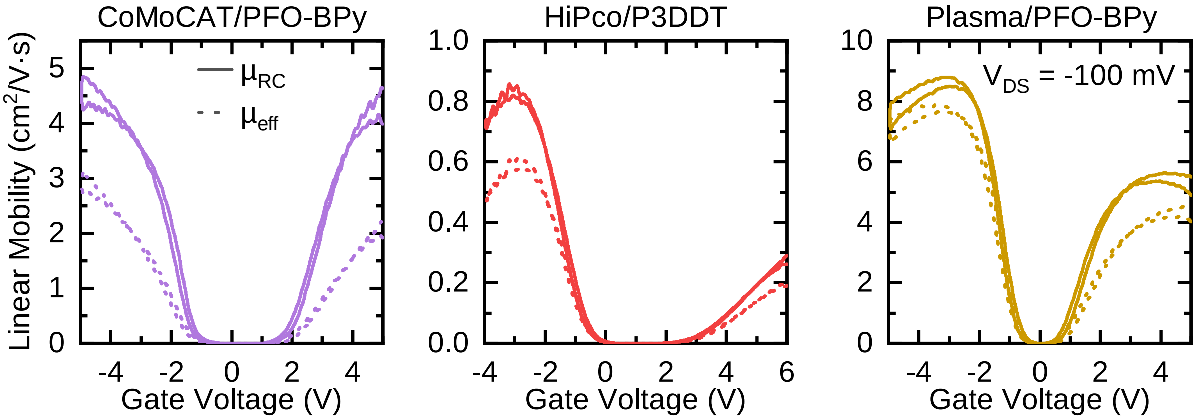

Figure 4.9: Gate voltage-dependent charge carrier mobilities of FETs with different network compositions: contact resistance-corrected linear mobility (μ_{RC}) and apparent linear mobility including contact effects (μ_{eff}) measured at small drain bias ($V_{DS} = -0.1$ V) at room temperature.

As a next step, the contact resistance-corrected carrier mobilities were calculated as described in Chapter 2.4.3.[320] A comparison of the apparent charge carrier mobility (μ_{eff}) with the R_C-corrected and thus intrinsic carrier mobility (μ_{RC}) is shown in Figure 4.8 for all SWNT network FETs. As for the contact resistance extraction, the charge carrier mobility values are only reliable in the linear regime, i.e., for $V_G \gg V_D$. The difference between μ_{eff} and μ_{RC} reveals a significant impact of the contact resistance on the extracted carrier mobilities, leading to a pronounced mobility underestimation of up to 50 % for all three network types. The disparity between the two mobility curves correlates with the respective R_C values, resulting in the smallest difference in mobility for the plasma torch network. Due to this pronounced impact of the contact resistance on the carrier mobilities all mobility values in this chapter are contact resistance-corrected.

The extracted device parameters including the directly measured gate capacitances utilized for the mobility calculations are summarized in Table 4.1. The similar capacitance values for all network compositions confirm the high nanotube network densities (≥40 µm^{-1}). Furthermore,

Table 4.1: Device parameters for FETs with CoMoCAT, HiPco and plasma torch SWNT networks extracted at room temperature.

SWNT Network	Gate Capacitance C_i (nF cm^{-2})	Onset Voltage V_{ON} (V)		Contact Resistance $R_C \cdot W$ (kΩ cm)		Carrier Mobility μ_{RC} (cm^2 V^{-1} s^{-1})	
		Holes	Electrons	Holes	Electrons	Holes	Electrons
CoMoCAT	125	-0.60	1.00	2.9	6.6	4.9	4.7
HiPco	110	0.45	1.65	4.7	41	0.8	0.2
Plasma	127	-0.05	0.1	0.07	0.48	9.3	5.6

they are in good agreement to geometrically calculated capacitances based on the dielectric layer thicknesses and the assumed nanotube diameters and densities (~110–120 nF cm^{-2}).[341] The resulting carrier mobilities corroborate the above mentioned differences in on-currents for the different network types. That is, higher mobilities for the (6,5) and the plasma torch SWNT networks (4.7–9.3 cm^2 V^{-1} s^{-1}) compared to the HiPco network with 5–20 times lower mobility values, especially for electrons (0.2–0.8 cm^2 V^{-1} s^{-1}). This discrepancy might be explained by the broad diameter and even broader bandgap distribution of nanotubes in the HiPco network compared to the other two networks (see Figure 4.4).

Within a network of different semiconducting SWNT species the charge transport could be restricted by a small amount of narrow bandgap nanotubes as suggested recently.[273] If the energetic difference between their band edge energy levels and the ones of adjacent SWNT species is large compared to the thermal energy defined by kT (with k – Boltzmann constant and T – temperature) the small bandgap tubes could act as charge traps at low charge carrier densities. In a mixed SWNT network with a broad distribution of bandgaps only a small fraction of percolating current paths might thus contribute to the overall charge transport. The resulting lower effective network density for charge transport should thus depend both on temperature and the number of charge carriers, i.e., on the gate voltage. Consequently, a temperature-dependent transport analysis should provide more evidence for this hypothesis, as shown in the next section 4.4.

4.4 Temperature-Dependent Transport Measurements

Based on the assumption that large energy level differences within a given SWNT network will limit the overall network transport, a more pronounced temperature-dependent transport is expected for the HiPco network compared to the other two SWNT networks. The temperature-dependent transfer curves from 100 to 300 K shown in Figure 4.10 confirm this notion. Reproducible transfer characteristics were also measured for lower temperatures down to 10 K for all network FETs. However, the temperature error is expected to be quite high (>10 %) for temperatures below 100 K due to Joule heating induced by the current flow through the devices. As a consequence, the temperature within the SWNT network FETs could differ significantly from the measured temperature inside the sample chamber especially for higher current densities and very low temperatures as shown by Nikoforov *et al.*[345] The investigated temperature range was thus restricted to 100–300 K in order to avoid distorted temperature-dependent carrier mobility values. To keep the overall Joule heating low, a low source-drain voltage was used resulting in lower current densities. For a typical temperature sweep, the sample was first cooled to the base temperature of the cryogenic chamber (10 K) and then heated up in steps of 20 K. Full equilibration of the system after each temperature step was enabled by introducing a hold time (20 min) before each transfer measurement.

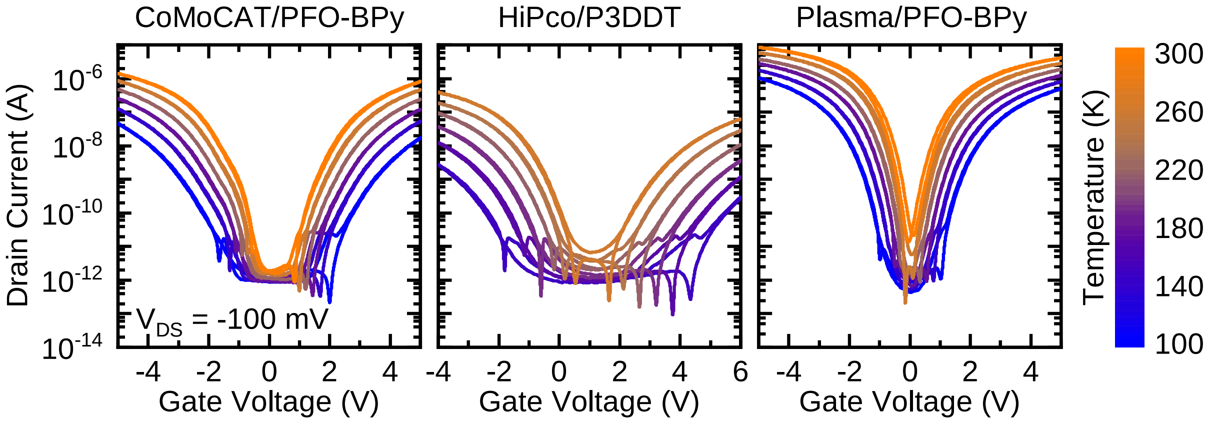

Figure 4.10: Transfer characteristics of FETs with all three SWNT network types (forward and reverse gate voltage sweeps at $V_{\mathrm{DS}} = -0.1$ V) measured with 20 K steps at temperatures from 100 to 300 K (for clarity, only every other curve shown).

Although all SWNT network FETs exhibit monotonously decreasing on-currents upon cooling, two distinct differences are evident. As expected, the temperature dependence of I_{D} indicates thermally activated transport for all network compositions, although to a quite different extent. From 300 to 100 K the on-current decrease is much more pronounced (two orders of magnitude) for the HiPco network compared to the other two network types, as suggested above. For the monochiral (6,5) SWNTs the drain current drops by only a factor of 30 upon cooling, whereas it decreases by less than one order of magnitude for the large diameter plasma torch nanotubes. The absolute values of the onset voltages for both holes and electrons increase with decreasing temperature for all network compositions as displayed in Figure 4.11. Again this temperature-dependent onset voltage shift is larger for the HiPco nanotubes (up to 3 V) than for the other two SWNT networks (about 1 V). This shift might be explained by the range of SWNT diameters and thus bandgaps in the different nanotube networks. Smaller bandgap SWNTs might act as trapping sites as long as they cannot form a percolating current path across the network. The energy level difference between those and adjacent SWNTs might be overcome at high temperatures and charge carrier densities, whereas at lower temperatures the narrow bandgap tubes act as deep traps resulting in an up-shifted onset voltage. Such intrinsic trap states should

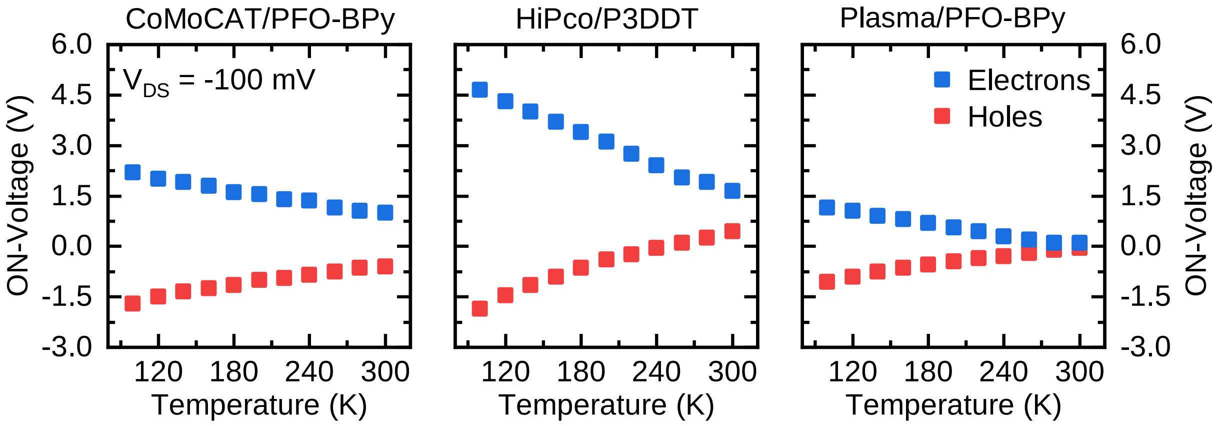

Figure 4.11: Temperature-dependent onset voltages (extracted at $V_{\mathrm{DS}} = -0.1$ V) for FETs with all three network compositions and for electron and hole transport.

influence electrons and holes equally which is the case for the studied networks. Consequently, the broader range of nanotube bandgaps within the HiPco mixture, compared to the other two network types would explain the observed stronger onset voltage shift for holes and electrons.

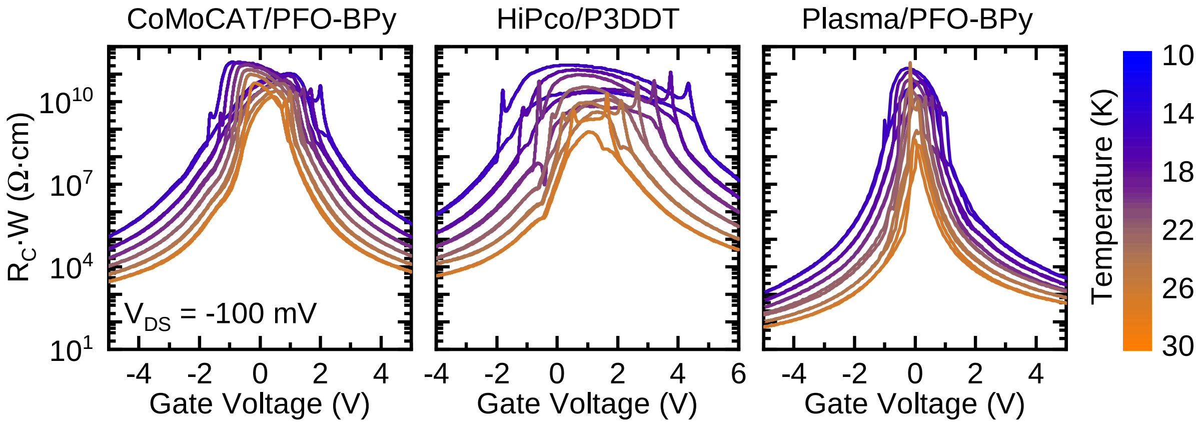

Figure 4.12: Gate voltage-dependent and width-normalized contact resistances (forward and reverse gate voltage sweeps at $V_{\mathrm{DS}} = -0.1$ V) measured at different temperatures from 100 to 300 K in steps of 20 K (for clarity, only every other curve shown) for all network compositions.

Furthermore, the observed gate voltage dependence of the contact resistances at room temperature (see Figure 4.8) persists over the whole temperature range for all three network compositions as shown in Figure 4.12. Their temperature dependence follows a trend similar to the on-currents and onset voltages, namely overall higher contact resistances at lower temperatures and a stronger increase in R_{C} upon cooling for the HiPco network compared to the other two SWNT networks.

The differences in onset voltages between the three network FETs and the temperature-dependent onset shifts within the same device raise the question: at what gate voltage should the carrier mobilities and contact resistances be extracted, as they both depend strongly on the charge carrier density.[156,158] In many studies, both are extracted at the highest applied gate bias or at the maximum of the transconductance if it can be reached within the used gate voltage range. However, even at room temperature the effective charge carrier concentration in the three network FETs differs significantly for a given gate voltage as shown in Figure 4.9. Thus, the carrier mobilities and R_C were extracted at a comparable gate overdrive defined as the difference between the applied gate voltage and the respective onset voltage.[218,220] In this chapter a gate overdrive of ±2 V corresponding to a mobile charge carrier concentration of $\sim 1 \times 10^{12}\,\mathrm{cm}^{-2}$ was used for the contact resistance and mobility calculation.

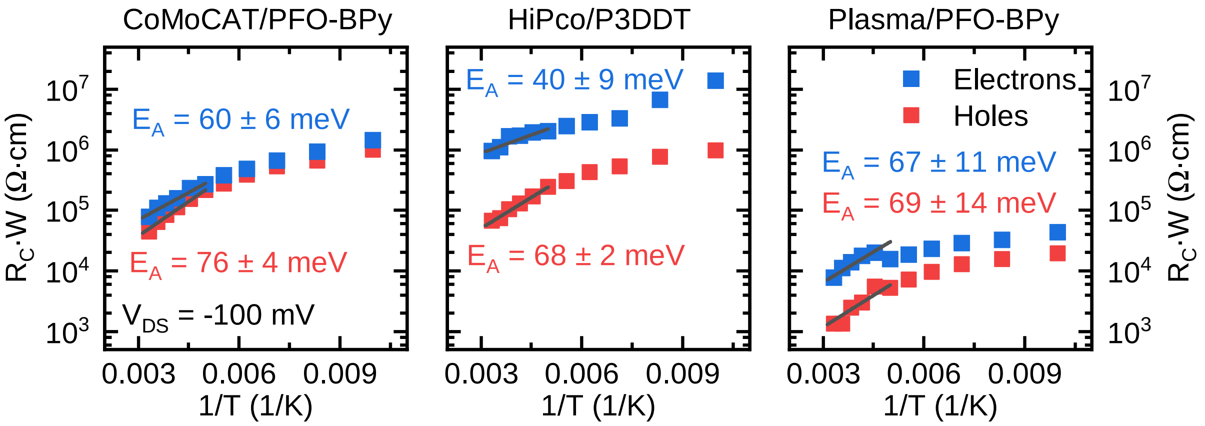

Figure 4.13: Temperature-dependent and width-normalized contact resistances of FETs with all three SWNT networks for electrons and holes. The resistance values are extracted at a 2 V gate overdrive. Solid lines between 200 and 300 K are Arrhenius fits to extract the activation energies (E_A) for electron and hole injection.

A detailed comparison of the extracted contact resistances for the three different SWNT network FETs between 300 and 100 K is depicted in Figure 4.13. The R_C values for holes and electrons increase for more than one order of magnitude upon cooling for all devices suggesting a thermally activated charge carrier injection process. Both for established semiconductors (organic or inorganic) and SWNTs the temperature dependence of the charge carrier injection is usually evaluated based on a thermionic emission mechanism with an Arrhenius-like relation, i.e., $R_C \propto \exp(E_A/kT)$, with E_A being the height of the injection barrier.[160,313,343,346] Yet, in this case the temperature-dependent contact resistance values of the three SWNT networks cannot be described with a single Arrhenius-type fit. Instead, two different gradients below and above 200 K were determined for the $\ln(R_C)$ *vs* $1/T$ plots. For higher temperatures than 200 K the R_C values could be more or less evaluated with an classical Arrhenius fit leading to activation energies of 40–70 meV. Given the fairly different contact resistances for the three nanotube networks, these overall quite similar activation energies suggest a more complex dependence of R_C than just on the energetic difference between the SWNT band edges and the electrode work function. Also the carrier mobility in vertical direction, the energetic disorder and the effective gate field might play a major role here, which would be similar to other disordered semiconductors.[339]

Nevertheless, the unequal temperature dependence of R_C for the three network types once more highlights the need for a proper contact resistance correction of the charge carrier mobilities.

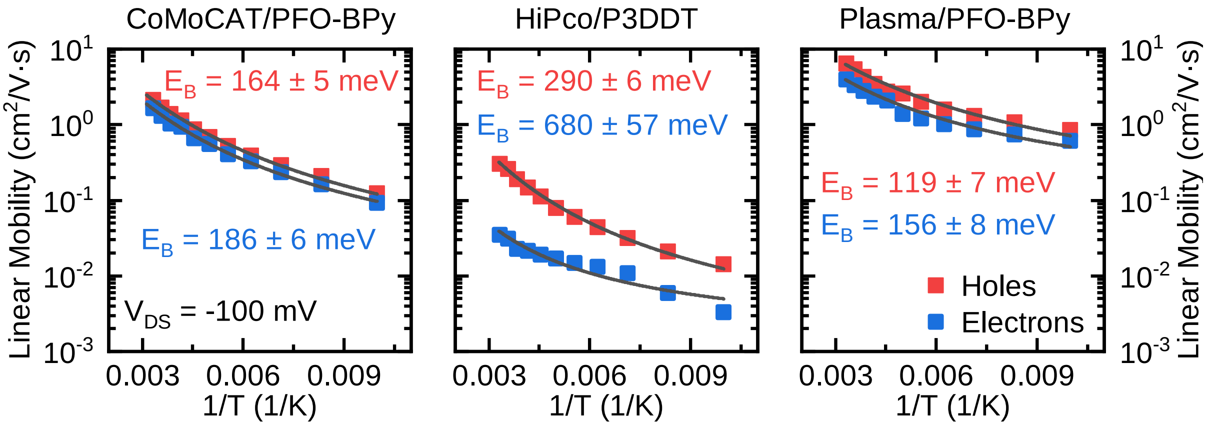

Figure 4.14: Temperature-dependent carrier mobilities for electrons and holes of FETs with all network compositions extracted at a 2 V gate overdrive. Solid lines are fits based on the fluctuation-induced tunneling (FIT) model with the tunneling barrier height E_B.

A comparison of the temperature-dependent corrected charge carrier mobilities (measured in the linear regime, see Figure 4.9) from 300 to 100 K for all three network types is shown in Figure 4.14. Again, the mobility values were extracted at a 2 V gate overdrive. In agreement with previous studies on polymer-sorted SWNT networks, the overall trend of the carrier mobilities is the same for all network types, i.e., a decreasing electron and hole mobility with decreasing temperature.[179,194,333] The decrease in field-effect mobility with decreasing temperature is monotonous, although with a slope that levels off for lower temperatures. Thus, the $\ln(\mu_{RC})$ *vs* $1/T$ plots cannot be described with a linear fit based on the VRH model, as commonly done for charge transport in conventional disordered semiconductors. Instead, the temperature-dependent mobility data was described best by the FIT model which is consistent with previous reports.[178,179,194] Based on this model the SWNTs are treated as long conducting segments separated by the nanotube-nanotube junctions which are described as tunneling barriers. Note, the model was originally developed for carbon-polyvinyl chloride composites and other disordered materials and lacks a direct physical relation to the characteristic properties of SWNTs. As shown in Equation 2.18 in Chapter 2.2.1, the carrier mobility can be expressed depending on the required temperature to surpass the tunneling barrier T_B.[196] Consequently, corresponding activation energies or energetic barrier heights, defined as $E_B = kT_B$ can be obtained by fitting the carrier mobilities based on the FIT model (see solid lines shown in Figure 4.14). The extracted tunneling barriers are somewhat lower for the large-diameter plasma torch nanotubes (E_B = 119–156 meV), indicating a less pronounced temperature dependence than for the large-bandgap (6,5) SWNT network (E_B = 164–186 meV). In agreement with their ambipolar transfer characteristics, both networks exhibit fairly balanced barrier heights for hole and electron conduction. However, the HiPco nanotubes with the broadest diameter and energy level distribution show considerably higher energy barriers (E_B = 290 meV) and a more pronounced temperature dependence for holes. Their electron mobilities exhibit even larger activation energies (E_B = 680 meV) even though the data could not be fitted as well for lower temperatures. In general, the extracted barrier height values should be treated with caution and should serve as a relative rather than as an absolute measure. Due to the non-linear relation of $\ln(\mu_{RC})$ *vs* $1/T$ within the FIT model and the employed least-square fitting algorithms, the extracted fit parameters are less reliable than for a conventional linearized Arrhenius fit. The calculated energy barriers vary significantly depending on the starting parameters (such as the prefactor A) or the chosen temperature range. Furthermore, the FIT model does not consider the intra-nanotube charge transport which might have an impact on the overall network properties. Still, the energy barriers were reproducibly higher for the HiPco nanotubes compared to the (6,5) or the plasma torch networks.

So far, the FIT model was applied to describe charge transport in SWNT networks with a large number of different network compositions, not only for polymer-sorted nanotube mixtures, but in some cases for networks without any surfactant[178] or including metallic nanotube species. Still, the role of the wrapping polymer remains unclear. Certainly, the application of two different conjugated polymers is not ideal for an unambiguous transport analysis, but was necessary to obtain the desired different SWNT diameter ranges free of any metallic impurities. The HiPco network with the highest energy barriers was sorted with P3DDT, whereas the other two networks with lower barrier heights were obtained using PFO-BPy as the dispersant. Similar to other wrapping polymers, both P3DDT and PFO-BPy are relatively insulating compared to the SWNTs. Thus, the polymers are often assumed to increase the energy barriers of the nanotube networks. Yet, the much larger energy gap between the highest occupied molecular orbital (HOMO) and the lowest unoccupied molecular orbital (LUMO) of PFO-BPy (3.2 eV) compared to the nanotube bandgaps should exclude any charge transfer from the nanotube to the polymer. The HOMO-LUMO gap of P3DDT (1.9 eV) is narrower but still sufficiently large to form type-I heterojunctions with all nanotube species of the HiPco SWNT mixture, making charge transfer from the SWNTs to this polymer also unlikely.[347,348]

4.5 Impact of the Wrapping Polymer

To assess the influence of the wrapping polymer and to confirm that the different temperature dependencies of the three SWNT network FETs indeed arises from their network composition only, polymer-removal experiments on a printed CoMoCAT/PFO-BPy network reference sample were performed (see Chapter 3.1.4). The utilized polymer-stripping method was introduced by Joo *et al.* and is based on the complexation of $Re(CO)_5Cl$ with the bipyridine moiety of the PFO-BPy polymer.[334,349] The chelating bipyridine unit is crucial for a stable complexation with the rhenium salt leading to the complete unwrapping of the polymer. Consequently, this method cannot be transferred to other wrapping polymers without this moiety and is applied for the removal of PFO-BPy only. The stripping protocol includes a vacuum annealing step (400 °C) of the freshly printed nanotube network to cleave off the alkyl side chains of the polymer, which is assumed to facilitate scission of the polymer chains into oligmers.[334] Second, to remove the oligomers the annealed SWNT networks were immersed in toluene with excess $Re(CO)_5Cl$ for several hours, followed by several washing steps. The stripping process was monitored by UV-vis-nIR absorption measurements as depicted in Figure 4.15. As mentioned above, the (6,5) SWNT dispersion and the pristine and THF-washed (6,5) nanotube network show a weakly pronounced absorption band around 350–370 nm suggesting an already low polymer content (see Figure 4.15a,b). Note, the S_{33} transition of the (6,5) SWNTs (350 nm) is located in the same spectral region as the shoulder produced by the PFO-BPy (362 nm),[335] which makes a quantitative analysis difficult. However, after the rhenium salt treatment the polymer shoulder disappeared as confirmed by the second derivative of the absorption in Figure 4.15c, which strongly implies a successful and complete removal of PFO-BPy from the SWNT network.

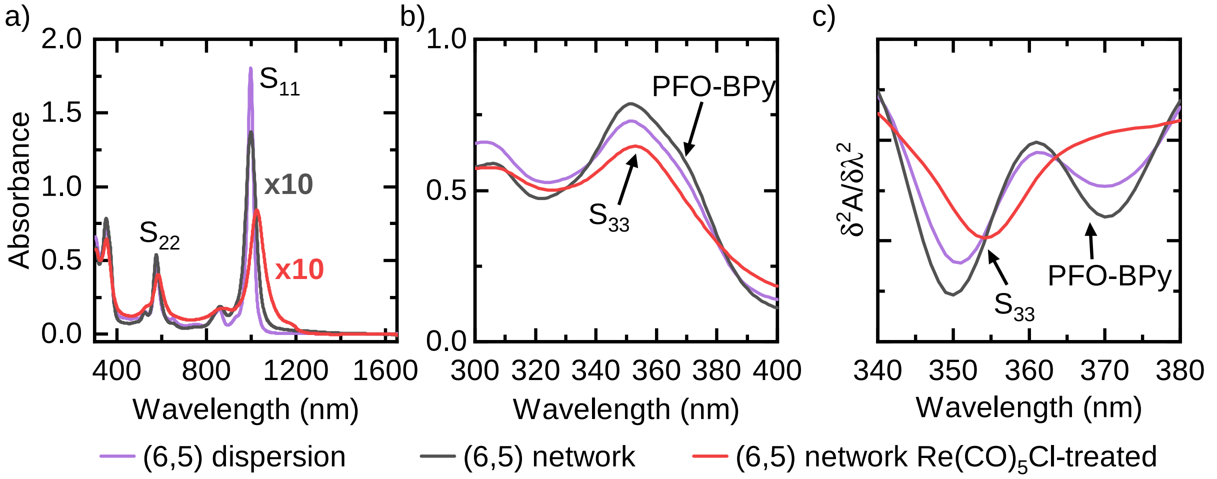

Figure 4.15: (a) UV-vis-nIR absorption spectra of (6,5) SWNT samples: purified CoMoCAT/PFO-BPy dispersion (purple), pristine aerosol-jet-printed (6,5) SWNT network (black) and after treatment with $Re(CO)_5Cl$ (red). For clarity, the absorbance values of the two network measurements were multiplied by ten. (b) The same absorption spectra in the UV-region only. (c) Second derivative of the absorption band at 350–370 nm.

The S_{11}, S_{22} and S_{33} absorption peaks of the (6,5) SWNTs were broadened and red-shifted after the treatment with $Re(CO)_5Cl$, which indicates increased SWNT bundling in the treated (6,5) nanotube network.[38,350] Owing to the overall high SWNT network density, a major part of the nanotube network is not in direct contact with the substrate and could reorganize during the rhenium treatment for several hours in hot solvent. Presumably, the bundling is facilitated by the removal of the wrapping polymer and further driven by strong capillary forces during the subsequent drying of the nanotube film. The atomic force micrograph of a $Re(CO)_5Cl$-treated (6,5) SWNT network depicted in Figure 4.16a shows an intact film with a high network density comparable to the other nanotube networks. Nevertheless, the treated SWNTs appear to be more bundled, which is in agreement with the results from the UV-vis-nIR absorption measurements and previous reports, in which the rhenium salt treatment of PFO-BPy-wrapped SWNTs led to nanotube aggregation.[334,349]

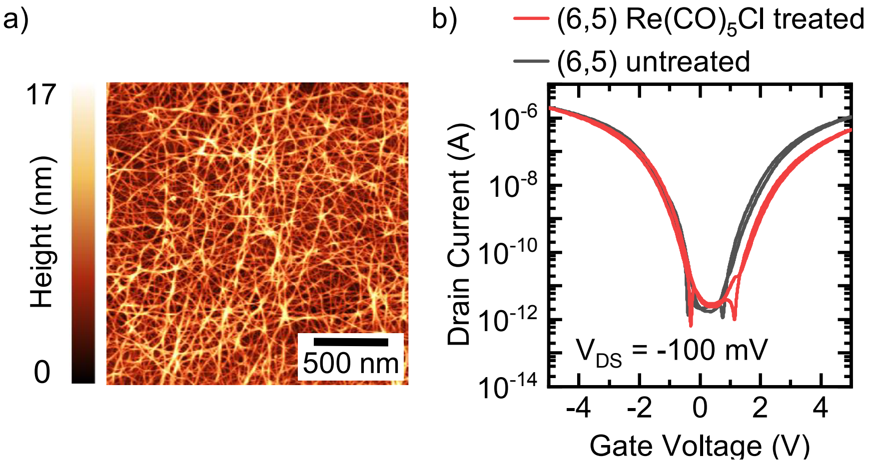

Figure 4.16: (a) Atomic force micrograph of a (6,5) SWNT network treated with $Re(CO)_5Cl$. (b) Transfer characteristics (forward and reverse V_G-sweeps at V_{DS} = −0.1 V) of an untreated and a $Re(CO)_5Cl$-treated (6,5) SWNT network.

To finally analyze the impact of the polymer stripping procedure on charge transport, the $Re(CO)_5Cl$-treated (6,5) SWNTs were integrated into gFPP-FET structures as shown above. The resulting devices did not show an enhanced charge transport compared to the untreated (6,5) SWNT network but slightly lower drain currents and carrier mobilities for holes (3.5 $cm^2\,V^{-1}\,s^{-1}$) and electrons (2.3 $cm^2\,V^{-1}\,s^{-1}$) as shown in Figure 4.16b. For electron transport, the onset voltage also increased by 0.5 V. These overall poorer device characteristics can be explained by a higher number of nanotube bundles. According to previous studies bundling leads to increased scattering of charge carriers, ineffective gating and consequently to lower conductivities within each individual nanotube.[167] In some cases the removal of the wrapping polymer chains (supramolecular or covalent) from the nanotubes resulted in a slightly improved SWNT network charge transport.[334,351–353] However, in these reports the overall polymer concentration estimated from UV-vis-nIR absorption measurements was fairly high and thus an improved nanotube network conductivity seems to be reasonable. In this work, the overall polymer concentration was very low and the associated polymer:SWNT surface coverage should be lower than 30 % as shown in Chapter 4.2. Hence, most of the SWNT-SWNT junctions should not be affected by the remaining wrapping polymer which instead might have the beneficial effect of preventing further nanotube bundling.

The charge carrier mobilities for electrons and holes in FETs with networks of rhenium salt-treated (6,5) SWNTs were slightly below those of the untreated (6,5) nanotube network as shown in Figure 4.17. The extracted tunneling barrier heights based on the FIT model (E_B = 181 meV for electrons and E_B = 159 meV for holes) were similar to those of the non-treated (6,5) SWNT network FET. This observation supports the notion that the influence of the remaining wrapping polymer on charge transport in the studied SWNT networks is indeed negligible. It further legitimizes the comparison of nanotube networks prepared from SWNT dispersions with different wrapping polymers.

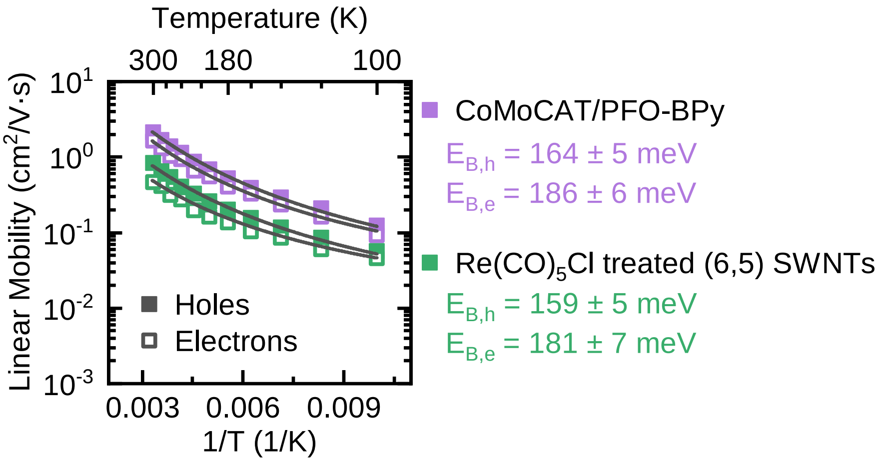

Figure 4.17: Temperature-dependent charge carrier mobilities for electrons and holes of FETs with untreated and Re(CO)$_5$Cl-treated (6,5) SWNT networks. The mobility values are extracted at a 2 V gate overdrive. Solid lines are fits based on the FIT model with the height of the tunneling barrier E_{B}.

To allow for a clearer comparison of the temperature-dependent charge transport in all SWNT networks, the relative decrease in hole mobilities from 300 to 100 K was plotted by normalizing the mobility values to their respective maximum at 300 K. The resulting plots in Figure 4.18 illustrate again the more pronounced decrease in mobility for the HiPco nanotubes. The (6,5) SWNTs (untreated and Re(CO)$_5$Cl−treated) show a lower temperature dependence, which should be ascribed to their different SWNT network composition (monochiral) compared to the broad SWNT diameter distribution within the HiPco network. As stated above, the FET channel conductivity in random SWNT networks is considered to be limited by the SWNT-SWNT junctions, across which the charge carriers have to hop. The junction resistance is significantly higher than the resistance along the individual nanotubes.[167,178,194] Due to the broad range of nanotube bandgaps within the HiPco mixture, there is a high chance for a large energy level mismatch between the conduction and/or valence bands of two adjacent nanotubes. These additional energy barriers in the range of 50–400 meV add to the activation energy for charge transfer between two nanotubes of the same species. The resulting very uneven energetic landscape forces the charge carriers to hop down or up in energy on their way through the nanotube network.[187] In the (6,5) SWNT network, the energy differences between adjacent hopping sites should lie in the range of 40–60 meV only caused by dipolar disorder in the SWNT film.[53,202,286] Consequently, the charges move through a much more even energy surface leading to higher carrier mobilities with a less pronounced temperature dependence, as it is observed in the experiments. Yet, this hypothesis cannot explain the higher mobilities with the least pronounced temperature dependence and the lowest extracted activation energies for the plasma torch SWNT network with large tube diameters. In this network the nanotube diameter distribution leads to an energetic spread of SWNT bandgaps of ~180 meV, which is smaller than within the HiPco mixture (~470 meV) but still significantly larger than the moderate energetic disorder in the (6,5) SWNT networks.

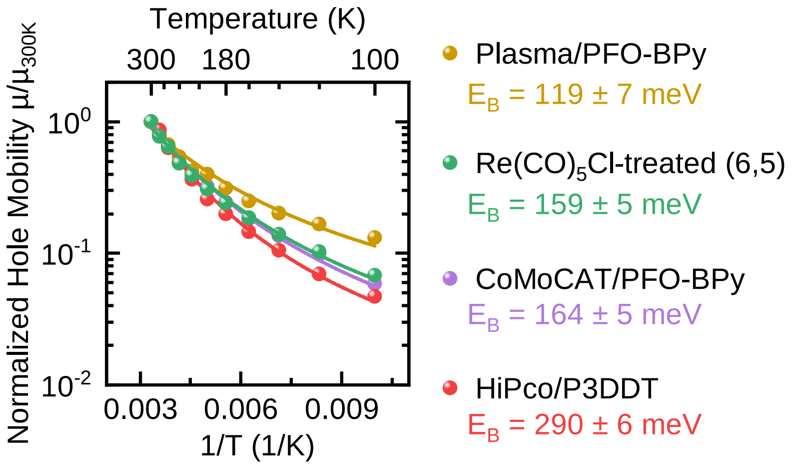

Figure 4.18: Relative comparison of the temperature-dependent hole mobilities for FETs including all three untreated SWNT networks and the $Re(CO)_5Cl$-treated (6,5) nanotube network extracted at a 2 V gate overdrive. The mobility values are normalized to their maximum at 300 K. Solid lines are fits to extract the energy barriers E_B based on the FIT model.

These observations reveal the shortcomings of the common notion, that only the nanotube-junctions determine the charge transport in randomly-oriented semiconducting SWNT networks. Apparently, the diameter- and temperature-dependent transport within each individual SWNT cannot be neglected completely. The intra-nanotube charge carrier mobility scales with $1/T$, while being proportional to the squared nanotube diameter $\left(d_t^2\right)$.[158] This temperature dependence of the carrier mobility is not as steep, but it counteracts the thermally activated inter-nanotube transport at the SWNT-SWNT junctions to some degree. The opposing temperature dependence of the intra-nanotube mobility is expected to be more pronounced for large-diameter SWNTs due to the strong nanotube diameter dependence. The same holds true for sparse or aligned SWNT networks, for which the number and impact of the junctions should be smaller. However, the overall charge carrier mobilities in random networks still remain thermally activated but not as strongly as in the VRH model. As a consequence, the experimentally observed temperature-dependent mobilities of the investigated networks might be explained as an interplay of the composition (energy level spread) and the temperature dependence of the inter-nanotube hopping and the temperature and diameter dependence of the intra-nanotube charge transport.

4.6 Random Resistor Network Simulations

To further evaluate this interplay between inter- and intra-nanotube transport, the experimental results are compared to the carrier mobilities of simulated SWNT networks based on a previously presented random resistor model, in which the intra-nanotube transport is neglected completely.[202] Despite this simplification, the model was recently shown to qualitatively describe charge transport in monochiral and mixed nanotube networks in good agreement with the experiment.[273,278] The nanotubes of an assigned species are modeled as one-dimensional sticks with a predefined length and DOS. They are randomly distributed in a two-dimensional box (see Chapter 2.2.2 for details). Each nanotube-nanotube junction, i.e., the intersection between two adjacent SWNT sticks, is treated as a resistor, whereas each nanotube is modeled as resistanceless node. The bond conductance at each junction resistor is evaluated based on a master equation approach for disordered systems, while the charge transfer between two energetic sites, i.e., the energy levels of the adjacent SWNTs, is described as hopping process.[186] The SWNT band edge energies were superimposed with a Gaussian energetic disorder of 45 meV to account for the dipolar disorder in the SWNT film. The hopping prefactor was kept constant for all tube-tube junctions and SWNT species. Based on Kirchhoff's current law and a MATLAB solver the resulting resistor networks were solved numerically to determine the network mobility depending on the charge carrier density.

Table 4.2: Nanotube chirality distributions for three simulated SWNT network compositions corresponding to the experimental nanotube networks.

SWNT Network		Composition							
(6,5) SWNTs	Chiralities	(6,5)							
	Fraction	1.0							
HiPco Mix	Chiralities	(6,5)	(7,5)	(7,6)	(8,6)	(9,7)	(10,5)	(10,6)	(10,9)
	Fraction	0.03	0.05	0.22	0.12	0.06	0.28	0.19	0.05
Plasma Mix	Chiralities	(9,8)	(10,8)	(10,9)	(12,7)	(13,5)	(14,6)	(15,4)	(15,7)
	Fraction	0.06	0.11	0.10	0.07	0.19	0.22	0.05	0.20

Three different SWNT networks representing the compositions of the experimental nanotube films were simulated in a $20 \times 20\,\mu\mathrm{m}^2$ box with a linear network density of $7\,\mu\mathrm{m}^{-1}$ and a log-normal nanotube length distribution of $1.5 \pm 0.9\,\mu\mathrm{m}$. Note, the much lower input network density compared to the experiment was chosen to keep the computational cost manageable. The respective nanotube species or 'chirality' distributions were estimated via the UV-vis-nIR absorption measurements of the SWNT dispersions (see Figure 4.2) and are summarized in Table 4.2. Based on these input parameters five equivalently created SWNT networks were simulated per network composition. Their charge carrier density-dependent network mobility was calculated and averaged for a temperature of 300 K as shown in Figure 4.19. As the model does not permit the calculation of absolute carrier mobility values, only the differences between normalized network mobilities can be discussed. For all three SWNT network compositions the normalized network mobilities reached a maximum at carrier densities between 1×10^{11} and 5×10^{11} cm^{-2}. This behavior is similar to the V_G-dependent experimental carrier mobilities and can be explained by filling of the first conduction subband of the SWNTs.[156] The network mobilities of the HiPco network are the lowest over the whole charge carrier density range.

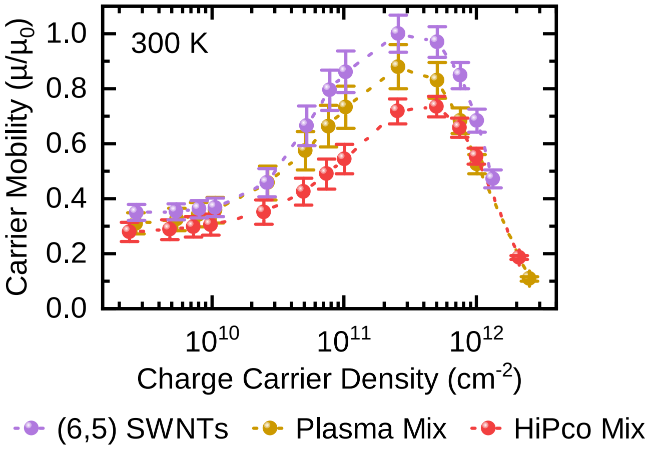

Figure 4.19: Simulated charge carrier density-dependent network mobilities for three nanotube network compositions comparable to the experimental SWNT networks at 300 K (normalized to the maximum value of the (6,5) SWNT network). Dashed lines represent guides to the eye. Per network composition five analogous networks were averaged and the standard deviation is represented by the error bars.

This trend persisted over a wide temperature range from 200 to 400 K as depicted in Figure 4.20 with the peak network mobility values extracted at each temperature step. Note, the network simulations did not converge for temperatures lower than 200 K, which is why the range was shifted to higher temperatures compared to the experiments. Overall, the simulated mobilities increase for higher temperatures, which is consistent with the Miller-Abrahams approach for describing the charge transport at the SWNT-SWNT junctions. The simulated temperature-dependent peak mobilities were further evaluated based on the FIT model and for each SWNT network composition a corresponding energy barrier height E_B was extracted as shown above. Besides the overall lowest mobility values the simulated HiPco network also exhibits the most pronounced temperature dependence resulting in the highest energy barriers of 42 meV. The barrier energies for the simulated (6,5) SWNT and plasma torch SWNT networks (20–24 meV) are considerably lower, revealing a less pronounced decrease in mobility upon cooling, as shown also in the experiment. Interestingly, over the whole temperature range the peak mobilities for the plasma torch network are lower than those of the (6,5) SWNTs contrary to the experiments.

These simulation results lead to two conclusions. First, the random resistor model can qualitatively predict the impact of a broad *vs* narrow SWNT diameter and thus energy level distribution on the transport properties of a given SWNT network. Second, the model is not able to meaningfully

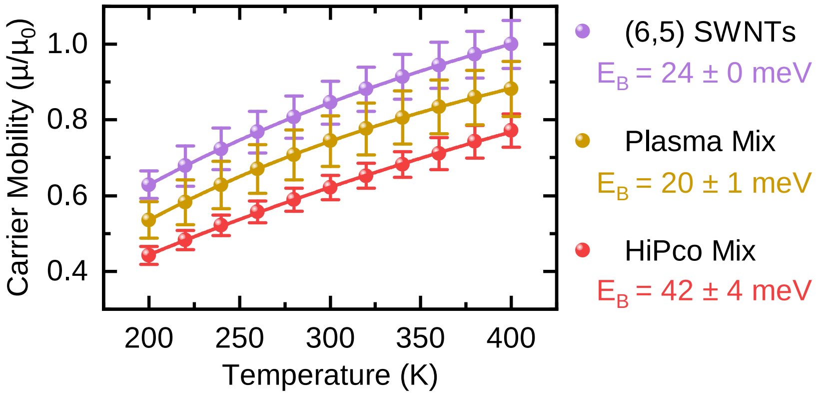

Figure 4.20: Simulated temperature-dependent charge carrier mobilities (normalized to the maximum value of the (6,5) nanotube network). Solid lines are fits based on the FIT model to obtain the respective energy barrier height E_B.

compare nanotube networks of completely different SWNT mean diameters as it only takes into account the energetic landscape created by the junctions and not the intra-nanotube transport with its specific diameter and temperature dependence. The latter seems to play a significant role in real SWNT network devices and should be considered when selecting semiconducting SWNT mixtures for transistor applications.

4.7 Summary

In this chapter the impact of the nanotube network composition on the charge transport properties of SWNT network transistors was examined. The active layer of the devices was prepared by aerosol-jet printing of three different polmyer-selected semiconducting nanotube dispersions with differing diameter and bandgap distributions based on combinations of commercially available SWNT raw materials with two wrapping polymers. Although all SWNT network FETs exhibited overall intrinsic transport behavior, a contact resistance correction allowed for the extraction of meaningful charge carrier mobilities. In all nanotube networks, residual amounts of the employed wrapping polymers were found to have negligible impact on charge transport. Based on temperature-dependent measurements a thermally activated transport mechanism for electrons and holes was found for all networks transistors that could be fitted best using the fluctuation-induced tunneling model, although it lacks a direct connection to specific nanotube properties. The SWNT film with the broadest diameter distribution showed the most pronounced temperature dependence and overall lowest carrier mobilities, which can be explained by the comparatively uneven energetic landscape of the network as confirmed by simulations based on a random resistor network model. However, the highest mobility and least pronounced temperature dependence was not found for the monochiral network of small-diameter (6,5) SWNTs that should be the ideal candidate according to network simulations that take only the energetic differences at the SWNT junctions into account. Instead, the large-diameter plasma torch network with a certain diameter and thus energy level distribution gave the highest mobilities and lowest temperature dependence. These observations clearly indicate that the nanotube junctions are not the only charge transport-limiting factor. The carrier mobility within the individual SWNTs with its own temperature (mobility $\propto 1/T$) and diameter (mobility $\propto d^2$) dependence seems to play an important role as well. Hence, networks containing only monochiral large-diameter SWNTs are expected to exhibit the highest carrier mobilities and least temperature dependence.

To further validate these hypotheses, tailored nanotube network compositions are studied in the next chapter.

CHAPTER 5

CHARGE TRANSPORT IN MIXED SWNT NETWORKS WITH TAILORED COMPOSITIONS

This chapter discusses the charge transport in mixed semiconducting SWNT networks consisting of small-diameter (6,5) nanotubes and large-diameter plasma torch SWNTs with various defined mixing ratios.

The data presented in this chapter was published in part in the article Brohmann *et al. ACS Nano* **2019**, 13, *6*, 7323-7332.[354] Modified figures and tables are presented with permission from the American Chemical Society. The carbon nanotube network simulations were performed based on a MATLAB code developed by Stefan Schießl.[202]

5.1 Introduction

As shown in the previous chapter, charge transport in polymer-sorted semiconducting SWNT networks is significantly influenced by its composition, i.e., the ensemble of present nanotube species with different diameters and bandgaps in the network. Large energetic differences between the band edges of adjacent SWNTs lead to inferior transport properties for networks with a broad nanotube diameter and thus energy level distribution.[324] Depending on the charge carrier density, parts of the SWNT network do not yet contribute to the transport (large bandgap SWNTs) while nanotubes with smaller bandgaps might act as trapping sites, as indicated previously, e.g., by electroluminescence measurements.[273] Furthermore, the above described behavior of the fabricated SWNT network transistors clearly suggested a non-negligible impact of the intra-nanotube transport and its diameter dependence on the overall network charge transport. This influence might also explain the apparent higher carrier mobilities in large-diameter SWNT networks compared to nanotube films with smaller SWNT diameters.[124,286,294] So far, all previous reports on charge transport in polymer-sorted SWNT films employed nanotube networks with certain distributions of SWNT species which were determined by the available SWNT raw materials and corresponding wrapping polymers. To gain further insights into the transport processes, a more controlled experimental system is desired that allows for an evaluation under optimized and identical conditions. The availability of SWNT dispersions with high semiconducting purity and defined nanotube species distributions enables the preparation of mixed SWNT networks with defined and systematically adjustable mixing ratios of small and large bandgap nanotubes. In contrast to other energetically or spatially disordered systems, such as amorphous organic semiconductors[355–357] or colloidal quantum dot films,[358,359] semiconducting nanotubes with different bandgaps are perfectly miscible without any phase segregation which makes such tailored SWNT networks an interesting model system.

In this chapter, small- and large-diameter SWNTs are polymer-sorted from two different nanotube raw materials and blended in various mixing ratios to form dense SWNT networks with defined compositions by spin-coating.[354] Although in the previous chapter the wrapping polymer was found to play a negligible role with respect to network charge transport, here, the same wrapping polymer PFO-BPy is used with both SWNT raw materials to exclude any possible impact. The mixed nanotube networks are integrated into field-effect transistors in order to systematically examine the effect of a gradually changing SWNT network composition on electron and hole transport. The experimental data are compared to the carrier mobilities of simulated mixed

SWNTs networks based on the above mentioned random resistor network model that only takes the nanotube-nanotube junctions into account. Together with temperature-dependent transport measurements the interplay between the thermally activated inter-nanotube hopping and the band transport within the individual SWNTs and their contribution to the overall charge transport is further clarified.

5.2 Mixed SWNT Dispersions

Semiconducting SWNTs were selectively dispersed and enriched in toluene as demonstrated in Chapter 4 based on established protocols (see Chapter 3.1.1). Here, the wrapping polymer PFO-BPy was combined with CoMoCAT SWNT raw material to obtain a quasi monochiral dispersion of small-diameter (6,5) SWNTs. The same polymer applied to plasma torch nanotubes resulted in dispersions with a range of semiconducting large-diameter SWNTs with small bandgaps as shown above.

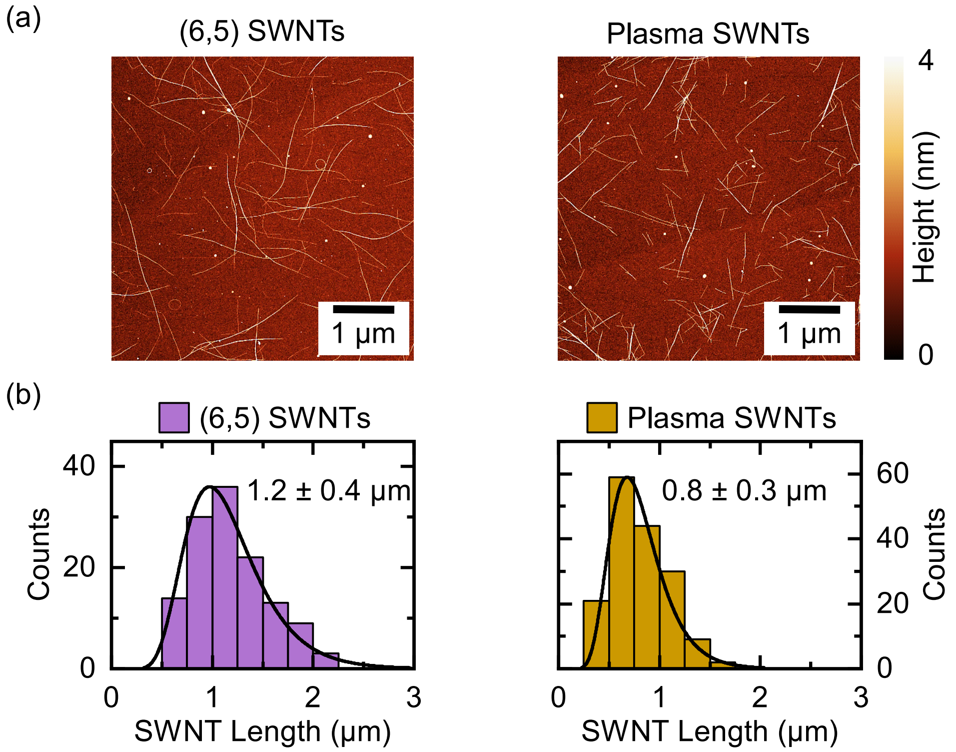

Figure 5.1: (a) Atomic force micrographs of sparse, non-percolating (6,5) and plasma torch SWNT networks. (b) Histograms showing the respective nanotube length distribution including mean length and standard deviation according to a log-normal fit.

To avoid cross-contamination, both stock dispersions were prepared by two different exfoliation methods, namely by shear-force mixing for the (6,5) nanotubes and bath sonication for the plasma torch SWNTs (see Chapter 3.1.1). As reported previously for polymer-wrapped nanotubes, the mean length of dispersed SWNTs is highly affected by the employed exfoliation method[8] and thus the length distribution in both dispersions was determined. As depicted in Figure 5.1 the (6,5) SWNTs were slightly longer (1.2 ± 0.4 µm) than the plasma torch nanotubes (0.8 ± 0.3 µm).

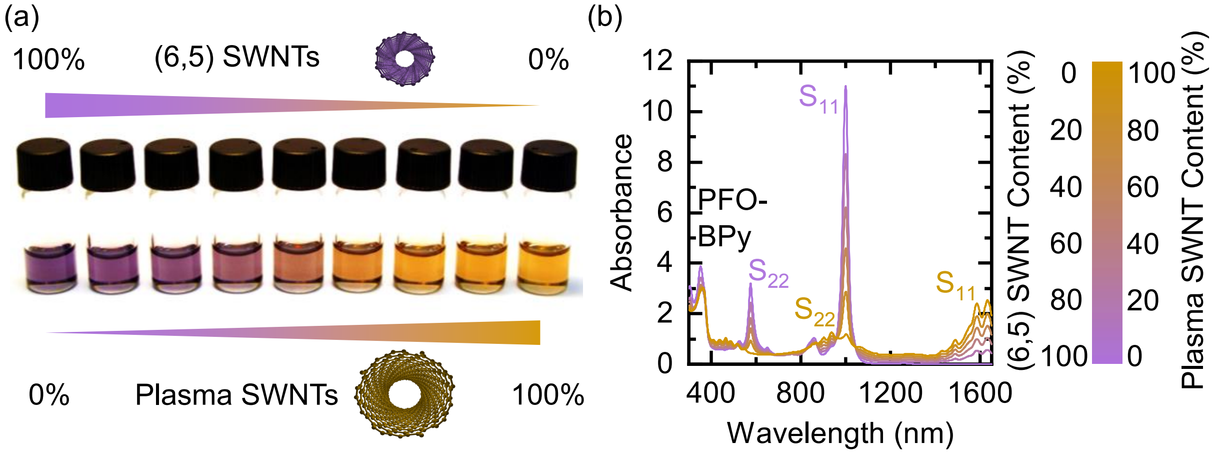

Figure 5.2: (a) Photograph of 4 ml vials filled with mixed (6,5)/plasma torch SWNT dispersions in various mixing ratios. (b) UV-vis-nIR absorption spectra of the mixed SWNT dispersions in steps of 20 % from 100 % (6,5) SWNTs to 100 % plasma torch SWNTs.

Both stock dispersions were mixed volumetrically in 10 % steps from 100 % (6,5) nanotube content to 100 % plasma torch SWNT content to prepare mixed (6,5)/plasma torch SWNT dispersions with defined compositions. A photograph of vials with the different mixed (6,5) SWNT (purple) *vs* plasma torch SWNT (amber) dispersions in various ratios is shown in Figure 5.2a. To enable a representative nanotube mixing and to achieve comparable SWNT concentrations in the two stock dispersions, it was necessary to equalize the integrated and baseline corrected peak absorbance of the characteristic S_{22} transitions of the (6,5) and the plasma torch SWNTs prior to mixing. The UV-vis-nIR absorption spectra of the unblended (6,5) and plasma torch SWNTs as well as of the mixed dispersions are shown in Figure 5.2b. Aside from the characteristic S_{11} and S_{22} transitions of the (6,5) and plasma torch nanotubes the spectra reveal a small and almost constant PFO-BPy absorption peak, which indicates a negligible and comparable polymer concentration in all SWNT dispersions.

5.3 Mixed SWNT Network Compositions

Next, all pure and mixed SWNT dispersions were deposited as nanotube networks with corresponding composition and similar network density. Since sufficient amounts of sorted (6,5) and plasma torch SWNT material were available, spin-coating was chosen as the deposition technique in this chapter. Given the high number of different SWNT dispersions, spin-coating allowed for a parallel and more reproducible SWNT network preparation compared to aerosol-jet printing. The dispersions were directly spin-coated onto photolithographically patterned gold bottom electrodes on top of glass substrates with the same conditions for all mixing ratios (see

Chapter 3.1.3 for details). In contrast to the previous chapter, the gold bottom-contacts were UV/ozone-treated prior to nanotube deposition, as it was found to result in higher network densities for a given SWNT dispersion concentration. As shown by atomic force micrographs of three representative networks in Figure 5.3 the SWNT network density was high ($\geq 40\,\mu m^{-1}$) and homogeneous throughout all SWNT network compositions. In addition, the amount of nanotube bundles was low and comparable for all mixing ratios. Given that the network densities of the different SWNT networks closely resemble each other, this observation clearly corroborates an almost equal nanotube concentration for all mixing ratios. The network density was adjusted to be high to enable a robust transport study that is less sensitive to minor density variations and to reduce current hysteresis in bottom-contact/top-gate FET geometries as discussed in Chapter 4. Furthermore, the difference in mean nanotube length between the (6,5) and plasma torch SWNTs is expected to have a less pronounced impact on the charge carrier mobilities in nanotube networks with a high density. In sparse SWNT network transistors the effective mobility is strongly affected by the average nanotube length as it defines the percolation threshold.[360–362]

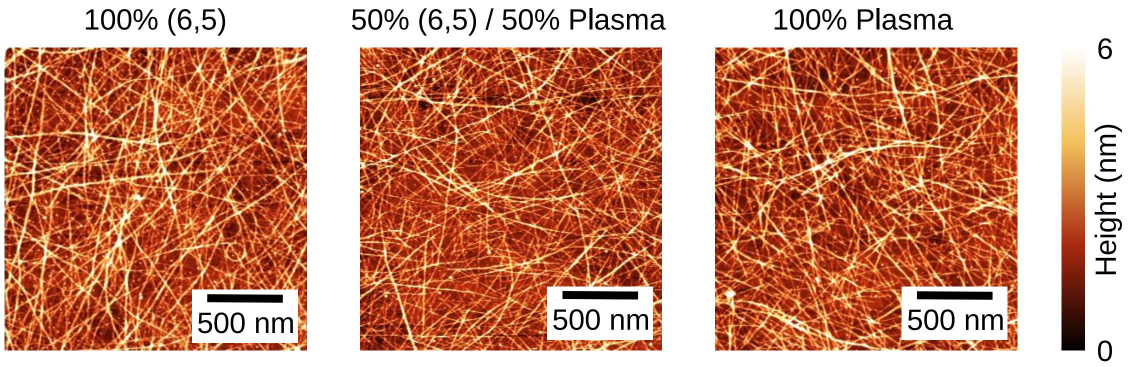

Figure 5.3: Atomic force microscopy images of representative nanotube films with three selected network compositions.

However, the comparable SWNT network morphology cannot guarantee that the nanotube species distribution within the network matches the initial SWNT composition in the dispersions. Thus, all pure and mixed nanotube networks were analyzed by Raman spectroscopy. Due to the much stronger resonance of the 532 nm and the 785 nm laser with both (6,5) and plasma torch SWNTs compared to an excitation at 633 nm, only these were included in this study (see Chapter 3.2.2). For each SWNT network more than 1600 Raman spectra were averaged over an area of $100 \times 100\,\mu m^2$. Almost constant Raman signal intensities over this large scanning area for all samples further confirmed a high homogeneity of the nanotube networks. According to previous reports not only the RBM but also the G-mode of SWNTs exhibit a pronounced diameter dependence and thus a significant difference in the Raman spectra is expected for the different nanotube networks.

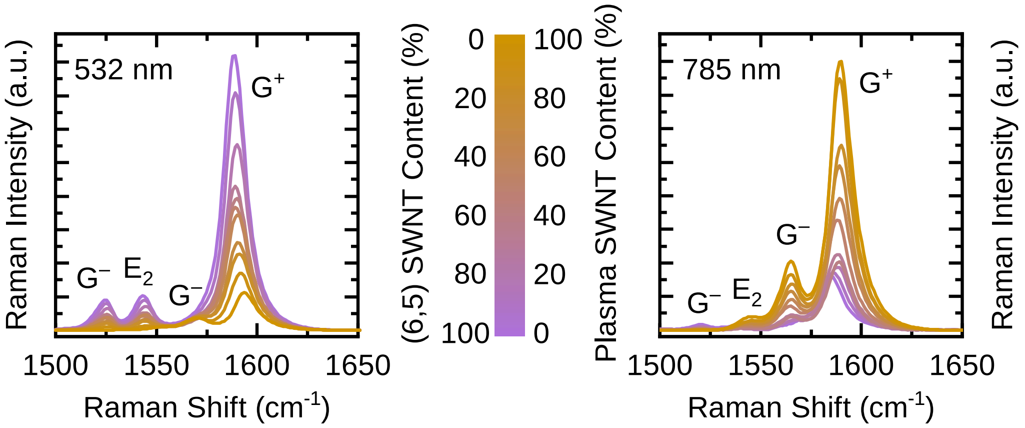

Figure 5.4: Averaged Raman spectra (G-mode region) excited with a 532 nm laser (left) and a 785 nm laser (right) for all nanotube network compositions.

Averaged Raman spectra of all mixed and pure SWNT networks in the G-mode region are shown in Figure 5.4 and feature the characteristic SWNT modes G^-, E_2 and G^+ (see Chapter 2.1.3 for details). For increasing plasma torch SWNT content the intensity of the G^--mode decreases at 1525 cm^{-1} (corresponds to (6,5) nanotubes) and increases at 1570 cm^{-1} (corresponding to large-diameter SWNTs) upon excitation with the 532 nm laser. Simultaneously, the G^+-mode shows a blue-shift from 1589 to 1594 cm^{-1}. When excited at 785 nm, the overall G-mode peak positions red-shift by 5 cm^{-1} although the magnitude of the nanotube diameter-dependent intensity and frequency shifts remains the same. The spectral position of the E_2-mode is not systematically affected by the SWNT network composition. These observations are consistent with previous studies in which the G^--mode was found to show a pronounced SWNT diameter dependence, i.e., higher wavenumbers for larger nanotube diameters while the G^+-mode showed only a weakly pronounced diameter-dependent shift.[363–365] Consequently, these G-mode shifts suggest a gradually changing nanotube diameter distribution and hence a representative mixing of the small-diameter (6,5) SWNTs and the large-diameter plasma torch nanotubes in all networks.

Furthermore, the RBM signals of all mixed and pure SWNT networks were analyzed as shown in Figure 5.5. The RBM spectra of the pure (6,5) and plasma torch SWNT networks (see Figures 5.5a and 5.5c) are in good agreement with the ones presented in Chapter 4.2 and confirm the assumed SWNT diameter ranges, namely 0.76 nm for the (6,5) SWNTs and 1.17–1.55 nm for the plasma torch nanotubes. Furthermore, the spectrum of the (6,5) SWNT network exhibits again a weakly pronounced RBM peak at 238 cm^{-1} upon excitation at 785 nm, implying the presence of a medium-diameter minority SWNT species. Yet, as this nanotube species could not be detected by UV-vis-nIR absorption measurements, its concentration must be very low and its impact on the overall network properties can be neglected. At first glance, the RBM spectra of all mixing ratios shown in Figures 5.5b and 5.5d suggest a gradually changing SWNT network composition with the assumed (6,5)/plasma torch SWNT mixing ratio, as deduced from the respective RBM intensities. As pointed out in Chapter 4.2, Raman measurements cannot provide a quantitative measure for the absolute concentration of a given SWNT species due to the different scattering cross sections. Nevertheless, assuming a comparable and homogeneous network density for all mixing ratios, the specific Raman intensities of the (6,5) SWNTs *vs* the plasma torch SWNTs should scale with the abundance of the respective nanotube species in each network.

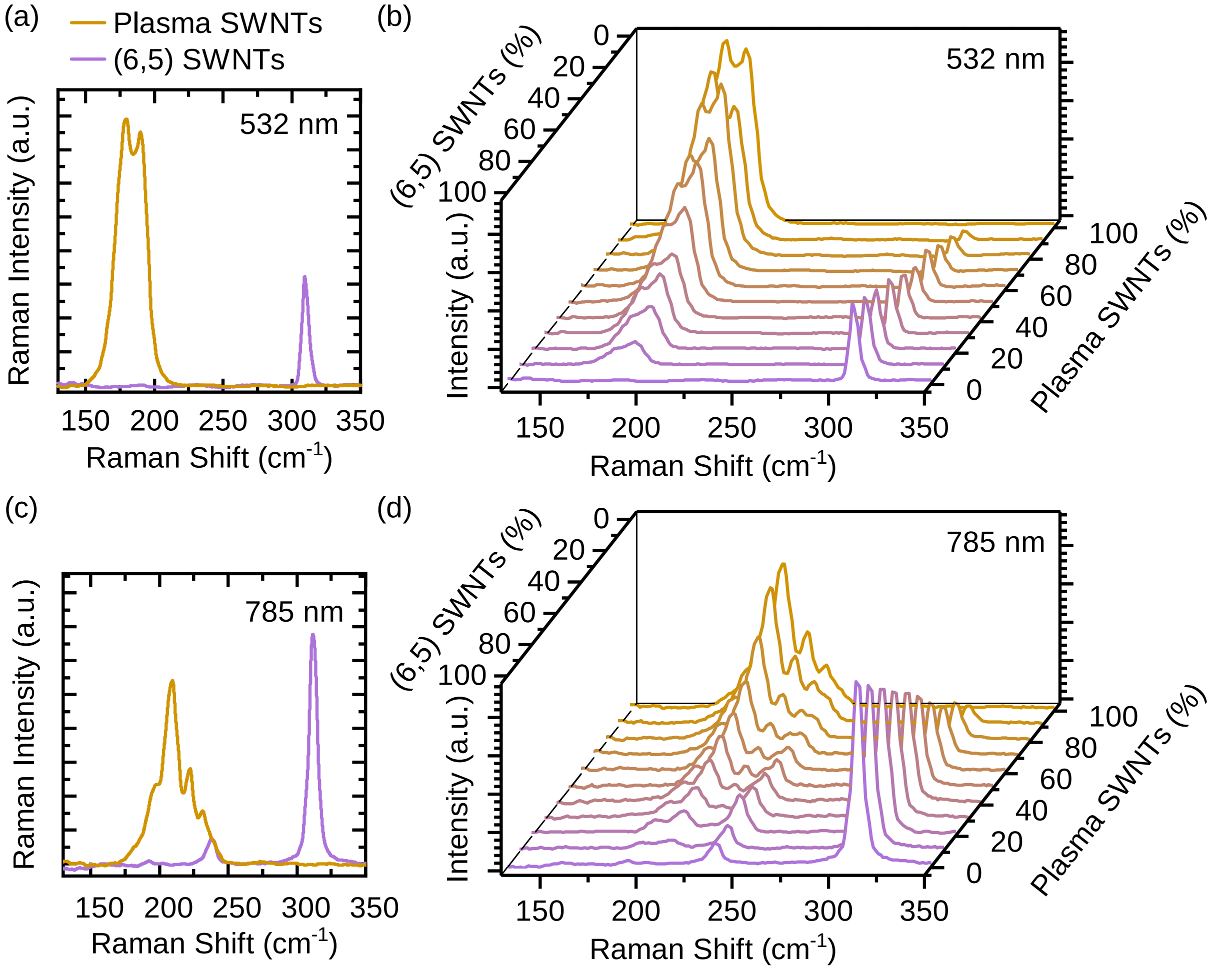

Figure 5.5: Averaged Raman RBM spectra of pure (6,5) and plasma torch SWNT networks excited at 532 nm (a) and 785 nm (c). RBM signals for all SWNT mixing ratios excited with laser wavelengths of 532 nm (b) and 785 nm (d).

To enable a more detailed analysis of the relative abundance of (6,5) *vs* plasma torch nanotubes in all SWNT networks the separate RBM peak areas corresponding to the (6,5) SWNTs ($A_{(6,5)}$) and the plasma torch SWNTs (A_{Plasma}) were compared. For all mixing ratios, the peak areas were determined by fitting with 1 to 4 linearly combined Lorentzian functions. The resulting relative RBM peak areas of the (6,5) and plasma torch SWNTs divided by the total peak area ($A_{(6,5)} + A_{\text{Plasma}}$) are depicted in Figure 5.6a. For both lasers the relative RBM peak areas change monotonously with changing network composition. Still, the variation in peak area is more imbalanced for the 532 nm laser, for which already small amounts of plasma torch nanotubes cause a steep increase in respective peak area. Upon excitation at 785 nm the peak area variation with changing network composition is more balanced. The different behavior could be explained by differences in the Raman RBM cross sections of the (6,5) *vs* the plasma torch SWNTs, which depend also on the excitation wavelength.

Assuming a linear relation between the RBM peak area A and the content of a given SWNT species X, the RBM peak areas of the (6,5) and the plasma torch SWNTs can be expressed by Equations 5.1 and 5.2

$$A_{(6,5)} = \sigma_{(6,5)} \cdot X_{(6,5)} \cdot \gamma_{\text{sample}} \tag{5.1}$$

$$A_{\text{Plasma}} = \sigma_{\text{Plasma}} \cdot X_{\text{Plasma}} \cdot \gamma_{\text{sample}} \tag{5.2}$$

with the respective Raman RBM cross section σ and a sample-specific variation in SWNT network density γ_{sample}. Consequently, the corresponding relative RBM peak areas can be described as follows:

$$\frac{A_{(6,5)}}{A_{(6,5)} + A_{\text{Plasma}}} = \frac{\sigma_{(6,5)} \cdot X_{(6,5)}}{\sigma_{(6,5)} \cdot X_{(6,5)} + \sigma_{\text{Plasma}} \cdot X_{\text{Plasma}}} \tag{5.3}$$

$$\frac{A_{\text{Plasma}}}{A_{(6,5)} + A_{\text{Plasma}}} = \frac{\sigma_{\text{Plasma}} \cdot X_{\text{Plasma}}}{\sigma_{(6,5)} \cdot X_{(6,5)} + \sigma_{\text{Plasma}} \cdot X_{\text{Plasma}}} \tag{5.4}$$

Next, the expressions 5.3 and 5.4 are linearized:

$$\left(\frac{A_{(6,5)}}{A_{(6,5)} + A_{\text{Plasma}}}\right)^{-1} = \frac{\sigma_{\text{Plasma}}}{\sigma_{(6,5)}} \cdot \frac{1}{X_{(6,5)}} - \frac{\sigma_{\text{Plasma}}}{\sigma_{(6,5)}} + 1 \tag{5.5}$$

$$\left(\frac{A_{\text{Plasma}}}{A_{(6,5)} + A_{\text{Plasma}}}\right)^{-1} = \frac{\sigma_{(6,5)}}{\sigma_{\text{Plasma}}} \cdot \frac{X_{(6,5)}}{X_{\text{Plasma}}} + 1 \tag{5.6}$$

For each excitation energy, the RBM cross section ratios of the (6,5) *vs* the plasma torch SWNTs can be obtained by linear fitting when Equation 5.5 is plotted against $1/X_{(6,5)}$ or Equation 5.6 against $X_{(6,5)}/X_{\text{Plasma}}$ as shown in Figure 5.6b. Apparently, the RBM cross section of the (6,5) SWNTs is about one order of magnitude smaller than that of the plasma torch SWNTs when the networks are excited at 532 nm. Upon excitation with the 785 nm laser, the plasma torch SWNTs appear to be twice as Raman active as the small-diameter (6,5) SWNTs, although the RBM cross sections are more balanced here. These values are in agreement with previous studies, that reported a pronounced chiral angle and mod dependence of the specific Raman RBM cross section for a given SWNT species.[365,366] The mod 1 SWNT species were found to exhibit much lower specific RBM intensities than mod 2 species, especially for SWNTs with smaller chiral angles (<25°). Interestingly, the used plasma torch SWNTs mixture consists of several mod 2 nanotube species with smaller chiral angles compared to the mod 1 (6,5) SWNTs.

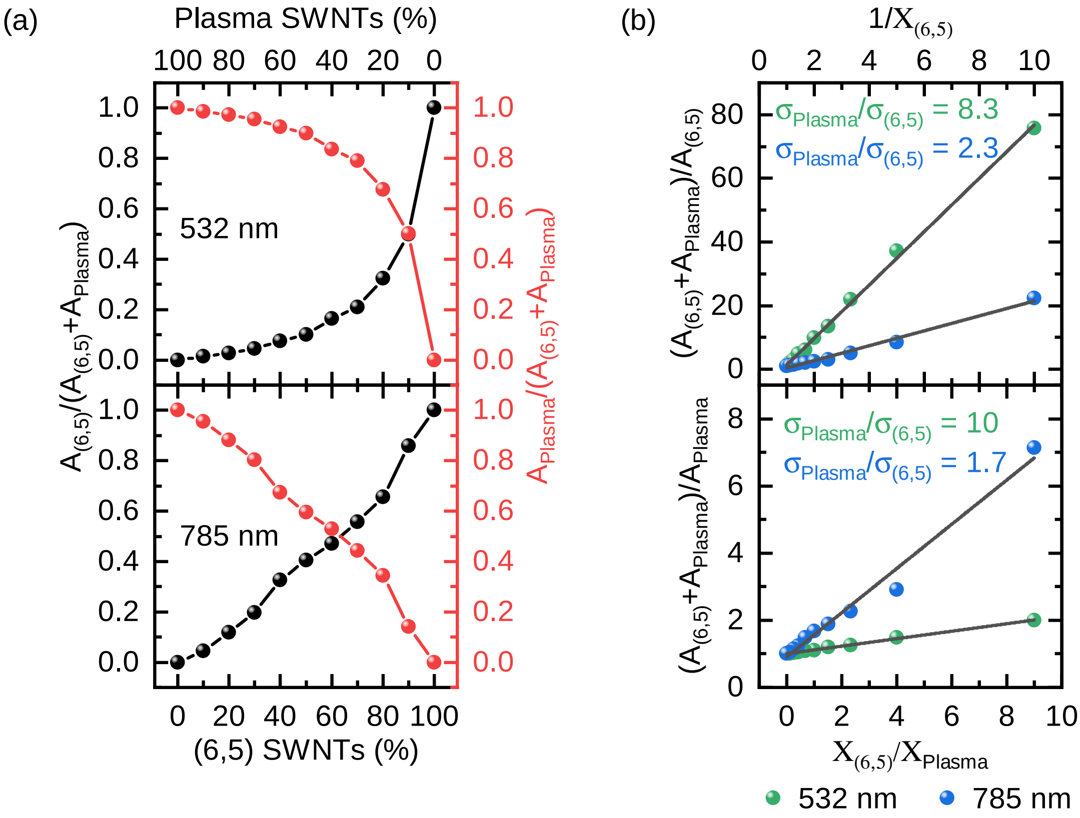

Figure 5.6: (a) Relative RBM peak areas of (6,5) nanotubes (black) and plasma torch SWNTs (red) for all network compositions upon excitation at 532 and 785 nm. (b) Linear plots of the inverted relative RBM peak areas of the (6,5) nanotubes *vs* $1/X_{(6,5)}$ (top) and of the plasma torch nanotubes *vs* $X_{(6,5)}/X_{\text{Plasma}}$ (bottom). Solid lines are fits for the extraction of the relative RBM cross sections of the (6,5) and plasma torch SWNTs.

Additionally, the resonance of both lasers might be stronger with the plasma torch SWNTs than with the (6,5) nanotubes. The 532 nm (2.33 eV) laser excites the S_{22} transition of the (6,5) nanotubes (2.19 eV) and the S_{33} transitions of the plasma torch SWNT ensemble (2.3–2.8 eV). The 785 nm laser (1.58 eV) excites the S_{11} transition (1.27 eV) as well as the phonon sideband of the (6,5) SWNTs and the S_{22} transitions of the plasma torch mixture (1.2–1.5 eV). Commonly, a resonance window of ±0.2 eV for G-Modes and of ±0.1 eV for RBM excitations is assumed,[364,365] which is consistent with the observed stronger resonance of the plasma torch SWNTs compared to the (6,5) SWNTs.

In summary, the RBM and G-mode signals change gradually with the proposed SWNT mixing ratios and reveal that all nanotube network compositions resemble the initial SWNT mixtures in the corresponding nanotube dispersions. Together with the AFM measurements, this suggests a comparable and homogeneous SWNT network density for all mixing ratios and representative SWNT network compositions can be assumed. Thus, the mixed nanotube networks fulfill the requirements for a meaningful charge transport analysis which is presented in the following section 5.4.

5.4 Device Performance of Mixed SWNT Network FETs

Bottom-contact/top-gate FETs with a gFPP electrode layout (see Figure 3.2a) were fabricated with the same device structure as described above in Chapter 4.3, Figures 4.5b and 4.5c using pure and mixed networks. Figure 5.7 shows the transfer characteristics of all pure and mixed SWNT network FETs at small source-drain voltage ($V_{\mathrm{DS}} = -0.1$ V). The current-voltage curves reveal balanced ambipolar transport with high on/off current ratios of 10^6 as well as low hysteresis and hence, nearly ideal transport properties without the presence of significant extrinsic transport limitations, such as charge traps. For both electron and hole conduction the maximum on-currents increase monotonously with increasing plasma torch SWNT content. This trend leads to four times higher drain-currents for the pure large-diameter plasma torch network compared to the small-diameter (6,5) SWNTs. Considering the significantly smaller average SWNT length of the plasma torch nanotubes compared to the (6,5) SWNTs, while both networks have a comparable network density, this observation might be surprising. Yet, it is in agreement with the SWNT diameter dependence ($\propto d^2$) of the intra-nanotube charge carrier mobility which was found to have an impact in SWNT networks as discussed in Chapter 4.[158,159,324]

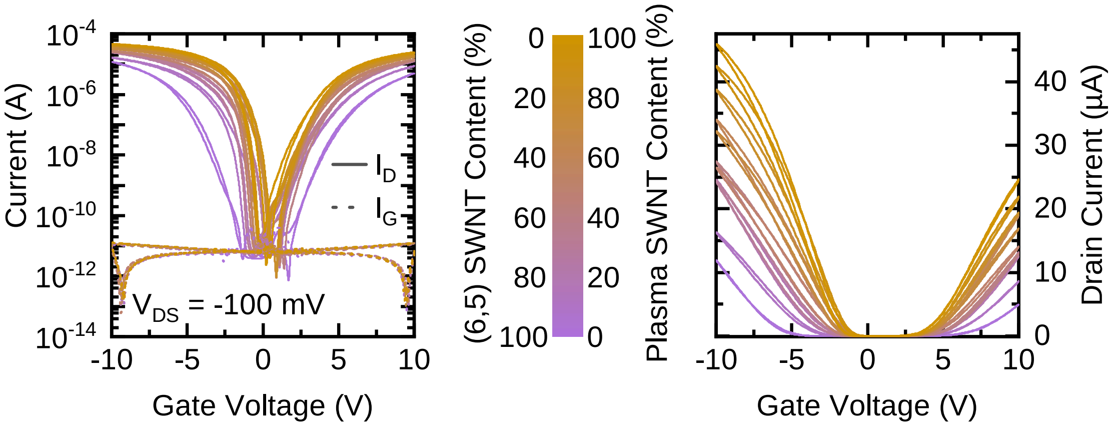

Figure 5.7: Transfer characteristics (forward and reverse V_{G}-sweeps at $V_{\mathrm{DS}} = -0.1$ V) of FETs with all SWNT network compositions in logarithmic (left) and linear scale (right).

The hole currents for all SWNT networks were twice as high compared to the electron currents. This slight imbalance can be explained by UV/ozone treatment of the gold bottom-contacts directly before the SWNT depositions, as it leads to a larger work function of the electrodes and thus to smaller (larger) contact resistances for holes (electrons).[367,368]

The output curves shown in Figure 5.8 confirm the significantly higher on-currents (by one order of magnitude in the saturation regime) for the pure plasma torch SWNT network compared to the (6,5) SWNTs and somewhat higher currents for holes than for electrons.

Furthermore, the onset voltages extracted from the respective forward sweep of the transfer characteristics presented in Figure 5.7 exhibit a pronounced SWNT network composition

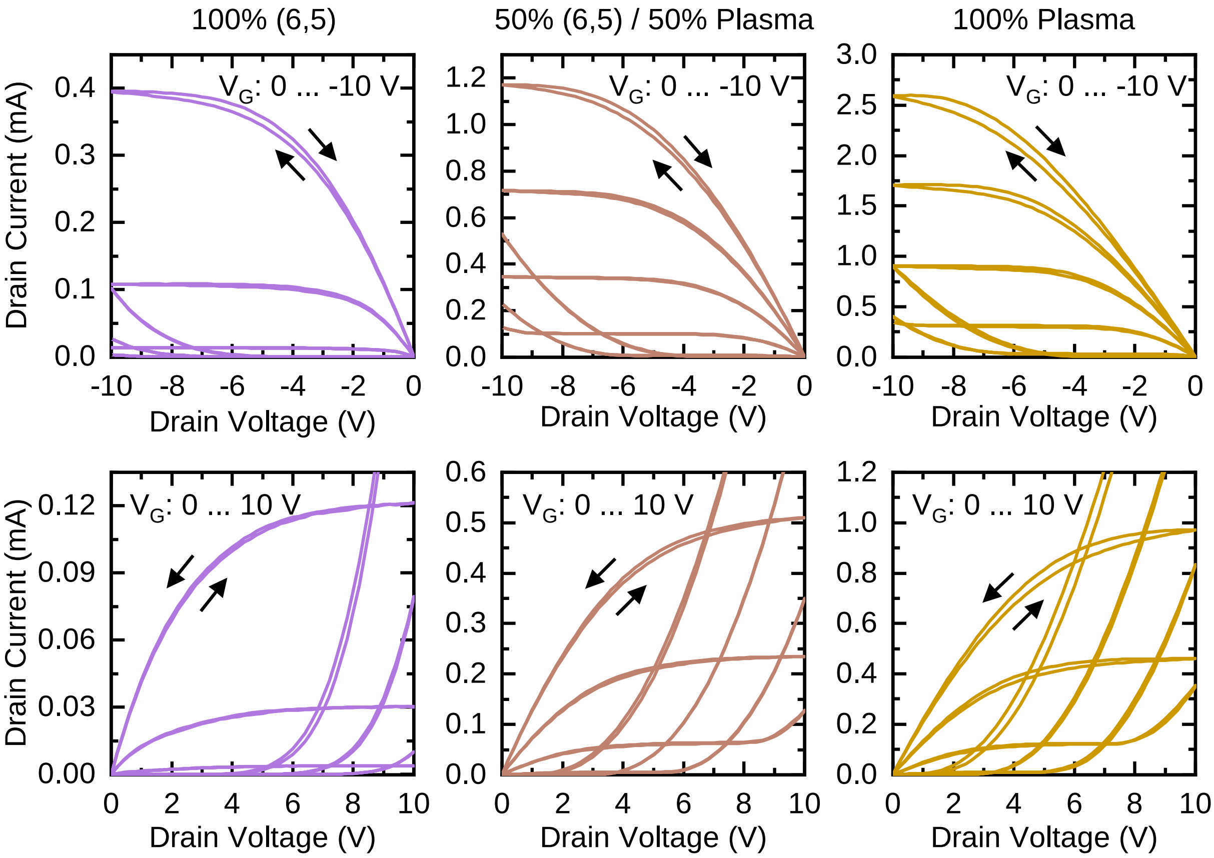

Figure 5.8: Output characteristics of SWNT network FETs with three representative network compositions for negative (top row) and positive (bottom row) applied voltages.

dependence as shown in Figure 5.9a. The decrease in onset voltage values with increasing contents of the small-bandgap plasma torch SWNTs is consistent with the correlation between the mean bandgap in a given SWNT network and its onset voltage (see Chapter 4.3).[324] Remarkably, the shift of the onset voltages with changing network composition is not gradual, but the ON-voltage decreases significantly already at small plasma torch SWNT contents of 10 % and reaches the onset values of the pure plasma torch network at 30 %. Considering the overall high SWNT network density, this behavior might be explained by percolation paths of only plasma torch SWNTs, that span the transistor channel and switch on at lower V_G compared to the (6,5) SWNTs. An equivalent observation was previously made for network FETs, in which a small number of narrow-bandgap SWNTs showed a stronger electroluminescence response implying a larger current share compared to the large-bandgap SWNTs, that formed the major part of the network.[273]

In addition, a small current hysteresis (quantified as difference in onset voltage between forward and reverse sweep) can be observed for both charge carriers that changes characteristically with the nanotube network composition as shown in Figure 5.9b. For the pure (6,5) SWNT network there is basically no hysteresis, whereas it increases with growing plasma torch SWNT contents up to a maximum value for mixed networks with equal amounts of (6,5) and plasma torch

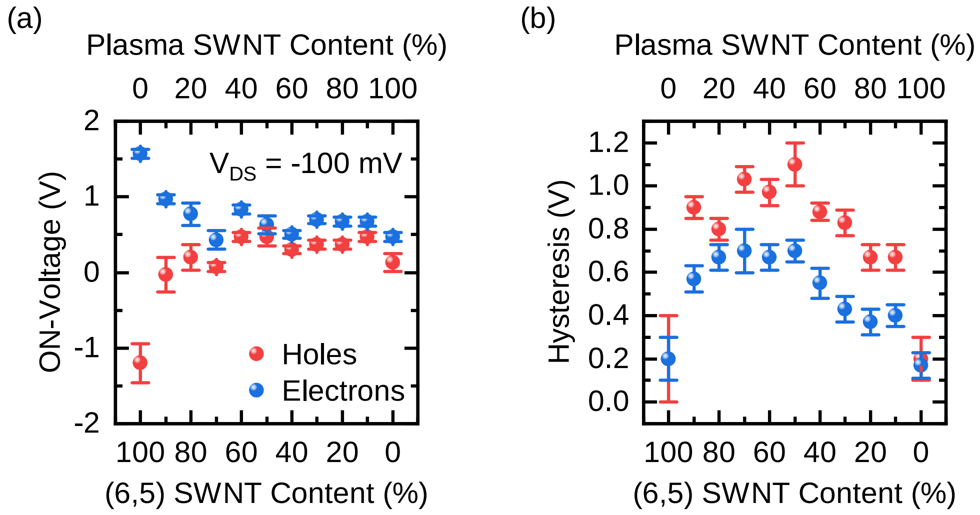

Figure 5.9: (a) Onset-voltages (extracted from the forward sweep) and (b) hysteresis (defined as difference between the onset voltages of forward and reverse sweep) of FETs with all SWNT network compositions for electron and hole transport. Error bars indicate standard deviations for three analogous devices.

nanotubes. When the plasma torch SWNT content is further increased, the current hysteresis decreases again with the (6,5) nanotube content until it nearly disappears for the pure plasma torch network. This observation might be explained by the rather large band edge energy offset of about 220 meV compared to kT between the plasma torch and the (6,5) SWNTs, possibly leading to charge trapping within the mixed SWNT networks. In principle, individually distributed narrow-bandgap plasma torch SWNTs could be seen as trapping sites in all mixed networks when located within a percolation path composed of mainly (6,5) nanotubes. The chance for this scenario is highest for a (6,5):plasma torch SWNT mixing ratio of 1:1.

Given the imbalanced hole and electron currents for all SWNT network FETs and considering the above reported differences with respect to charge injection between the plasma torch and (6,5) SWNTs, a detailed contact resistance analysis was performed. The utilized gFPP device structure allowed for the direct measurement of the contact resistances (see Chapter 4.3) for FETs with all network compositions as shown in Figure 5.10. The gate voltage dependence (Figure 5.10a) reveals a pronounced modulation of the contact resistances, i.e., decreasing R_C values with increasing V_G for all SWNT network compositions, as also seen in the previous chapter. Note, the dashed lines indicate again V_G ranges, for which the calculated contact resistances are unreliable, as the gFPP measurements lead to meaningful results in the linear regime only.

When comparing the minimum R_C values extracted at gate voltages of ±10 V for all SWNT network FETs as shown in Figure 5.10b, a pronounced network composition dependence is apparent. In agreement with previous reports, the contact resistances increase monotonously with increasing (6,5) SWNT contents culminating in resistance values that are one order of magnitude higher for the pure (6,5) SWNTs networks than for the pure plasma torch networks.[124,324]

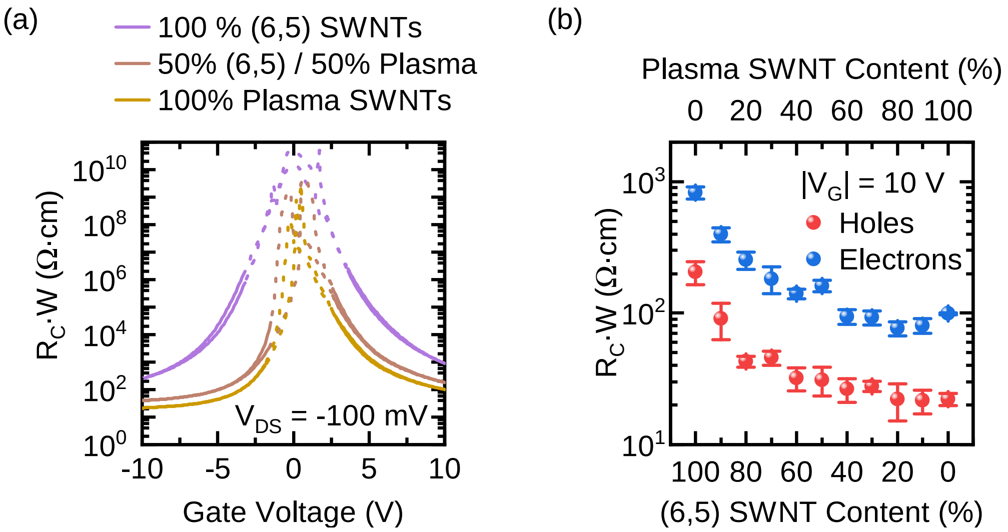

Figure 5.10: Width-normalized contact resistances: (a) gate voltage dependence for FETs with three selected network compositions and (b) minimum R_C vales for all network compositions extracted at the maximum gate voltage for electron and hole transport. Error bars indicate standard deviations for three analogous devices.

For the pure plasma torch SWNTs the minium R_C values were 100 Ω cm for electrons and 20 Ω cm for holes, whereas the pure (6,5) SWNTs showed minimum contact resistance values of 820 Ω cm for electrons and 210 Ω cm for holes. Also for the other SWNT mixing ratios, the R_C values were about four times times lower for hole injection than for electron injection, which corroborates the proposed impact of the UV/ozone electrode treatment and explains the overall lower electron currents. As illustrated in Chapter 4.4, a contact resistance correction of the effective charge carrier mobilities (μ_{eff}) is essential for an undistorted analysis of the SWNT network composition-dependent charge transport, especially when considering the varying R_C values for the different mixing ratios.

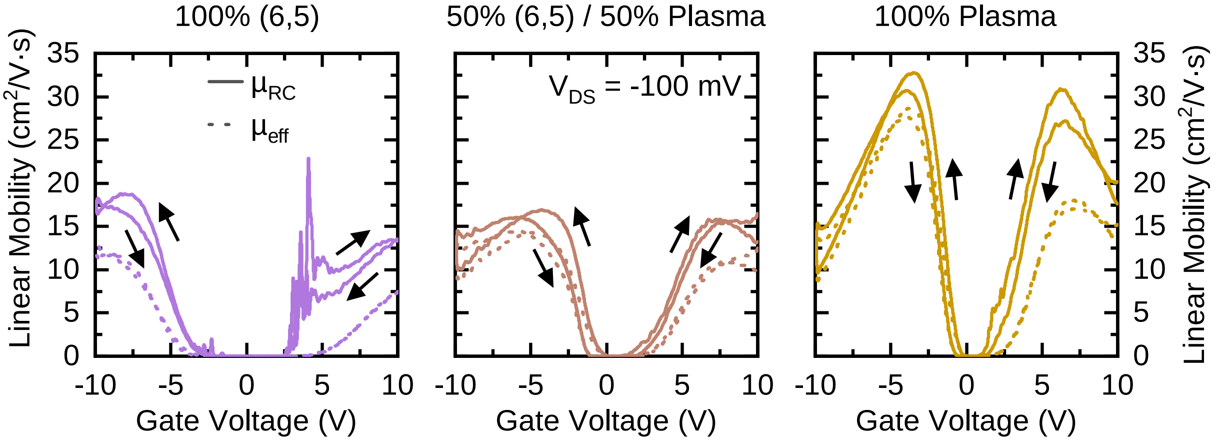

Figure 5.11: Gate voltage-dependent comparison between the apparent linear charge carrier mobility with contact effects (μ_{eff}) and the R_C-corrected linear mobility (μ_{RC}) for three representative SWNT network FETs.

Figure 5.11 compares μ_{eff} with the R_{C}-corrected carrier mobilities (μ_{RC}) of three selected SWNT network transistors over the whole gate voltage range and reveals up to 80 % higher μ_{RC} values than for the uncorrected mobilities. Hence, all reported charge carrier mobilities in this chapter are contact resistance-corrected. The gate voltage dependence of the carrier mobilities further reveals, that all SWNT network FETs (containing both mixed and pure (6,5) and plasma torch SWNTs) reach a mobility maximum for hole and electron transport within the V_{G}-range of ±10 V. This specific behavior is typically observed for SWNT networks and individual nanotubes. At high charge carrier densities, the first van Hove singularities of the SWNTs are filled until the second subband is reached, resulting in interband phonon scattering and consequently decreasing carrier mobilities for higher gate voltages.[153,156,158,159] Thus, the SWNT network composition-dependent linear carrier mobilities in Figure 5.12 were extracted at the respective maximum of the mobility curve for all network types, disregarding the artifact in the μ_{RC}-plot for the pure (6,5) nanotubes.

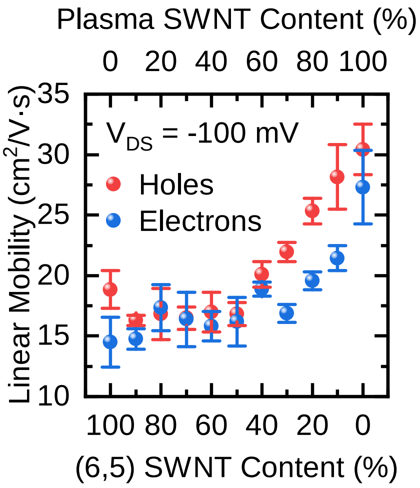

Figure 5.12: Contact resistance-corrected peak hole and electron mobilities for FETs with different network compositions. Error bars indicate standard deviations of three analogous devices.

The extracted, contact resistance-corrected electron and hole mobilities are quite balanced. In agreement with the observed trends for the on-currents, the charge carrier mobilities increase with increasing plasma torch SWNT content. Interestingly, this composition-dependent increase in carrier mobility is clearly discontinuous. For (6,5) SWNT contents of ≥50 %, the carrier mobilities remain nearly unchanged when the plasma torch content is increased. Yet, as soon as the large-diameter SWNTs represent the major component of the network (more than 50 %) the mobilities increase monotonously with their abundance. This composition dependence of the carrier mobility is rather unexpected and does not follow any of the two proposed simple models for charge transport in mixed SWNT networks which are outlined in the next section 5.5.

5.5 Modeling Charge Transport in Mixed SWNT Networks

Charge transport in semiconducting SWNT networks is considered to consist of two primary processes, namely the inter-nanotube transport across the junctions and the intra-nanotube transport along the individual nanotubes. However, so far a holistic model that combines both sides for the description of transport in SWNT networks is still missing. Thus, the two extreme cases, i.e., intra-nanotube transport only *vs* inter-nanotube transport only are compared here.

To model the composition dependence of the carrier mobility when just the nanotube-nanotube junctions are taken into consideration, SWNT networks with compositions equal to the experimental mixing ratios were simulated based on the random resistor model introduced in Chapter 4.6.[202] Using the same input parameters, such as energetic disorder, SWNT length, etc. and SWNT species distributions in the pure (6,5) and plasma torch mixtures as listed in Table 4.2, two-dimensional stick networks were modeled for all mixing ratios (see Figure 5.13a).

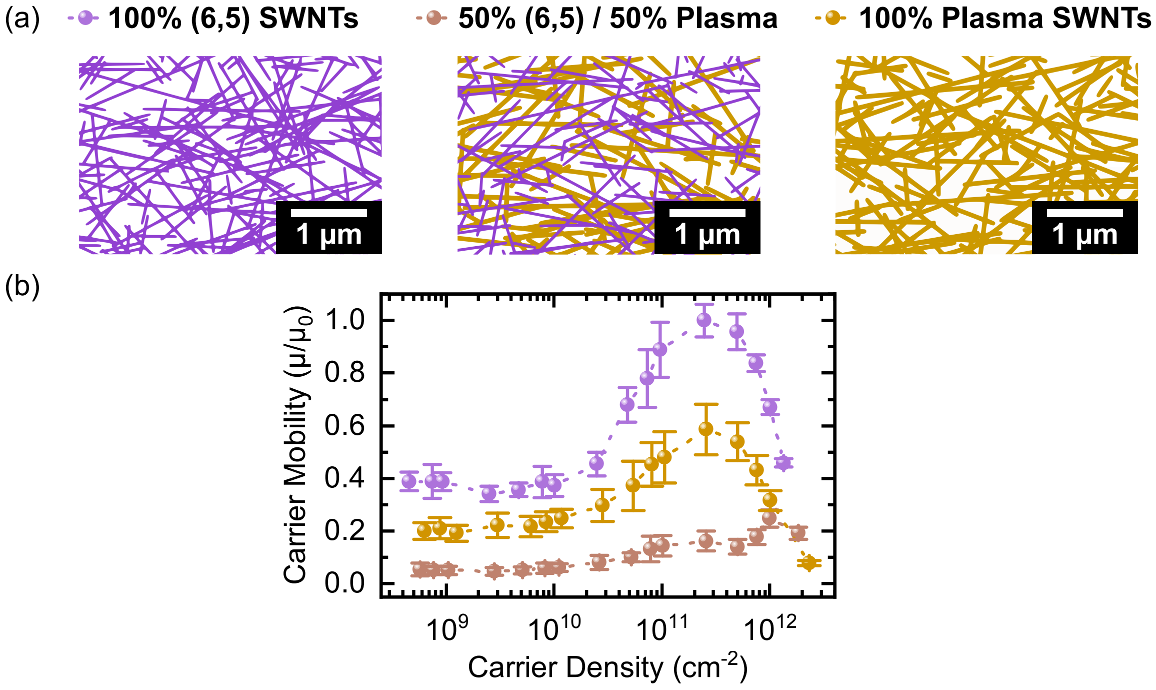

Figure 5.13: (a) Simulated two-dimensional stick networks with analogous composition but lower network density (7 µm^{-1}) compared to the experimental SWNT networks illustrating the respective content of (6,5) nanotubes (purple) and plasma torch SWNTs (amber) for three selected mixing ratios. (b) Charge carrier density-dependent network mobilities of these simulated networks (normalized to the maximum mobility value of the pure (6,5) SWNT network). Dotted lines represent guides to the eye. Five equivalent networks were averaged per network composition, the error bars indicate the respective standard deviation.

As described in Chapter 2.2.2, the charge carrier density-dependent mobilities were calculated for these networks based on a Miller-Abrahams hopping approach to mimic the inter-nanotube charge transfer, while neglecting the transport along the individual nanotubes (see Figure 5.13b).

For all simulated SWNT networks the extracted normalized mobilities (averaged over five equivalently simulated networks) exceed their maximum between carrier densities of 2×10^{11} and $1 \times 10^{12}\,\mathrm{cm}^{-2}$, which is consistent with the gate voltage dependence of the experimental mobilities. Figure 5.14a depicts the extracted simulated peak mobilities (black) for all mixing ratios, revealing a pronounced mobility decrease with growing plasma torch SWNT contents until a minimum is reached for parity mixing of (6,5) *vs* plasma torch nanotubes. As soon as the plasma torch SWNTs dominate the network composition, the network mobilities increase again with increasing plasma torch content up to the peak mobility of the unblended plasma torch SWNT network. The resulting asymmetric dip in the composition-dependent peak mobility plot is reminiscent of the behavior of disordered organic host-guest systems (both in simulations and in experiments).[355–357] These systems consist of guest species with a narrow bandgap within a matrix of host molecules with a large bandgap. Here, the guest molecules act as trapping sites resulting in an overall mobility drop when their content is increased until they form the major part of the system. Above this point, the mobility increases again with the concentration of the guest molecules as they now form their own percolating transport paths and become the host system.

When comparing the network composition-dependent trends of the simulated mobilities and the experimental SWNT network mobilities presented in Figure 5.12, it becomes clear that they barely correlate with each other. In contrast to the experimental observations, the simulated network mobility for the pure plasma torch network is significantly lower than for the pure (6,5) SWNTs. As illustrated above, the rather narrow band edge energy distribution within the plasma torch network (~80 meV) still results in a less efficient charge carrier hopping between adjacent SWNTs and consequently in lower simulated peak mobilities than for the monochiral (6,5) nanotubes.[324] Again, the carrier mobility along the individual nanotubes and its quadratic dependence on the SWNT diameter is not considered in this transport model.[158,159]

A fundamentally different approach to describe the composition-dependent carrier mobilities in the studied SWNT network transistors would be a model that treats mixed SWNT networks as composites consisting of nanotubes with different intra-nanotube mobilities while disregarding the inter-nanotube transport through the energetic landscape of the SWNT film. Most commonly, material properties of composite materials, such as elastic modulus or thermal conductivity, are described by a so-called 'rule of mixtures' dependence.[369] In the simplest case, the material property of the composite can be predicted by the weighted average of the individual component properties depending linearly on their relative abundance. Applied to the mixed SWNT networks this dependence would lead to a linear increase in carrier mobility from the pure (6,5) nanotube network ($\sim 15\,\mathrm{cm}^2\,\mathrm{V}^{-1}\,\mathrm{s}^{-1}$) to the pure plasma torch SWNT network ($\sim 30\,\mathrm{cm}^2\,\mathrm{V}^{-1}\,\mathrm{s}^{-1}$). Clearly, this approach also does not provide a qualitative fit with the experimental data. As concluded in Chapter 4, both the charge transport across the nanotube-nanotube junctions and the intra-nanotube transport within the individual SWNTs seem to be relevant for the overall nanotube network mobility.

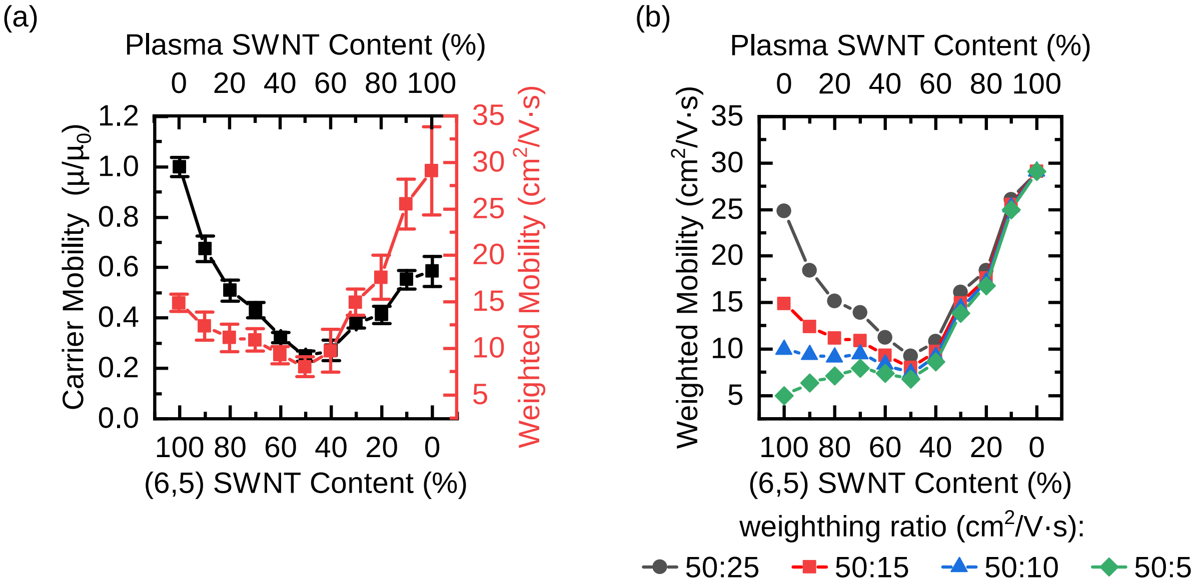

Figure 5.14: (a) Simulated composition-dependent charge carrier mobilities for all mixing ratios corresponding to the experimental SWNT networks without any intra-nanotube transport contribution (black) and weighted by a mobility weighting factor of 50:15 cm^2 V^{-1} s^{-1} for plasma torch *vs* (6,5) SWNTs (red). (b) Composition-dependent and weighted simulated mobilities for different plasma torch *vs* (6,5) SWNT weighting ratios. Error bars represent standard deviations for five equivalently simulated SWNT networks. Solid lines represent guides to the eye.

Hence, to combine both sides, a mobility weighting factor is introduced to modify the simulated network mobilities. Given the quadratic diameter dependence of the intra-nanotube mobility, this factor was chosen based on the difference in squared average SWNT diameters of the pure (6,5) SWNT *vs* the plasma torch nanotube networks and the magnitude of their experimental network mobility values. Assuming a mean diameter of 0.76 nm for the (6,5) SWNTs and of 1.36 nm for the plasma torch network resulted in a weighting factor of 50:15 cm^2 V^{-1} s^{-1} to modify the simulated mobilities as shown by the red squares in Figure 5.14a. The thus obtained weighted mobilities give a much better fit to the network composition dependence of the experimental carrier mobility data. For the (6,5) SWNT contents between 100 % and 50 % a significant discrepancy remains between the model and the experiment. The random resistor network model relies on several simplifications that might result in quantitative mobility deviations such as a fixed hopping prefactor for all nanotube species and the inclusion of the first SWNT van Hove singularities only.[202] Furthermore, a uniform input SWNT length distribution of 1.5 ± 0.9 µm for all SWNT species was utilized for the simulations, which is not consistent with the experimentally observed nanotube lengths. As shown in Figure 5.14b a better fit of the weighted mobilities to the experimental data can be achieved for lower mobility weights of the (6,5) SWNTs.

Overall, the similarity between the network composition dependence of the experimental mobility values and the simulated weighted mobilities provides further evidence that charge transport in mixed SWNT networks should be seen as superposition of intra- and inter-nanotube processes. Based on this interplay, the nearly constant experimental charge carrier mobilities for plasma torch SWNT contents of ≤50 % shown in Figure 5.14 can be explained. In this mixing range, the share of large-diameter SWNTs with higher intra-nanotube mobilities increases with increasing plasma torch nanotube content, whereas additional energy barriers are formed at the junctions between (6,5) and plasma torch SWNTs. As soon as the plasma torch SWNT content exceeds 50 % the mean intra-nanotube mobility increases further with plasma torch nanotube share, while the energetic disorder at the SWNT-SWNT junctions decreases, resulting in monotonously increasing network mobilities.

5.6 Temperature-dependent Charge Transport

To further confirm that the overall SWNT network charge transport depends on the superposition of intra- and inter-nanotube transport, temperature-dependent current-voltage measurements were performed on FETs with selected SWNT network compositions. Transfer characteristics measured at temperatures between 60 and 300 K of a pure (6,5) SWNT network, of a 50 %/50 % mixed SWNT network and of a pure plasma torch SWNT network are presented in Figure 5.15.

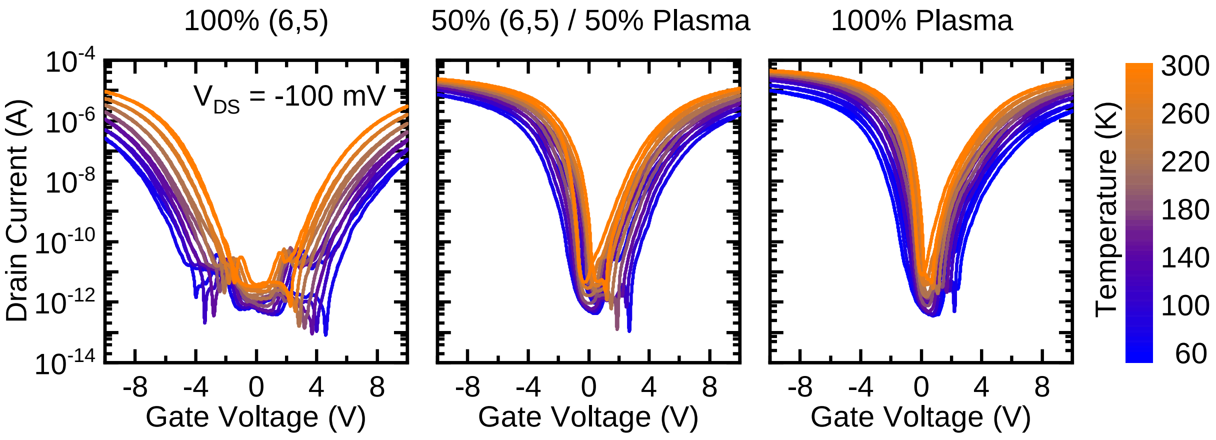

Figure 5.15: Transfer characteristic (forward and reverse gate voltage sweeps at $V_{\mathrm{DS}} = -0.1\,\mathrm{V}$) measured in 20 K steps at temperatures between 60 and 300 K (for clarity, only every other curve shown) for FETs with three selected SWNT network compositons.

Similar to the observations in Chapter 4.4, the ambipolarity, low hysteresis and high on/off current ratios of all three devices persisted over the full temperature range. All transistors exhibit the characteristic thermally activated transport with decreasing on-currents and increasing onset voltages upon cooling despite some significant disparities between the different network compositions. In good agreement with the results in Chapter 4.4 the drop in on-current with decreasing temperature is more pronounced for the monochiral (6,5) nanotubes (by a factor of 30–60) than for the 50 %/50 % mixed and the pure plasma torch SWNT networks (less than one order of magnitude) which resemble each other.

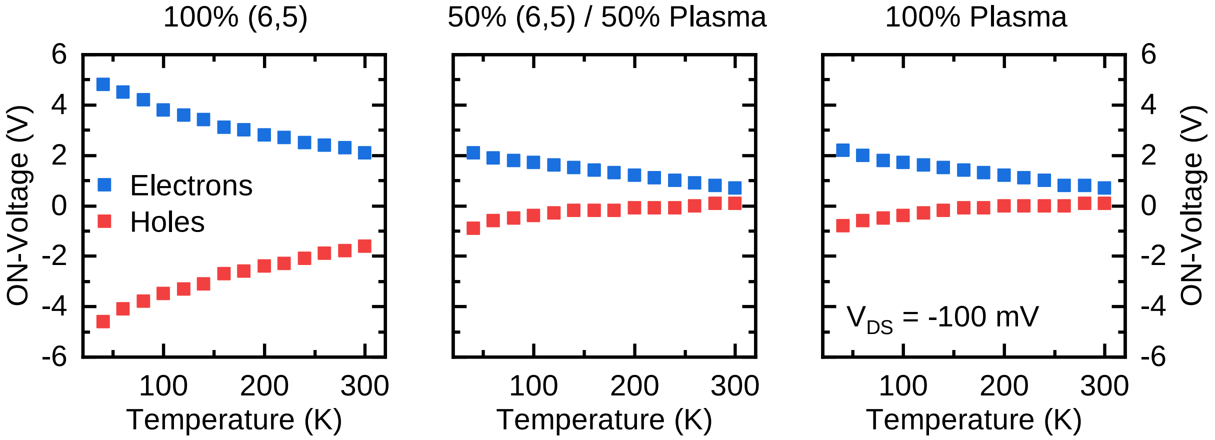

Figure 5.16: Temperature-dependent onset voltages (for electron and hole transport, extracted at $V_{DS} = -0.1$ V) for FETs with three selected SWNT network compositions.

The same applies to the onset voltage shift to higher voltages at lower temperatures, which is larger for the small-diameter (6,5) SWNTs (about 3 V) compared to the mixed and the 100 % plasma torch network (up to 1.5 V) as depicted in Figure 5.16.

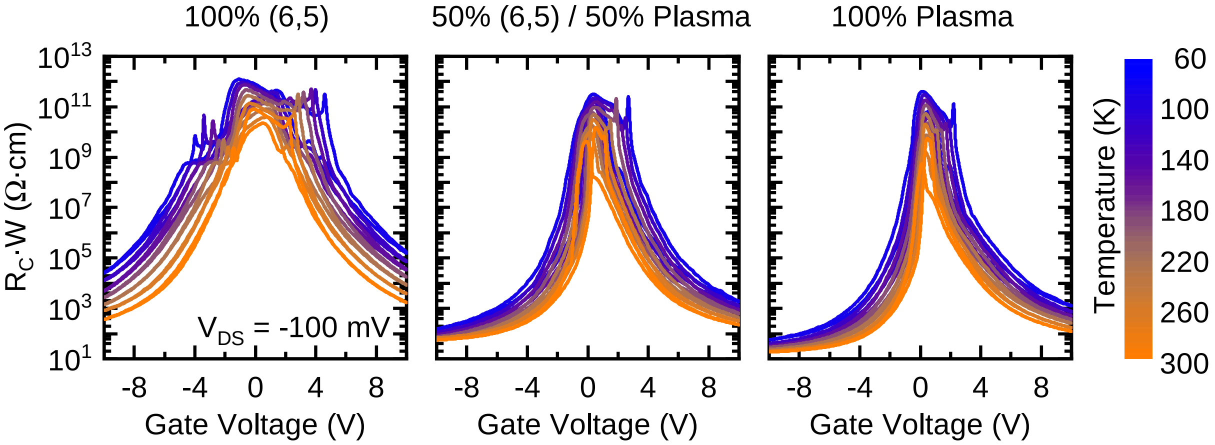

Figure 5.17: Gate voltage-dependent and width-normalized contact resistances measured at temperatures between 60 and 300 K in steps of 20 K (for clarity, only every other curve shown) for three selected network compositions.

Figure 5.17 shows the temperature- and V_G-dependent width-normalized contact resistances of all three SWNT network transistors, revealing a similar trend, i.e., a more pronounced increase in R_C upon cooling for the (6,5) SWNT network (almost two orders of magnitude) than for the pure plasma torch nanotubes and the mixed network (by a factor of 3–8). The overall similarity of the 50 %/50 % mixed SWNT network and the pure plasma torch nanotubes with respect to their current-voltage characteristics further corroborates the assumption that already a large number of percolating paths consisting of plasma torch SWNTs only are present within the mixed nanotube network.

The differences in onset voltage and its temperature-dependent shift between the three SWNT network FETs again requires a carrier mobility extraction at equal conditions as discussed in detail in Chapter 4.6.[324] Hence, all R_C-corrected and temperature-dependent carrier mobilities were extracted at a ±5 V gate overdrive corresponding to a carrier concentration of ~3×10^{12} cm^{-2}.

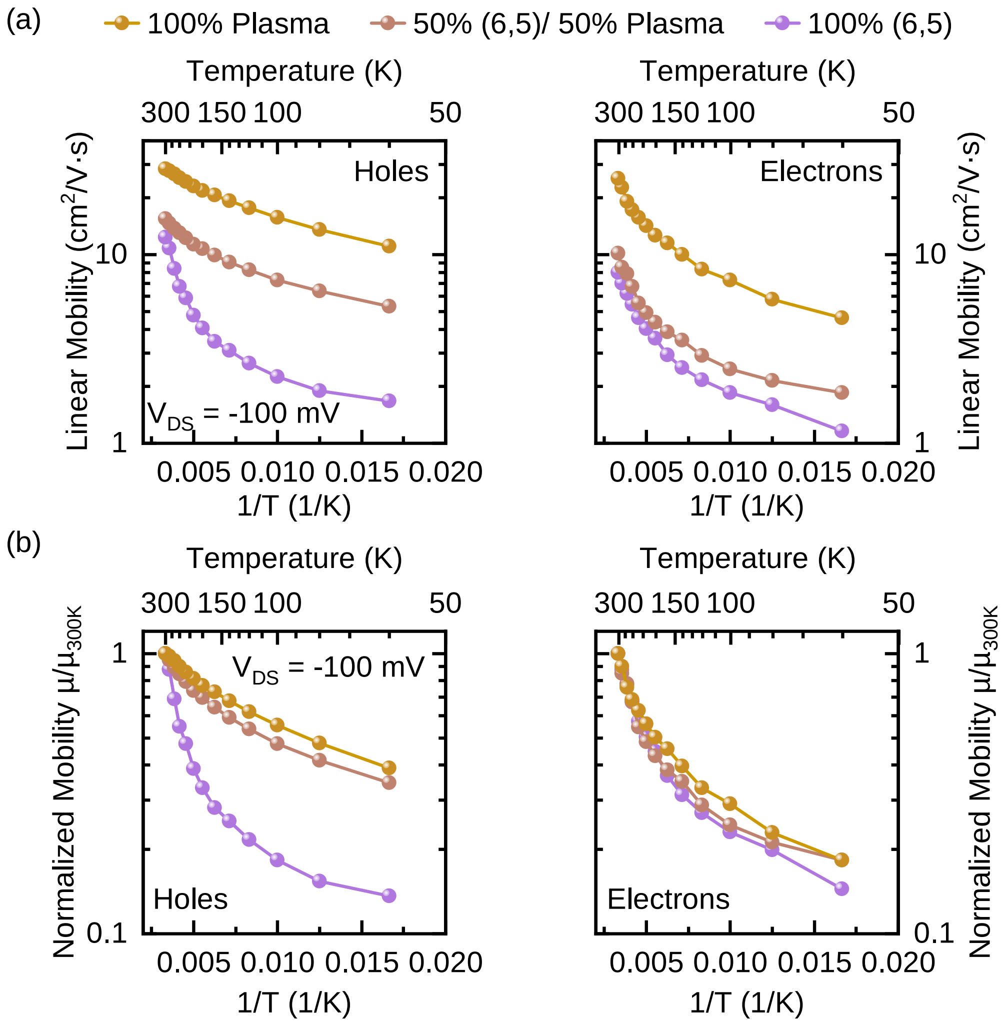

Figure 5.18: Temperature-dependent carrier mobilities for holes (left) and electrons (right) extracted at a 5 V gate overdrive for three selected network compositions: absolute values (a) and normalized to their respective mobility maximum at 300 K (b). Solid lines are guides to the eye.

The respective hole and electron mobilities are shown in Figure 5.18a and emphasize the overall thermally activated charge transport for all three SWNT network types. In agreement with the observations in Chapter 4.4 the temperature dependence of the mobilities cannot be properly described with the VRH model, especially for low temperatures. Despite possibly better fitting results when using the FIT model, no further activation energies or energetic barrier heights based on it are extracted here, as the model lacks a direct context to the specific properties of semiconducting nanotube networks. The VRH and the FIT model have in common that they do not consider the temperature dependence of the intra-nanotube charge transport ($\mu \propto 1/T$) but only take the charge transfer across the SWNT-SWNT junctions into account. For a better understanding, the temperature-dependent charge carrier mobilities of the three SWNT networks are compared only qualitatively by normalization of the respective hole and electron mobility values to their maximum at 300 K as shown in Figure 5.18b. The relative decrease in hole mobility with decreasing temperatures is much more pronounced for the small-diameter (6,5) SWNTs than for the mixed network and the pure large-diameter plasma torch nanotubes. The qualitiative trend is the same for electron transport, although the differences between the three SWNT networks are significantly smaller, potentially caused by residual electron traps or contact resistance effects. However, the overall behavior of the temperature-dependent mobilities demonstrates the obvious impact of the intra-nanotube transport processes with its quadratic SWNT diameter and inverse temperature dependence on the overall SWNT network charge transport.

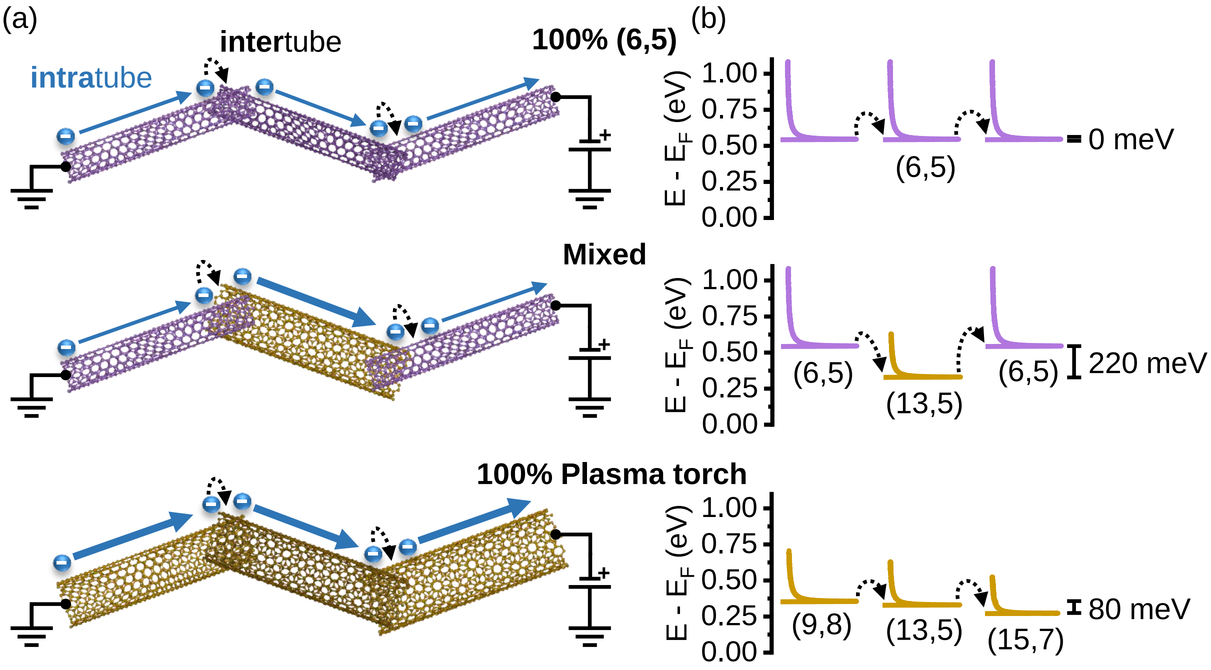

Figure 5.19: (a) Schematic illustration of inter- and intra-nanotube electron transport in three nanotube networks with different compositions. Arrow widths scale with the respective mobility along the individual nanotubes. (b) Energy level differences between the first van Hove singularities of representative SWNT species affecting the inter-nanotube transport at the SWNT-SWNT junctions.

Evidently, the charge carrier mobilities in polymer-sorted semiconducting SWNT films and their dependence on the network composition should indeed be interpreted as superposition of inter- and intra-nanotube transport processes, as summarized in Figure 5.19a. While the carrier mobilities within the individual SWNT is significantly higher for large-diameter SWNTs (as indicated by the arrow widths), the thermally activated inter-nanotube hopping between adjacent SWNTs is mainly determined by the energetic differences between their first van Hove singularities, as illustrated in Figure 5.19b.

5.7 Summary

The results of this chapter once more highlight the impact of the nanotube network composition on the overall charge transport properties in polymer-sorted semiconducting SWNT films confirming the observations in Chapter 4. FETs based on mixed SWNT networks of small-diameter (6,5) nanotubes and large-diameter plasma torch SWNTs in various mixing ratios showed that the charge carrier mobilities overall increase with the contents of the plasma torch SWNTs. Yet, the observed non-linear shape of this composition-dependent mobility increase can neither be explained by only the energy landscape of the SWNT-SWNT junctions, nor solely by the respective distribution of nanotube species with a certain intrinsic intra-nanotube carrier mobility depending on the SWNT diameter. Instead, the interplay of both, namely the thermally activated inter-nanotube hopping and the SWNT diameter-dependent intra-nanotube transport determines the effective carrier mobility of a given network.

Considering the detrimental effect of energetic disorder caused by the energy level mismatch of adjacent SWNTs together with significantly higher intra-nanotube mobilities in nanotubes with larger diameters, long and monochiral large-diameter nanotube species ($\geq$1.2 nm) should represent the optimum composition for SWNT network transistors with record-breaking carrier mobilities. However, an upper SWNT diameter limit will be set depending on the desired achievable on/off current ratio, which is expected to decrease for network transistors containing nanotubes with lower bandgaps due to strong ambipolarity.[216] So far, various established experimental routes for the purification of monochiral SWNT dispersions of several small-diameter nanotube species ($<$1.0 nm) have been developed.[103,370,371] Although the aqueous two-phase extraction technique was recently shown to enable the purification of monochiral large-diameter SWNTs, the procedure is quite elaborate and lacks potential for scalability.[107,372] Further SWNT purification efforts for nanotube network transistors should thus be focused on the selection of tube diameters in the range of 1.2–1.6 nm.

Aside from the nanotube network composition, charge transport in semiconducting SWNT networks is affected by other factors, such as the gate dielectric. In the following chapter, the influence of optically switchable molecules embedded in the dielectric of SWNT network FETs on the transport properties is examined.

CHAPTER 6

CHARGE TRANSPORT MODIFICATION IN SWNT NETWORKS BY PHOTOSWITCHABLE DIELECTRICS

This chapter describes how adding photoswitchable spiropyran molecules to the dielectric layer affects charge transport and allows for the manipulation of current pathways in (6,5) SWNT network field-effect transistors.

The experiments presented in this chapter were partially built upon previous works of Niklas Herrmann, Simon Angstenberger and Sonja Wieland who wrote their Bachelor and Master theses under my supervision.[373–375] All data was acquired by myself if not labeled explicitly. Parts of the results were published in the article Brohmann *et al. ACS Applied Materials & Interfaces* **2020**, 12, *25*, 28392-28403.[376] Adapted figures and tables are presented with permission from the American Chemical Society.

6.1 Introduction

As shown in the two previous chapters, charge transport in semiconducting SWNT networks is strongly influenced by the exact nanotube network composition. Consequently, the device performance can be optimized by tailoring the ensemble of employed SWNT species. The recent availability of such high-mobility SWNT network FETs allows for the question of whether charge transport in such devices can be dynamically modulated in a useful way to implement additional functionalities aside from the plain electrical transistor response. The responsiveness to external stimuli of such multifunctional devices can make them attractive for the development of novel applications in the field of sensing, optical memory or smart displays.[377–380] Among other external stimuli, such as pH, mechanical pressure, magnetic field, etc., stimulation by light provides several advantages like non-invasiveness, high temporal and spatial resolution as well as a tunability with respect to wavelength and intensity.[381] Typically, optical switchability can be realized by embedding photochromic molecules or moieties in the active semiconducting layer, the dielectric or at the device interfaces of a thin-film transistor.[382,383] These photochromic species possess the ability to reversibly switch between two (meta-)stable isomers upon excitation with UV or visible light. The resulting change in molecular conformation is generally associated with considerably different physical properties, i.e., energy levels or dipole moments.[384,385] When these molecules are incorporated in devices, the optically induced change in electronic properties can significantly affect the device performance and lead to a reversible current modulation by several orders of magnitude in, e.g., organic FETs.[386–389] Such light-driven modification of charge transport was shown not only for whole devices but also with spatial resolution, i.e., only in selected areas of the transistor channel.[390,391]

Aside from azobenzenes and diarylethenes one of the most important classes of photoswitchable compounds are spiropyran (SP) derivatives which show a large change in molecular dipole moment of more than 10 D upon photoactivation.[392–397] The increase in dipole moment is the result of UV-induced isomerization of the thermodynamically more stable closed SP form (4–6 D) to the open merocyanine (MC) isomer (14–18 D) with a more extended π-conjugation and hence also strongly red-shifted absorption as shown in Figure 6.1a.[398,399] The reverse reaction can be induced by heating or illumination with visible light. Despite lower quantum efficiencies this photoisomerization capability is retained even when the spiropyran molecules are embedded in a PMMA matrix as shown by the UV-vis absorption spectra of a SP-filled PMMA thin-film in Figure 6.1b. These spectra reveal the typical absorption peaks of the SP form (272–351 nm) and of the MC form (550–600 nm).[400,401] In such PMMA/SP films the changing dipole moment upon photoisomerization of the SP species leads to a concomitant modulation of the permittivity and enables applications as gate dielectric with switchable capacitances and thus drain currents in unipolar organic FETs.[402–404]

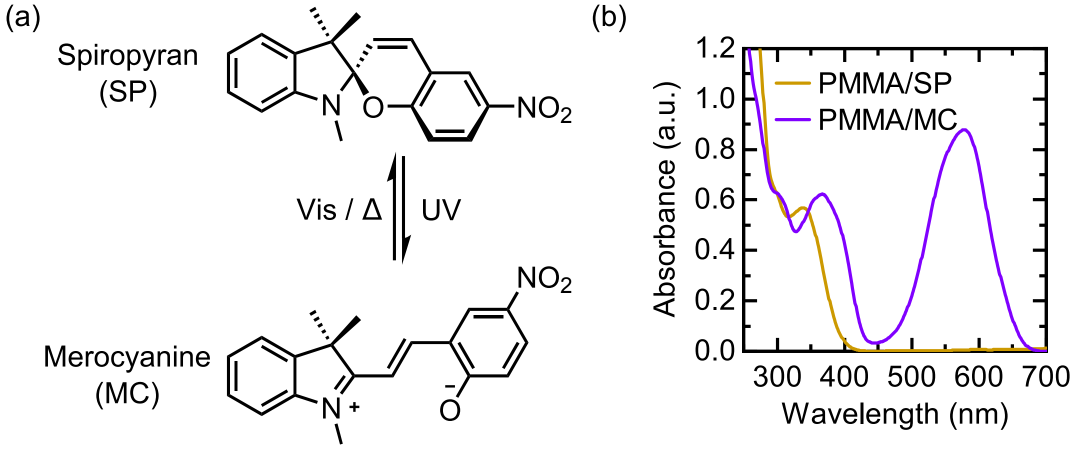

Figure 6.1: (a) Molecular structures illustrating the photoisomerization process of a spiropyran compound and (b) UV-vis absorption spectra of a spiropyran/PMMA thin-film before (SP) and after UV illumination (MC). Measurements performed by N. Herrmann.[373]

Spiropyran as a photoswitchable molecule has also been applied to SWNTs. FETs with single SWNTs that were non-covalently functionalized with SP moieties were tested for photoswitchability and showed a reversible decrease in on-current by a factor of 3 upon UV illumination. This effect was explained with charge trapping or scattering due to the stronger dipoles.[405] Furthermore, the (non-)covalent functionalization of SWNTs with SP in dispersion appeared to enable reversible photodoping of the SWNTs even providing a novel approach for super-resolution imaging applications in the near infrared.[406–411] Overall, the effects of spiropyran/merocyanine on the optical and electronic properties of SWNTs vary and depend on the specific type of functionalization.

Monochiral random SWNT networks can be more or less described as spatially homogeneous semiconducting layer if the SWNT network density is sufficiently high. Yet, the question arises how the network charge transport is affected by purposefully inserted inhomogeneities. The integration of photoswitchable molecules in an SWNT network transistor may enable optical imprinting of preferred transport paths with micrometer resolution.

The intrinsic ambipolarity of semiconducting SWNTs, that is retained in SWNT network transistors, enables the observation of electroluminescence (EL) in the near infrared originating from hole-electron recombination in these devices.[139,232,234] Imaging of the EL allows for the direct visualization of charge transport paths with a high spatial resolution.[272,273,362,412] Changing these local transport pathways in an SWNT network by means of photoswitchable additives could thus be mapped by the EL.

In this chapter, a photoswitchable spiropyran compound is added to the PMMA/AlO_x hybrid dielectric employed in monochiral (6,5) SWNT network transistors. The impact of the photochromic SP molecules on the overall charge transport characteristics before and after irradiation with UV light is analyzed for different SP loadings. Temperature-dependent transport measurements are used to examine the underlying mechanism of the resulting changes in carrier mobility. Finally, the ability to reversibly manipulate the charge carrier pathways in these (6,5) SWNT network transistors by selective photopatterning is demonstrated with the help of EL imaging.

6.2 Device Layout

To fabricate (6,5) SWNT network transistors with photoswitchable molecules, the nanotubes were first purified by selective dispersion of CoMoCAT raw material with PFO-BPy in toluene as described above (see Chapter 3.1.1 for details). The obtained quasi-monochiral (6,5) nanotube dispersion showed the characterisic UV-vis-nIR absorption features as shown in Figure 6.2a and was spin-coated onto photolithographically patterned gold bottom electrodes on glass substrates. The resulting (6,5) SWNT networks exhibited a homogeneous and high network density of ($\geq 40\,\mu m^{-1}$) as shown in Figure 6.2b. In addition to the gFPP electrode layout illustrated above in Figure 3.2a another bottom electrode structure with wider channels ($W = 5000\,\mu m$, $L = 40\,\mu m$) and without voltage probes (see Figure 3.2b) was utilized for EL measurements.

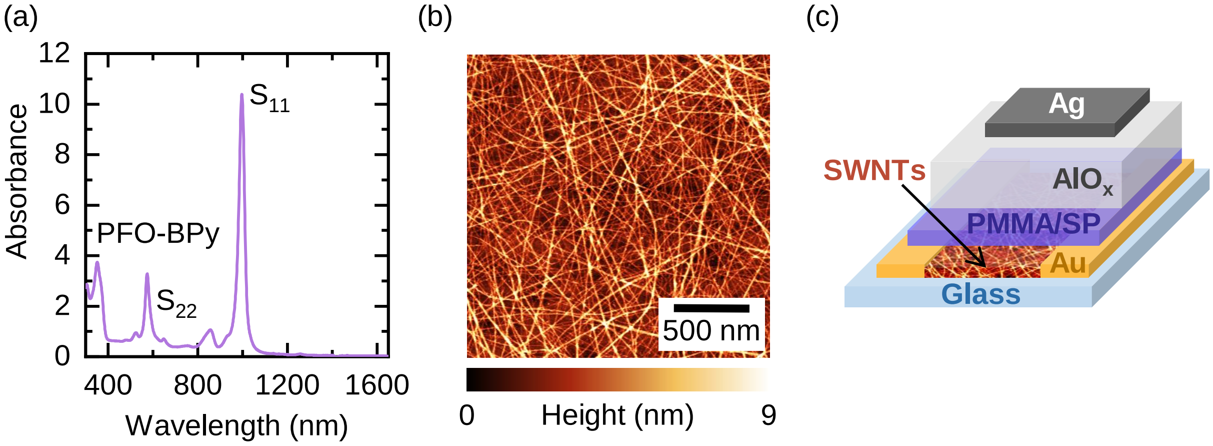

Figure 6.2: (a) UV-vis-nIR absorption spectrum of the employed (6,5) SWNT dispersion, (b) atomic force micrograph of a representative (6,5) nanotube network and (c) device structure of a SWNT network transistor containing a PMMA/AlO_x dielectric with SP in the PMMA film (layers are shifted for better visibility).

A 20 nm PMMA layer with three different spiropyran loadings (without SP, low SP content and high SP content, as shown in Table 3.2) was spin-coated onto the SWNT network. The upper layer of the hybrid dielectric consisted of 100 nm of AlO_x that was deposited by ALD instead of HfO_x. This modification allowed for shorter reaction times at lower temperatures as heating was expected to result in aggregation of the SP molecules and consequently in a lower photoswitching.[373,413] Another reason for the utilization of AlO_x was the formation of cracks in the oxide layer when HfO_x was grown on top of the PMMA/SP layer.[374] Analogous to the two previous chapters a 30 nm top-gate electrode was evaporated on top of the dielectric (see Figure 6.2c for the complete device structure).

6.3 Impact of Spiropyran on Charge Transport

Based on previous findings the addition of SP to the gate dielectric was expected to result in photoswitchable and overall higher dielectric capacitances. The closed SP and the open MC isomers of spiropyran possess much higher dipole moments compared to PMMA (~1.3 D) that change significantly upon UV illumination.[402,403,414] This notion was confirmed by Herrmann and Angstenberger who observed a higher capacitance in plate capacitors that was increased by up to 6 % for SP-filled PMMA and by 3 % for a SP-filled PMMA/AlO_x bilayer upon photoisomerization of the SP to the MC form.[373,374] However, (6,5) SWNT network FETs with a SP-loaded hybrid dielectric showed decreasing on-currents and carrier mobilities with increasing SP loading. The drain currents were further reduced upon photoisomerization to the MC isomer as observed by Angstenberger and Wieland.[374,375]

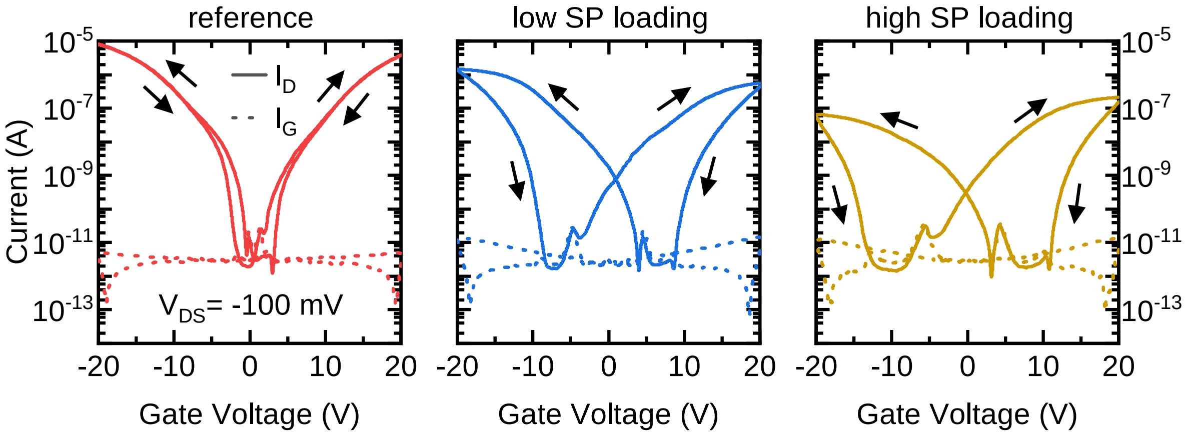

Figure 6.3: Transfer characteristics (forward and reverse gate voltage sweeps at $V_{DS} = -0.1$ V) of (6,5) SWNT network FETs with three different SP:PMMA mass ratios: without SP (reference), SP:PMMA = 0.19 (low SP loading) and SP:PMMA = 0.38 (high SP loading) before UV illumination.

The transfer characteristics of the SP-free reference (6,5) SWNT FET and two equivalent SP-filled devices with a low SP loading (mass ratio SP:PMMA = 0.19) and a high SP loading (SP:PMMA = 0.38) are shown in Figure 6.3. Similar to the (6,5) SWNT networks in the two previous chapters the reference transistor showed almost hysteresis-free balanced ambipolar transport with an on/off current ratio of 10^6 and on-currents in the range of 3.8–8.0 µA. The FETs with SP loading showed significantly lower on-currents of 0.6–1.4 µA for the lower SP content and of up to 0.2 µA for the higher SP loading. Simultaneously, the lower currents for the SWNT network FETs containing SP were accompanied by a pronounced current hysteresis (defined as onset voltage difference between forward and reverse sweep) of about 12 V for the lower SP content and of about 16 V for the higher SP loading. The hysteresis direction for both SP-filled devices was the same as indicated by the arrows in Figure 6.3 and resulted in lower off-sweep currents compared to the on-sweep currents, confirming previous observations by Angstenberger and Wieland.[374,375]

For all three (6,5) SWNT transistors the gate capacitances were measured to be ~40 nF cm^{-2} which is in good agreement with geometrically calculated values based on the respective layer thicknesses (without SP contribution) as well as the nanotube network density and diameter. Apparently, the employed SP concentrations were not high enough to result in significant capacitance differences that cannot explain the observed changes in transport characteristics.

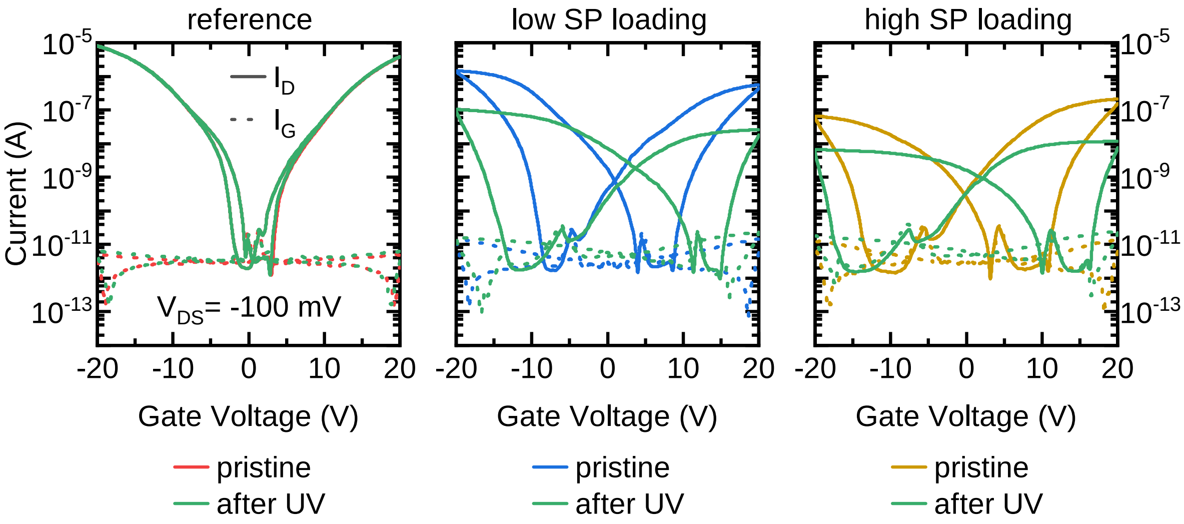

Figure 6.4: Transfer characteristics (forward and reverse gate voltage sweeps at $V_{\mathrm{DS}} = -0.1$ V) of (6,5) SWNT network FETs with different SP:PMMA mass ratios before and after UV illumination.

Instead, the lower on-currents together with the considerably larger current hysteresis suggest interfacial charge carrier trapping and/or scattering in the SP-filled (6,5) SWNT transistors.[415–417] This effect becomes even clearer when the devices are illuminated by a dose of 1000 mJ cm^{-2} UV light (365 nm, see Chapter 3.2.7 for details). As illustrated in Figure 6.1a UV irradiation induces the isomerization of the spiropyran molecules from the SP form to the MC form with a considerably larger dipole moment. While the charge transport in the reference transistor was essentially unaffected, both SP-filled devices showed a much larger current hysteresis exceeding ±20 V and reduced on-currents upon UV illumination as shown in Figure 6.4. However, the overall large hysteresis for the devices with SP raises the question where to extract the onset voltages and charge carrier mobilities in a meaningful way. Based on observations by Wieland, the hysteresis in the transfer characteristics of (6,5) SWNT network FETs with a SP-filled dielectric can be reduced significantly when the V_G-sweep range is limited to negative or positive gate voltages only.[375]

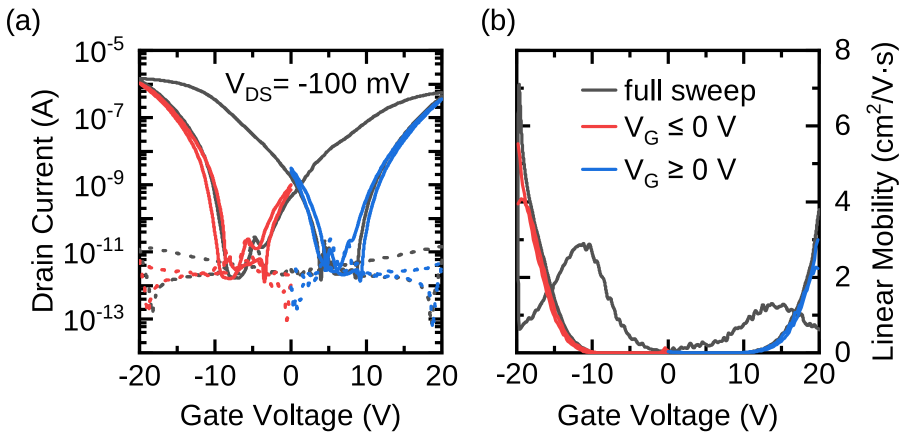

Figure 6.5: Impact of the V_G-sweep range on hysteresis of a representative (6,5) SWNT network transistor with low SP loading: (a) transfer characteristics and (b) linear carrier mobility plots measured in a full forward and reverse V_G-sweep from positive to negative voltages (black) and separated into two half-sweeps with positive (blue) or negative (red) gate voltages only.

As shown in Figure 6.5a the current hysteresis for a full forward and reverse V_G-sweep from positive to negative voltages of a representative (6,5) SWNT network device with low SP content nearly vanishes when the device is operated in separate V_G-sweeps with positive or negative gate voltages only. For higher SP loadings and after UV illumination the remaining hysteresis is somewhat larger, but still much smaller than the one observed during a full sweep. The corresponding gate voltage-dependent and contact resistance-corrected linear carrier mobility curves also appear to be much more defined and lead to somewhat higher mobility values compared to the mobility curves calculated for the full V_G-sweep (see Figure 6.5b). This gate voltage range dependence suggests transient charge carrier trapping at high carrier densities resulting in an onset voltage shift for the opposite carrier type and subsequent recombination or detrapping of carriers at lower or opposite electric fields as a possible explanation for the observed hysteresis behavior.

Accordingly, the onset voltages and charge carrier mobilities of the SP-filled devices were extracted from the separate V_G-sweeps to enable a more reliable comparison with the reference transistor as listed in Table 6.1. The (6,5) SWNT network FET without SP exhibited low onset voltages and quite balanced maximum carrier mobilities for electrons and holes similar to the results for the pure (6,5) SWNT network in the previous chapter. On the other hand, the devices with SP incorporated in the dielectric showed lower carrier mobilities by a factor of 3–5 for the low SP loading and by more than one order of magnitude for the high SP content and significantly larger onset voltages with increasing SP concentration. After UV illumination and thus photoisomerization to the more polar MC form, the discrepancy between the reference FET

Table 6.1: Onset voltages and charge carrier mobilities for electron and hole transport of (6,5) SWNT network FETs with three different SP loadings.

SP-content	Onset Voltage V_{ON} (V) before UV		Onset Voltage V_{ON} (V) after UV		Carrier Mobility μ_{RC} (cm^2 V^{-1} s^{-1}) before UV		Carrier Mobility μ_{RC} (cm^2 V^{-1} s^{-1}) after UV	
	Holes	Electrons	Holes	Electrons	Holes	Electrons	Holes	Electrons
reference	-0.6	1.8	-0.6	1.8	13.3	12.5	13.2	12.7
low SP	-8.8	8.2	-11.8	15.2	4.1	2.3	0.7	0.06
high SP	-13.8	11.8	-15.8	16.6	0.3	0.8	0.05	0.02

and the SP-filled devices with respect to their carrier mobilities and onset voltages becomes much larger. Overall, the SP molecules, especially when switched to the MC isomer, appear to strongly impede charge transport in (6,5) SWNT networks as revealed by the inferior device performance of the SWNT network transistors with SP in their dielectric. This behavior might be explained by trapping or scattering of charge carriers at the SWNT-SWNT junctions and/or within the individual nanotubes. A previous study on charge transport in polymer-sorted SWNT network top-gate/bottom-contact transistors by Lee *et al.* revealed a significant impact of the structure of the gate dielectric on the device performance.[194] For higher permittivities of the insulating layer they found reduced carrier mobilities and higher activation energies as supported by temperature-dependent current-voltage measurements. Referring to the behavior of amorphous polymer semiconductors they ascribed this effect to a larger dipolar disorder caused by randomly oriented dipoles at the interface between the transistor channel and the dielectric for insulating materials with higher ϵ_r.[217] The embedded SP in the PMMA layer of the presented (6,5) SWNT FETs might lead to an analogous effect that is further strengthened when its polarity is further increased upon photoisomerization to the MC form.

To test this hypothesis and to gain further insights into the origin of the impeded charge transport upon SP incorporation into the gate dielectric temperature-dependent transport measurements were performed and are discussed in the next section.

6.4 Investigation of the Photoswitching Mechanism

Transfer characteristics were recorded at temperatures from 60–300 K for a reference (6,5) SWNT network transistor and for a device with an SP-filled PMMA layer (low SP loading) before and after UV illumination as shown in Figure 6.6. Note, all temperature sweeps were performed in the dark starting from the lowest temperature to limit the reverse isomerization from the MC to the SP form induced by thermal energy or visible light. In agreement with the results in Chapter 5.6 the (6,5) SWNT reference transistor shows balanced ambipolar transport with low hysteresis for all temperatures and thermally activated transport as indicated by the decreasing on-currents upon cooling. This temperature-dependent transport behavior of the SWNT network is retained when SP is embedded in the PMMA layer both before and after photoactivation and also the onset voltage shifts show the same trend as for the reference device. However, the decrease in electron current with decreasing temperature is significantly more pronounced for the SP-filled device compared to the reference FET, while the relative decrease in hole current upon cooling is similar for both. This discrepancy between electron and hole transport for the SP-loaded FET is even larger after UV illumination, resulting in an incomplete turn-on for electrons at low temperatures.

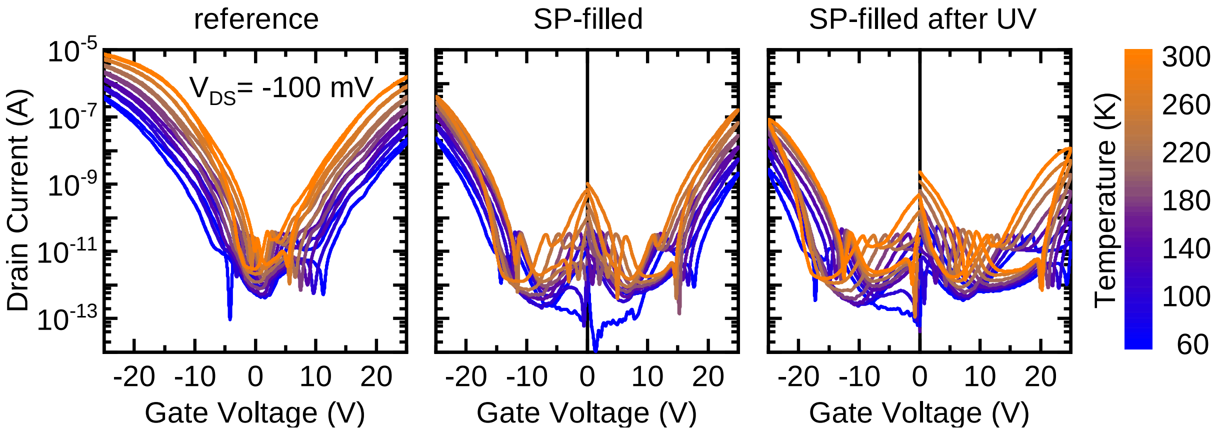

Figure 6.6: Temperature-dependent transfer characteristics at $V_{DS} = -0.1$ V measured in 20 K steps from 60 to 300 K (for clarity, every other curve shown) for a FET without SP and a SP-filled device before and after UV illumination. Note, separate V_G-sweeps for positive and negative gate biases were recorded for the SP-filled devices, while the reference transistor was measured in a full sweep.

The onset voltage shifts of the SP-free and SP-filled devices between 60 and 300 K provide a similar image, that is, comparable values for hole transport (≤5 V) but significantly larger electron onset voltage shifts for the SP-loaded FET after UV illumination (8 V) than for the reference (5 V) as shown in Figure 6.7. Overall, the absolute onset voltage values for both electron and hole conduction are considerably larger (by up to 10 V) for transistors with SP in the dielectric compared to the reference FET.

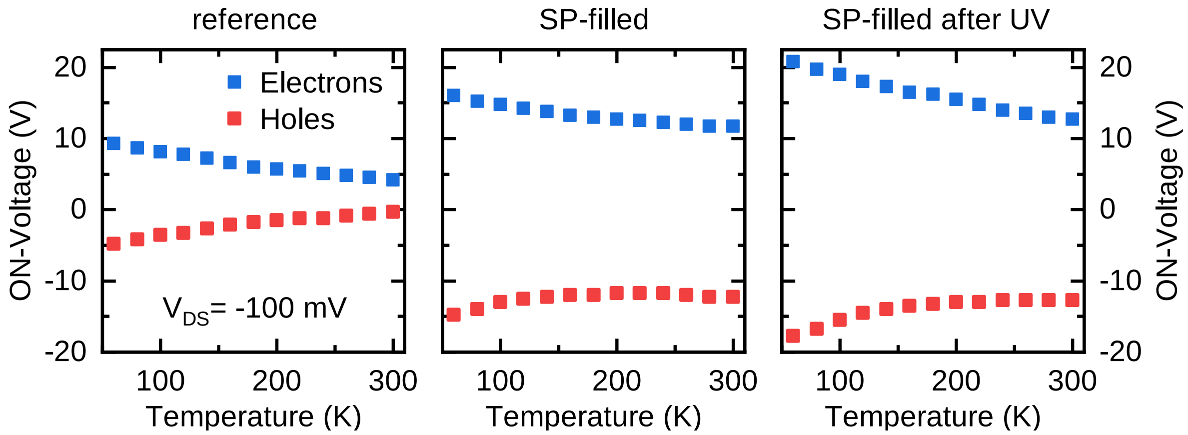

Figure 6.7: Temperature-dependent onset voltages (extracted at $V_{DS} = -0.1$ V) of a reference (6,5) SWNT network FET and a SP-filled device before and after UV illumination.

The gate voltage- and temperature-dependent, width-normalized contact resistances were analyzed to assess whether a less efficient charge injection caused by the SP molecules might be responsible for the lower on-currents as depicted in Figure 6.8. Interestingly, the minimum contact resistances increase by more than one order of magnitude upon SP incorporation before UV illumination and by more than another order of magnitude after photoswitching, whereas the R_C values for the reference transistor are in good agreement with the values for the (6,5) SWNT network extracted in Chapter 5.6. This behavior might be explained with a reduction of carrier mobility also in the vertical direction through the up to 5-10 nm thick nanotube film. Due to the porous open SWNT network structure, the SP molecules are likely to be present throughout the entire film and the same mechanisms that lead to an overall decrease of mobility take effect in the transport from the electrodes to the accumulation channel as well. Thinner SWNTs network may not suffer from the same effect, however, this was not tested here.

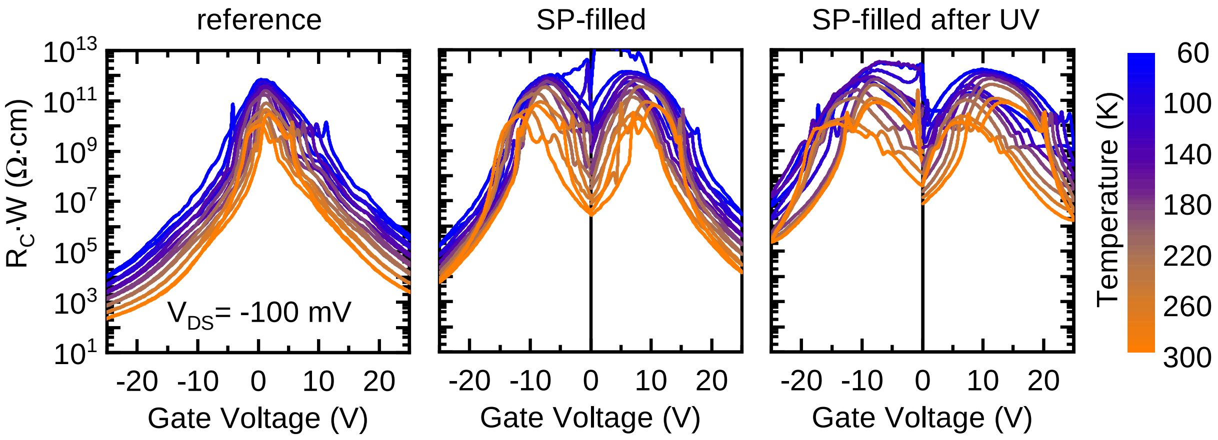

Figure 6.8: Gate voltage-dependent and width-normalized contact resistances measured between 60 and 300 K in steps of 20 K (for clarity, every other curve shown) for a reference (6,5) SWNT network FET and a SP-loaded device before and after UV illumination.

It should be noted that the contact resistance analysis is based on several assumptions, e.g., a linear potential gradient in the channel. Given the high onset voltages and incomplete turn-on at lower temperatures for the SP-filled FETs especially after UV illumination, it remains unclear whether these are fulfilled here and hence the absolute R_C values should be interpreted with caution. Still, the considerably different contact resistances for the reference FET and the SP-filled device before and after UV illumination once more demonstrates the necessity for a correction of the charge carrier mobilities using the gFPP measurements.

A reliable comparison of the three devices required mobility extraction at comparable conditions to counter the effects of different onset-voltages and their temperature dependence. The contact resistance-corrected, temperature-dependent carrier mobilities were extracted at a gate overdrive of ±10 V and a corresponding charge carrier density of ~2.5×10^{12} cm^{-2}. Figure 6.9a shows the respective hole and electron mobilities at different temperatures. They confirm the observed differences in temperature-dependent on-currents, i.e., overall lower carrier mobilities for the

SP-filled device and a significant mobility reduction after UV-induced photoswitching compared to the reference. The reduced on-currents are therefore not just a result of the higher contact resistance but of overall lower charge transport in the nanotube network in the presence of SP or MC. Furthermore, the differences of the temperature-dependent mobilities between the FETs with and without SP are much more pronounced for electrons than for hole transport. This observation is further corroborated by normalizing the carrier mobilities to their respective maximum value at 300 K as shown in Figure 6.9b. While there is essentially no difference in the relative hole mobility decrease upon cooling among all three devices, the temperature dependence of the electron mobilities is more pronounced for the SP-filled FET compared to the reference. UV illumination of the device with SP results in an even stronger temperature dependence for electrons, whereas it has no effect on the relative decrease in hole mobilities.

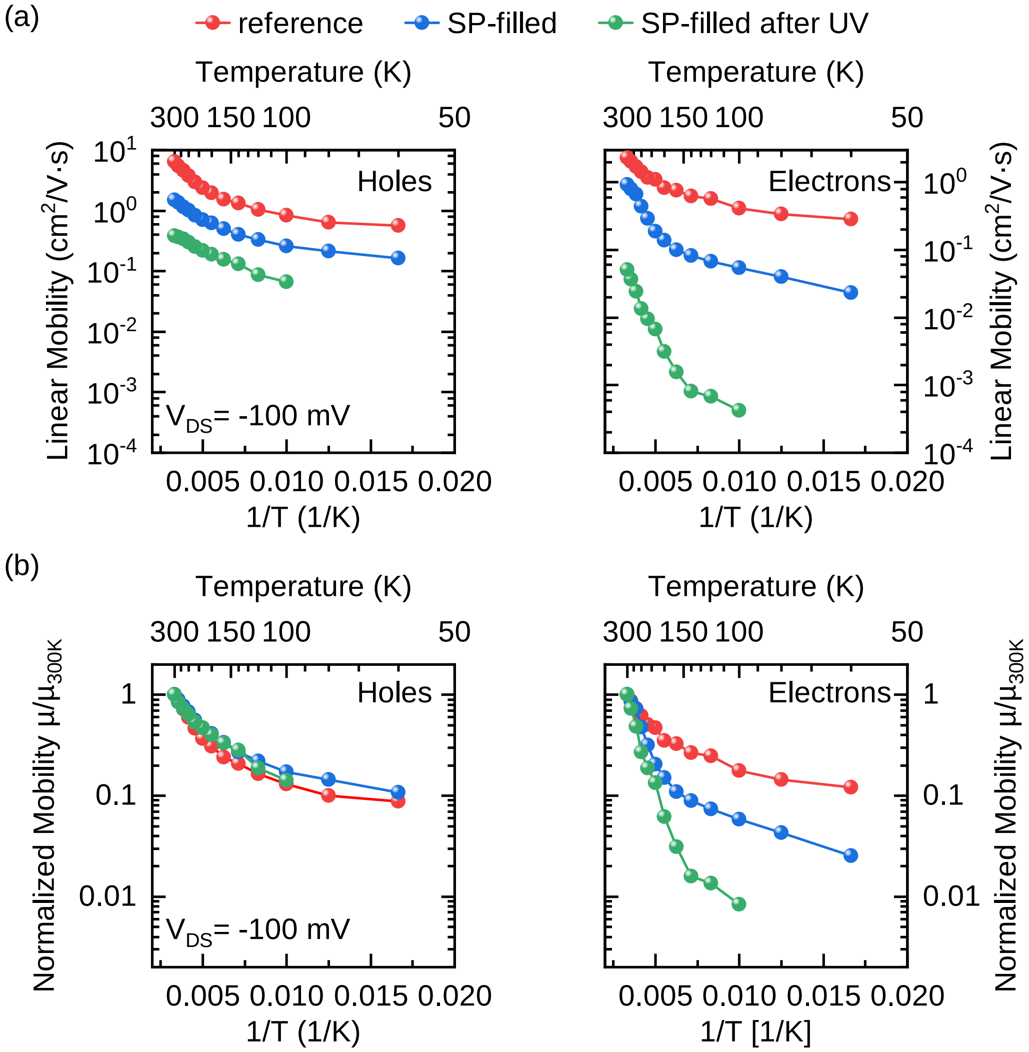

Figure 6.9: Temperature-dependent charge carrier mobilities for hole (left) and electron transport (right) extracted at a 10 V gate overdrive for (6,5) SWNT network FETs with and without SP in the dielectric, before and after UV exposure: (a) absolute values and (b) normalized to their respective mobility maximum at 300 K. Solid lines are guides to the eye. Note that after UV illumination a gate overdrive of ±10 V could not be reached below 100 K and hence these data points are left out.

The difference in temperature dependence between hole and electron mobilities indicates that the impact of SP molecules in the PMMA matrix goes beyond simply increasing dipolar disorder and thus decreasing carrier mobility as this should affect both electron and hole transport equally. Despite overall lower mobility it appears that electron transport is much more affected by the polar SP molecules than hole transport. This behavior might be explained by the energetic positions of the (6,5) SWNT band edges compared to the HOMO and LUMO of the SP molecules in the closed form and for the MC isomer. The (6,5) SWNTs possess a narrow bandgap of 1.27 eV with corresponding band edges at about −3.8 eV for the conduction band and −5.0 eV for the valence band.[49,418,419] On the other hand, the UV-vis absorption edges of both spiropyran isomers (see Figure 6.1b) can serve as a rough measure for their much larger HOMO-LUMO gaps, namely ~2.8 eV for the closed SP form and ~1.9 eV for the MC form. Although no measurements of the ionization potential or the electron affinity have been reported for directly comparable spiropyran systems, the available theoretical and experimental data imply HOMO levels of −5.3 eV and −5.4 eV for the SP and the MC isomer respectively.[386,420–422] Hence, both are significantly lower than the valence band of the (6,5) SWNTs and neither of them can act as a hole trap. Similarly, the corresponding reported LUMO levels of the SP form (−2.5 eV) and the MC isomer (−3.5 eV) should neither result in electron trapping, despite the much stronger energetic shift of the LUMO compared to the HOMO upon photoswitching from SP to MC. However, in the vicinity to proton sources, such as possibly residual carboxylic groups in the PMMA matrix, water or the polar glass substrate, the MC isomer is susceptible to form the protonated MCH^+ species with a considerably lower LUMO level of −4.0 eV which would act as strong trap for electrons.[420,423,424] Consequently, electron trapping caused by this species could explain not only the higher thermal activation energies for electrons but also the aforementioned pronounced current hysteresis that increased further after UV exposure. Yet, even before photoactivation already a small amount of the MC might be present in the devices with SP leading to the more pronounced decrease in electron mobility upon cooling compared to the reference FET. Shallow electron trapping by MCH^+ could thus be one part of the mechanism behind the hindered charge transport upon UV photoswitching in SP-filled (6,5) SWNT network FETs.

While the stronger temperature dependence of the electron transport can be explained with traps, the overall lower mobility of both holes and electrons may be explained with an impact of the polar SP and MC molecules on intra-nanotube transport and increased charge scattering. Previously, it was shown that charge transport within individual SWNTs can be influenced significantly by surface polar phonon scattering when the nanotube is situated on a polar substrate.[425] This phonon scattering results in up to one order of magnitude lower carrier mobilities at room temperature when SiO_2 is used as insulator. For dielectric materials with higher ϵ_r even stronger scattering rates were found.[426] Possibly, the SP molecules close to the nanotube surface have a similar effect on the intra-nanotube mobilities which is significantly increased upon photoactivation due to the higher dipole moment of the MC isomer. This charge carrier scattering within the SWNTs is expected to affect both holes and electrons and should not have a significant impact on the relative temperature dependence, instead lowering only the mobility prefactor. Thus, the strongly reduced charge transport after photoactivation of (6,5) SWNT network FETs with SP molecules could be explained as a combination two main effects. First, the electron trapping caused by the protonated MCH^+ species inhibits the inter-nanotube transport and results in current hysteresis as well as higher thermal activation energies for electrons. Second, the dipole-induced charge carrier scattering within the individual SWNTs reduces the intratube mobilities.

Although this proposed mechanism cannot be further investigated and corroborated here, the UV illumination can be utilized to convert a semiconducting SWNT network with high carrier mobilities into one with considerably lower mobilities. As shown previously, this photoswitching can also be reversed by illumination with visible light or by heating, which induces the back reaction from the MC to the SP isomer.[374,375] However, 100 % reversibility could not be achieved, as the hole currents reached only 33 % of the pristine value, while the electron currents recovered completely.[375] This behavior could be explained by a heat-induced aggregation of the MC isomers in the PMMA/SP layers and/or by a stabilizing effect of the SWNTs on the MC form.[406,413]

Furthermore, the illustrated photoswitching ability of (6,5)-SWNT network FETs with added SP does not have to be applied to the whole semiconducting network, but can be restricted to certain channel areas, e.g., by illumination through a photomask, thereby creating areas of low and high carrier mobilities in the transistor channel as shown in the next section.

6.5 Guiding Charge Transport by Local Photoswitching

The concept of photopatterning current pathways in SP-filled (6,5) SWNT network transistors is illustrated in Figure 6.10a. The device with SP molecules in the dielectric is irradiated with UV light through a chromium-on-glass photomask with a certain pattern. While the covered areas of the SWNT network retain their high carrier mobility as the SP molecules remain in their closed form, the nanotube network regions exposed to UV light are converted into areas with considerably lower mobility, leading to a divided transistor channel. It is expected that charges will follow the path of least resistance and hence will move mainly or as much as possible through the high mobility areas.

To monitor the spatial distribution of current density before and after the UV photopatterning, a large number of EL images were recorded with an InGaAs camera while devices were operated in the ambipolar current regime (see Chapter 3.2.6 for details). As described in Chapter 2.3.2 the EL recombination zone has a narrow width in the range of one micrometer and a distinct position in the transistor channel for a given gate voltage. The local EL intensity is generally proportional to the current density at each point along the emission zone and the photoluminescence quantum yield of the emitting material. As shown by Wieland neither the photoluminescence nor the EL

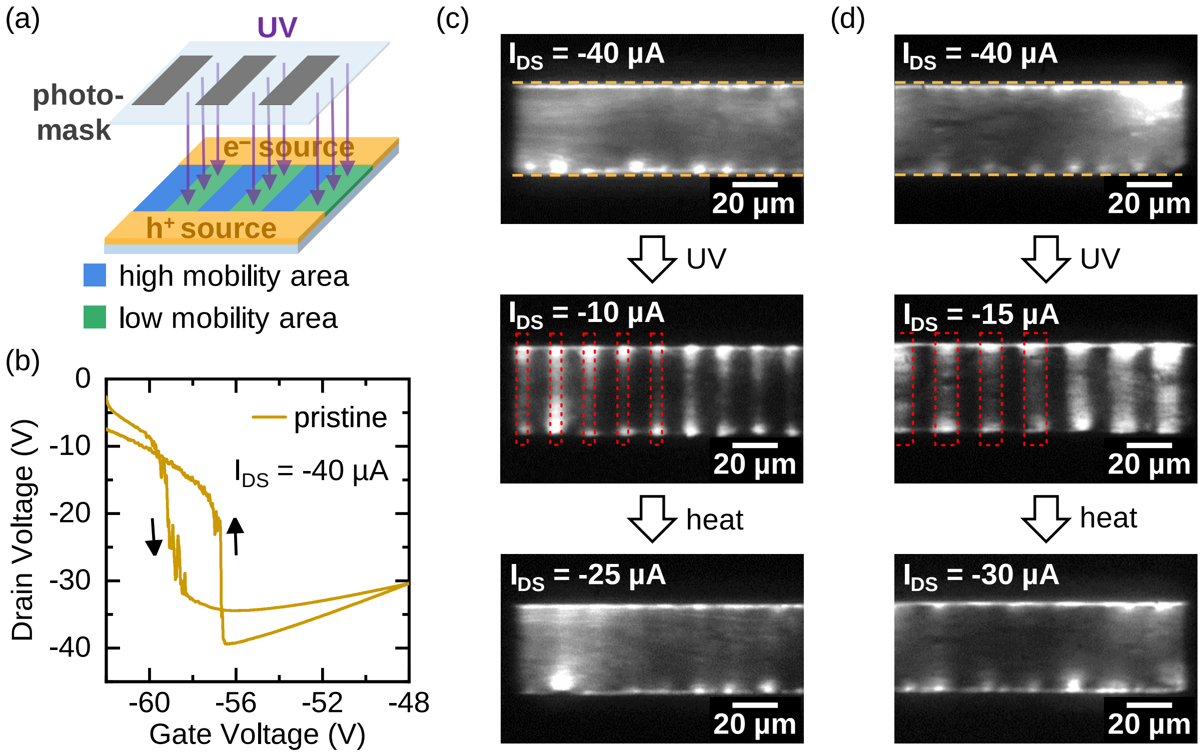

Figure 6.10: Impact of selective UV photopatterning on the local EL intensity of SP-filled (6,5) SWNT network FETs with high SP loading: (a) Schematic representation of local photoswitching by UV illumination through a photomask to convert parts of the FET channel into low mobility areas, (b) representative V_D *vs* V_G curve (constant-current mode at $I_{DS} = -40\,\mu A$) illustrating the employed voltage sweeps to move the emission zone through the transistor channel, (c,d) EL composite images of two SP-filled networks FETs before UV illumination (top), after UV patterning utilizing a photomask (middle) with a stripe pattern and after heating at 90 °C to promote the reverse isomerization (bottom). The stripes have a 10 μm spacing and widths of 5 μm (c) and of 10 μm (d). Orange dashed lines indicate electrode edges, red dashed lines indicate the photomask pattern.

spectra of (6,5) SWNT networks were significantly affected by the presence of SP or MC species or by UV illumination.[375] Hence, it is assumed that the EL intensity contrast is mainly determined by the differences in path resistance and thus the carrier mobility contrast between regions with SP *vs* those with MC in the dielectric and not the result of luminescence quenching. A series of EL images were converted into composite images, displaying the maximum intensity of each pixel during a whole constant current sweep. This mode is used to avoid intensity variations along the channel and especially close to the electrodes due to current variations of up to orders of magnitude that would occur during a constant drain voltage (transfer) sweep. Instead, the drain voltage is adjusted during the gate voltage sweep to maintain a constant current, as depicted in Figure 6.10b for a representative FET before UV photopatterning. The EL composite images of two SP-filled (6,5) SWNT network FETs with high SP loading are shown in Figure 6.10c,d. As the actual transistor channel width is much broader ($W = 5000\,\mu m$) than the field of view of the camera, these images show only the left (c) or the right (d) channel edge of the respective FET to ensure an exact retrieval of the measuring spot before and after the SP switching.

Before the photopatterning step, both FETs exhibit a fairly homogeneous EL emission throughout the channel. After UV exposure the EL composite images of both devices show a pronounced stripe pattern that closely resembles the structures on the employed photomasks as indicated by the red dashed lines. In agreement with observations by Wieland, in the illuminated channel regions the EL emission is significantly lower most likely due to the reduced carrier mobility in these areas resulting from the isomerization of the SP molecules to the MC form and hence lower current density.[375] After heating the devices at 90 °C for 60 min, the homogeneous EL emission throughout the channel area is almost completely restored, as the reverse isomerization of the SP molecules from the MC to the SP form was thermally induced. Remaining traces of the stripe patterns are consistent with the above mentioned incomplete reverse reaction due to aggregation of the MC isomers. Still, this observations clearly demonstrate the ability of SP-filled dielectrics to vary the local carrier mobility within the channel and thus to determine the current pathways in (6,5) SWNT network FETs by selective illumination with UV light.

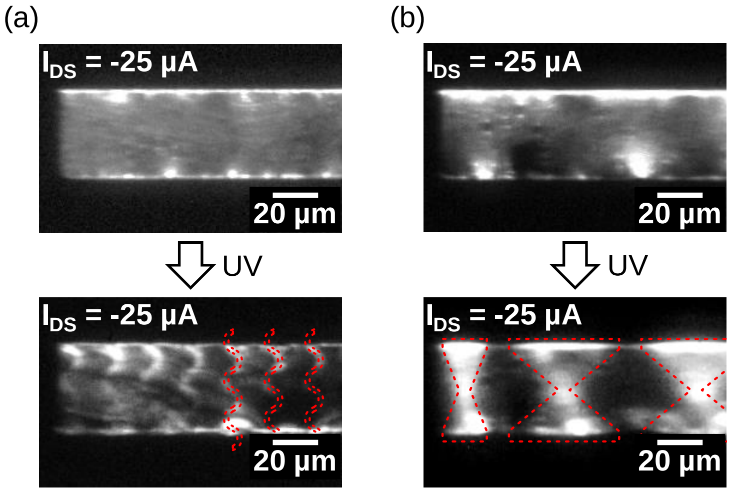

Figure 6.11: Impact of UV photopatterning on the local EL intensity of two devices with high SP loading using various photomask designs: EL composite images recorded in constant current mode before and after UV patterning with wavy line structures (a) as well as with narrow and wide hourglass structures (b). Red dashed lines indicate the respective layout of the photomask utilized to cover parts of the transistor channel.

This photopatterning of current pathways is not limited to simple and straight patterns only. Even fairly complex patterns can be written into the transistor channel as also demonstrated by Wieland.[375] These include wave and hourglass patterns as shown in Figure 6.11. Yet, the wavy line pattern is only partially visible in the EL composite image and the contrast between illuminated low mobility areas and high mobility areas is low, as a significant share of the current goes through the low mobility areas. Following the path of highest mobility would require substantial deviation from the direction of the applied lateral electric field and a longer effective channel length for the charge carriers. Hence, a balance between path length, electric field direction and mobility creates a lower current and EL contrast. Nevertheless, the transfer of wavy line patterns of only 2 µm width into the EL emission of the (6,5) SWNT network FET indicates that a spatial resolution of a couple of micrometers can be achieved in this process. As shown in Figure 6.11b for effective and well-defined photopatterning a homogeneous EL intensity throughout the transistor channel prior to the UV illumination is desired, as the photoisomerization cannot erase substantial differences in charge injection at the electrodes or differences in local network resistance, e.g., due to impurities or SWNT bundling.

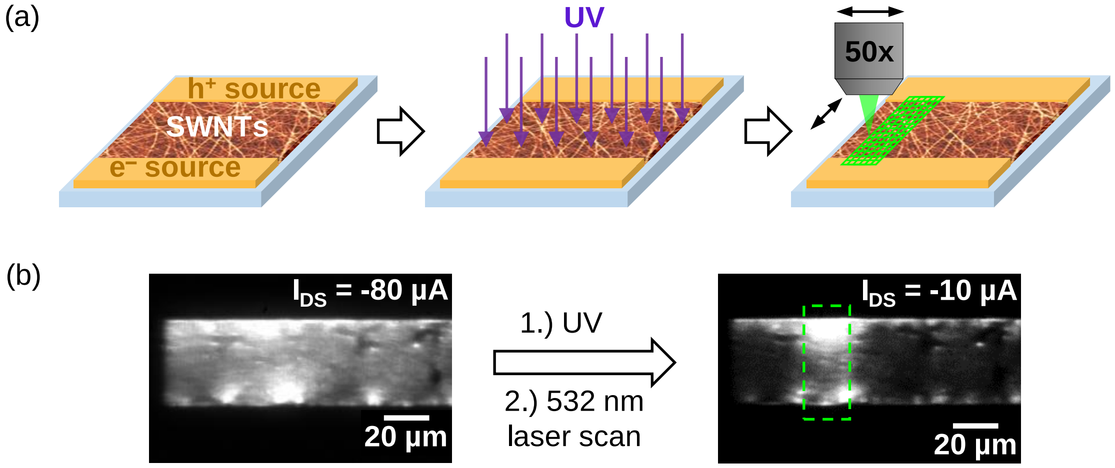

Figure 6.12: Inverse photopatterning of (6,5) SWNT network FETs with low SP loading: (a) schematic representation of the inverse photopatterning process consisting of UV illumination of the entire FET channel followed by laser scanning (532 nm) of a selected channel area to induce the reverse photoisomerization, (b) EL composite images recorded in constant current mode of a device before (left) and after UV illumination and consecutive scanning with a green laser (right). Green dashed lines indicate laser scanning area.

The described UV-induced patterning of preferred current pathways and thus of the EL emission relied on the photoisomerization from the SP to the MC form. However, EL photopatterning can also be achieved vice versa, i.e., by selective reverse isomerization from the MC to the closed SP isomer. Figure 6.12a shows this inverse photopatterning process, that starts with a UV illumination step of the whole device to switch the SP molecules to the MC isomer. This step is followed by scanning with a focused 532 nm laser, whose wavelength matches the absorption band of the MC isomer (see Chapter 3.2.7 for details), over a selected channel segment. Before UV illumination the (6,5) SWNT network FET with low SP loading shows a fairly homogeneous EL throughout the transistor channel as shown in Figure 6.12b. After global illumination with UV light and subsequent scanning of the laser spot across a $50 \times 20\,\mu\text{m}^2$ grid with 0.5 µm steps over a period of ~30 min the EL composite image shows a higher emission and thus increased current density and carrier mobility in the scanned area. The mask-less and direct-written pattern based on this ’inverse’ process shows less defined edges compared to the approach using a photomask and UV light. The lower resolution might be due to additional local heating, but further optimization of the exposure parameters should be feasible. Nevertheless, it represents a proof of concept that mask-free photopatterning of high and low mobility areas is possible in these devices by selectively inducing the back reaction from the MC to the SP isomer.

6.6 Summary

In this chapter, the impact of photoswitchable SP molecules as an additive in the PMMA layer of the hybrid dielectric of (6,5) SWNT network FETs on the overall network charge transport was demonstrated. Overall, these photochromic molecules had a detrimental effect on the device performance. Both hole and electron mobility were lowered and current hysteresis was observed depending on the concentration of the added amount of SP. UV illumination and thus optically induced isomerization of the closed SP form (smaller dipole moment) to the MC form with a considerably higher dipole moment further resulted in one order of magnitude lower charge carrier mobilities. Most likely, a combination of charge carrier scattering within the individual nanotubes and electron trapping at the SWNT-SWNT junctions caused by the protonated MCH^+ species might be responsible for the observed photoswitching as implied by temperature-dependent current-voltage measurements.

This optical switchability introduced by the SP was further utilized to modulate the charge transport and the spatial distribution of current pathways by selective UV illumination through a photomask as visualized by EL imaging. This way, a range of patterns could be produced with micrometer-resolution compared to the initially homogeneous EL emission throughout the transistor channel. These structures could be erased again by heating, which induced the reverse isomerization of the SP. However, the recovery of mobility and thus emission was not complete, presumably due to aggregation of the MC isomers resulting in an incomplete back reaction. Moreover, deliberate manipulation of current pathways could be realized with a mask-free process in the reverse direction using a green laser to locally create SP isomers in a fully UV-illuminated film. In any case, the presented reversible photopatterning of transport pathways and their direct visualization by EL composite images once more emphasizes the suitability of EL imaging for understanding charge transport in ambipolar SWNT network FETs.

The results in this chapter demonstrate that polymer dielectrics with photoswitchable molecules such as spiropyran represent an interesting approach to introduce light-responsiveness and thus additional functionalities into semiconducting SWNT network FETs. The direct interaction of SP and MC molecules with the nanotube network at the dielectric interface is particularly helpful to create a large impact on charge transport. However, several obstacles are yet to be solved such as the incomplete recovery of the SP molecules which is essential to enable the required cyclability for applications. With such a long-term cyclability the demonstrated selective photoswitching could be utilized to reversibly control the preferential current distribution in novel multi-terminal SWNT network devices, e.g., as position sensitive optical detectors.

CHAPTER 7

CONCLUSION AND OUTLOOK

This chapter summarizes the conclusions drawn in this thesis and gives suggestions for future research based on semiconducting carbon nanotube networks and their application in field-effect transistors and other optoelectronic devices.

In this work charge transport in SWNT network FETs was investigated with a focus on the impact of the nanotube network composition, i.e., the distribution of present SWNT species with different diameters and thus energy levels. Furthermore, intentional transport modification in such transistors by the use of photochromic SP molecules as an additive in the dielectric was analyzed and evaluated with regard to possible applications in multifunctional devices.

At the outset of this thesis most charge transport studies on semiconducting SWNT network transistors evaluated the device performance mainly based on geometric parameters, such as network density, length of the incorporated nanotubes and degree of alignment. The large variety of reported SWNT mixtures in network FETs with vastly different sample quality, often distorted by extrinsic factors, e.g., trap states, dopants or contact barriers, made a meaningful comparison of these reports difficult.

Consequently, this work started with a controlled comparative study of three randomly-oriented semiconducting nanotube network types with different SWNT species and thus diameter distributions, that were polymer-sorted from three commercially available SWNT sources. The utilized bottom-contact/top-gate FETs with a hybrid dielectric and a pair of voltage sensing probes in the transistor channel allowed for the reproducible observation of intrinsic ambipolar charge transport and for the correction of any contact resistance effects. Although two different wrapping polymers had to be used for the selection of the respective SWNT ensembles, no direct impact of residual polymer amounts on the network charge transport could be detected. In agreement with previous reports, temperature-dependent current-voltage measurements revealed an overall thermally activated charge transport for all SWNT network compositions similar to conventional disordered semiconductors. The lowest carrier mobilities and strongest temperature dependence were found for the network with the broadest nanotube diameter distribution. This behavior could be rationalized by the comparatively large energetic barriers at the junctions between nanotubes with significantly different diameters. Surprisingly, the lowest activation energies and highest carrier mobilities were observed for mixed networks of large-diameter SWNTs with a certain energy level spread and not for the nearly monochiral networks of small-diameter nanotubes. Contrary to the common assumption, that only the nanotube-nanotube junction resistances determine the overall charge transport through the SWNT network, this result suggested a significant contribution of the diameter- and temperature-dependent carrier mobility along each individual nanotube as well.

This hypothesis could be further corroborated by a subsequent charge transport analysis on SWNT network FETs with tailored compositions. These semiconducting nanotube networks were fabricated by defined mixing of large-diameter nanotubes with a comparatively narrow diameter distribution and nearly monochiral small-diameter SWNTs, that were sorted using the same wrapping polymer, in various ratios. With this unprecedented control over the composition in semiconducting SWNT networks the impact of a stepwise change in composition on charge transport could be assessed in more detail. The observed monotonous but non-linear increase of the network mobilities with growing contents of the large-diameter SWNTs could be explained by a superposition of two different factors: the intra-nanotube transport with its characteristic SWNT-diameter and temperature dependence and the thermally activated inter-nanotube hopping within a more or less disordered energy landscape.

These observations indicate that the available charge transport models for semiconducting SWNT networks are incomplete and require additional parameters and assumptions. Although a few of these approaches can reproduce experimental results for mixed nanotube networks, as long as the difference in tube diameters is not too large, a more holistic model is still missing for a more reliable and SWNT-specific description and prediction of charge transport properties. An adapted modeling approach should thus include both the diameter-dependent charge transfer across the SWNT-SWNT junctions[202] and the intra-nanotube mobility, taking into account the specific temperature and carrier density dependencies for each nanotube species.

Aside from the theoretical perspective, additional experiments would be helpful to further corroborate and complement the insights into the fundamental charge transport mechanisms of semiconducting SWNT networks gained in this work. A combined analysis of the charge carrier mobilities and thermoelectric properties (Seebeck coefficient) depending on the temperature and carrier density could further refine the understanding of the impact of the inter- *vs* intra-nanotube transport. The results obtained from this approach may also have implications for the development of a proper theoretical charge transport model.

Furthermore, the presented temperature- and network composition-dependent analyses of the carrier mobilities only deliver a macroscopic picture of the overall charge transport across a whole nanotube network. On a microscopic scale, the impact of, e.g., the network composition or the charge carrier density on individual current paths within a network still remains unclear. For example, conductive AFM measurements could enable a spatial charge transport investigation in (sparse) nanotube networks, although access to the open network structure and thus a different FET architecture (e.g, bottom-gate/top-contact) would be required. With this method it could be possible to trace even single charge transport paths depending on the SWNT network composition and morphology (density and alignment), while tuning the gate voltage. In addition, this approach could be used to directly measure and thus deconvolute the SWNT species-dependent intra-nanotube and junction resistances in very sparse, mixed SWNT networks or ’chains’, consisting of only a few junctions.

Another complementary technique to examine the charge carrier density-dependent contributions of the different SWNT species to the overall current in the tailored mixed networks of small- and large-diameter nanotubes is charge modulation spectroscopy. In comparison to conventional photoluminescence or absorption measurements on SWNT network FETs, this method offers also the advantage that only mobile charge carriers are probed whereas trapped charges are excluded. While this technique was recently utilized to successfully determine the chirality-specific current share in mixed networks of small- and medium-diameter SWNTs,[427] a temperature-dependent study of the current share in networks with tailored compositions would be very interesting.

Although several questions about the underlying transport mechanisms in semiconducting SWNT networks still remain unanswered, the findings presented in this work already provide a rational design guideline for composition optimizations in random SWNT network FETs. In order to realize network transistors with maximum carrier mobilities beyond $100\,\mathrm{cm^2\,V^{-1}\,s^{-1}}$, future SWNT purification approaches should aim at monochiral large-diameter nanotubes. Given the limitation of the achievable on/off current ratio for small-bandgap SWNTs,[216] a trade-off between mobility and current modulation has to be found and will likely result in optimum tube diameters in the range of 1.2–1.6 nm. Depending on the respective performance requirements the purification effort also has to be considered as SWNT sorting of single species is still associated with higher costs.

The ability to fabricate high-mobility SWNT network FETs with reproducible device properties enables the integration of additional functionalities into those transistors aside from the common gate modulation. The second part of this work investigated a novel approach to implement such extra functionalities into (6,5) SWNT network FETs through the intentional modification of charge transport using photoswitchable spiropyran compounds as additives in the dielectric layer. These photochromic molecules and their photoisomerization to merocyanine had a large impact on the electron and hole mobilities. Upon UV illumination and thus isomerization from spiropyran to merocyanine the carrier mobilities were reduced by one order of magnitude, an effect that could be reversed, although not completely, by annealing or illumination with visible light. This switchability in addition to the gate modulation gave these modified (6,5) SWNT network FETs the ability to serve as basic optical memory device but at significantly higher carrier mobilities and thus drive currents compared to previous examples based on organic semiconductors. Using temperature-dependent current-voltage measurements the underlying mechanism was investigated and it became apparent that two main effects are most likely responsible for the observed carrier mobility reduction. On the one hand, charge carrier scattering induced by the strong dipoles of the spiropyran and merocyanine molecules reduced the intra-nanotube mobilities for both electrons and holes. On the other hand, electron trapping by protonated merocyanine species at the junctions impeded inter-nanotube hopping and resulted in higher activation energies for electrons.

This photoinduced carrier mobility modulation was successfully utilized to reversibly pattern areas of lower and higher resistance within the channel of a (6,5) SWNT network FET with micrometer resolution by selective exposure with UV or visible light. This way it was possible to direct the current predominantly through high mobility-areas of the channel as revealed by imaging of the EL of the ambipolar (6,5) SWNTs. Even more elaborate mobility and thus current density patterns could be created and erased again by local switching of the spiropyran isomers, even though their realization was limited by the respective deviation from the lateral electric field within the FET channel.

Although the here presented approach showed potential to implement light-responsiveness in SWNT network FETs, some obstacles still remain for the realization of actual multifunctional devices. Most importantly, the observed incomplete reverse isomerization from merocyanine to spiropyran needs to be tackled to retain the required switchability over a vast number of switching cycles. One promising route to address this issue could be the covalent functionalization of the wrapping polymer chains with spiropyran moieties instead of the simple incorporation of spiropyran in the dielectric as recently shown for two-terminal devices based on (6,5) SWNT/polymer hybrid films.[428] In this way, a uniform distribution of photoactive spiropyran-units with a defined distance to the SWNTs and from each other could be realized, thus preventing unwanted aggregation of the merocyanine isomers and resulting in a much more controlled interaction with the active layer. A substantially improved cyclability could eventually pave the way for next-generation SWNT network FETs and applications, e.g., in the fields of optical sensing or even neuromorphic computing.[429]

To conclude, semiconducting SWNT networks are a fascinating and intriguing material that by now can be readily prepared from purified dispersions while exhibiting competitive device performances when integrated into FETs. However, various network and parameter variations still remain a problem for large-scale application. This work provides new insights into the fundamental charge transport and its limits in those networks and formulates a rational guideline for FET performance optimizations by tailoring the network composition. The deliberate modification of charge transport in SWNT network FETs additionally offers a range of possibilities to integrate further device functionalities for applications that go beyond simple circuits. Overall, semiconducting nanotube networks have the potential to enable future developments of flexible, solution-processed circuits that operate at high frequencies and can be tuned by external stimuli such as light.

BIBLIOGRAPHY

(1) Gaviria Rojas, W. A.; Hersam, M. C. *Advanced Materials* **2020**, *32*, 1905654, DOI: `10.1002/adma.201905654`.

(2) Haensch, W.; Nowak, E. J.; Dennard, R. H.; Solomon, P. M.; Bryant, A.; Dokumaci, O. H.; Kumar, A.; Wang, X.; Johnson, J. B.; Fischetti, M. V. *IBM Journal of Research and Development* **2006**, *50*, 339–361, DOI: `10.1147/rd.504.0339`.

(3) Ahmed, K.; Schuegraf, K. *IEEE Spectrum* **2011**, *48*, 50–66, DOI: `10.1109/MSPEC.2011.6056626`.

(4) Tulevski, G. S.; Franklin, A. D.; Frank, D.; Lobez, J. M.; Cao, Q.; Park, H.; Afzali, A.; Han, S.-J.; Hannon, J. B.; Haensch, W. *ACS Nano* **2014**, *8*, 8730–8745, DOI: `10.1021/nn503627h`.

(5) Chang, J. S.; Facchetti, A. F.; Reuss, R. *IEEE Journal on Emerging and Selected Topics in Circuits and Systems* **2017**, *7*, 7–26, DOI: `10.1109/JETCAS.2017.2673863`.

(6) Petti, L.; Münzenrieder, N.; Vogt, C.; Faber, H.; Büthe, L.; Cantarella, G.; Bottacchi, F.; Anthopoulos, T. D.; Tröster, G. *Applied Physics Reviews* **2016**, *3*, 021303, DOI: `10.1063/1.4953034`.

(7) Nish, A.; Hwang, J.-Y.; Doig, J.; Nicholas, R. J. *Nature Nanotechnology* **2007**, *2*, 640–646, DOI: `10.1038/nnano.2007.290`.

(8) Graf, A.; Zakharko, Y.; Schießl, S. P.; Backes, C.; Pfohl, M.; Flavel, B. S.; Zaumseil, J. *Carbon* **2016**, *105*, 593–599, DOI: `10.1016/j.carbon.2016.05.002`.

(9) Miyata, Y.; Shiozawa, K.; Asada, Y.; Ohno, Y.; Kitaura, R.; Mizutani, T.; Shinohara, H. *Nano Research* **2011**, *4*, 963–970, DOI: `10.1007/s12274-011-0152-7`.

(10) Liang, X.; Xia, J.; Dong, G.; Tian, B.; Peng, L. *Topics in Current Chemistry* **2016**, *374*, 80, DOI: `10.1007/s41061-016-0083-6`.

(11) Zhao, J.; Chi, Z.; Yang, Z.; Chen, X.; Arnold, M. S.; Zhang, Y.; Xu, J.; Chi, Z.; Aldred, M. P. *Nanoscale* **2018**, *10*, 5764–5792, DOI: `10.1039/C7NR09472H`.

(12) Xiang, L.; Zhang, H.; Hu, Y.; Peng, L.-M. *Journal of Materials Chemistry C* **2018**, *6*, 7714–7727, DOI: `10.1039/C8TC02280A`.

(13) Hirsch, A. *Nature Materials* **2010**, *9*, 868–871, DOI: `10.1038/nmat2885`.

(14) Kroto, H. W.; Heath, J. R.; O'Brien, S. C.; Curl, R. F.; Smalley, R. E. *Nature* **1985**, *318*, 162–163, DOI: `10.1038/318162a0`.

(15) Dennler, G.; Scharber, M. C.; Brabec, C. J. *Advanced Materials* **2009**, *21*, 1323–1338, DOI: `10.1002/adma.200801283`.

(16) Partha, R.; Conyers, J. L. *International Journal of Nanomedicine* **2009**, *4*, 261–275, DOI: `10.2147/IJN.S5964`.

(17) Novoselov, K. S.; Geim, A. K.; Morozov, S. V.; Jiang, D.; Zhang, Y.; Dubonos, S. V.; Grigorieva, I. V.; Firsov, A. A. *Science* **2004**, *306*, 666–669, DOI: `10.1126/science.1102896`.

(18) Geim, A. K.; Novoselov, K. S. *Nature Materials* **2007**, *6*, 183–191, DOI: `10.1038/nmat1849`.

(19) Avouris, P. *Nano Letters* **2010**, *10*, 4285–4294, DOI: `10.1021/nl102824h`.

(20) Balandin, A. A. *Nature Materials* **2011**, *10*, 569–581, DOI: `10.1038/nmat3064`.

(21) Bonaccorso, F.; Sun, Z.; Hasan, T.; Ferrari, A. C. *Nature Photonics* **2010**, *4*, 611–622, DOI: `10.1038/nphoton.2010.186`.

(22) Lee, C.; Wei, X.; Kysar, J. W.; Hone, J. *Science* **2008**, *321*, 385–388, DOI: `10.1126/science.1157996`.

(23) Iijima, S. *Nature* **1991**, *354*, 56–58, DOI: `10.1038/354056a0`.

(24) Iijima, S.; Ichihashi, T. *Nature* **1993**, *363*, 603–605, DOI: `10.1038/363603a0`.

(25) Wang, X.; Li, Q.; Xie, J.; Jin, Z.; Wang, J.; Li, Y.; Jiang, K.; Fan, S. *Nano Letters* **2009**, *9*, 3137–3141, DOI: `10.1021/nl901260b`.

(26) Baughman, R. H.; Zakhidov, A. A.; de Heer, W. A. *Science* **2002**, *297*, 787–92, DOI: `10.1126/science.1060928`.

(27) Saito, R.; Fujita, M.; Dresselhaus, G.; Dresselhaus, M. S. *Applied Physics Letters* **1992**, *60*, 2204–2206, DOI: `10.1063/1.107080`.

(28) Léonard, F., *The Physics of Carbon Nanotube Devices*; William Andrew: Norwich, 2009.

(29) Wong, H.-S. P.; Akinwande, D., *Carbon Nanotube and Graphene Device Physics*; Cambridge University Press: Cambridge, 2011.

(30) Charlier, J.-C.; Blase, X.; Roche, S. *Reviews of Modern Physics* **2007**, *79*, 677–732, DOI: `10.1103/RevModPhys.79.677`.

(31) Reich, S.; Thomsen, C.; Maltzsch, J., *Carbon Nanotubes: Basic Concepts and Physical Properties*; WILEY-VCH Verlag: Weinheim, 2004.

(32) Saito, R.; Dresselhaus, G; Dresselhaus, M. S., *Physical Properties of Carbon Nanotubes*; Imperial College Press: London, 1998, DOI: `10.1142/p080`.

(33) Reich, S.; Maultzsch, J.; Thomsen, C.; Ordejón, P. *Physical Review B* **2002**, *66*, 035412, DOI: `10.1103/PhysRevB.66.035412`.

(34) Saito, R.; Dresselhaus, G.; Dresselhaus, M. S. *Physical Review B* **2000**, *61*, 2981–2990, DOI: `10.1103/PhysRevB.61.2981`.

(35) Samsonidze, G. G.; Saito, A. R.; Jorio, D. A.; Pimenta, E. M. A.; Souza Filho, E. A. G.; Grüneis, F. A.; Dresselhaus, D. G.; Dresselhausa, M. S. *Journal of Nanoscience and Nanotechnology* **2003**, *3*, 431–458, DOI: `10.1166/jnn.2003.231`.

(36) Ilani, S.; McEuen, P. L. *Annual Review of Condensed Matter Physics* **2010**, *1*, 1–25, DOI: `10.1146/annurev-conmatphys-070909-103928`.

(37) Wilder, J. W. G.; Venema, L. C.; Rinzler, A. G.; Smalley, R. E.; Dekker, C. *Nature* **1998**, *391*, 59–62, DOI: `10.1038/34139`.

(38) O'Connell, M. J.; Bachilo, S. M.; Huffman, C. B.; Moore, V. C.; Strano, M. S.; Haroz, E. H.; Rialon, K. L.; Boul, P. J.; Noon, W. H.; Kittrell, C.; Ma, J.; Hauge, R. H.; Weisman, R. B.; Smalley, R. E. *Science* **2002**, *297*, 593–596, DOI: `10.1126/science.1072631`.

(39) Bachilo, S. M.; Strano, M.; Kittrell, C.; Hauge, R. H.; Smalley, R. E.; Weisman, R. B. *Science* **2002**, *298*, 2361–2366, DOI: `10.1126/science.1078727`.

(40) Vaisman, L.; Wagner, H. D.; Marom, G. *Advances in Colloid and Interface Science* **2006**, *128-130*, 37–46, DOI: `10.1016/j.cis.2006.11.007`.

(41) Reich, S; Thomsen, C; Ordejón, P. *Physical Review B* **2002**, *65*, 155411, DOI: `10.1103/PhysRevB.65.155411`.

(42) Spataru, C. D.; Ismail-Beigi, S.; Benedict, L. X.; Louie, S. G. *Physical Review Letters* **2004**, *92*, 077402, DOI: `10.1103/PhysRevLett.92.077402`.

(43) Wang, F.; Dukovic, G.; Brus, L. E.; Heinz, T. F. *Science* **2005**, *308*, 838–41, DOI: `10.1126/science.1110265`.

(44) Maultzsch, J.; Pomraenke, R.; Reich, S.; Chang, E.; Prezzi, D.; Ruini, A.; Molinari, E.; Strano, M. S.; Thomsen, C.; Lienau, C. *Physical Review B* **2005**, *72*, 241402, DOI: `10.1103/PhysRevB.72.241402`.

(45) Benedict, L. X.; Louie, S. G.; Cohen, M. L. *Physical Review B* **1995**, *52*, 8541–8549, DOI: `10.1103/PhysRevB.52.8541`.

(46) Lefebvre, J.; Fraser, J. M.; Finnie, P.; Homma, Y. *Physical Review B* **2004**, *69*, 075403, DOI: `10.1103/PhysRevB.69.075403`.

(47) Takase, M.; Ajiki, H.; Mizumoto, Y.; Komeda, K.; Nara, M.; Nabika, H.; Yasuda, S.; Ishihara, H.; Murakoshi, K. *Nature Photonics* **2013**, *7*, 550–554, DOI: `10.1038/nphoton.2013.129`.

(48) Kataura, H.; Kumazawa, Y.; Maniwa, Y.; Umezu, I.; Suzuki, S.; Ohtsuka, Y.; Achiba, Y. *Synthetic Metals* **1999**, *103*, 2555–2558, DOI: `10.1016/S0379-6779(98)00278-1`.

(49) Weisman, R. B.; Bachilo, S. M. *Nano Letters* **2003**, *3*, 1235–1238, DOI: `10.1021/nl034428i`.

(50) Lebedkin, S.; Hennrich, F.; Skipa, T.; Kappes, M. M. *The Journal of Physical Chemistry B* **2003**, *107*, 1949–1956, DOI: `10.1021/jp027096z`.

(51) Ichida, M.; Mizuno, S.; Tani, Y.; Saito, Y.; Nakamura, A. *Journal of the Physical Society of Japan* **1999**, *68*, 3131–3133, DOI: `10.1143/JPSJ.68.3131`.

(52) Liu, X.; Pichler, T.; Knupfer, M.; Golden, M. S.; Fink, J.; Kataura, H.; Achiba, Y. *Physical Review B* **2002**, *66*, 045411, DOI: `10.1103/PhysRevB.66.045411`.

(53) Graf, A.; Tropf, L.; Zakharko, Y.; Zaumseil, J.; Gather, M. C. *Nature Communications* **2016**, *7*, 13078, DOI: `10.1038/ncomms13078`.

(54) Vialla, F.; Roquelet, C.; Langlois, B.; Delport, G.; Santos, S. M.; Deleporte, E.; Roussignol, P.; Delalande, C.; Voisin, C.; Lauret, J.-S. *Physical Review Letters* **2013**, *111*, 137402, DOI: `10.1103/PhysRevLett.111.137402`.

(55) Streit, J. K.; Bachilo, S. M.; Ghosh, S.; Lin, C.-W.; Weisman, R. B. *Nano Letters* **2014**, *14*, 1530–1536, DOI: `10.1021/nl404791y`.

(56) Schöppler, F.; Mann, C.; Hain, T. C.; Neubauer, F. M.; Privitera, G.; Bonaccorso, F.; Chu, D.; Ferrari, A. C.; Hertel, T. *The Journal of Physical Chemistry C* **2011**, *115*, 14682–14686, DOI: `10.1021/jp205289h`.

(57) Oudjedi, L.; Parra-Vasquez, A. N. G.; Godin, A. G.; Cognet, L.; Lounis, B. *The Journal of Physical Chemistry Letters* **2013**, *4*, 1460–1464, DOI: `10.1021/jz4003372`.

(58) Dieing, T.; Hollricher, O.; Toporski, J., *Confocal Raman Microscopy*; Dieing, T., Hollricher, O., Toporski, J., Eds.; Springer Series in Optical Sciences, Vol. 158; Springer-Verlag Berlin Heidelberg: Berlin, Heidelberg, 2011, DOI: `10.1007/978-3-642-12522-5`.

(59) Maultzsch, J.; Telg, H.; Reich, S.; Thomsen, C. *Physical Review B* **2005**, *72*, 205438, DOI: `10.1103/PhysRevB.72.205438`.

(60) Dresselhaus, M. S.; Jorio, A.; Hofmann, M.; Dresselhaus, G.; Saito, R. *Nano Letters* **2010**, *10*, 751–758, DOI: `10.1021/nl904286r`.

(61) Jorio, A.; Souza Filho, A. G.; Dresselhaus, G.; Dresselhaus, M. S.; Saito, R.; Hafner, J. H.; Lieber, C. M.; Matinaga, F. M.; Dantas, M. S. S.; Pimenta, M. A. *Physical Review B* **2001**, *63*, 245416, DOI: `10.1103/PhysRevB.63.245416`.

(62) Jorio, A.; Saito, R.; Hafner, J. H.; Lieber, C. M.; Hunter, M.; McClure, T.; Dresselhaus, G.; Dresselhaus, M. S. *Physical Review Letters* **2001**, *86*, 1118–1121, DOI: `10.1103/PhysRevLett.86.1118`.

(63) Dresselhaus, M. S.; Dresselhaus, G.; Jorio, A.; Souza Filho, A. G.; Pimenta, M. A.; Saito, R. *Accounts of Chemical Research* **2002**, *35*, 1070–1078, DOI: `10.1021/ar0101537`.

(64) Rao, A. M.; Richter, E.; Bandow, S.; Chase, B.; Eklund, P. C.; Williams, K. A.; Fang, S.; Subbaswamy, K. R.; Menon, M.; Thess, A.; Smalley, R. E.; Dresselhaus, G.; Dresselhaus, M. S. *Science* **1997**, *275*, 187–191, DOI: `10.1126/science.275.5297.187`.

(65) Jorio, A; Pimenta, M. A.; Filho, A. G. S.; Saito, R; Dresselhaus, G; Dresselhaus, M. S. *New Journal of Physics* **2003**, *5*, 139, DOI: `10.1088/1367-2630/5/1/139`.

(66) Brown, S. D. M.; Jorio, A.; Dresselhaus, M. S.; Dresselhaus, G. *Physical Review B* **2001**, *64*, 073403, DOI: `10.1103/PhysRevB.64.073403`.

(67) Dresselhaus, M.; Dresselhaus, G.; Jorio, A.; Souza Filho, A.; Saito, R. *Carbon* **2002**, *40*, 2043–2061, DOI: `10.1016/S0008-6223(02)00066-0`.

(68) Jorio, A.; Dresselhaus, G.; Dresselhaus, M. S.; Souza, M.; Dantas, M. S. S.; Pimenta, M. A.; Rao, A. M.; Saito, R.; Liu, C.; Cheng, H. M. *Physical Review Letters* **2000**, *85*, 2617–2620, DOI: `10.1103/PhysRevLett.85.2617`.

(69) Magg, M.; Kadria-Vili, Y.; Oulevey, P.; Weisman, R. B.; Bürgi, T. *The Journal of Physical Chemistry Letters* **2016**, *7*, 221–225, DOI: `10.1021/acs.jpclett.5b02612`.

(70) Dragin, F.; Pénicaud, A.; Iurlo, M.; Marcaccio, M.; Paolucci, F.; Anglaret, E.; Martel, R. *ACS Nano* **2011**, *5*, 9892–9897, DOI: `10.1021/nn203591j`.

(71) Kalbac, M.; Kavan, L. *Carbon* **2010**, *48*, 832–838, DOI: `10.1016/j.carbon.2009.10.036`.

(72) Tsang, J. C.; Freitag, M.; Perebeinos, V.; Liu, J.; Avouris, P. *Nature Nanotechnology* **2007**, *2*, 725–730, DOI: `10.1038/nnano.2007.321`.

(73) Grimm, S.; Schießl, S. P.; Zakharko, Y.; Rother, M.; Brohmann, M.; Zaumseil, J. *Carbon* **2017**, *118*, 261–267, DOI: `10.1016/j.carbon.2017.03.040`.

(74) Prasek, J.; Drbohlavova, J.; Chomoucka, J.; Hubalek, J.; Jasek, O.; Adam, V.; Kizek, R. *Journal of Materials Chemistry* **2011**, *21*, 15872, DOI: `10.1039/c1jm12254a`.

(75) Nessim, G. D. *Nanoscale* **2010**, *2*, 1306, DOI: `10.1039/b9nr00427k`.

(76) Jourdain, V.; Bichara, C. *Carbon* **2013**, *58*, 2–39, DOI: `10.1016/j.carbon.2013.02.046`.

(77) Nikolaev, P.; Bronikowski, M. J.; Bradley, R.; Rohmund, F.; Colbert, D. T.; Smith, K.; Smalley, R. E. *Chemical Physics Letters* **1999**, *313*, 91–97, DOI: `10.1016/S0009-2614(99)01029-5`.

(78) Bronikowski, M. J.; Willis, P. A.; Colbert, D. T.; Smith, K. A.; Smalley, R. E. *Journal of Vacuum Science & Technology A: Vacuum, Surfaces, and Films* **2001**, *19*, 1800–1805, DOI: `10.1116/1.1380721`.

(79) Lolli, G.; Zhang, L.; Balzano, L.; Sakulchaicharoen, N.; Tan, Y.; Resasco, D. E. *The Journal of Physical Chemistry B* **2006**, *110*, 2108–2115, DOI: `10.1021/jp056095e`.

(80) Bachilo, S. M.; Balzano, L.; Herrera, J. E.; Pompeo, F.; Resasco, D. E.; Weisman, R. B. *Journal of the American Chemical Society* **2003**, *125*, 11186–11187, DOI: `10.1021/ja036622c`.

(81) Guo, T.; Nikolaev, P.; Thess, A.; Colbert, D.; Smalley, R. *Chemical Physics Letters* **1995**, *243*, 49–54, DOI: `10.1016/0009-2614(95)00825-O`.

(82) Journet, C.; Maser, W. K.; Bernier, P.; Loiseau, A.; de la Chapelle, M. L.; Lefrant, S.; Deniard, P.; Lee, R.; Fischer, J. E. *Nature* **1997**, *388*, 756–758, DOI: `10.1038/41972`.

(83) Ando, Y.; Zhao, X.; Hirahara, K.; Suenaga, K.; Bandow, S.; Iijima, S. *Chemical Physics Letters* **2000**, *323*, 580–585, DOI: `10.1016/S0009-2614(00)00556-X`.

(84) Smiljanic, O.; Stansfield, B.; Dodelet, J.-P.; Serventi, A.; Désilets, S. *Chemical Physics Letters* **2002**, *356*, 189–193, DOI: `10.1016/S0009-2614(02)00132-X`.

(85) Hahn, J.; Han, J. H.; Yoo, J.-E.; Jung, H. Y.; Suh, J. S. *Carbon* **2004**, *42*, 877–883, DOI: `10.1016/j.carbon.2004.01.073`.

(86) Kim, K. S.; Cota-Sanchez, G.; Kingston, C. T.; Imris, M.; Simard, B.; Soucy, G. *Journal of Physics D: Applied Physics* **2007**, *40*, 2375–2387, DOI: `10.1088/0022-3727/40/8/S17`.

(87) Kim, K. S.; Imris, M.; Shahverdi, A.; Alinejad, Y.; Soucy, G. *The Journal of Physical Chemistry C* **2009**, *113*, 4340–4348, DOI: `10.1021/jp810096k`.

(88) Kim, K. S.; Kingston, C. T.; Ruth, D.; Barnes, M.; Simard, B. *Chemical Engineering Journal* **2014**, *250*, 331–341, DOI: `10.1016/j.cej.2014.03.117`.

(89) Coleman, J. N. *Advanced Functional Materials* **2009**, *19*, 3680–3695, DOI: `10.1002/adfm.200901640`.

(90) Bergin, S. D.; Nicolosi, V.; Streich, P. V.; Giordani, S.; Sun, Z.; Windle, A. H.; Ryan, P.; Niraj, N. P. P.; Wang, Z.-T. T.; Carpenter, L.; Blau, W. J.; Boland, J. J.; Hamilton, J. P.; Coleman, J. N. *Advanced Materials* **2008**, *20*, 1876–1881, DOI: `10.1002/adma.200702451`.

(91) Mouri, S.; Miyauchi, Y.; Matsuda, K. *The Journal of Physical Chemistry C* **2012**, *116*, 10282–10286, DOI: `10.1021/jp212040y`.

(92) Hennrich, F.; Krupke, R.; Arnold, K.; Rojas Stütz, J. A.; Lebedkin, S.; Koch, T.; Schimmel, T.; Kappes, M. M. *The Journal of Physical Chemistry B* **2007**, *111*, 1932–1937, DOI: `10.1021/jp065262n`.

(93) McDonald, T. J.; Engtrakul, C.; Jones, M.; Rumbles, G.; Heben, M. J. *The Journal of Physical Chemistry B* **2006**, *110*, 25339–25346, DOI: `10.1021/jp065281x`.

(94) White, B.; Banerjee, S.; O'Brien, S.; Turro, N. J.; Herman, I. P. *Journal of Physical Chemistry C* **2007**, *111*, 13684–13690, DOI: `10.1021/jp070853e`.

(95) Angelikopoulos, P.; Bock, H. *Physical Chemistry Chemical Physics* **2012**, *14*, 9546–9557, DOI: `10.1039/c2cp23436j`.

(96) Nakashima, N.; Okuzono, S.; Murakami, H.; Nakai, T.; Yoshikawa, K. *Chemistry Letters* **2003**, *32*, 456–457, DOI: `10.1246/cl.2003.456`.

(97) Zheng, M.; Jagota, A.; Semke, E. D.; Diner, B. A.; Mclean, R. S.; Lustig, S. R.; Richardson, R. E.; Tassi, N. G. *Nature Materials* **2003**, *2*, 338–342, DOI: `10.1038/nmat877`.

(98) Zheng, M.; Jagota, A.; Strano, M. S.; Santos, A. P.; Barone, P.; Chou, S. G.; Diner, B. A.; Dresselhaus, M. S.; McLean, R. S.; Onoa, G. B.; Samsonidze, G. G.; Semke, E. D.; Usrey, M.; Walls, D. J. *Science* **2003**, *302*, 1545–1548, DOI: `10.1126/science.1091911`.

(99) Tu, X.; Manohar, S.; Jagota, A.; Zheng, M. *Nature* **2009**, *460*, 250–253, DOI: `10.1038/nature08116`.

(100) Arnold, M. S.; Stupp, S. I.; Hersam, M. C. *Nano Letters* **2005**, *5*, 713–718, DOI: `10.1021/nl050133o`.

(101) Arnold, M. S.; Green, A. A.; Hulvat, J. F.; Stupp, S. I.; Hersam, M. C. *Nat. Nanotechnol.* **2006**, *1*, 60–65, DOI: `10.1038/nnano.2006.52`.

(102) Liu, H.; Nishide, D.; Tanaka, T.; Kataura, H. *Nature Communications* **2011**, *2*, 309, DOI: `10.1038/ncomms1313`.

(103) Liu, H.; Tanaka, T.; Urabe, Y.; Kataura, H. *Nano Letters* **2013**, *13*, 1996–2003, DOI: `10.1021/nl400128m`.

(104) Hirano, A.; Tanaka, T.; Kataura, H. *ACS Nano* **2012**, *6*, 10195–10205, DOI: `10.1021/nn303985x`.

(105) Tulevski, G. S.; Franklin, A. D.; Afzali, A. *ACS Nano* **2013**, *7*, 2971–2976, DOI: `10.1021/nn400053k`.

(106) Fagan, J. A.; Khripin, C. Y.; Silvera Batista, C. A.; Simpson, J. R.; Hároz, E. H.; Hight Walker, A. R.; Zheng, M. *Advanced Materials* **2014**, *26*, 2800–2804, DOI: `10.1002/adma.201304873`.

(107) Fagan, J. A.; Hároz, E. H.; Ihly, R.; Gui, H.; Blackburn, J. L.; Simpson, J. R.; Lam, S.; Hight Walker, A. R.; Doorn, S. K.; Zheng, M. *ACS Nano* **2015**, *9*, 5377–5390, DOI: `10.1021/acsnano.5b01123`.

(108) Samanta, S. K.; Fritsch, M.; Scherf, U.; Gomulya, W.; Bisri, S. Z.; Loi, M. A. *Accounts of Chemical Research* **2014**, *47*, 2446–2456, DOI: `10.1021/ar500141j`.

(109) Chen, F.; Wang, B.; Chen, Y.; Li, L.-J. *Nano Letters* **2007**, *7*, 3013–3017, DOI: `10.1021/nl071349o`.

(110) Gomulya, W.; Costanzo, G. D.; De Carvalho, E. J. F.; Bisri, S. Z.; Derenskyi, V.; Fritsch, M.; Fröhlich, N.; Allard, S.; Gordiichuk, P.; Herrmann, A.; Marrink, S. J.; Dos Santos, M. C.; Scherf, U.; Loi, M. A. *Advanced Materials* **2013**, *25*, 2948–2956, DOI: `10.1002/adma.201300267`.

(111) Mistry, K. S.; Larsen, B. A.; Blackburn, J. L. *ACS Nano* **2013**, *7*, 2231–2239, DOI: `10.1021/nn305336x`.

(112) Tange, M.; Okazaki, T.; Iijima, S. *ACS Applied Materials & Interfaces* **2012**, *4*, 6458–6462, DOI: `10.1021/am302327j`.

(113) Lemasson, F. A.; Strunk, T.; Gerstel, P.; Hennrich, F.; Lebedkin, S.; Barner-Kowollik, C.; Wenzel, W.; Kappes, M. M.; Mayor, M. *Journal of the American Chemical Society* **2011**, *133*, 652–655, DOI: `10.1021/ja105722u`.

(114) Lemasson, F.; Berton, N.; Tittmann, J.; Hennrich, F.; Kappes, M. M.; Mayor, M. *Macromolecules* **2012**, *45*, 713–722, DOI: `10.1021/ma201890g`.

(115) Lee, H. W. et al. *Nature Communications* **2011**, *2*, 541, DOI: `10.1038/ncomms1545`.

(116) Wang, H.; Koleilat, G. I.; Liu, P.; Jiménez-Osés, G.; Lai, Y.-C.; Vosgueritchian, M.; Fang, Y.; Park, S.; Houk, K. N.; Bao, Z. *ACS Nano* **2014**, *8*, 2609–2617, DOI: `10.1021/nn406256y`.

(117) Lei, T.; Lai, Y.-C.; Hong, G.; Wang, H.; Hayoz, P.; Weitz, R. T.; Chen, C.; Dai, H.; Bao, Z. *Small* **2015**, *11*, 2946–2954, DOI: `10.1002/smll.201403761`.

(118) Lei, T.; Pitner, G.; Chen, X.; Hong, G.; Park, S.; Hayoz, P.; Weitz, R. T.; Wong, H.-S. P.; Bao, Z. *Advanced Electronic Materials* **2016**, *2*, 1500299, DOI: `10.1002/aelm.201500299`.

(119) Berton, N.; Lemasson, F.; Tittmann, J.; Stürzl, N.; Hennrich, F.; Kappes, M. M.; Mayor, M. *Chemistry of Materials* **2011**, *23*, 2237–2249, DOI: `10.1021/cm200275v`.

(120) Ozawa, H.; Fujigaya, T.; Niidome, Y.; Hotta, N.; Fujiki, M.; Nakashima, N. *Journal of the American Chemical Society* **2011**, *133*, 2651–2657, DOI: `10.1021/ja109399f`.

(121) Ouyang, J.; Ding, J.; Lefebvre, J.; Li, Z.; Guo, C.; Kell, A. J.; Malenfant, P. R. L. *ACS Nano* **2018**, *12*, 1910–1919, DOI: `10.1021/acsnano.7b08818`.

(122) Gao, J.; Loi, M. A.; De Carvalho, E. J. F.; Dos Santos, M. C. *ACS Nano* **2011**, *5*, 3993–3999, DOI: `10.1021/nn200564n`.

(123) Jakubka, F.; Schießl, S. P.; Martin, S.; Englert, J. M.; Hauke, F.; Hirsch, A.; Zaumseil, J. *ACS Macro Letters* **2012**, *1*, 815–819, DOI: `10.1021/mz300147g`.

(124) Schießl, S. P.; Fröhlich, N.; Held, M.; Gannott, F.; Schweiger, M.; Forster, M.; Scherf, U.; Zaumseil, J. *ACS Applied Materials & Interfaces* **2015**, *7*, 682–689, DOI: `10.1021/am506971b`.

(125) Hwang, J.-Y.; Nish, A.; Doig, J.; Douven, S.; Chen, C.-W.; Chen, L.-C.; Nicholas, R. J. *Journal of the American Chemical Society* **2008**, *130*, 3543–3553, DOI: `10.1021/ja0777640`.

(126) Han, J.; Ji, Q.; Qiu, S.; Li, H.; Zhang, S.; Jin, H.; Li, Q. *Chem. Commun.* **2015**, *51*, 4712–4714, DOI: `10.1039/C5CC00167F`.

(127) Wang, H.; Hsieh, B.; Jiménez-Osés, G.; Liu, P.; Tassone, C. J.; Diao, Y.; Lei, T.; Houk, K. N.; Bao, Z. *Small* **2015**, *11*, 126–133, DOI: `10.1002/smll.201401890`.

(128) Gomulya, W.; Rios, J. M. S.; Derenskyi, V.; Bisri, S. Z.; Jung, S.; Fritsch, M.; Allard, S.; Scherf, U.; Dos Santos, M. C.; Loi, M. A. *Carbon* **2015**, *84*, 66–73, DOI: `10.1016/j.carbon.2014.11.037`.

(129) Liang, S.; Li, H.; Flavel, B. S.; Adronov, A. *Chemistry - A European Journal* **2018**, *24*, 9799–9806, DOI: `10.1002/chem.201801515`.

(130) Ozawa, H.; Ide, N.; Fujigaya, T.; Niidome, Y.; Nakashima, N. *Chemistry Letters* **2011**, *40*, 239–241, DOI: `10.1246/cl.2011.239`.

(131) Tans, S. J.; Verschueren, A. R. M.; Dekker, C. *Nature* **1998**, *393*, 49–52, DOI: `10.1038/29954`.

(132) Martel, R.; Schmidt, T.; Shea, H. R.; Hertel, T.; Avouris, P. *Applied Physics Letters* **1998**, *73*, 2447–2449, DOI: `10.1063/1.122477`.

(133) Schindler, G.; Steinlesberger, G.; Engelhardt, M.; Steinhögl, W. *Solid-State Electronics* **2003**, *47*, 1233–1236, DOI: `10.1016/S0038-1101(03)00042-X`.

(134) Dürkop, T.; Getty, S. A.; Cobas, E.; Fuhrer, M. S. *Nano Letters* **2004**, *4*, 35–39, DOI: `10.1021/nl034841q`.

(135) Javey, A.; Guo, J.; Wang, Q.; Lundstrom, M.; Dai, H. *Nature* **2003**, *424*, 654–657, DOI: `10.1038/nature01797`.

(136) Purewal, M. S.; Hong, B. H.; Ravi, A.; Chandra, B.; Hone, J.; Kim, P. *Physical Review Letters* **2007**, *98*, 2–5, DOI: `10.1103/PhysRevLett.98.186808`.

(137) Suzuura, H.; Ando, T. *Physical Review B* **2002**, *65*, 235412, DOI: `10.1103/PhysRevB.65.235412`.

(138) Jiang, J.; Saito, R.; Samsonidze, G. G.; Chou, S. G.; Jorio, A.; Dresselhaus, G.; Dresselhaus, M. S. *Physical Review B* **2005**, *72*, 235408, DOI: `10.1103/PhysRevB.72.235408`.

(139) Adam, E.; Aguirre, C. M.; Marty, L.; St-Antoine, B. C.; Meunier, F.; Desjardins, P.; Ménard, D.; Martel, R. *Nano Letters* **2008**, *8*, 2351–2355, DOI: `10.1021/nl8011825`.

(140) Chen, Y.-F.; Fuhrer, M. S. *Physical Review Letters* **2005**, *95*, 236803, DOI: `10.1103/PhysRevLett.95.236803`.

(141) Yao, Z.; Kane, C. L.; Dekker, C. *Physical Review Letters* **2000**, *84*, 2941–2944, DOI: `10.1103/PhysRevLett.84.2941`.

(142) Javey, A.; Guo, J.; Paulsson, M.; Wang, Q.; Mann, D.; Lundstrom, M.; Dai, H. *Physical Review Letters* **2004**, *92*, 106804, DOI: `10.1103/PhysRevLett.92.106804`.

(143) Liao, A.; Zhao, Y.; Pop, E. *Physical Review Letters* **2008**, *101*, 256804, DOI: `10.1103/PhysRevLett.101.256804`.

(144) Perebeinos, V.; Avouris, P. *Physical Review B* **2006**, *74*, 121410, DOI: `10.1103/PhysRevB.74.121410`.

(145) Park, J.-Y.; Rosenblatt, S.; Yaish, Y.; Sazonova, V.; Üstünel, H.; Braig, S.; Arias, T. A.; Brouwer, P. W.; McEuen, P. L. *Nano Letters* **2004**, *4*, 517–520, DOI: `10.1021/nl035258c`.

(146) Pop, E.; Mann, D. A.; Goodson, K. E.; Dai, H. *Journal of Applied Physics* **2007**, *101*, 093710, DOI: `10.1063/1.2717855`.

(147) Kong, J.; Yenilmez, E.; Tombler, T. W.; Kim, W.; Dai, H.; Laughlin, R. B.; Liu, L.; Jayanthi, C. S.; Wu, S. Y. *Physical Review Letters* **2001**, *87*, 106801, DOI: `10.1103/PhysRevLett.87.106801`.

(148) Bandaru, P. R. *Journal of Nanoscience and Nanotechnology* **2007**, *7*, 1239–1267, DOI: `10.1166/jnn.2007.307`.

(149) Liang, W.; Bockrath, M.; Bozovic, D.; Hafner, J. H.; Tinkham, M; Park, H. *Nature* **2001**, *411*, 665–669, DOI: `10.1038/35079517`.

(150) Biercuk, M. J.; Mason, N.; Martin, J.; Yacoby, A.; Marcus, C. M. *Physical Review Letters* **2005**, *94*, 026801, DOI: `10.1103/PhysRevLett.94.026801`.

(151) Li, S.; Yu, Z.; Rutherglen, C.; Burke, P. J. *Nano Letters* **2004**, *4*, 2003–2007, DOI: `10.1021/nl048687z`.

(152) Znidarsic, A.; Kaskela, A.; Laiho, P.; Gaberscek, M.; Ohno, Y.; Nasibulin, A. G.; Kauppinen, E. I.; Hassanien, A. *The Journal of Physical Chemistry C* **2013**, *117*, 13324–13330, DOI: `10.1021/jp403983y`.

(153) Perebeinos, V.; Tersoff, J.; Avouris, P. *Nano Letters* **2006**, *6*, 205–208, DOI: `10.1021/nl052044h`.

(154) Ilani, S.; Donev, L. A. K.; Kindermann, M.; McEuen, P. L. *Nature Physics* **2006**, *2*, 687–691, DOI: `10.1038/nphys412`.

(155) Liang, J.; Akinwande, D.; Wong, H.-S. P. *Journal of Applied Physics* **2008**, *104*, 064515, DOI: `10.1063/1.2986216`.

(156) Shimotani, H.; Tsuda, S.; Yuan, H.; Yomogida, Y.; Moriya, R.; Takenobu, T.; Yanagi, K.; Iwasa, Y. *Advanced Functional Materials* **2014**, *24*, 3305–3311, DOI: `10.1002/adfm.201303566`.

(157) Rosenblatt, S.; Yaish, Y.; Park, J.; Gore, J.; Sazonova, V.; McEuen, P. L. *Nano Letters* **2002**, *2*, 869–872, DOI: `10.1021/nl025639a`.

(158) Zhou, X.; Park, J.-Y.; Huang, S.; Liu, J.; McEuen, P. L. *Physical Review Letters* **2005**, *95*, 146805, DOI: `10.1103/PhysRevLett.95.146805`.

(159) Perebeinos, V.; Tersoff, J.; Avouris, P. *Physical Review Letters* **2005**, *94*, 086802, DOI: `10.1103/PhysRevLett.94.086802`.

(160) Martel, R.; Derycke, V.; Lavoie, C.; Appenzeller, J.; Chan, K. K.; Tersoff, J.; Avouris, P. *Physical Review Letters* **2001**, *87*, 256805, DOI: `10.1103/PhysRevLett.87.256805`.

(161) Heinze, S.; Tersoff, J.; Martel, R.; Derycke, V.; Appenzeller, J.; Avouris, P. *Physical Review Letters* **2002**, *89*, 106801, DOI: `10.1103/PhysRevLett.89.106801`.

(162) Jarillo-Herrero, P.; Sapmaz, S.; Dekker, C.; Kouwenhoven, L. P.; van der Zant, H. S. J. *Nature* **2004**, *429*, 389–392, DOI: `10.1038/nature02568`.

(163) Kim, W.; Javey, A.; Vermesh, O.; Wang, Q.; Li, Y.; Dai, H. *Nano Letters* **2003**, *3*, 193–198, DOI: `10.1021/nl0259232`.

(164) Aguirre, C. M.; Levesque, P. L.; Paillet, M.; Lapointe, F.; St-Antoine, B. C.; Desjardins, P.; Martel, R. *Advanced Materials* **2009**, *21*, 3087–3091, DOI: `10.1002/adma.200900550`.

(165) Fuhrer, M. S.; Nygard, J.; Shih, L.; Forero, M.; Yoon, Y.-G.; Mazzoni, M. S. C.; Choi, H. J.; Ihm, J.; Louie, S. G.; Zettl, A.; McEuen, P. L. *Science* **2000**, *288*, 494–497, DOI: `10.1126/science.288.5465.494`.

(166) Stadermann, M.; Papadakis, S. J.; Falvo, M. R.; Novak, J.; Snow, E.; Fu, Q.; Liu, J.; Fridman, Y.; Boland, J. J.; Superfine, R.; Washburn, S. *Physical Review B - Condensed Matter and Materials Physics* **2004**, *69*, 10–12, DOI: `10.1103/PhysRevB.69.201402`.

(167) Nirmalraj, P. N.; Lyons, P. E.; De, S.; Coleman, J. N.; Boland, J. J. *Nano Letters* **2009**, *9*, 3890–3895, DOI: `10.1021/nl9020914`.

(168) Garrett, M. P.; Ivanov, I. N.; Gerhardt, R. A.; Puretzky, A. A.; Geohegan, D. B. *Applied Physics Letters* **2010**, *97*, 163105, DOI: `10.1063/1.3490650`.

(169) Topinka, M. A.; Rowell, M. W.; Goldhaber-Gordon, D.; McGehee, M. D.; Hecht, D. S.; Gruner, G. *Nano Letters* **2009**, *9*, 1866–1871, DOI: `10.1021/nl803849e`.

(170) Snow, E. S.; Campbell, P. M.; Ancona, M. G.; Novak, J. P. *Applied Physics Letters* **2005**, *86*, 033105, DOI: `10.1063/1.1854721`.

(171) Kumar, S.; Murthy, J. Y.; Alam, M. A. *Physical Review Letters* **2005**, *95*, 066802, DOI: `10.1103/PhysRevLett.95.066802`.

(172) Hecht, D.; Hu, L.; Grüner, G. *Applied Physics Letters* **2006**, *89*, 133112, DOI: `10.1063/1.2356999`.

(173) Kumar, S.; Pimparkar, N.; Murthy, J. Y.; Alam, M. A. *Applied Physics Letters* **2006**, *88*, 123505, DOI: `10.1063/1.2187401`.

(174) Pimparkar, N.; Kocabas, C.; Seong Jun Kang; Rogers, J.; Alam, M. *IEEE Electron Device Letters* **2007**, *28*, 593–595, DOI: `10.1109/LED.2007.898256`.

(175) Rouhi, N.; Jain, D.; Burke, P. J. *ACS Nano* **2011**, *5*, 8471–8487, DOI: `10.1021/nn201828y`.

(176) Rouhi, N.; Jain, D.; Zand, K.; Burke, P. J. *Advanced Materials* **2011**, *23*, 94–99, DOI: `10.1002/adma.201003281`.

(177) Yanagi, K.; Udoguchi, H.; Sagitani, S.; Oshima, Y.; Takenobu, T.; Kataura, H.; Ishida, T.; Matsuda, K.; Maniwa, Y. *ACS Nano* **2010**, *4*, 4027–4032, DOI: `10.1021/nn101177n`.

(178) Itkis, M. E.; Pekker, A.; Tian, X.; Bekyarova, E.; Haddon, R. C. *Accounts of Chemical Research* **2015**, *48*, 2270–2279, DOI: `10.1021/acs.accounts.5b00107`.

(179) Gao, J.; Loo, Y.-L. L. *Advanced Functional Materials* **2015**, *25*, 105–110, DOI: `10.1002/adfm.201402407`.

(180) Mott, N. F.; Twose, W. D. *Advances in Physics* **1961**, *10*, 107–163, DOI: `10.1080/00018736100101271`.

(181) Mott, N. F. *The Philosophical Magazine: A Journal of Theoretical Experimental and Applied Physics* **1969**, *19*, 835–852, DOI: `10.1080/14786436908216338`.

(182) Le Comber, P. G.; Spear, W. E. *Physical Review Letters* **1970**, *25*, 509–511, DOI: `10.1103/PhysRevLett.25.509`.

(183) Horowitz, G.; Hajlaoui, R.; Delannoy, P. *Journal de Physique III* **1995**, *5*, 355–371, DOI: `10.1051/jp3:1995132`.

(184) Horowitz, G.; Hajlaoui, M. E.; Hajlaoui, R. *Journal of Applied Physics* **2000**, *87*, 4456–4463, DOI: `10.1063/1.373091`.

(185) Bässler, H. *physica status solidi (b)* **1993**, *175*, 15–56, DOI: `10.1002/pssb.2221750102`.

(186) Miller, A.; Abrahams, E. *Physical Review* **1960**, *120*, 745–755, DOI: `10.1103/PhysRev.120.745`.

(187) Tessler, N.; Preezant, Y.; Rappaport, N.; Roichman, Y. *Advanced Materials* **2009**, *21*, 2741–2761, DOI: `10.1002/adma.200803541`.

(188) Mott, N. *Journal of Non-Crystalline Solids* **1968**, *1*, 1–17, DOI: `10.1016/0022-3093(68)90002-1`.

(189) Mott, N. F.; Davis, E. A., *Electronic Processes in Non-Crystalline Materials*, 2nd ed.; Oxford University Press: New York, 1979.

(190) Ambegaokar, V.; Halperin, B. I.; Langer, J. S. *Physical Review B* **1971**, *4*, 2612–2620, DOI: `10.1103/PhysRevB.4.2612`.

(191) Sarachik, M. P.; Dai, P. *Europhysics Letters* **2002**, *59*, 100–106, DOI: `10.1209/epl/i2002-00164-y`.

(192) Kaiser, A. B.; Skákalová, V. *Chemical Society Reviews* **2011**, *40*, 3786, DOI: `10.1039/c0cs00103a`.

(193) Ravi, S.; Kaiser, A. B.; Bumby, C. W. *physica status solidi (b)* **2013**, *250*, 1463–1467, DOI: `10.1002/pssb.201300033`.

(194) Lee, S.-H.; Xu, Y.; Khim, D.; Park, W.-T.; Kim, D.-Y.; Noh, Y.-y. *ACS Applied Materials & Interfaces* **2016**, *8*, 32421–32431, DOI: `10.1021/acsami.6b06882`.

(195) Sheng, P.; Sichel, E. K.; Gittleman, J. I. *Physical Review Letters* **1978**, *40*, 1197–1200, DOI: `10.1103/PhysRevLett.40.1197`.

(196) Sheng, P. *Physical Review B* **1980**, *21*, 2180–2195, DOI: `10.1103/PhysRevB.21.2180`.

(197) Kaiser, A. B. *Advanced Materials* **2001**, *13*, 927–941, DOI: `10.1002/1521-4095(200107)13:12/13<927::AID-ADMA927>3.0.CO;2-B`.

(198) Van der Holst, J. J. M.; van Oost, F. W. A.; Coehoorn, R.; Bobbert, P. A. *Physical Review B* **2011**, *83*, 085206, DOI: `10.1103/PhysRevB.83.085206`.

(199) Pasveer, W. F.; Cottaar, J.; Tanase, C.; Coehoorn, R.; Bobbert, P. A.; Blom, P. W. M.; de Leeuw, D. M.; Michels, M. A. J. *Physical Review Letters* **2005**, *94*, 206601, DOI: `10.1103/PhysRevLett.94.206601`.

(200) Coehoorn, R.; Pasveer, W. F.; Bobbert, P. A.; Michels, M. A. J. *Physical Review B* **2005**, *72*, 155206, DOI: `10.1103/PhysRevB.72.155206`.

(201) Cottaar, J.; Koster, L. J. A.; Coehoorn, R.; Bobbert, P. A. *Physical Review Letters* **2011**, *107*, 136601, DOI: `10.1103/PhysRevLett.107.136601`.

(202) Schießl, S. P.; de Vries, X.; Rother, M.; Massé, A.; Brohmann, M.; Bobbert, P. A.; Zaumseil, J. *Physical Review Materials* **2017**, *1*, 046003, DOI: `10.1103/PhysRevMaterials.1.046003`.

(203) Tans, S. J.; Devoret, M. H.; Dai, H.; Thess, A.; Smalley, R. E.; Geerligs, L. J.; Dekker, C. *Nature* **1997**, *386*, 474–477, DOI: `10.1038/386474a0`.

(204) Sze, S.; Ng, K., *Physics of Semiconductor Devices*; John Wiley & Sons, Inc.: Hoboken, 2006.

(205) Shockley, W. *Proceedings of the IRE* **1952**, *40*, 1365–1376, DOI: `10.1142/9789814503464_0058`.

(206) Zaumseil, J.; Sirringhaus, H. *Chemical Reviews* **2007**, *107*, 1296–1323, DOI: `10.1021/cr0501543`.

(207) Kalb, W. L.; Batlogg, B. *Physical Review B - Condensed Matter and Materials Physics* **2010**, *81*, 1–13, DOI: `10.1103/PhysRevB.81.035327`.

(208) Schmechel, R.; Ahles, M.; von Seggern, H. *Journal of Applied Physics* **2005**, *98*, 084511, DOI: `10.1063/1.2106009`.

(209) Kang, M. S.; Frisbie, C. D. *ChemPhysChem* **2013**, *14*, 1547–1552, DOI: `10.1002/cphc.201300014`.

(210) Frank, D.; Dennard, R.; Nowak, E.; Solomon, P.; Taur, Y.; Hon-Sum Philip Wong *Proceedings of the IEEE* **2001**, *89*, 259–288, DOI: `10.1109/5.915374`.

(211) Chua, L.-L.; Ho, P. K. H.; Sirringhaus, H.; Friend, R. H. *Applied Physics Letters* **2004**, *84*, 3400–3402, DOI: `10.1063/1.1710716`.

(212) Uemura, T.; Rolin, C.; Ke, T.-H.; Fesenko, P.; Genoe, J.; Heremans, P.; Takeya, J. *Advanced Materials* **2016**, *28*, 151–155, DOI: `10.1002/adma.201503133`.

(213) Xu, Y.; Sun, H.; Liu, A.; Zhu, H.; Li, B.; Minari, T.; Balestra, F.; Ghibaudo, G.; Noh, Y.-y. *Advanced Functional Materials* **2018**, *28*, 1803907, DOI: `10.1002/adfm.201803907`.

(214) Lamport, Z. A.; Haneef, H. F.; Anand, S.; Waldrip, M.; Jurchescu, O. D. *Journal of Applied Physics* **2018**, *124*, 071101, DOI: `10.1063/1.5042255`.

(215) Cong, S.; Cao, Y.; Fang, X.; Wang, Y.; Liu, Q.; Gui, H.; Shen, C.; Cao, X.; Kim, E. S.; Zhou, C. *ACS Nano* **2016**, *10*, 10068–10074, DOI: `10.1021/acsnano.6b04951`.

(216) Zhao, Y.; Candebat, D.; Delker, C.; Zi, Y.; Janes, D.; Appenzeller, J.; Yang, C. *Nano Letters* **2012**, *12*, 5331–5336, DOI: `10.1021/nl302684s`.

(217) Veres, J.; Ogier, S.; Leeming, S.; Cupertino, D.; Mohialdin Khaffaf, S. *Advanced Functional Materials* **2003**, *13*, 199–204, DOI: `10.1002/adfm.200390030`.

(218) Hoffman, R. L. *Journal of Applied Physics* **2004**, *95*, 5813–5819, DOI: `10.1063/1.1712015`.

(219) Hong, D.; Yerubandi, G.; Chiang, H. Q.; Spiegelberg, M. C.; Wager, J. F. *Critical Reviews in Solid State and Materials Sciences* **2008**, *33*, 101–132, DOI: `10.1080/10408430701384808`.

(220) Pecunia, V.; Banger, K.; Sirringhaus, H. *Advanced Electronic Materials* **2015**, *1*, 1400024, DOI: `10.1002/aelm.201400024`.

(221) Takahashi, T.; Takenobu, T.; Takeya, J.; Iwasa, Y. *Applied Physics Letters* **2006**, *88*, 033505, DOI: `10.1063/1.2166698`.

(222) Anthopoulos, T. D.; Tanase, C.; Setayesh, S.; Meijer, E. J.; Hummelen, J. C.; Blom, P. W. M.; de Leeuw, D. M. *Advanced Materials* **2004**, *16*, 2174–2179, DOI: `10.1002/adma.200400309`.

(223) Meijer, E. J.; de Leeuw, D. M.; Setayesh, S.; van Veenendaal, E.; Huisman, B. H.; Blom, P. W. M.; Hummelen, J. C.; Scherf, U.; Klapwijk, T. M. *Nature Materials* **2003**, *2*, 678–682, DOI: `10.1038/nmat978`.

(224) Chesterfield, R.; Newman, C.; Pappenfus, T.; Ewbank, P.; Haukaas, M.; Mann, K.; Miller, L.; Frisbie, C. *Advanced Materials* **2003**, *15*, 1278–1282, DOI: `10.1002/adma.200305200`.

(225) Smits, E. C. P.; Anthopoulos, T. D.; Setayesh, S.; van Veenendaal, E.; Coehoorn, R.; Blom, P. W. M.; de Boer, B.; de Leeuw, D. M. *Physical Review B* **2006**, *73*, 205316, DOI: `10.1103/PhysRevB.73.205316`.

(226) Tersoff, J.; Freitag, M.; Tsang, J. C.; Avouris, P. *Applied Physics Letters* **2005**, *86*, 263108, DOI: `10.1063/1.1957116`.

(227) Zaumseil, J.; Friend, R. H.; Sirringhaus, H. *Nature Materials* **2006**, *5*, 69–74, DOI: `10.1038/nmat1537`.

(228) Swensen, J.; Moses, D.; Heeger, A. J. *Synthetic Metals* **2005**, *153*, 53–56, DOI: `10.1016/j.synthmet.2005.07.258`.

(229) Zaumseil, J.; Donley, C. L.; Kim, J.-S.; Friend, R. H.; Sirringhaus, H. *Advanced Materials* **2006**, *18*, 2708–2712, DOI: `10.1002/adma.200601080`.

(230) Takahashi, T.; Takenobu, T.; Takeya, J.; Iwasa, Y. *Advanced Functional Materials* **2007**, *17*, 1623–1628, DOI: `10.1002/adfm.200700046`.

(231) Hotta, S.; Yamao, T.; Bisri, S. Z.; Takenobu, T.; Iwasa, Y. *J. Mater. Chem. C* **2014**, *2*, 965–980, DOI: `10.1039/C3TC31998A`.

(232) Misewich, J. A.; Martel, R.; Avouris, P.; Tsang, J. C.; Heinze, S.; Tersoff, J. *Science* **2003**, *300*, 783–786, DOI: `10.1126/science.1081294`.

(233) Freitag, M.; Chen, J.; Tersoff, J; Tsang, J.; Fu, Q.; Liu, J.; Avouris, P. *Physical Review Letters* **2004**, *93*, 076803, DOI: `10.1103/PhysRevLett.93.076803`.

(234) Engel, M.; Small, J. P.; Steiner, M.; Freitag, M.; Green, A. A.; Hersam, M. C.; Avouris, P. *ACS Nano* **2008**, *2*, 2445–2452, DOI: `10.1021/nn800708w`.

(235) Paasch, G.; Lindner, T.; Rost-Bietsch, C.; Karg, S.; Riess, W.; Scheinert, S. *Journal of Applied Physics* **2005**, *98*, 084505, DOI: `10.1063/1.2085314`.

(236) Charrier, D.; de Vries, T.; Mathijssen, S.; Geluk, E.-J.; Smits, E.; Kemerink, M.; Janssen, R. *Organic Electronics* **2009**, *10*, 994–997, DOI: `10.1016/j.orgel.2009.03.010`.

(237) Kemerink, M.; Charrier, D. S. H.; Smits, E. C. P.; Mathijssen, S. G. J.; de Leeuw, D. M.; Janssen, R. A. J. *Applied Physics Letters* **2008**, *93*, 033312, DOI: `10.1063/1.2963488`.

(238) Roelofs, W. S. C.; Adriaans, W. H.; Janssen, R. A. J.; Kemerink, M.; de Leeuw, D. M. *Advanced Functional Materials* **2013**, *23*, 4133–4139, DOI: `10.1002/adfm.201203568`.

(239) Zaumseil, J. *Advanced Functional Materials* **2020**, *30*, 1905269, DOI: `10.1002/adfm.201905269`.

(240) Zaumseil, J.; Kline, R. J.; Sirringhaus, H. *Applied Physics Letters* **2008**, *92*, 073304, DOI: `10.1063/1.2836790`.

(241) Zaumseil, J.; Groves, C.; Winfield, J. M.; Greenham, N. C.; Sirringhaus, H. *Advanced Functional Materials* **2008**, *18*, 3630–3637, DOI: `10.1002/adfm.200800863`.

(242) Cao, Q.; Rogers, J. A. *Advanced Materials* **2009**, *21*, 29–53, DOI: `10.1002/adma.200801995`.

(243) Sun, D.-M.; Liu, C.; Ren, W.-C.; Cheng, H.-M. *Small* **2013**, *9*, 1188–1205, DOI: `10.1002/smll.201203154`.

(244) Park, S.; Vosguerichian, M.; Bao, Z. *Nanoscale* **2013**, *5*, 1727, DOI: `10.1039/c3nr33560g`.

(245) Jariwala, D.; Sangwan, V. K.; Lauhon, L. J.; Marks, T. J.; Hersam, M. C. *Chem. Soc. Rev.* **2013**, *42*, 2824–2860, DOI: `10.1039/C2CS35335K`.

(246) Bisri, S. Z.; Piliego, C.; Gao, J.; Loi, M. A. *Advanced Materials* **2014**, *26*, 1176–1199, DOI: `10.1002/adma.201304280`.

(247) Zaumseil, J. *Semiconductor Science and Technology* **2015**, *30*, 074001, DOI: `10.1088/0268-1242/30/7/074001`.

(248) Sun, D.; Liu, C.; Ren, W.; Cheng, H. *Advanced Electronic Materials* **2016**, 1–22, DOI: `10.1002/aelm.201600229`.

(249) Zaumseil, J. *Advanced Electronic Materials* **2019**, *5*, 1800514, DOI: `10.1002/aelm.201800514`.

(250) Hirotani, J.; Ohno, Y. *Topics in Current Chemistry* **2019**, *377*, 3, DOI: `10.1007/s41061-018-0227-y`.

(251) Franklin, A. D.; Luisier, M.; Han, S.-J.; Tulevski, G.; Breslin, C. M.; Gignac, L.; Lundstrom, M. S.; Haensch, W. *Nano Letters* **2012**, *12*, 758–762, DOI: `10.1021/nl203701g`.

(252) Cao, Q.; Han, S.-j.; Tersoff, J.; Franklin, A. D.; Zhu, Y.; Zhang, Z.; Tulevski, G. S.; Tang, J.; Haensch, W. *Science* **2015**, *350*, 68–72, DOI: `10.1126/science.aac8006`.

(253) Zhang, Y.; Chang, A.; Cao, J.; Wang, Q.; Kim, W.; Li, Y.; Morris, N.; Yenilmez, E.; Kong, J.; Dai, H. *Applied Physics Letters* **2001**, *79*, 3155–3157, DOI: `10.1063/1.1415412`.

(254) Ismach, A.; Kantorovich, D.; Joselevich, E. *Journal of the American Chemical Society* **2005**, *127*, 11554–11555, DOI: `10.1021/ja052759m`.

(255) Orofeo, C. M.; Ago, H.; Ikuta, T.; Takahasi, K.; Tsuji, M. *Nanoscale* **2010**, *2*, 1708, DOI: `10.1039/c0nr00170h`.

(256) Kang, S. J.; Kocabas, C.; Ozel, T.; Shim, M.; Pimparkar, N.; Alam, M. A.; Rotkin, S. V.; Rogers, J. A. *Nature Nanotechnology* **2007**, *2*, 230–236, DOI: `10.1038/nnano.2007.77`.

(257) Collins, P. G.; Arnold, M. S.; Avouris, P. *Science* **2001**, *292*, 706–709, DOI: `10.1126/science.1058782`.

(258) Zhang, G.; Qi, P.; Wang, X.; Lu, Y.; Li, X.; Tu, R.; Bangsaruntip, S.; Mann, D.; Zhang, L.; Dai, H. *Science* **2006**, *314*, 974–977, DOI: `10.1126/science.1133781`.

(259) Cao, Q.; Han, S.-j.; Tulevski, G. S.; Zhu, Y.; Lu, D. D.; Haensch, W. *Nature Nanotechnology* **2013**, *8*, 180–186, DOI: `10.1038/nnano.2012.257`.

(260) Joo, Y.; Brady, G. J.; Arnold, M. S.; Gopalan, P. *Langmuir* **2014**, *30*, 3460–3466, DOI: `10.1021/la500162x`.

(261) Brady, G. J.; Joo, Y.; Wu, M.-Y.; Shea, M. J.; Gopalan, P.; Arnold, M. S. *ACS Nano* **2014**, *8*, 11614–11621, DOI: `10.1021/nn5048734`.

(262) Brady, G. J.; Way, A. J.; Safron, N. S.; Evensen, H. T.; Gopalan, P.; Arnold, M. S. *Science Advances* **2016**, *2*, 1–9, DOI: `10.1126/sciadv.1601240`.

(263) Hennrich, F.; Li, W.; Fischer, R.; Lebedkin, S.; Krupke, R.; Kappes, M. M. *ACS Nano* **2016**, *10*, 1888–1895, DOI: `10.1021/acsnano.5b05572`.

(264) Takahashi, T.; Takei, K.; Gillies, A. G.; Fearing, R. S.; Javey, A. *Nano Letters* **2011**, *11*, 5408–5413, DOI: `10.1021/nl203117h`.

(265) Asada, Y.; Miyata, Y.; Ohno, Y.; Kitaura, R.; Sugai, T.; Mizutani, T.; Shinohara, H. *Advanced Materials* **2010**, *22*, 2698–2701, DOI: `10.1002/adma.200904006`.

(266) Chen, B.; Zhang, P.; Ding, L.; Han, J.; Qiu, S.; Li, Q.; Zhang, Z.; Peng, L.-M. *Nano Letters* **2016**, *16*, 5120–5128, DOI: `10.1021/acs.nanolett.6b02046`.

(267) Bisri, S. Z.; Gao, J.; Derenskyi, V.; Gomulya, W.; Iezhokin, I.; Gordiichuk, P.; Herrmann, A.; Loi, M. A. *Advanced Materials* **2012**, *24*, 6147–6152, DOI: `10.1002/adma.201202699`.

(268) Ding, J.; Li, Z.; Lefebvre, J.; Cheng, F.; Dubey, G.; Zou, S.; Finnie, P.; Hrdina, A.; Scoles, L.; Lopinski, G. P.; Kingston, C. T.; Simard, B.; Malenfant, P. R. L. *Nanoscale* **2014**, *6*, 2328, DOI: `10.1039/c3nr05511f`.

(269) Chen, X. Q.; Saito, T.; Yamada, H.; Matsushige, K. *Applied Physics Letters* **2001**, *78*, 3714–3716, DOI: `10.1063/1.1377627`.

(270) Senthil Kumar, M.; Lee, S.; Kim, T.; Kim, T.; Song, S.; Yang, J.; Nahm, K.; Suh, E.-K. *Solid-State Electronics* **2003**, *47*, 2075–2080, DOI: `10.1016/S0038-1101(03)00258-2`.

(271) Shekhar, S.; Stokes, P.; Khondaker, S. I. *ACS Nano* **2011**, *5*, 1739–1746, DOI: `10.1021/nn102305z`.

(272) Jakubka, F.; Grimm, S. B.; Zakharko, Y.; Gannott, F.; Zaumseil, J. *ACS Nano* **2014**, *8*, 8477–8486, DOI: `10.1021/nn503046y`.

(273) Rother, M.; Schießl, S. P.; Zakharko, Y.; Gannott, F.; Zaumseil, J. *ACS Applied Materials & Interfaces* **2016**, *8*, 5571–5579, DOI: `10.1021/acsami.6b00074`.

(274) Derenskyi, V.; Gomulya, W.; Rios, J. M. S.; Fritsch, M.; Fröhlich, N.; Jung, S.; Allard, S.; Bisri, S. Z.; Gordiichuk, P.; Herrmann, A.; Scherf, U.; Loi, M. A. *Advanced Materials* **2014**, *26*, 5969–5975, DOI: `10.1002/adma.201401395`.

(275) Gu, J.; Han, J.; Liu, D.; Yu, X.; Kang, L.; Qiu, S.; Jin, H.; Li, H.; Li, Q.; Zhang, J. *Small* **2016**, *12*, 4993–4999, DOI: `10.1002/smll.201600398`.

(276) LeMieux, M. C.; Roberts, M.; Barman, S.; Jin, Y. W.; Kim, J. M.; Bao, Z. *Science* **2008**, *321*, 101–104, DOI: `10.1126/science.1156588`.

(277) Schießl, S. P.; Gannott, F.; Etschel, S. H.; Schweiger, M.; Grünler, S.; Halik, M.; Zaumseil, J. *Advanced Materials Interfaces* **2016**, *3*, 1600215, DOI: `10.1002/admi.201600215`.

(278) Schießl, S. P.; Rother, M.; Lüttgens, J.; Zaumseil, J. *Applied Physics Letters* **2017**, *111*, 193301, DOI: `10.1063/1.5006877`.

(279) Zhao, J.; Gao, Y.; Gu, W.; Wang, C.; Lin, J.; Chen, Z.; Cui, Z. *Journal of Materials Chemistry* **2012**, *22*, 20747, DOI: `10.1039/c2jm34598f`.

(280) Kim, B.; Jang, S.; Geier, M. L.; Prabhumirashi, P. L.; Hersam, M. C.; Dodabalapur, A. *Nano Letters* **2014**, *14*, 3683–3687, DOI: `10.1021/nl5016014`.

(281) Bucella, S. G.; Salazar-Rios, J. M.; Derenskyi, V.; Fritsch, M.; Scherf, U.; Loi, M. A.; Caironi, M. *Advanced Electronic Materials* **2016**, *2*, 1600094, DOI: `10.1002/aelm.201600094`.

(282) Homenick, C. M.; James, R.; Lopinski, G. P.; Dunford, J.; Sun, J.; Park, H.; Jung, Y.; Cho, G.; Malenfant, P. R. L. *ACS Applied Materials & Interfaces* **2016**, *8*, 27900–27910, DOI: `10.1021/acsami.6b06838`.

(283) Ha, M.; Xia, Y.; Green, A. A.; Zhang, W.; Renn, M. J.; Kim, C. H.; Hersam, M. C.; Frisbie, C. D. *ACS Nano* **2010**, *4*, 4388–4395, DOI: `10.1021/nn100966s`.

(284) Ha, M.; Seo, J.-W. T.; Prabhumirashi, P. L.; Zhang, W.; Geier, M. L.; Renn, M. J.; Kim, C. H.; Hersam, M. C.; Frisbie, C. D. *Nano Letters* **2013**, *13*, 954–960, DOI: `10.1021/nl3038773`.

(285) Cao, C.; Andrews, J. B.; Kumar, A.; Franklin, A. D. *ACS Nano* **2016**, *10*, 5221–5229, DOI: `10.1021/acsnano.6b00877`.

(286) Rother, M.; Brohmann, M.; Yang, S.; Grimm, S. B.; Schießl, S. P.; Graf, A.; Zaumseil, J. *Advanced Electronic Materials* **2017**, *3*, 1700080, DOI: `10.1002/aelm.201700080`.

(287) Rother, M.; Kruse, A.; Brohmann, M.; Matthiesen, M.; Grieger, S.; Higgins, T. M.; Zaumseil, J. *ACS Applied Nano Materials* **2018**, *1*, 3616–3624, DOI: `10.1021/acsanm.8b00756`.

(288) Cardenas, J. A.; Catenacci, M. J.; Andrews, J. B.; Williams, N. X.; Wiley, B. J.; Franklin, A. D. *ACS Applied Nano Materials* **2018**, *1*, 1863–1869, DOI: `10.1021/acsanm.8b00269`.

(289) Lau, P. H.; Takei, K.; Wang, C.; Ju, Y.; Kim, J.; Yu, Z.; Takahashi, T.; Cho, G.; Javey, A. *Nano Letters* **2013**, *13*, 3864–3869, DOI: `10.1021/nl401934a`.

(290) Koo, H.; Lee, W.; Choi, Y.; Sun, J.; Bak, J.; Noh, J.; Subramanian, V.; Azuma, Y.; Majima, Y.; Cho, G. *Scientific Reports* **2015**, *5*, 14459, DOI: `10.1038/srep14459`.

(291) Liu, Z.; Zhao, J.; Xu, W.; Qian, L.; Nie, S.; Cui, Z. *ACS Applied Materials & Interfaces* **2014**, *6*, 9997–10004, DOI: `10.1021/am502168x`.

(292) Nouchi, R.; Tomita, H.; Ogura, A.; Kataura, H.; Shiraishi, M. *Applied Physics Letters* **2008**, *92*, 253507, DOI: `10.1063/1.2949686`.

(293) Zhang, J.; Wang, C.; Fu, Y.; Che, Y.; Zhou, C. *ACS Nano* **2011**, *5*, 3284–3292, DOI: `10.1021/nn2004298`.

(294) Schneider, S.; Brohmann, M.; Lorenz, R.; Hofstetter, Y. J.; Rother, M.; Sauter, E.; Zharnikov, M.; Vaynzof, Y.; Himmel, H.-J.; Zaumseil, J. *ACS Nano* **2018**, *12*, 5895–5902, DOI: `10.1021/acsnano.8b02061`.

(295) Qian, Q.; Li, G.; Jin, Y.; Liu, J.; Zou, Y.; Jiang, K.; Fan, S.; Li, Q. *ACS Nano* **2014**, *8*, 9597–9605, DOI: `10.1021/nn503903y`.

(296) Fukumaru, T.; Fujigaya, T.; Nakashima, N. *Scientific Reports* **2015**, *5*, 7951, DOI: `10.1038/srep07951`.

(297) Geier, M. L.; Moudgil, K.; Barlow, S.; Marder, S. R.; Hersam, M. C. *Nano Letters* **2016**, *16*, 4329–4334, DOI: `10.1021/acs.nanolett.6b01393`.

(298) Lee, S. Y.; Lee, S. W.; Kim, S. M.; Yu, W. J.; Jo, Y. W.; Lee, Y. H. *ACS Nano* **2011**, *5*, 2369–2375, DOI: `10.1021/nn200270e`.

(299) Shim, M.; Javey, A.; Shi Kam, N. W.; Dai, H. *Journal of the American Chemical Society* **2001**, *123*, 11512–11513, DOI: `10.1021/ja0169670`.

(300) Ha, T.-J.; Chen, K.; Chuang, S.; Yu, K. M.; Kiriya, D.; Javey, A. *Nano Letters* **2015**, *15*, 392–397, DOI: `10.1021/nl5037098`.

(301) Klauk, H. *Advanced Electronic Materials* **2018**, *4*, 1700474, DOI: `10.1002/aelm.201700474`.

(302) Han, S.-J.; Tang, J.; Kumar, B.; Falk, A.; Farmer, D.; Tulevski, G.; Jenkins, K.; Afzali, A.; Oida, S.; Ott, J.; Hannon, J.; Haensch, W. *Nature Nanotechnology* **2017**, *12*, 861–865, DOI: `10.1038/nnano.2017.115`.

(303) Panzer, M. J.; Frisbie, C. D. In *Organic Field-Effect Transistors*, Bao, Z., Locklin, J., Eds.; CRC Press: Boca Raton, 2007.

(304) Caironi, M.; Bird, M.; Fazzi, D.; Chen, Z.; Di Pietro, R.; Newman, C.; Facchetti, A.; Sirringhaus, H. *Advanced Functional Materials* **2011**, *21*, 3371–3381, DOI: `10.1002/adfm.201100592`.

(305) Svensson, J.; Campbell, E. E. B. *Journal of Applied Physics* **2011**, *110*, 111101, DOI: `10.1063/1.3664139`.

(306) Waldrip, M.; Jurchescu, O. D.; Gundlach, D. J.; Bittle, E. G. *Advanced Functional Materials* **2020**, *30*, 1904576, DOI: `10.1002/adfm.201904576`.

(307) Léonard, F.; Tersoff, J. *Physical Review Letters* **2000**, *84*, 4693–4696, DOI: `10.1103/PhysRevLett.84.4693`.

(308) Léonard, F.; Talin, A. A. *Physical Review Letters* **2006**, *97*, 026804, DOI: `10.1103/PhysRevLett.97.026804`.

(309) Svensson, J.; Sourab, A. A.; Tarakanov, Y.; Lee, D. S.; Park, S. J.; Baek, S. J.; Park, Y. W.; Campbell, E. E. B. *Nanotechnology* **2009**, *20*, 175204, DOI: `10.1088/0957-4484/20/17/175204`.

(310) Chen, Z.; Appenzeller, J.; Knoch, J.; Lin, Y.-m.; Avouris, P. *Nano Letters* **2005**, *5*, 1497–1502, DOI: `10.1021/nl0508624`.

(311) Lu, C.; An, L.; Fu, Q.; Liu, J.; Zhang, H.; Murduck, J. *Applied Physics Letters* **2006**, *88*, 133501, DOI: `10.1063/1.2190707`.

(312) Allain, A.; Kang, J.; Banerjee, K.; Kis, A. *Nature Materials* **2015**, *14*, 1195–1205, DOI: `10.1038/nmat4452`.

(313) Appenzeller, J.; Radosavljević, M.; Knoch, J.; Avouris, P. *Physical Review Letters* **2004**, *92*, 048301, DOI: `10.1103/PhysRevLett.92.048301`.

(314) Jung, K.-D.; Kim, Y. C.; Kim, B.-J.; Park, B.-G.; Shin, H.; Lee, J. D. *Japanese Journal of Applied Physics* **2008**, *47*, 3174–3178, DOI: `10.1143/JJAP.47.3174`.

(315) Gundlach, D. J.; Zhou, L.; Nichols, J. A.; Jackson, T. N.; Necliudov, P. V.; Shur, M. S. *Journal of Applied Physics* **2006**, *100*, 024509, DOI: `10.1063/1.2215132`.

(316) Pesavento, P. V.; Puntambekar, K. P.; Frisbie, C. D.; McKeen, J. C.; Ruden, P. P. *Journal of Applied Physics* **2006**, *99*, 094504, DOI: `10.1063/1.2197033`.

(317) Bürgi, L.; Sirringhaus, H.; Friend, R. H. *Applied Physics Letters* **2002**, *80*, 2913–2915, DOI: `10.1063/1.1470702`.

(318) Xu, Y.; Minari, T.; Tsukagoshi, K.; Chroboczek, J. A.; Ghibaudo, G. *Journal of Applied Physics* **2010**, *107*, 114507, DOI: `10.1063/1.3432716`.

(319) Minari, T.; Miyadera, T.; Tsukagoshi, K.; Aoyagi, Y.; Ito, H. *Applied Physics Letters* **2007**, *91*, 053508, DOI: `10.1063/1.2759987`.

(320) Podzorov, V.; Sysoev, S. E.; Loginova, E.; Pudalov, V. M.; Gershenson, M. E. *Applied Physics Letters* **2003**, *83*, 3504–3506, DOI: `10.1063/1.1622799`.

(321) Chesterfield, R. J.; McKeen, J. C.; Newman, C. R.; Frisbie, C. D.; Ewbank, P. C.; Mann, K. R.; Miller, L. L. *Journal of Applied Physics* **2004**, *95*, 6396–6405, DOI: `10.1063/1.1710729`.

(322) Pesavento, P. V.; Chesterfield, R. J.; Newman, C. R.; Frisbie, C. D. *Journal of Applied Physics* **2004**, *96*, 7312–7324, DOI: `10.1063/1.1806533`.

(323) Choi, H. H.; Cho, K.; Frisbie, C. D.; Sirringhaus, H.; Podzorov, V. *Nature Materials* **2017**, *17*, 2–7, DOI: `10.1038/nmat5035`.

(324) Brohmann, M.; Rother, M.; Schießl, S. P.; Preis, E.; Allard, S.; Scherf, U.; Zaumseil, J. *The Journal of Physical Chemistry C* **2018**, *122*, 19886–19896, DOI: `10.1021/acs.jpcc.8b04302`.

(325) Cao, Y.; Cong, S.; Cao, X.; Wu, F.; Liu, Q.; Amer, M. R.; Zhou, C. *Topics in Current Chemistry* **2017**, *375*, 75, DOI: `10.1007/s41061-017-0160-5`.

(326) Zhang, H.; Xiang, L.; Yang, Y.; Xiao, M.; Han, J.; Ding, L.; Zhang, Z.; Hu, Y.; Peng, L.-M. *ACS Nano* **2018**, *12*, 2773–2779, DOI: `10.1021/acsnano.7b09145`.

(327) Geier, M. L.; McMorrow, J. J.; Xu, W.; Zhu, J.; Kim, C. H.; Marks, T. J.; Hersam, M. C. *Nature Nanotechnology* **2015**, *10*, 944–948, DOI: `10.1038/nnano.2015.197`.

(328) Tang, J.; Cao, Q.; Tulevski, G.; Jenkins, K. A.; Nela, L.; Farmer, D. B.; Han, S.-J. *Nature Electronics* **2018**, *1*, 191–196, DOI: `10.1038/s41928-018-0038-8`.

(329) Gaviria Rojas, W. A.; McMorrow, J. J.; Geier, M. L.; Tang, Q.; Kim, C. H.; Marks, T. J.; Hersam, M. C. *Nano Letters* **2017**, *17*, 4976–4981, DOI: `10.1021/acs.nanolett.7b02118`.

(330) Berger, F. J.; Higgins, T. M.; Rother, M.; Graf, A.; Zakharko, Y.; Allard, S.; Matthiesen, M.; Gotthardt, J. M.; Scherf, U.; Zaumseil, J. *ACS Applied Materials & Interfaces* **2018**, *10*, 11135–11142, DOI: `10.1021/acsami.8b00643`.

(331) Graf, A.; Held, M.; Zakharko, Y.; Tropf, L.; Gather, M. C.; Zaumseil, J. *Nature Materials* **2017**, *16*, 911–917, DOI: `10.1038/nmat4940`.

(332) Ye, Y.; Bindl, D. J.; Jacobberger, R. M.; Wu, M.-Y.; Roy, S. S.; Arnold, M. S. *Small* **2014**, *10*, 3299–3306, DOI: `10.1002/smll.201400696`.

(333) Bisri, S. Z.; Derenskyi, V.; Gomulya, W.; Salazar-Rios, J. M.; Fritsch, M.; Fröhlich, N.; Jung, S.; Allard, S.; Scherf, U.; Loi, M. A. *Advanced Electronic Materials* **2016**, *2*, 1500222, DOI: `10.1002/aelm.201500222`.

(334) Joo, Y.; Brady, G. J.; Kanimozhi, C.; Ko, J.; Shea, M. J.; Strand, M. T.; Arnold, M. S.; Gopalan, P. *ACS Applied Materials & Interfaces* **2017**, *9*, 28859–28867, DOI: `10.1021/acsami.7b06850`.

(335) Haroz, E. H.; Bachilo, S. M.; Weisman, R. B.; Doorn, S. K. *Physical Review B* **2008**, *77*, 125405, DOI: `10.1103/PhysRevB.77.125405`.

(336) Nanot, S.; Hároz, E. H.; Kim, J.-H.; Hauge, R. H.; Kono, J. *Advanced Materials* **2012**, *24*, 4977–4994, DOI: `10.1002/adma.201201751`.

(337) Held, M.; Schießl, S. P.; Miehler, D.; Gannott, F.; Zaumseil, J. *Applied Physics Letters* **2015**, *107*, 083301, DOI: `10.1063/1.4929461`.

(338) Bittle, E. G.; Basham, J. I.; Jackson, T. N.; Jurchescu, O. D.; Gundlach, D. J. *Nature Communications* **2016**, *7*, 10908, DOI: `10.1038/ncomms10908`.

(339) Natali, D.; Caironi, M. *Advanced Materials* **2012**, *24*, 1357–1387, DOI: `10.1002/adma.201104206`.

(340) Choi, H. H.; Rodionov, Y. I.; Paterson, A. F.; Panidi, J.; Saranin, D.; Kharlamov, N.; Didenko, S. I.; Anthopoulos, T. D.; Cho, K.; Podzorov, V. *Advanced Functional Materials* **2018**, *28*, 1707105, DOI: `10.1002/adfm.201707105`.

(341) Cao, Q.; Xia, M.; Kocabas, C.; Shim, M.; Rogers, J. A.; Rotkin, S. V. *Applied Physics Letters* **2007**, *90*, 023516, DOI: `10.1063/1.2431465`.

(342) Yoon, J.; Lee, D.; Kim, C.; Lee, J.; Choi, B.; Kim, D. M.; Kim, D. H.; Lee, M.; Choi, Y.-K.; Choi, S.-J. *Applied Physics Letters* **2014**, *105*, 212103, DOI: `10.1063/1.4902834`.

(343) Bürgi, L.; Richards, T. J.; Friend, R. H.; Sirringhaus, H. *Journal of Applied Physics* **2003**, *94*, 6129–6137, DOI: `10.1063/1.1613369`.

(344) Richards, T. J.; Sirringhaus, H. *Journal of Applied Physics* **2007**, *102*, 094510, DOI: `10.1063/1.2804288`.

(345) Nikiforov, G. O.; Venkateshvaran, D.; Mooser, S.; Meneau, A.; Strobel, T.; Kronemeijer, A.; Jiang, L.; Lee, M. J.; Sirringhaus, H. *Advanced Electronic Materials* **2016**, *2*, 1600163, DOI: `10.1002/aelm.201600163`.

(346) Hamadani, B. H.; Natelson, D. *Applied Physics Letters* **2004**, *84*, 443–445, DOI: `10.1063/1.1639945`.

(347) Ramuz, M. P.; Vosgueritchian, M.; Wei, P.; Wang, C.; Gao, Y.; Wu, Y.; Chen, Y.; Bao, Z. *ACS Nano* **2012**, *6*, 10384–10395, DOI: `10.1021/nn304410w`.

(348) Ramuz, M. P.; Vosgueritchian, M.; Wei, P.; Wang, C.; Gao, Y.; Wu, Y.; Chen, Y.; Bao, Z. *ACS Nano* **2013**, *7*, 4692–4692, DOI: `10.1021/nn401864e`.

(349) Joo, Y.; Brady, G. J.; Shea, M. J.; Oviedo, M. B.; Kanimozhi, C.; Schmitt, S. K.; Wong, B. M.; Arnold, M. S.; Gopalan, P. *ACS Nano* **2015**, *9*, 10203–10213, DOI: `10.1021/acsnano.5b03835`.

(350) Naumov, A. V.; Ghosh, S.; Tsyboulski, D. A.; Bachilo, S. M.; Weisman, R. B. *ACS Nano* **2011**, *5*, 1639–1648, DOI: `10.1021/nn1035922`.

(351) Chortos, A.; Pochorovski, I.; Lin, P.; Pitner, G.; Yan, X.; Gao, T. Z.; To, J. W. F.; Lei, T.; Will, J. W.; Wong, H.-S. P.; Bao, Z. *ACS Nano* **2017**, *11*, 5660–5669, DOI: `10.1021/acsnano.7b01076`.

(352) MacLeod, B. A.; Stanton, N. J.; Gould, I. E.; Wesenberg, D.; Ihly, R.; Owczarczyk, Z. R.; Hurst, K. E.; Fewox, C. S.; Folmar, C. N.; Holman Hughes, K.; Zink, B. L.; Blackburn, J. L.; Ferguson, A. J. *Energy & Environmental Science* **2017**, *10*, 2168–2179, DOI: `10.1039/C7EE01130J`.

(353) Norton-Baker, B.; Ihly, R.; Gould, I. E.; Avery, A. D.; Owczarczyk, Z. R.; Ferguson, A. J.; Blackburn, J. L. *ACS Energy Letters* **2016**, *1*, 1212–1220, DOI: `10.1021/acsenergylett.6b00417`.

(354) Brohmann, M.; Berger, F. J.; Matthiesen, M.; Schießl, S. P.; Schneider, S.; Zaumseil, J. *ACS Nano* **2019**, *13*, 7323–7332, DOI: `10.1021/acsnano.9b03699`.

(355) Yimer, Y. Y.; Bobbert, P. A.; Coehoorn, R. *Journal of Physics: Condensed Matter* **2008**, *20*, 335204, DOI: `10.1088/0953-8984/20/33/335204`.

(356) Coehoorn, R.; Bobbert, P. A. *physica status solidi (a)* **2012**, *209*, 2354–2377, DOI: `10.1002/pssa.201228387`.

(357) Pai, D. M.; Yanus, J. F.; Stolka, M. *The Journal of Physical Chemistry* **1984**, *88*, 4714–4717, DOI: `10.1021/j150664a054`.

(358) Lee, S.; Zhitomirsky, D.; Grossman, J. C. *Advanced Functional Materials* **2016**, *26*, 1554–1562, DOI: `10.1002/adfm.201504816`.

(359) Liu, Y.; Gibbs, M.; Puthussery, J.; Gaik, S.; Ihly, R.; Hillhouse, H. W.; Law, M. *Nano Letters* **2010**, *10*, 1960–1969, DOI: `10.1021/nl101284k`.

(360) Kuwahara, Y.; Nihey, F.; Ohmori, S.; Saito, T. *Carbon* **2015**, *91*, 370–377, DOI: `10.1016/j.carbon.2015.05.008`.

(361) Gui, H.; Chen, H.; Khripin, C. Y.; Liu, B.; Fagan, J. A.; Zhou, C.; Zheng, M. *Nanoscale* **2016**, *8*, 3467–3473, DOI: `10.1039/C5NR07329D`.

(362) Malhofer, A.; Rother, M.; Zakharko, Y.; Graf, A.; Schießl, S. P.; Zaumseil, J. *Organic Electronics* **2017**, *45*, 151–158, DOI: `10.1016/j.orgel.2017.03.010`.

(363) Paillet, M.; Michel, T.; Meyer, J. C.; Popov, V. N.; Henrard, L.; Roth, S.; Sauvajol, J.-L. *Physical Review Letters* **2006**, *96*, 257401, DOI: `10.1103/PhysRevLett.96.257401`.

(364) Telg, H.; Duque, J. G.; Staiger, M.; Tu, X.; Hennrich, F.; Kappes, M. M.; Zheng, M.; Maultzsch, J.; Thomsen, C.; Doorn, S. K. *ACS Nano* **2012**, *6*, 904–911, DOI: `10.1021/nn2044356`.

(365) Piao, Y.; Simpson, J. R.; Streit, J. K.; Ao, G.; Zheng, M.; Fagan, J. A.; Hight Walker, A. R. *ACS Nano* **2016**, *10*, 5252–5259, DOI: `10.1021/acsnano.6b01031`.

(366) Popov, V. N.; Henrard, L.; Lambin, P. *Physical Review B* **2005**, *72*, 035436, DOI: `10.1103/PhysRevB.72.035436`.

(367) Rentenberger, S.; Vollmer, A.; Zojer, E.; Schennach, R.; Koch, N. *Journal of Applied Physics* **2006**, *100*, 053701, DOI: `10.1063/1.2336345`.

(368) Stadlober, B.; Haas, U.; Gold, H.; Haase, A.; Jakopic, G.; Leising, G.; Koch, N.; Rentenberger, S.; Zojer, E. *Advanced Functional Materials* **2007**, *17*, 2687–2692, DOI: `10.1002/adfm.200700294`.

(369) Askeland, D. R.; Fulay, P. P.; Wright, W. J., *The Science and Engineering of Materials*, 6th ed.; Cengage Learning: Stamford, 2011.

(370) Li, H.; Gordeev, G.; Garrity, O.; Reich, S.; Flavel, B. S. *ACS Nano* **2019**, *13*, 2567–2578, DOI: `10.1021/acsnano.8b09579`.

(371) Zeng, X.; Yang, D.; Liu, H.; Zhou, N.; Wang, Y.; Zhou, W.; Xie, S.; Kataura, H. *Advanced Materials Interfaces* **2018**, *5*, 1700727, DOI: `10.1002/admi.201700727`.

(372) Fagan, J. A. *Nanoscale Advances* **2019**, *1*, 3307–3324, DOI: `10.1039/C9NA00280D`.

(373) Herrmann, N. Photosensitive Dielektrika auf der Basis von Spiropyran, Bachelor thesis, Universität Heidelberg, 2018.

(374) Angstenberger, S. Photoswitchable carbon nanotube transistors, Bachelor thesis, Universität Heidelberg, 2018.

(375) Wieland, S. Patterning the NIR Emission from (6,5) Carbon Nanotubes in Thin-Film Field-Effect Transistors, Master thesis, Universität Heidelberg, 2019.

(376) Brohmann, M.; Wieland, S.; Angstenberger, S.; Herrmann, N. J.; Lüttgens, J.; Fazzi, D.; Zaumseil, J. *ACS Applied Materials & Interfaces* **2020**, *12*, 28392–28403, DOI: `10.1021/acsami.0c05640`.

(377) Li, H.; Shi, W.; Song, J.; Jang, H.-J.; Dailey, J.; Yu, J.; Katz, H. E. *Chemical Reviews* **2019**, *119*, 3–35, DOI: `10.1021/acs.chemrev.8b00016`.

(378) Yoshida, M.; Suemori, K.; Uemura, S.; Hoshino, S.; Takada, N.; Kodzasa, T.; Kamata, T. *Japanese Journal of Applied Physics* **2010**, *49*, 1–4, DOI: `10.1143/JJAP.49.04DK09`.

(379) Leydecker, T.; Herder, M.; Pavlica, E.; Bratina, G.; Hecht, S.; Orgiu, E.; Samorì, P. *Nature Nanotechnology* **2016**, *11*, 769–775, DOI: `10.1038/nnano.2016.87`.

(380) Hou, L.; Zhang, X.; Cotella, G. F.; Carnicella, G.; Herder, M.; Schmidt, B. M.; Pätzel, M.; Hecht, S.; Cacialli, F.; Samorì, P. *Nature Nanotechnology* **2019**, *14*, 347–353, DOI: `10.1038/s41565-019-0370-9`.

(381) Zhang, X.; Hou, L.; Samorì, P. *Nature Communications* **2016**, *7*, 11118, DOI: `10.1038/ncomms11118`.

(382) Orgiu, E.; Crivillers, N.; Herder, M.; Grubert, L.; Pätzel, M.; Frisch, J.; Pavlica, E.; Duong, D. T.; Bratina, G.; Salleo, A.; Koch, N.; Hecht, S.; Samorì, P. *Nature Chemistry* **2012**, *4*, 675–679, DOI: `10.1038/nchem.1384`.

(383) Orgiu, E.; Samorì, P. *Advanced Materials* **2014**, *26*, 1827–1845, DOI: `10.1002/adma.201304695`.

(384) Russew, M.-M.; Hecht, S. *Advanced Materials* **2010**, *22*, 3348–3360, DOI: `10.1002/adma.200904102`.

(385) Zhang, J.; Zou, Q.; Tian, H. *Advanced Materials* **2013**, *25*, 378–399, DOI: `10.1002/adma.201201521`.

(386) Li, Y.; Zhang, H.; Qi, C.; Guo, X. *J. Mater. Chem.* **2012**, *22*, 4261–4265, DOI: `10.1039/C1JM14872A`.

(387) El Gemayel, M.; Börjesson, K.; Herder, M.; Duong, D. T.; Hutchison, J. A.; Ruzié, C.; Schweicher, G.; Salleo, A.; Geerts, Y.; Hecht, S.; Orgiu, E.; Samorì, P. *Nature Communications* **2015**, *6*, 6330, DOI: `10.1038/ncomms7330`.

(388) Hayakawa, R.; Petit, M.; Higashiguchi, K.; Matsuda, K.; Chikyow, T.; Wakayama, Y. *Organic Electronics* **2015**, *21*, 149–154, DOI: `10.1016/j.orgel.2015.03.011`.

(389) Kurokawa, Y.; Hayakawa, R.; Shimada, S.; Higashiguchi, K.; Noguchi, Y.; Matsuda, K.; Wakayama, Y. *Organic Electronics* **2019**, *64*, 205–208, DOI: `10.1016/j.orgel.2018.10.020`.

(390) Gobbi, M.; Bonacchi, S.; Lian, J. X.; Vercouter, A.; Bertolazzi, S.; Zyska, B.; Timpel, M.; Tatti, R.; Olivier, Y.; Hecht, S.; Nardi, M. V.; Beljonne, D.; Orgiu, E.; Samorì, P. *Nature Communications* **2018**, *9*, 2661, DOI: `10.1038/s41467-018-04932-z`.

(391) Tsuruoka, T.; Hayakawa, R.; Kobashi, K.; Higashiguchi, K.; Matsuda, K.; Wakayama, Y. *Nano Letters* **2016**, *16*, 7474–7480, DOI: `10.1021/acs.nanolett.6b03162`.

(392) Zhou, X.; Zifer, T.; Wong, B. M.; Krafcik, K. L.; Léonard, F.; Vance, A. L. *Nano Letters* **2009**, *9*, 1028–1033, DOI: `10.1021/nl8032922`.

(393) Raimondo, C.; Crivillers, N.; Reinders, F.; Sander, F.; Mayor, M.; Samori, P. *Proceedings of the National Academy of Sciences* **2012**, *109*, 12375–12380, DOI: `10.1073/pnas.1203848109`.

(394) Simmons, J. M.; In, I.; Campbell, V. E.; Mark, T. J.; Léonard, F.; Gopalan, P.; Eriksson, M. A. *Physical Review Letters* **2007**, *98*, 086802, DOI: `10.1103/PhysRevLett.98.086802`.

(395) Tsujioka, T.; Hamada, Y.; Shibata, K.; Taniguchi, A.; Fuyuki, T. *Applied Physics Letters* **2001**, *78*, 2282–2284, DOI: `10.1063/1.1366365`.

(396) Tian, H.; Yang, S. *Chemical Society Reviews* **2004**, *33*, 85, DOI: `10.1039/b302356g`.

(397) Klajn, R. *Chem. Soc. Rev.* **2014**, *43*, 148–184, DOI: `10.1039/C3CS60181A`.

(398) Bletz, M.; Pfeifer-Fukumura, U.; Kolb, U.; Baumann, W. *The Journal of Physical Chemistry A* **2002**, *106*, 2232–2236, DOI: `10.1021/jp012562q`.

(399) Bunker, B. C.; Kim, B. I.; Houston, J. E.; Rosario, R.; Garcia, A. A.; Hayes, M.; Gust, D.; Picraux, S. T. *Nano Letters* **2003**, *3*, 1723–1727, DOI: `10.1021/nl034759v`.

(400) Tyer, N. W.; Becker, R. S. *Journal of the American Chemical Society* **1970**, *92*, 1289–1294, DOI: `10.1021/ja00708a031`.

(401) Dvornikov, A. S.; Malkin, J; Rentzepis, P. M. *The Journal of Physical Chemistry* **1994**, *98*, 6746–6752, DOI: `10.1021/j100078a016`.

(402) Shen, Q.; Wang, L.; Liu, S.; Cao, Y.; Gan, L.; Guo, X.; Steigerwald, M. L.; Shuai, Z.; Liu, Z.; Nuckolls, C. *Advanced Materials* **2010**, *22*, 3282–3287, DOI: `10.1002/adma.201000471`.

(403) Lutsyk, P.; Janus, K.; Sworakowski, J.; Generali, G.; Capelli, R.; Muccini, M. *The Journal of Physical Chemistry C* **2011**, *115*, 3106–3114, DOI: `10.1021/jp108982x`.

(404) Zhang, H.; Hui, J.; Chen, H.; Chen, J.; Xu, W.; Shuai, Z.; Zhu, D.; Guo, X. *Advanced Electronic Materials* **2015**, *1*, 1500159, DOI: `10.1002/aelm.201570031`.

(405) Guo, X.; Huang, L.; O'Brien, S.; Kim, P.; Nuckolls, C. *Journal of the American Chemical Society* **2005**, *127*, 15045–15047, DOI: `10.1021/ja054335y`.

(406) Bluemmel, P.; Setaro, A.; Maity, C.; Hecht, S.; Reich, S. *Journal of Physics: Condensed Matter* **2012**, *24*, 394005, DOI: `10.1088/0953-8984/24/39/394005`.

(407) Bluemmel, P.; Setaro, A.; Maity, C.; Hecht, S.; Reich, S. *physica status solidi (b)* **2012**, *249*, 2479–2482, DOI: `10.1002/pssb.201200387`.

(408) Malic, E.; Setaro, A.; Bluemmel, P.; Sanz-Navarro, C. F.; Ordejón, P.; Reich, S.; Knorr, A. *Journal of Physics: Condensed Matter* **2012**, *24*, 394006, DOI: `10.1088/0953-8984/24/39/394006`.

(409) Setaro, A.; Bluemmel, P.; Maity, C.; Hecht, S.; Reich, S. *Advanced Functional Materials* **2012**, *22*, 2425–2431, DOI: `10.1002/adfm.201102451`.

(410) Setaro, A.; Adeli, M.; Glaeske, M.; Przyrembel, D.; Bisswanger, T.; Gordeev, G.; Maschietto, F.; Faghani, A.; Paulus, B.; Weinelt, M.; Arenal, R.; Haag, R.; Reich, S. *Nature Communications* **2017**, *8*, 14281, DOI: `10.1038/ncomms14281`.

(411) Godin, A. G.; Setaro, A.; Gandil, M.; Haag, R.; Adeli, M.; Reich, S.; Cognet, L. *Science Advances* **2019**, *5*, eaax1166, DOI: `10.1126/sciadv.aax1166`.

(412) Jakubka, F.; Backes, C.; Gannott, F.; Mundloch, U.; Hauke, F.; Hirsch, A.; Zaumseil, J. *ACS Nano* **2013**, *7*, 7428–7435, DOI: `10.1021/nn403419d`.

(413) Tomioka, H.; Itoh, T. *J. Chem. Soc., Chem. Commun.* **1991**, 532–533, DOI: `10.1039/C39910000532`.

(414) Shima, M.; Sato, M.; Atsumi, M.; Hatada, K. *Polymer Journal* **1994**, *26*, 579–585, DOI: `10.1295/polymj.26.579`.

(415) Egginger, M.; Bauer, S.; Schwödiauer, R.; Neugebauer, H.; Sariciftci, N. S. *Monatshefte für Chemie - Chemical Monthly* **2009**, *140*, 735–750, DOI: `10.1007/s00706-009-0149-z`.

(416) Sharma, A.; Janssen, N. M. A.; Mathijssen, S. G. J.; de Leeuw, D. M.; Kemerink, M.; Bobbert, P. A. *Physical Review B* **2011**, *83*, 125310, DOI: `10.1103/PhysRevB.83.125310`.

(417) Jin, S. H.; Islam, A. E.; Kim, T.-i.; Kim, J.-h.; Alam, M. A.; Rogers, J. A. *Advanced Functional Materials* **2012**, *22*, 2276–2284, DOI: `10.1002/adfm.201102814`.

(418) Tanaka, Y.; Hirana, Y.; Niidome, Y.; Kato, K.; Saito, S.; Nakashima, N. *Angewandte Chemie International Edition* **2009**, *48*, 7655–7659, DOI: `10.1002/anie.200902468`.

(419) Balcı Leinen, M.; Berger, F. J.; Klein, P.; Mühlinghaus, M.; Zorn, N. F.; Settele, S.; Allard, S.; Scherf, U.; Zaumseil, J. *The Journal of Physical Chemistry C* **2019**, *123*, 22680–22689, DOI: `10.1021/acs.jpcc.9b07291`.

(420) Kinashi, K.; Nakamura, S.; Imamura, M.; Ishida, K.; Ueda, Y. *Journal of Physical Organic Chemistry* **2012**, *25*, 462–466, DOI: `10.1002/poc.1926`.

(421) Bronner, C.; Schulze, G.; Franke, K. J.; Pascual, J. I.; Tegeder, P. *Journal of Physics: Condensed Matter* **2011**, *23*, 484005, DOI: `10.1088/0953-8984/23/48/484005`.

(422) Shiraishi, Y.; Adachi, K.; Itoh, M.; Hirai, T. *Organic Letters* **2009**, *11*, 3482–3485, DOI: `10.1021/ol901399a`.

(423) Sumaru, K.; Kameda, M.; Kanamori, T.; Shinbo, T. *Macromolecules* **2004**, *37*, 4949–4955, DOI: `10.1021/ma049661x`.

(424) Shiraishi, Y.; Itoh, M.; Hirai, T. *Physical Chemistry Chemical Physics* **2010**, *12*, 13737, DOI: `10.1039/c0cp00140f`.

(425) Perebeinos, V.; Rotkin, S. V.; Petrov, A. G.; Avouris, P. *Nano Letters* **2009**, *9*, 312–316, DOI: `10.1021/nl8030086`.

(426) Fischetti, M. V.; Neumayer, D. A.; Cartier, E. A. *Journal of Applied Physics* **2001**, *90*, 4587–4608, DOI: `10.1063/1.1405826`.

(427) Zorn, N. F.; Scuratti, F.; Berger, F. J.; Perinot, A.; Heimfarth, D.; Caironi, M.; Zaumseil, J. *ACS Nano* **2020**, *14*, 2412–2423, DOI: `10.1021/acsnano.9b09761`.

(428) Balcı Leinen, M.; Klein, P.; Sebastian, F. L.; Zorn, N. F.; Adamczyk, S.; Allard, S.; Scherf, U.; Zaumseil, J. *Advanced Electronic Materials* **2020**, 2000717, DOI: `10.1002/aelm.202000717`.

(429) Van de Burgt, Y.; Melianas, A.; Keene, S. T.; Malliaras, G.; Salleo, A. *Nature Electronics* **2018**, *1*, 386–397, DOI: `10.1038/s41928-018-0103-3`.

EIDESSTATTLICHE VERSICHERUNG

Eidesstattliche Versicherung gemäß §8 der Promotionsordnung für die Naturwissenschaftlich-Mathematische Gesamtfakultät der Universität Heidelberg

1. Bei der eingereichten Dissertation zu dem Thema *Investigation and Modification of Charge Transport in Semiconducting Carbon Nanotube Networks* handelt es sich um meine eigenständig erbrachte Leistung.

2. Ich habe nur die angegebenen Quellen und Hilfsmittel benutzt und mich keiner unzulässigen Hilfe Dritter bedient. Insbesondere habe ich wörtlich oder sinngemäß aus anderen Werken übernommene Inhalte als solche kenntlich gemacht.

3. Die Arbeit oder Teile davon habe ich nicht an einer Hochschule des In- oder Auslands als Bestandteil einer Prüfungs- oder Qualifikationsleitung vorgelegt.

4. Die Richtigkeit der vorstehenden Erklärungen bestätige ich.

5. Die Bedeutung der eidesstattlichen Versicherung und die strafrechtlichen Folgen einer unrichtigen oder unvollständigen eidesstattlichen Versicherung sind mir bekannt.

Ich versichere an Eides statt, dass ich nach bestem Wissen die reine Wahrheit erklärt und nichts verschwiegen habe.

Heidelberg, 30. Oktober 2020

Maximilian Brohmann